X-ray Bragg Projection Ptychography for nano-materials

by Nicolas Georges Gilbert Burdet

Submitted for the requirements for the degree of Doctor of Philosophy at University College London

Supervised by Prof. Ian K. Robinson

London Centre for Nanotechnology & Department of Physics and Astronomy
University College London
December 2014

Declaration

I, Nicolas Georges Gilbert Burdet confirm that the work presented in this thesis is my own. Where information has been derived from other sources, I confirm that this has been indicated in the thesis.

Nicolas Georges Gilbert Burdet, December 2014

Abstract

Progress in nanotechnology critically relies on high resolution probing tools, and X-ray coherent diffraction imaging (CDI) is certainly an attractive method for exploring science at such small scales. Thus, the aim of this PhD is to study structural properties of nano-materials using X-ray CDI, with a special motivation to combine Bragg CDI with ptychography. The former has ability to retrieve the complex density and strain maps of nano-meso crystalline objects, and the latter uses translational diversity to produce quantitative maps of the complex transmission function of non-crystalline objects. As both techniques promote highly sensitive phase-contrast properties, the thesis exploits their agreement to reveal the morphology of domain structures in metallic thin films. Additionally, it is demonstrated that Bragg-ptychography is an evolutionary improvement to probe the structure of 'highly' strained crystals, with respect to its Bragg-CDI counterpart. However, the adaptation of ptychography to the Bragg geometry is not without difficulties and comes with more experimental cost. Therefore, the effects of experimental uncertainties, e.g., scan positions undetermination, partial coherence, and time-varying probes are assessed throughout the thesis and corrected for by implementation of suitable refinement methods. Furthermore, it is shown how the set-up at beamline 34-ID-C at the Advanced Photon Source, used for the experimental measurements can be optimized for better ptychographical reconstructions.

Contents

1 Introduction 22

2 Coherent Diffraction Imaging 25

- 2.1 Propagation of scalar fields 26
  - 2.1.1 X-ray interaction with matter 29
- 2.2 Coherence of wavefields 30
  - 2.2.1 Spatial or transverse coherence 32
  - 2.2.2 Measuring coherence 33
  - 2.2.3 Temporal or longitudinal coherence 34
- 2.3 Synchrotron source 34
- 2.4 Focusing optics 39
- 2.5 Measuring and inverting the diffraction patterns 43
  - 2.5.1 X-ray detection systems 43
  - 2.5.2 Resolution 44
  - 2.5.3 Sampling requirements 47
  - 2.5.4 Phase retrieval algorithm 48
- 2.6 Advances in Coherent Diffractive imaging 52

3 Ptychography 56

- 3.1 Ptychographic Iterative Engines 56
  - 3.1.1 Difference Map 59
- 3.2 Simulation and experimental parameters 63
  - 3.2.1 Error assessment 65
  - 3.2.2 Scans 66
- 3.3 Positions determination 69
  - 3.3.1 Annealing based algorithm for ptychography 71
  - 3.3.2 Cross-correlation based position determination 77
- 3.4 Partial coherence correction 78
  - 3.4.1 Theory behind partial coherence correction 79

3.4.2 Simulations . . . 81
3.4.3 Interpretation of reconstruction results . . . 85
3.4.4 Multimodal decomposition . . . 86
3.5 Towards real-time ptychographic reconstruction . . . 89
3.5.1 Parallelisation strategy . . . 90
3.5.2 Dynamical probe reconstruction . . . 91
3.6 Ptychography-tomography . . . 94
3.6.1 3D spatial structure of aluminium epoxy anti-corrosive marine coatings . . . 97
3.6.2 3D spatial structure of virus crystals . . . 98

4 Experimental realisation at APS 101
4.1 Experimental set-up . . . 102
4.1.1 Focusing optics . . . 105
4.1.2 Experimental data handling . . . 105
4.1.3 Test pattern for APS . . . 107
4.2 Wavefield characterization . . . 108
4.2.1 Intro . . . 108
4.2.2 KB mirror . . . 113
4.3 Probe bandwidth experiment . . . 116
4.3.1 Probe diversity: simulations . . . 119
4.3.2 Discussion . . . 120

5 Bragg Ptychography 126
5.1 Bragg CDI . . . 126
5.1.1 Theory behind Bragg CDI . . . 126
5.1.2 Ptychography in Bragg geometry . . . 133
5.1.3 Ptychography on gold nanocrystals . . . 135
5.1.4 Simulations: crystal contained within the beam . . . 139
5.1.5 Zeolite micro-crystal . . . 140
5.2 Bragg projection ptychography of domains in metal thin films . . . 146
5.2.1 Introduction to thin films . . . 147
5.2.2 Bragg projections . . . 150
5.2.3 Simulations on domain structure . . . 151
5.2.4 Experimental parameters . . . 157
5.2.5 Reconstruction attempts . . . 159
5.2.6 Analysis of the phase domains . . . 171
5.2.7 Reconstructions of Molybdenum data . . . 175

6 Conclusions **180**

List of Figures

2.1 Wave-front decomposition of an outgoing wave-vector 28

2.2 Schematic sketch of the Young's double slit experiment 31

2.3 Longitudinal coherence length 34

2.4 Synchrotron radiation 35

2.5 Spectral brightness of x-ray sources 37

2.6 Storage rings 38

2.7 Typical set-up of elliptical mirrors used at synchrotron radiation sources for focusing 40

2.8 A schematic of a binary zone plate 41

2.9 Hard x-ray focusing optics 42

2.10 Matlab histogram of a photon count for a typical experimental data set coming from a CCD. The first photon peak is used for the noise threshold. 44

2.11 Numerical aperutre for a conventional imaging setup and for a diffractive imaging system 45

2.12 The maximum resolution achievable with CDI for the maximum tolerable dose 46

2.13 Coherent diffraction measurement of a continuous fringed intensity pattern 48

2.14 Flow chart for Error Reduction 49

2.15 Error metric showings local minima and a global minimum. 51

2.16 Three dimensional reconstruction of a buried object 52

2.17 Three dimensional reconstruction of a chromosome 53

2.18 Reconstruction of a nanotube using electron CDI 54

2.19 Schematic depiction of single-particle coherent diffractive imaging with an XFEL pulse 55

3.1 Ptychographic scheme 57

3.2 Essai. 59

3.3 Difference map scheme 60
3.4 Sketch of the behaviour of ER and DM algorithms as projections onto convex sets 62
3.5 HSV plot of pinholes 65
3.6 Ptychographic scans 66
3.7 Left to right: A typical diffraction pattern with its number of photons and hence SNR decreasing. 69
3.8 Scan positions correction 71
3.9 Reconstructed complex-valued image of a Winter Jasmine flower . . . 73
3.10 A schematic representation of the position-correcting algorithm . . . 74
3.11 simulated error in positions 75
3.12 Positions retrieval 76
3.13 Difference map scheme for cross-correlation based position determination 78
3.14 A source of decoherence affects the measured intensity distribution by reducing the visibility of the fringes (here on the left side, the blurring is exagerated). 79
3.15 Reconstructions of a gold nano-crystal 82
3.16 Reconstructions of a simulated nano-crystal 83
3.17 Lena image used for simulations 84
3.18 Results of reconstructions using both the PC and FC projections . . . 84
3.19 Plot of the error metric value for the partial coherence simulations . . 85
3.20 Results of reconstructed coherence function 86
3.21 Results of reconstructions using multiple modes in the illumination . 88
3.22 A Matlab benchmark as a function of FFTs performed with and without transfer between CPU and GPU 90
3.23 Four quadrants of an image reconstructed independently 91
3.24 Pupilar function propagated along the z direction 93
3.25 Reconstructed images with and without dynamical probe correction. Lower row: reconstruction of the probe as a function of its evolution. Scale bar, 2μm. 93
3.26 Illustration of the the Fourier slice theorem 94
3.27 Schematic of data collection in a ptycho-tomo experiment 96
3.28 Scheme used by Guizar for ptychography tomography [1] 97
3.29 Results of the aluminium epoxy marine coating obtained by 3D ptychographic X-ray tomography 98

3.30 Slice of a tomogram showing a slurry of dried crystals inside the tip of a capillary . . . 99
3.31 An image of one of the raw diffraction images which went in to the ptychographic reconstructions . . . 100

4.1 Image of roller-blade slits . . . 103
4.2 Schematic of x-ray propagation at APS . . . 104
4.3 Simulation of x-ray beam propagation . . . 104
4.4 Schematic of KB mirror bender . . . 106
4.5 Images of a test pattern . . . 107
4.6 Sketch of the experimental setup at 34-ID-C . . . 109
4.7 Schematic of the Quiney cycle for an FZP . . . 111
4.8 Reconstructions of an x-ray focused beam . . . 112
4.9 Propagation of a FZP focused x-ray beam . . . 113
4.10 Reconstructed tungsten pin with difference map. Scale bar, 1μm. . . 113
4.11 Reconstructed probe coming from a pair of KB mirror . . . 114
4.12 Propagation of a KB focused x-ray beam . . . 115
4.13 Plot of the focal sizes for the Kirkpatrick-Baez (KB) mirror system . 115
4.14 Reconstructed objects and probes for detectors located at different distances from the sample . . . 118
4.15 Simulated Siemens star of size,11.4 μm . . . 120
4.16 Images of simulated probes diversity . . . 121
4.17 Images for the reconstructions on simulated diversity . . . 122
4.18 Metrics comparison for the reconstructions on phase diversity . . . 123
4.19 Reconstruction of 3 KB modes . . . 124
4.20 SEM image of randomly-positioned drilled holes . . . 125

5.1 Two dimensional real and reciprocal space infinite lattices . . . 128
5.2 Ewald circle construction of a monochromatic scattering experiment 128
5.3 2D slices from the 3D scattered amplitude of an octahedral fcc crystal 130
5.4 Bragg scattering from a strained lattice . . . 131
5.5 Simulated amplitudes and phases of strong phase structures in 2D . 132
5.6 A typical schematic layout of a Newport Six-Axis Kappa diffractometer . . . 133
5.7 Schematic of the SLS experiment . . . 136
5.8 Reconstructed phase and amplitude of a gold nanocrystal . . . 138
5.9 Unsuccessful ptychographic reconstruction of a gold nano-crystal. . . 138

5.10 Illustration of a crystal scanning the extent of the complex illumination function. 139
5.11 Simulated crystals 141
5.12 Reconstructed objects and probe of simulated crystals for scan with 150 nm radial steps 141
5.13 Reconstructed objects and probe of simulated crystals for scan with 250 nm radial steps 142
5.14 Reconstruted objects and probe of simulated crystals for scan with 250 nm radial steps 143
5.15 Calculated 3D CXD patterns for a hexagonal parallelepiped 144
5.16 Ptychographic reconstruction of zeolite micro-crystal, shown in hue color. Scale bar, 1μm. 145
5.17 Model of the Nb(110) Sapphire(1120) interface 148
5.18 Three-dimensional epitaxial relationship between Nb and Al2O3, shown for the different substrate orientations. Figure and caption taken from [2]. 150
5.19 Bragg projection ptychography geometry 151
5.20 Scale bar 152
5.21 Two-phase system simulated object 154
5.22 Images showing the progress of convergence for simulated domains . 155
5.23 Reconstructed amplitude and phase domain for 150 iterations of DM when full convergence is obtained, zoom over the central part of the objects. 156
5.24 Amplitude and phase domain reconstructed from an 'untransformed' scan, zoom over the central part of the objects. 156
5.25 Reconstructed images of simulated domains from three different random start 157
5.26 Typical coherent diffraction pattern taken at the Nb (110) specular Bragg peak. 159
5.27 Plot of the speckle profile 160
5.28 Images of first experimental reconstructions 161
5.29 Dynamical scan transformations analysis 164
5.30 Ptychographic reconstruction using 2 dynamical probes 165
5.31 Ptychographic reconstruction using 8 dyncamical probes 166
5.32 Ptychographic reconstruction using 14 probes 167
5.33 Plot of difference map error metric final value as function of illuminations number D in the ptychographic reconstructions 168

5.34 Plot of the corrected positional points as a function of illuminations number . . . 169
5.35 Mean error (Δ_{avg}^{final}) as a function of illuminations number (D) used in the ptychographic reconstruction of Nb(110) data. The amplitude of the mean error depends on the ability of the algorithm to retrieve the illumination fluctuations. . . . 170
5.36 Plot of difference map error metrics as a function of illuminations number used in the reconstruction of Nb(110) data. The best error metric (yellow) corresponds to the use of 2 probes. . . . 170
5.37 Central region of phase objects reconstructed with 8 dynamical probes 171
5.38 Central region of phase objects reconstructed with 8 dynamical probes 174
5.39 Central region of phase objects with suppressed phase ramp . . . 175
5.40 Typical coherent diffraction pattern taken at the Mo (110) specular Bragg peak . . . 177
5.41 Mean error (Δ_{avg}^{final}) as a function of illuminations number used in the reconstruction of data S027. The amplitude of the mean error seems to be depending on the ability of the algorithm to retrieve the illumination fluctuations. Mean error for the x direction is given (cyan plot). . . . 177
5.42 Metrics as a function of illuminations number used in the reconstruction of data S036. The best error metric (violet) corresponds to the use of 8 probes. . . . 178
5.43 Zoom on phase objects reconstructed with 8 dynamical probes . . . 179

Chapter 1

Introduction

X-ray coherent diffraction imaging is a versatile tool for nanosciences that can image the fine structure of non-crystalline and crystalline materials to resolutions of better than 20 nm at synchrotron facilities worldwide. The best spatial resolution achieved so far is 2 nm and as the method has the inherent potential for wavelength limited only resolution, efforts are being pursued to reach sub-nanometer resolution in a near future. The applications of CDI at the ultra-bright fourth generation light sources being developed around the world will accelerate this trend and most importantly will allow the imaging of ultra-fast processes in nanomaterials at ultra-high resolution.

Bragg geometry CDI has the ability to map the strain present in nano-materials with pico meter resolution, because it couples a large q-vector to the small displacements. Strain is a tensorial quantity related to stress that arises from chemical, electrical, magnetic, mechanical forces, and which due to the increased surface area to volume ratio in nanomaterials is rather distinctive from bulk materials. Ptychography is derived from scanning electron transmission microscopy and uses redundancy in acquired data to produce a quantitative map of the complex sample transmission function, with the added advantage of measuring the 3D distribution without strenuous sample preparation that is for example necessary in electron microscopy. In ptychography, a real-space constraint is formed by rastering a partially overlapping illumination, and provides enough robustness as to recover at the same time, the complex features of the probe and object, and experimental information such as the degree of coherence properties of the illumination, positional uncertainties and vibrations. While ptychography has been considered as a phase diverse technique, the introduction of another of degree phase-diversity in the probe was tested by simulations, in order to understand how to optimise experiments requiring a low X-ray dose. Development of ptychography in Bragg geometry is important because of its great potential for understanding nano-structural physics.

Chapter 2 introduces the fundamental principles behind x-ray coherent diffraction imaging, such as propagation of x-rays through free-space, their interactions with matter, the requirements on their degree of coherence, brightness and focus for experiments that rely on diffracted intensities. Based on the formalism of Fourier-space propagation, the concepts of detection, sampling, and algorithmic procedures to construct a high spatial resolution object from the lost Fourier phase components in the diffraction intensity, are reviewed.

Chapter 3 is dedicated to the generality of refinement methods for ptychography that correct for experimental nuisances, such as scan positions undetermination, partial coherence, and time-dependant variations in illumination. As these nuisances are likely to affect the ptychographic reconstructions, their implementations into the difference map algorithm and their numerical behaviours are thoroughly evaluated by means of simulated complex-valued samples. The refinement methods being algorithmically demanding, optimisation and parallelisation of the reconstruction algorithms are briefly discussed. The chapter then culminates with beautiful examples of 3D ptychographical images of the inner structure of radiation hard and biological objects, obtained by combining angular ptychographical projections with the techniques of tomography.

Chapter 4 discusses the developments of ptychography at beamline 34-ID-C of the Advanced Photon Source along with the performances of experimental measurements using test objects. Once the remarkable ability of ptychography to characterize complex wavefields is demonstrated by mean of Fresnel propagation, the impact of wavefields bandwidth and diversity on the resolution of the reconstructed images is investigated experimentally. Preliminary simulations on illumination phase-diversity to surpass the resolution limitations of the ptychographical reconstructions at 34 ID-C APS are provided, together with a general discussion on how to vary high and low phase-diversity both in the sample and illumination for future improvements at this beamline.

Chapter 5 first considers the necessary geometrical transformations to extend ptychography to the Bragg geometry, before detailing the experiments performed on nano- and micro-crystalline samples. While the suitability of Bragg-ptychography for 'highly' strained crystals will be demonstrated, the main motivation of this chapter is to demonstrate that the highly sensitive phase-contrast properties of Bragg CDI measurements combined with the translational diversity of ptychography can provide a Bragg 'dark field' imaging method capable of revealing the exact morphology of domain structure in metallic thin films. After assessing suitability for reconstructions of simulated two-phase domains by modelling of the experimental variables likely to prevent a successful implementation of the method, experimental diffraction data taken from epitaxially grown niobium and molybdenum metallic thin films; are analysed with help of a careful combination of implemented correcting mechanisms (developed in chapter 3).

Chapter 2

Coherent Diffraction Imaging

This chapter introduces the theoretical and physical tools necessary to grasp the concepts behind the experiments described in later chapters and, despite being elementary, constitutes the fundamental background of coherent diffraction imaging (CDI). Forming an image traditionally involves a set of lenses (at least a condenser and an objective) but they limit the 'quantity' of information coming from an object and at x-ray wavelength are difficult to manufacture without aberrations. While the limit set by a lens is the diffraction limit due to the classical wave nature of light, it is however possible to take advantage of light's ability to diffract, to circumvent the need for lenses. When the light approaches full coherence, the scattered light arising from interaction with the sample forms a fringed diffraction pattern from interference effects. When collected in the far-field, the relation to the local structure of the illuminated object to the diffraction pattern is simply a Fourier transform. Diffraction from interference patterns has been known since the work of Young in 1807 [3], but the invention of lasers in 1960 brought forward the theories and applications of coherent diffraction [4].

X-rays can penetrate thick samples due to their weak interactions with matter. Their relatively low wavelength ($\sim$ Å) coupled with repeated copies of a sample can reach atomic resolution of periodic objects, i.e., crystallography. X-ray microscopy can provide images of non-periodic objects but the current technology of x-ray optics limits the resolution to $\sim$10-15 nm [5, 6]. X-ray CDI or x-ray lensless imaging, which was first proposed by Sayre in the 1950's [7], fuses elements of crystallography with full-field microscopy to provide images of non-periodic objects. It now has the possibility to fill the gap and overcome the limitations of both techniques, thanks to the advent of ultra-bright coherent sources (section 2.3), efficient pixelated detectors (section 2.5.1) and computerised algorithms (section 2.5.4), all dedicated to a proper inversion of the Fourier space. It should be mentioned that electron microscopy has already elucidated many relevant structures of the nano-world due to the ultra small De-Broglie wavelength (pm) of the electrons [8]. Their high kinetic energy, strong interaction and ability to focus to sub-ångström probe, already allows dynamic imaging of single atoms [9]. Thus, electrons will always give higher resolution than X-rays in an analogous measurement. However, their strong interaction also means only thin sample (100's nm) can be used and can be hard to image in natural environments (i.e., not vacuum). X-rays can relax these demands as they can be used in almost any environment since they penetrate lots of materials in environments such as liquids, high pressure, high temperature, etc.. but also bio-materials in their natural habitat without much change to the experimental setup.

Even so, when it comes to sensitive biological materials both x-rays and electron imaging techniques are limited by radiation damage (section 2.5.2) and only the ultrashort and ultra-intense pulses of fourth generation light sources will outrun this problem by recording the unperturbed scattering or signal before destruction of the object. It is hoped that this small introduction clearly highlights the advantages for x-ray CDI in nanoscience. This chapter does not claim to present original research, but is rather a brief and specific introduction to the techniques used later.

2.1 Propagation of scalar fields

Scalar diffraction and Fourier optics constitute an essential part of the necessary comprehension of image formation in coherent diffraction imaging. Diffraction is considered when geometrical optics fail to explain an observed image (see fig. 2.6) after the perturbation of a propagating wave and is of critical importance for applications involving high resolution, i.e., astronomical imaging, lithographic processes, etc. The propagation behaviour of an electromagnetic wave is governed by Maxwell's equations, which are vector equations but a complete treatment of diffraction becomes very 'heavy' for obstacles or perturbations of any form. Ideally, when monochromatic light propagates through an ideal medium (linear, isotropic, non-dispersive and nonmagnetic), the spatial and temporal variations of the six components can be separated and the spatial variations are identical. This leads to a simplified scalar field equation, from which a wave-front in the $x - y$ plane is expressed with a phasor as:

$$U(x, y) = A(x, y).e^{i\Phi(x,y)}, \tag{2.1}$$

where $A(x, y)$ is the amplitude and $\Phi(x, y)$ is the phase which represents a deviation from a reference, i.e., a flat phase. This phasor expression aids in mathematical manipulation because the temporal term is suppressed and so a wave-front at at any other plane can be expressed as a superposition of secondary spherical wave originating from each point in the first plane. This is known as the Huygens-Fresnel principle, the foundation of the scalar diffraction theory:

$$U_2(x_2, y_2, z) = \frac{i}{\lambda} \int \int U_1(x_1, y_1) \frac{\exp{(ikr)}}{r} \cos \hat{r} dx_1 dy_1, \tag{2.2}$$

where r is the length connecting the point (x_2, y_2) with (x_2, y_2) along the unit vector $\hat{r}$. It will be assumed that z is the fundamental direction of propagation. Even if this formulation is very intuitive, the process of solving an integral over all the contributing wavelets is very demanding. Fresnel later introduced some important assumptions which are known as the paraxial approximations. Assuming the object size is small compared to the distance of the plane of observation, the cosine angle of integration is approximated to one and the spherical term is rearranged using the approximation $\sqrt{1+\epsilon} \approx 1 + \epsilon/2$. Now, given a source-plane optical field $U(x_1, y_1)$, an observation-plane field $U(x_2, y_2)$ is given by the Fresnel diffraction integral:

$$U_2(x_2, y_2) = \frac{e^{ik\Delta z}}{i\lambda\Delta z} \int_{-D/2}^{D/2} \int_{-D/2}^{D/2} U_1(x_1, y_1) e^{\frac{ik}{2\Delta Z}[(x_1-x_2)^2+(y_1-y_2)^2]} dx_1 dy_1, \tag{2.3}$$

where λ is the wavelenght, D the spatial extent of the source, ΔZ is the distance between plane, $k = 2\pi/\lambda$ is the wave-vector and the $e^{ik\Delta z}$ terms represent the phase-wave variation along the path $\Delta z = z_2 - z_1$. The square terms inside the exponential can be simplified by factoring portions out of the integral, to yield:

$$U_2(x_2, y_2) = \frac{e^{ik\Delta Z}}{i\lambda\Delta z} e^{\frac{ik}{2\Delta Z}(x_2^2+y_2^2)} \int_{-\infty}^{\infty} \int_{-\infty}^{\infty} U_1(x_1, y_1) e^{\frac{-2\pi}{\lambda\Delta Z}(x_1^2+y_1^2)} e^{\frac{ik}{2\Delta Z}[(x_1.x_2)+(y_1.y_2)]} dx1dy1. \tag{2.4}$$

If a change of variable is made,$f_{x,y} = (x, y)/(\lambda\Delta z)$, which give the relation between spatial frequencies and angle of inclination, it is realised that a bidimensionnal Fourier transform is expressed. In textbooks [10, 11], operator notation is used for more clarity, such as:

- $Q[\frac{1}{\Delta z}, r]\{U(r)\} = e^{i\frac{k}{2\Delta z}|r|^2} U(r)$ for the quadratic phase factor
- $\alpha[\frac{1}{\Delta z}, r]U(r) = \frac{1}{\Delta z} U(\frac{1}{\Delta z} r)$ for the scaling
- $F[r, f]U(r) = \int_{-\infty}^{\infty} U(r) e^{-i2\pi f.r} dr$ for the Fourier transform

- **r** is used for plane coordinates and **f** for frequency plane coordinates,

thus leaving the Fresnel integral as:

$$U_2(\mathbf{r}, z) = Q[\frac{1}{\Delta z}, r_2].\alpha[\frac{1}{\lambda \Delta Z}, r_2].F[r_1, f_1].Q[\frac{1}{\Delta Z}, r_1]\{U_1(r)\}. \tag{2.5}$$

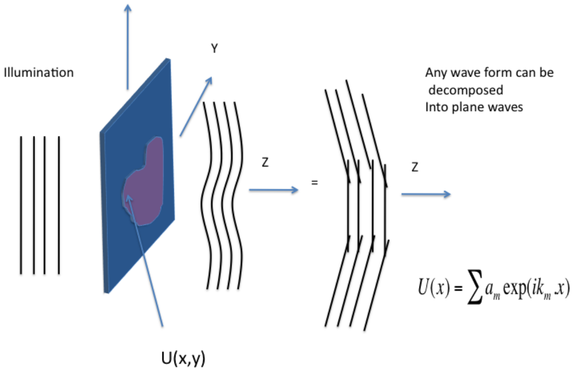

Figure 2.1: Wave-front decomposition. A wave-front can be visualised by surfaces of constant phase.

The Fresnel diffraction expression is appealing in simulations since it fits different propagation scenarios and is easy to compute [10, 11]. The Fresnel transfer propagator is routinely used for short propagation distance:

$$U_2(r_2) = F^{-1}[r_1, f_1]\left[H(f_1).F[r_1, f_1]\{U_1(r)\}\right], \tag{2.6}$$

which incorporates the transfer function H:

$$H(f) = e^{ik\Delta z}. \exp\left(-i\pi\Delta z(|\mathbf{f}|^2)\right), \tag{2.7}$$

and which could be more or less understood as the propagation of the Fourier domain. With the assumption of an extended Δz, it is possible to approximate the quadratic phase factor Q as being flat over one pixel. Specifically clarified when $\Delta z > D^2/\lambda$, where D is the maximum spatial extent of the source-plane field. This is refered to as the Fraunhofer approximation,

$$U_2(r) = F[r_1, f_1].\{U_1(r)\}. \tag{2.8}$$

In this regime the angular distribution of the diffracted wave no longer changes with increasing distance from the sample. Thus, a plane-wave after passing through the planar function $U_1(\mathbf{r})$ can be considered as a superposition of plane waves propagating in different directions (see Fig.2.1). The vast knowledge of analytic Fourier transforms may be used but for arbitrary functions, fast numerical algorithms are necessary to calculate the Fourier transform. The basic codes written for simulation of propagation and used in this thesis were compared with known analytical solutions, such as the Fresnel sine and cosine integrals for a square aperture at a given distance:

$$U(r_2) = \frac{e^{ik\Delta Z}}{2i}\{[C(\alpha_2) - C(\alpha_1)] + iS(\alpha_2) - S(\alpha_1)]\} \tag{2.9}$$

$$\times\{[C(\beta_2) - C(\beta_1)] + iS(\beta_2) - S(\beta_1)]\}, \tag{2.10}$$

where $\alpha_{1,2}$ and $\beta_{1,2}$ are constants found based on the dimension of a square aperture. S(x) and C(x) are respectively the sine and cosine of the Fresnel integral:

$$S(x) = \int_0^x \sin(\frac{\pi t^2}{2})dt, \tag{2.11}$$

and

$$C(x) = \int_0^x \cos(\frac{\pi t^2}{2})dt. \tag{2.12}$$

2.1.1 X-ray interaction with matter

X-ray imaging is explained here from the macroscopic mechanisms behind x-ray interaction with a material, rather than from the microscopic (atomic or electronic) interaction. In the X-ray regime, the complex refractive index of a material is defined by $n(\mathbf{r}, z) = 1 - \delta(\mathbf{r}, z) - i\beta(\mathbf{r}, z)$ which is directly proportional to the electron density distribution. Its spatial variation will thus give rise to differences in phase and amplitude to a wavefield propagating through an object. For a given material, the values of δ and β, which are related to the real and imaginary parts of the atomic scattering factor (microscopic-to-macroscopic), are given respectively by:

$$\beta = \frac{n_a r_e \lambda^2}{2\pi} f_1^0(\lambda), \tag{2.13}$$

and

$$\delta = \frac{n_a r_e \lambda^2}{2\pi} f_2^0(\lambda), \tag{2.14}$$

where n_a is the atomic density, given in atoms per unit volume, $r_e = 2,82 \times 10^{-13} m$ is the electron radius and f_1^0 and f_2^0 are the real and imaginary parts of the atomic scattering factor. While determination of the imaginary part does not pose difficulties since it is a measure of absorption, the determination of the real part, which manifests as a phase shift, proves to be more difficult to measure with precision (even with interferometric techniques). Fortunately, they are mathematically related through the Kramers-Kronig relations as long as the energy dependance of one of the factor is known through a broad range [12].

For our experimental parameters (far from the absorption edges of the atomic species), the transmissivity of a sample $T(r,z)$ is well approximated by a complex-valued projection approximation [13], separated into amplitude and phase components:

$$\begin{aligned}\psi(r) &= \exp\left[-k\int_0^Z \delta(r,z) - i\beta(r,z)\right] dz.\psi_o(r,0) && (2.15)\\ &= A(r)e^{i\phi(r)}.\psi_o(r) && (2.16)\\ &= T(r).\psi_o(r,0), && (2.17)\\ & && (2.18)\end{aligned}$$

where the integral is taken along the thickness of the object. Thereby, the recovered image is a map which encodes both the absorption $A(r)$ and phase shift $e^{i\phi(r)}$ produced by the sample. This complex transmission function (also coined as the "projection propagator" due to the accumulated variations in phase and amplitude [14]) is valid as long as the illuminating wavefront $\psi_o(r)$ is planar or possess a low degree of curvature [14]. A three dimensional map of the electron density distribution can only be recovered by solving different orientations with a computer tomography method (section 3.6).

2.2 Coherence of wavefields

Wavefield propagation between planes, as described earlier, intrinsically involves full coherence of the illumination. This assumption is central to the iterative methods of CDI which propose to study non-crystalline and semi-crystalline specimens through far-field interference patterns. However x-ray sources present some degree of partial coherence and this departure from perfectly coherent illumination, results in a blurry version of the pattern and is of critical importance for the phase retrieval (section 3.4). Thus, the concepts of coherence are reviewed in this section by means of the canonical Young's double-slit experiment. As Feynman was wont to say : "that all of quantum mechanics can be gleaned from carefully thinking through the implications of this single experiment" [15]; one can certainly see how this model of diffraction model can be used to qualitatively and quantitatively probe the coherence function of x-ray.

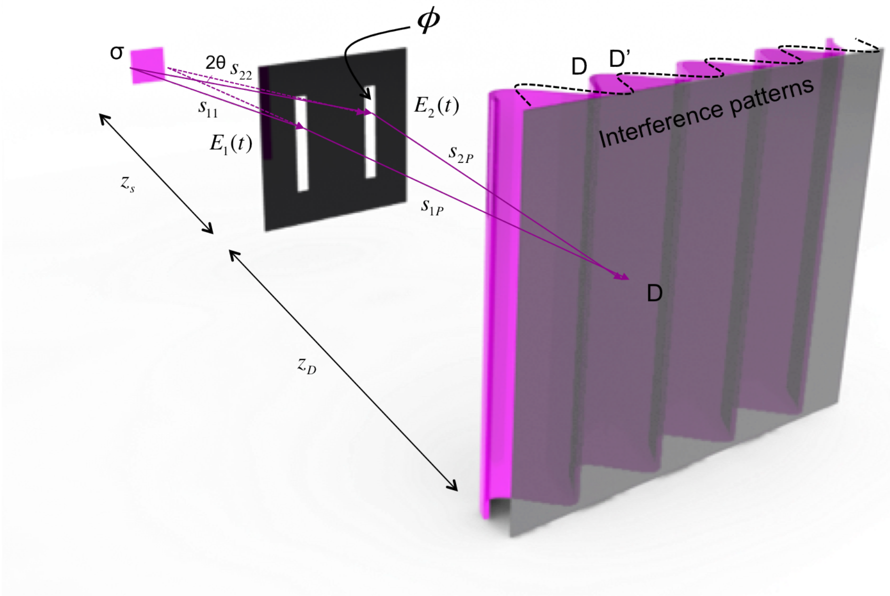

Figure 2.2: Schematic of the legendary Young's double slit experiment used to measure the transverse coherence length of x-ray sources. The mutual coherence function Γ_{12} describes the correlation of the wave field at two arbitrary points E_1 and E_2 in the plane of the slits. Figure and caption derived from [16, 17].

Recalling Huygen's principle (section 2.1), the illuminated points in the two slits from the source, are themselves the source of spherical waves with amplitude $E_1(t)$ and $E_2(t)$. A point D on the detector measures the modulus square of the two varying electric field with the relationship of their time-averaged product formed as:

$$\Gamma_{12}(\tau) =< E_1(t)E_2^*(t+\tau) >, \tag{2.19}$$

where τ is the relative delay in time produced by the path difference. This is a first order cross-correlation function, also known as the mutual coherence function (MCF). A more general MCF is given for an ensemble average realizations (<>) over a scalar wavefield $\psi(\mathbf{r}, t)$,

$$\Gamma(r_1, r_2, \tau) =< \psi(r_1, t)\psi^*(r_2, t+\tau) > . \tag{2.20}$$

The first order treatment of the MCF is in agreement with demonstrated Gaussian characteristics [13] of wavefields coming from synchrotron light sources (section 2.3). The degree of coherence is given by normalising the MCF:

$$\gamma(r_1, r_2, \tau) = \frac{\Gamma(r_1, r_2, \tau)}{\sqrt{\Gamma(r_1, r_2, 0)\Gamma(r_1, r_2, 0)}} \tag{2.21}$$

$$= \frac{\Gamma(r_1, r_2, \tau)}{\sqrt{I_1}\sqrt{I_2}}. \tag{2.22}$$

For total incoherence, $|\gamma| = 0$. Examining of the interference pattern (solid violet, Fig.2.6) at point D a constructive interference is found, however if the phase slit s_2 is retarded by any value ϕ, it will have the effect to shift the location of the minima and maxima (D'). Then, partial coherence can be qualitatively understood as the random variation of ϕ, which over long intensity measurement produce reduced fringe contrast [18]. In what follows, the degree of coherence is quantitatively deduced from the contrast of the Young's two slit experiment fringes.

2.2.1 Spatial or transverse coherence

To derive a condition for transverse spatial coherence of a wavefield, the schematic of Young's double slit experiment is now reviewed from a geometrical point of view. Two light paths emanating from the extremities of a source σ illuminates a pair of thin slits s_1 and s_2. The waves recombining at D must have a difference in path length $\Delta\varphi = k(s_{12} - s_{11} - s_{22} + s_{21}) = 2k\theta\sigma < \pi$, and using a small angle approximation, the transverse coherence length can be described in term of the angular relationship between the two waves, to give an angular condition:

$$\theta\sigma < \lambda/4. \tag{2.23}$$

Using another geometric condition for the maximal distance the slits can be separated ($d = 2.\theta.z_s$), the transverse coherence length is deduced as:

$$l_{xy} = \frac{\lambda z_s}{2\sigma_{x,y}}, \tag{2.24}$$

where $\sigma_{x,y}$ is the finite source related to the sizes of accelerated electrons from which synchrotron X-rays are produced, z_s being the distance the incident X-ray travels from the source to the screen (it was considered that $\sigma_{x,y} \ll z$). Horizontal and vertical source sizes are different due to the path the oscillating electrons take through the machine and undulator.

2.2.2 Measuring coherence

The contrast measured at the detector plane coming from the fringes of the diffraction model of Fig.2.6, gives intensity maximum and minimum called the "visibility", defined as:

$$\nu(\mathbf{r}) = \frac{I_{max} - I_{min}}{I_{max} + I_{min}}. \tag{2.25}$$

Again, using the Young's double slit experiment it is possible to relate the visibility (Eq.2.25) to the degree of coherence (Eq.2.21). In a conventional laser interferometric set-up, the measured intensity from both pinholes illuminated, I, is given by the sum of the individual intensities. For the partially coherent x-ray case, an interference term, which depends on the degree of coherence in the wavefield is inserted:

$$I = I_1 + I_2 + 2\sqrt{I_1 I_2}|\gamma(r_1, r_2, \tau)| \cos(\Phi_{12}(r_1, r_2, \tau)), \tag{2.26}$$

where Φ_{12} is the phase difference between the interfering wavefields [14]. Under the assumption that the pinholes are identical together with their equal illuminating intensity ($I_1 = I_2$), it has been demonstrated in [19] that

$$\nu(\mathbf{r}) = |\gamma(r_1, r_2, \tau)|. \tag{2.27}$$

Perfect coherence should result in the intensity dropping to zero between fringes maxima whereas full incoherence washes the fringes out. Fitting of this formula at synchrotron sources have yielded confirmation of the assumed Gaussian character [20]. This explained by the thermal fluctuations of the source that have a Gaussian distribution.

For a very narrow bandwidth (coined as quasi-monochromaticity), the MCF is approximated with:

$$\gamma^1(r_1, r_2, \tau) = J(r_1, r_2) \exp(-i\omega\tau), \tag{2.28}$$

where ω_0 is the central angular frequency of the wave field and J is the MOI [21]:

$$J(r_1, r_2) = \psi(r_1)\psi(r_2)g(r_1 - r_2), \tag{2.29}$$

and $g(r_1 - r_2)$ is the coherence factor. Assuming a source with Gaussian distribution and using the Van Cittert-Zernike theorem [22], this factor becomes
$\exp\left(-|r_1 - r_2|^2/2l_{xy}^2\right)$.

2.2.3 Temporal or longitudinal coherence

The longitudinal coherence length (l_l) is regarded as the length at which two incident (X-ray) waves λ and $\lambda + \Delta\lambda$, initially in phase become anti-phase (see fig.2.3). Two waves starting with the same phase but differing in frequency by a small $\Delta\lambda$ value will be exactly out of phase after a distance l_l, as illustrated in Fig.2.3, with the shorter wave having N+1 maxima at $2l_l$, as opposed to the N maxima of the longer one. Equating:

$$2l_l = N\lambda = (N+1)(\lambda - \Delta\lambda), \tag{2.30}$$

gives under the assumption that $\Delta\lambda \ll \lambda$, the longitudinal coherence length before the phase difference between the two waves is 2π is:

$$l_l = \frac{\lambda^2}{2\Delta\lambda}. \tag{2.31}$$

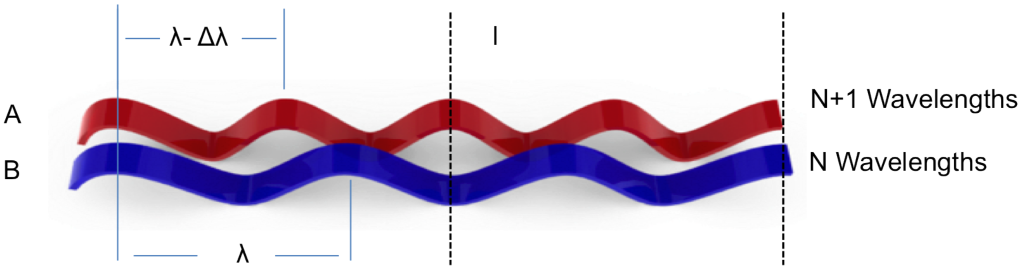

Figure 2.3: Two waves with slightly different wavelengths λ and $\lambda - \Delta\lambda$ starting in phase will arrive out of phase after traveling a distance l_l.

The length of l_l is inversely proportional to the bandpass of the beamline optics, usually achieved with the (111) reflection of a perfect Si crystal. A typical fractional bandwidth given by a double crystal monochromater is $\Delta\lambda \simeq 1.4.10^{-4}$ and leads to the reasonable assumption of monochromaticity due to this ability of synchrotron to produce quasi-monochromatic light. After the X-ray beam passes through a Si(111) double crystal monochromator, it typically produces a relative bandwidth of approximately $\Delta\lambda/\lambda$.

2.3 Synchrotron source

This section briefly reviews the central features of synchrotron radiation which are sources of sufficiently coherent and bright x-rays for coherent diffraction experiments. As it is well known, any charged particle moving in an non uniform fashion produces an electromagnetic field, and when accelerated to relativistic speed along curved trajectories, it is called synchrotron radiation [23]. Synchrotron radiation took a major importance when it was realised that radiation emitted in storage rings constituted a source of exceptional intensity and spectral brightness, particularly at short wavelengths. Whereas the continuous loss of energy was first seen as a hindrance in particle physics, the shrewed exploitation of this radiation gave birth to the construction of a large number of so-called 2nd generation synchrotron rings dedicated to all sorts of experiments, where the high brightness and the low divergence (similar to laser properties) would be the key for numerous advances in condensed matter. They used powerful bending electromagnets in the accelerators to generate the radiation with the relativistic electrons forced to travel in a closed path by strong magnetic fields (Lorentz force), with the lost of energy replenished through the use of radio frequency cavities placed at various points along the ring.

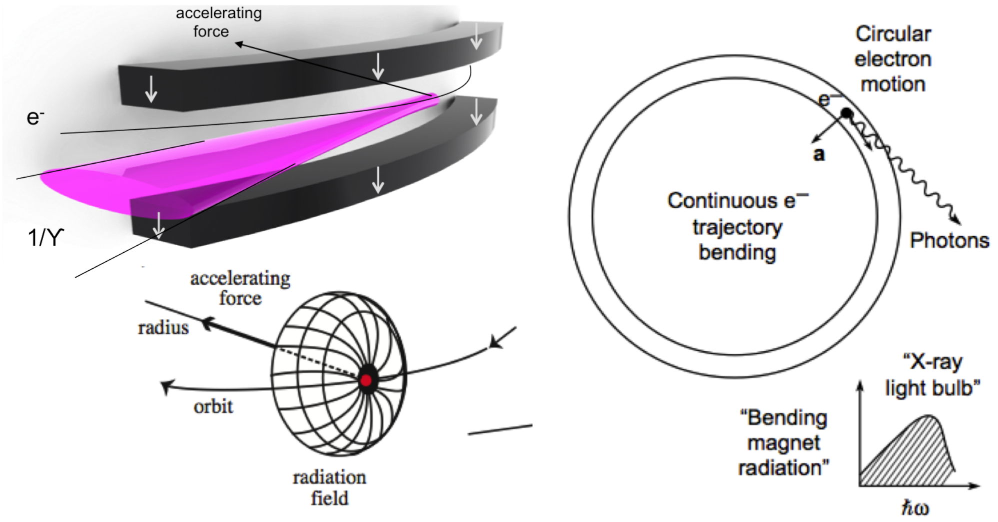

Figure 2.4: Early synchrotron radiation facility were electrons are bent around a quasi circular path producing a cone of radiation (shown in violet) in the forward direction with an opening angle $1/\gamma$. Although, in the center-of-mass moving frame, the e^- behave like an Hertzian dipole [12].

For electrons circulating in a microscopic atom, the laws of quantum mechanics apply and 'surprisingly' to a large system like a synchrotron accelerator as well, as it can be regarded as a macroscopic atom. But has the energy state can be regarded has having a large quantum number, a classical treatment is a very good approximation [24]. Maxwell equations can be used to determine the characteristics of the synchrotron radiation but an approach based on the known classical results of Hertzian dipole radiation subject to Lorentzian transformation is an easier approach

[12]. In fact, synchrotron radiation can be qualitatively understood by considering a moving antenna. Two dramatic effects arise from the relativistic effect, first the change in frequency due to the Doppler effect which brings the radiation in the X-ray range and secondly, the isotropic radiation that is distorted into an extremely forward pointing cone of radiation due to Lorentz compression (Fig.2.4). This latter compression of the well known $sin^2(\Theta)$ radiation, result in a cone with an opening angle $1/\gamma$ in the laboratory system. In the frame of special relativity, its half angle, θ_r is described by the factor γ:

$$\theta_r = \frac{1}{\gamma} = \frac{1}{\sqrt{1-\beta^2}}, \tag{2.32}$$

where β denotes the relativistic particle velocity given by $\beta = v/c$, with v is the particle velocity and c the velocity of light. This equation highlights the importance of the ability for synchrotrons to accelerate electrons to near the speed of light, reducing the angle of emission, and thus producing lower emittance, and a brighter X-ray beam. Spectral brightness B is an important parameter to qualify the quality of an x-ray source, and is defined by:

$$B = \frac{\Phi(E_\nu)}{4\pi^2 \epsilon_x \epsilon_y}, \tag{2.33}$$

where E_ν the spectral flux, defined as the number of photons per time interval at a certain energy of 0.1 bandwidth normalized by the emittance $\epsilon_{x,y}$ (product of the divergence $\theta_{x,y}$ and the lateral extent of x-ray beam $\sigma_{x,y}$ [13]). Fig.2.5 displays a graph comparing the spectral brightness of various sources [25, 21].

The latest synchrotrons, the so-called third-generation make use of magnetic multipole structures between the bending magnets of the storage ring. These specialized devices that are generically referred to as insertion devices present two different modes of operation depending on the strength of their periodic magnetic field and differentiated by a single parameter:

$$K = \frac{eB_0\lambda_u}{2\pi m_e c}, \tag{2.34}$$

where B_0 is the magnetic field strength, e and m_e are the charge and mass of the electrons and λ_u is the undulator wavelength.

When the magnetic field is relatively weak, $K \ll 1$, the angular excursion of the electrons is smaller than the natural emission angle of the synchrotron radiation, and the radiation resulting from the coherent interference of the harmonic oscillation of the electrons has a very narrow spectrum with small angular divergence $(1/\sqrt{N}\gamma)$.

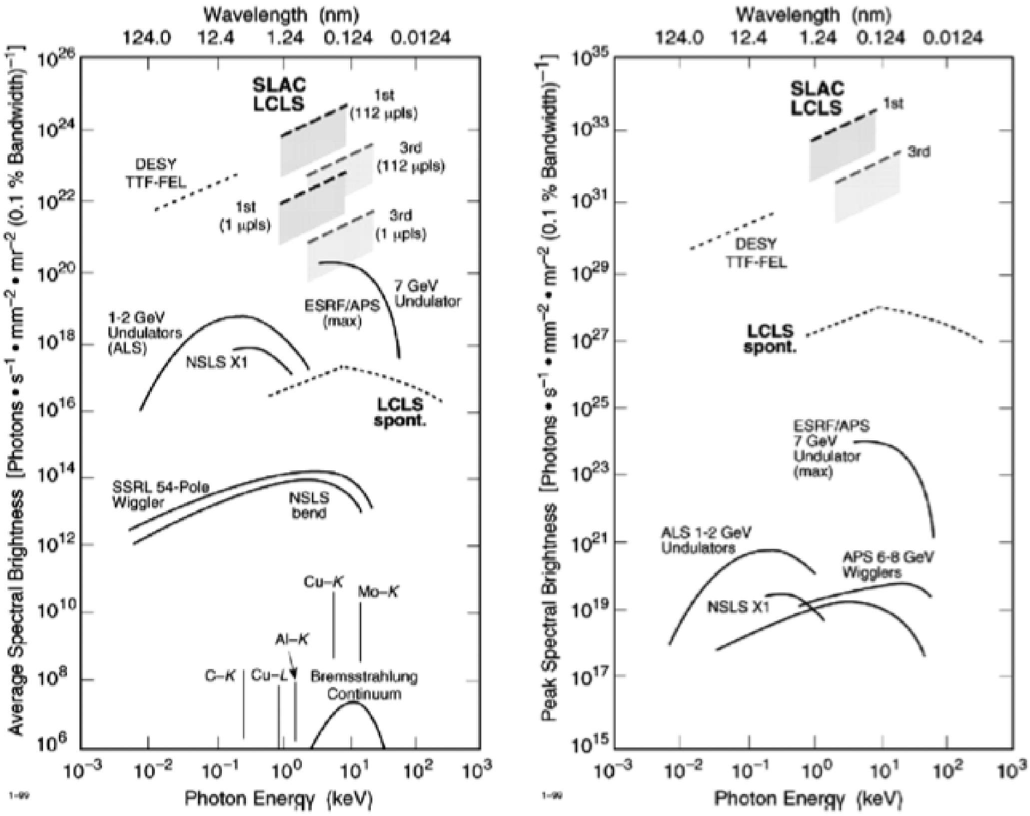

Figure 2.5: Comparison of average spectral brightness (left) and peak spectral brightness (right) for various sources (i.e., wigglers, undulators and XFELs). Comparison of spectral brightness for synchrotron radiation sources (Undulators, Wigglers and Bends), to lab based sources such as rotating anodes and stationary anodes. Stationary anodes have a spectral brightness in the low end of the range, and rotating anodes are in the middle range. The difference in brightness between synchrotron sources and stationary laboratory sources can be up to 10 orders of magnitude. Figure and caption taken from [25, 21].

In this mode, the insertion device is called an undulator and is ideal for coherent diffraction experiments because of it laser like properties. While it obviously does not alleviate the need for a monochromator, it still minimizes the heat load on the beam line components.

A wiggler is the strong magnetic field version of an undulator with, $K \gg 1$, and as the angular excursion of the electrons is larger than the natural emission angle of the synchrotron, the radiation produced has a broad smooth spectrum resulting from the incoherent sum of the large harmonics. The radiation from a wiggler is more similar to synchrotron radiation except that its spectrum is shifted towards higher photon energy and increased to $2N$ photon flux.

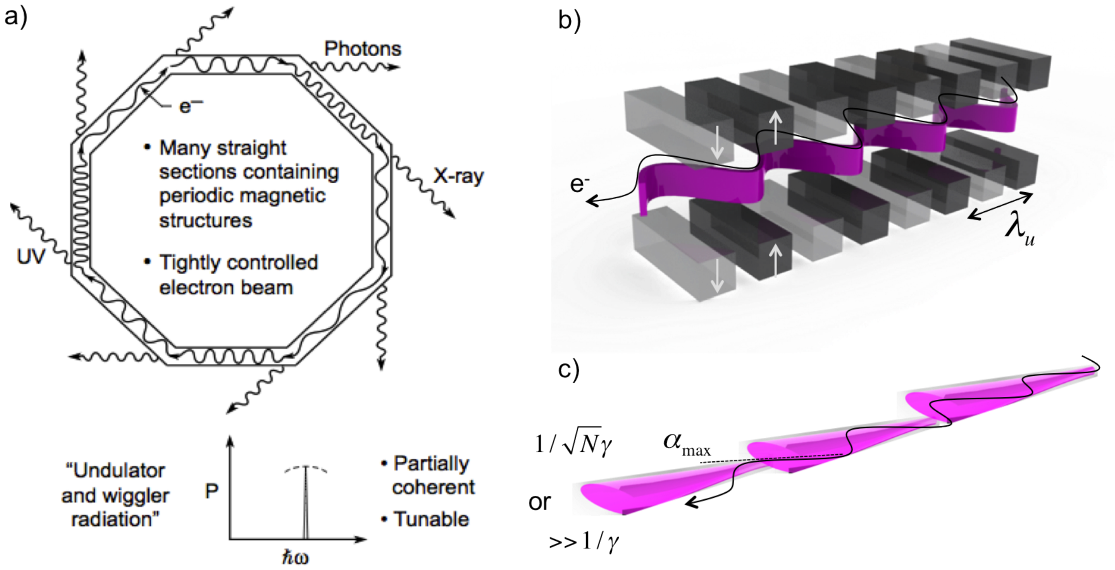

Figure 2.6: a) Modern storage ring optimized for high spectral brightness through the inclusion of insertion devices [12]. b) The array of N dipole magnets forces the relativistic electrons to follow a sinusoidal wave with periodicity λ_u. c) When the magnetic field is relatively weak, $K \ll 1$, the angular excursion of the electrons is smaller than the natural emission angle of the synchrotron radiation, and the radiation resulting from the coherent interference of the harmonic oscillation of the electrons has a very narrow spectrum with small angular divergence $(1/\sqrt{N}\gamma)$. In this mode, the insertion device is called an undulator. In the the strong magnetic field version of an undulator with $K \gg 1$, the angular excursion of the electrons is larger than the natural emission angle of the synchrotron, the radiation produced has a broad smooth spectrum resulting from the incoherent sum of the large harmonics. In this mode, the insertion device is called a wiggler with radiation more similar to synchrotron radiation except that its spectrum is shifted towards higher photon energy and increased to $2N$ photon flux. . Caption and figure derived from [12, 14] .

2.4 Focusing optics

X-ray experiments are reliant on beam shaping optics [26], which one manipulates the energetic beams to obtain higher numerical aperture (NA) by taking advantage of the different interaction types of light with matter, such as diffraction (Fresnel zone plates), reflection (mirrors) and refraction (lenses). In coherent imaging, an increase of the NA increases the size of the fringes in the diffraction pattern, thus enabling oversampling while providing better signal to noise ratio (SNR) at high diffracting angles. As it will be seen in ptychographic sections, focusing is used to select parts of the sample. The choice of focusing devices is usually done based on the experimental needs, such as photon energy, bandwidth, efficiency, and an adequate choice for those performed in CDI are Kirkpatrick-Baez mirrors (KB) and Fresnel Zone Plates (FZP). Both produce a curved wave-front upon incidence of a plane wave illumination and use constructive interference at the actual focusing point, however, KB mirrors have much higher efficiencies for coherent X-ray than FZP. A review of their characteristics is presented below.

KB mirrors. In a historic 1948 paper, Kirkpatrick and Baez introduced their focusing mirror [27], signalling the beginning of X-ray optics and thus the very birth of X-ray microscopy [28]. In fact, Roentgen himself proclaimed that it would be impossible to focus X-rays with lenses since the index of refraction of x-rays is smaller than unity, but external reflection occurs as Compton realised in 1922. A KB mirror is an elliptically shaped (total) reflective mirror which keeps the distance from a point source S to the focal point F constant, thus a spherical wave emerging from S interferes constructively in F [26] , see Fig.2.7 (a). Two-dimensional focusing seem to require mirrors of three-dimensional ellipsoidal shape at first sight, but hopefully the two dimensions decouple, and a common focal plane is achieved by placing two one-dimensional mirrors orthogonally. The desired elliptical profile is realised with elastic emission machining (EEM) [29] and advanced polishing techniques, to achieve figure errors (i.e., deviation from the ideal profile) well below 1 nm and roughness of less than 0.1 nm.

Fresnel Zone Plate. The quasi-periodic structures of FZP act like binary circular diffraction gratings, which alternate between transparent and opaque (or phase shifting) rib zones to scatter an incoming wave in such a way that the multiple scattered waves interfere constructively at the focus [26]. As the distance from the optical axis increases, the density of alternating zones increases as to diffract the light at the same focusing point. The focal length of a zone plate is given by $f = D\Delta r/\lambda$. with D is the diameter of the zone plate, δr is the finest spacing of the

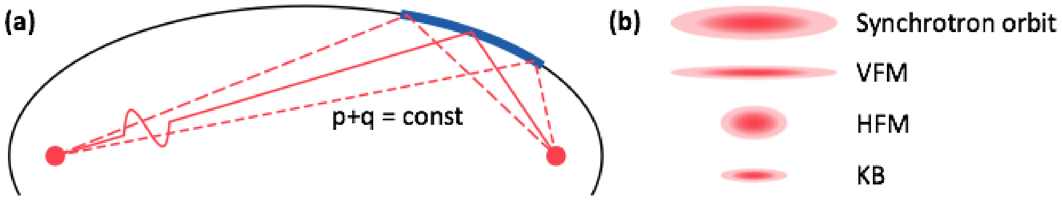

Figure 2.7: Typical set-up of elliptical mirrors used at synchrotron radiation sources for focusing. In (a), the one-dimensional focusing principle based on the elliptical shape is illustrated; in (b) illustration of the stages for the uncoupled dimensions (VFM, HFM) in the KB geometry of two sequential mirrors. Caption and figure from [26].

outermost zone. The binary structure produces successive higher order focal lenghts of $f_m = (1, 3, .., 2m{+}1)$ with the even orders producing destructive interference. As a consequence of the multiple diffracting orders, an order sorting aperture (OSA) and a central stop are needed to let pass only the first order (which has an efficiency of about 10%) and to block the undiffracted light (zeroth order 25 %). The efficiency can be increased by using fully transparent zone plate with alternating 0 and π phase shift ring zones rather than transparent and opaque, although such a zone plate works only for one energy. Important properties of a FZP are given by:

$$R_{res} = 1.22\delta r, \tag{2.35}$$

and

$$R_{depth} = \frac{4\delta r^2}{\lambda}, \tag{2.36}$$

where the width of last zone sets the resolution R_{res} and depth of field R_{depth} [14]. An high aspect ratio is necessary for focusing efficiency and near the edge, where the zones are thinner and thinner. This is achieved by electron-beam lithography with gold as material of choice for keeping this high aspect ratio. To further increase the resolution, FZPs based on iridium using atomic layer deposition (ALD) with zone doubling is under development [30].

Advances in X-ray focusing optics. Early researchers focused their efforts on curved reflective optics, and it was accepted that optics based on total external reflection were fundamentally limited by the critical angle $\theta_c = \sqrt{2\delta}$ to around 10 nm. This limit was also speculated to apply to all types of single optics but new advances in nanofabrication capabilities like electron beam nano-lithography, thin film deposition, pulsed laser deposition (PLD), focused ion beam (FIB) allows us to take advantage of all types of interactions of light with matter, in addition to recent

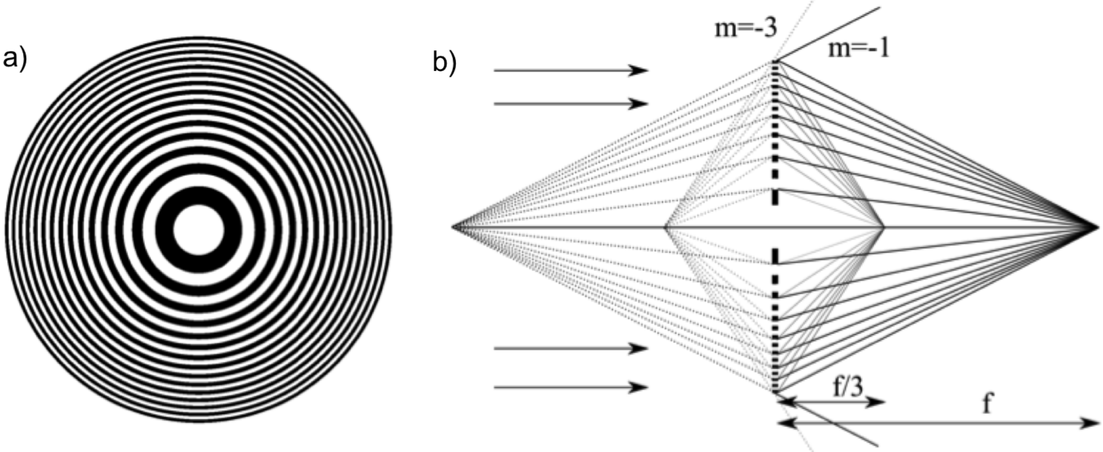

Figure 2.8: a) A schematic of a binary zone plate composed of an alternation of transparent and opaque rings. b) Schematic showing zone plate focussing for incident radiation originating from the left. The m = 1 order is focussed at f while the m = 3 is focussed at f/3. The schematic also depicts the virtual focus behind the zone plate (dotted lines) that is composed of negative orders. Image and caption from [21].

theoretical work, promise spot sizes < 1 nm. They are for example competing techniques such as thick tilted zone plates [31] (see Fig.2.9 c)) or sequential arrays of hundred refractive lenses in a row [32] (see Fig.2.9 b)), Multi Layer Laue (MLL) lenses, laterally graded multilayer mirrors, waveguides, and compound kinoform lenses.

To push the focal spot size into the sub 10 nm regime, a reflective mirror using an adaptative mirror to compensate for phase errors has been recently demonstrated (see Fig.2.9 a)). However, the determination of the focal spot size was not co-instantaneous as the mirror has been rotated for measurements in x and y. Of further advantage, compound optics such as a combination of high gain KB mirror (acting as pre-focusing) with a multilayer zone plate has very recently exploited and shown to reach 5 sub-nm point focusing (see Fig.2.9 e)). In fact, multilayer zone plate that are fabricated by PLD on a rotating wire seem to provide unlimited aspect ratio as compared to conventional FZP where high aspect ratio is hard to prepare with e-beam lithography. Two-step focusing scheme also appears to be indispensable to capture the higher possible bandwidth offered by the 10^4 zones while exhibiting less dispersion [33].

These highly efficient nano-focusing optics will also benefit analytical methods reliant on the exceptional properties of hard x-rays such as fluorescence, spectrometry, phase-contrast, etc. and this is the reason why nanotechnology centres are being established at synchrotrons.

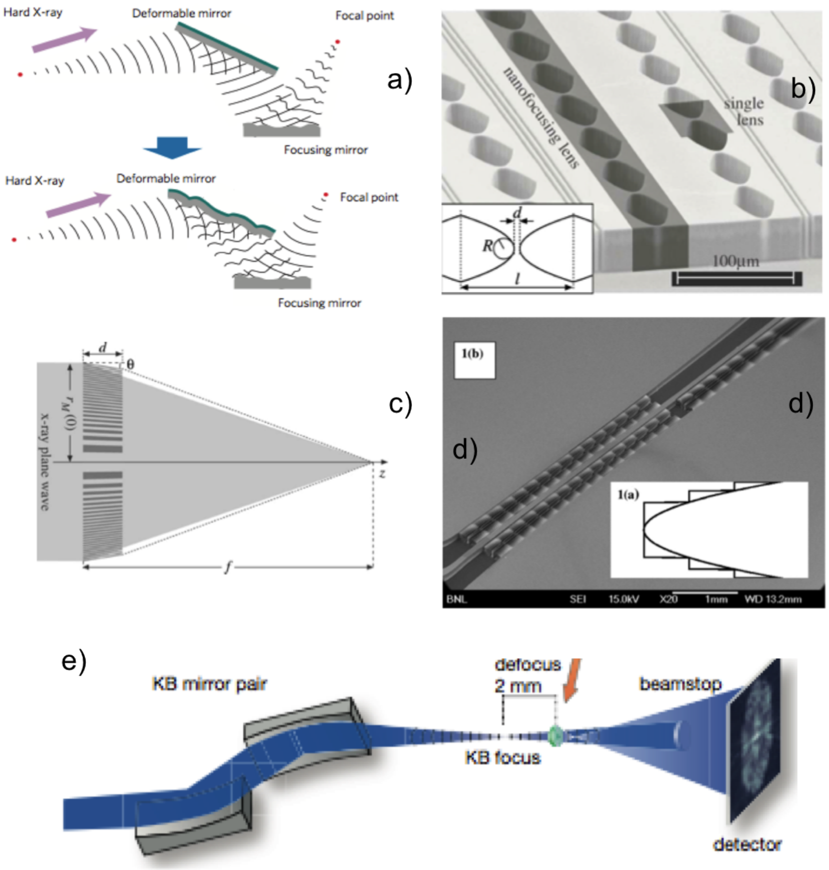

Figure 2.9: a) Schematic of hard-X-ray focusing system with an adaptive or deformable upstream mirror used to correct for the wavefront error that was not ideal owing to figure errors (figure from [34]). b) Scanning electron micrograph of a nanofocusing lense unit (figure from [31]). c) Focusing geometry for a thick Fresnel zone plate with tilted zones [35]. d) An electron microscope image showing the single lens in one channel and the first two lenses of the four-lens array (figure from [32]). e) Concept of compound optics, in which the MZP is to be found slightly downstream of the KB focus (figure from [33]).

2.5 Measuring and inverting the diffraction patterns

2.5.1 X-ray detection systems

To measure the fine fringes of a diffraction pattern that can vary over many orders of magnitude in amplitude, the ideal detector must possess high resolution and output a linear count over a high dynamic range in response to the photons impinging on a pixel. To help choose the correct detector, the X-ray data booklet from Berkeley [36] provides a good summary.

For the main experiments undertaken in this thesis, a Princeton Charge Coupled Device of format 1024×1024 pixels measuring $20 \times 20\mu$m was used. A photon, after absorption within the semiconductor (depletion layer) generates an electron-hole pair (average energy required is 3.65 eV). In each pixel, an electric field discourage the recombination and charge accumulate, then converted to the internal units of a CCD, the Analog to Digital Units (ADU), which are related to its gain [37]. Although, noise is also generated in the counting process and their effects in the diffraction imaging system must be understood for correct inversion of the diffraction pattern. The primary source of noise is due to the quantum nature of light, thus an inherent statistical Poisson noise, proportional to the square root of the number of photons ($\sqrt{N}$) is present in the detection of photons. In the detection process, thermal effects act to add a background count. Fortunately, this dark current noise can be removed from a CCD image by taking an image under the same experimental conditions without being exposed to any photons (a mean from many exposures accounts for the stochastic nature of the process). As the dark current describes the rate of generation of thermal electrons at a given CCD temperature [37], cooling is necessary to damp it. When the photon count is low, the dominant source is the read noise.

A statically accurate signal for the detection is then given by the total signal to noise ratio (SNR),

$$SNR = \frac{S}{\sqrt{S + N_{dc}^2 + N_{readout}^2}}. \tag{2.37}$$

Where S is the signal, N_{dc} is the dark current noise, $N_{readout}$ is the readout noise. The first photon peak (Gaussian distributed) in the photon count histogram is used for the noise threshold, see Fig.2.10. For a more formal processing of the CCD frames and to correct for the different type of noises, it is possible to measure the varying response across the device area, the so-called flat field measurement using the analysis equation given in the Princeton instrument booklet [37]:

$$E_c = \frac{(E-D) \times \frac{1}{N}\sum^{pixels}(F-D)}{(F-D)}, \tag{2.38}$$

where E_c is the corrected frame, E is an experimental diffraction pattern, D is the time dependant dark exposure, F is the uniform illumination flat field.

Commercially available CCD detectors are being surpassed by hybrid detector pixels descended directly from high energy research like done at the European Organization for Nuclear Research (CERN), such as the Medipix [38] now installed at beamline 34-ID-C of APS and the Pilatus [39] (developed at Swiss Light Source) which are single photon counting and very large dynamic range of up to 2^{20} photons, with no instrumental noise.

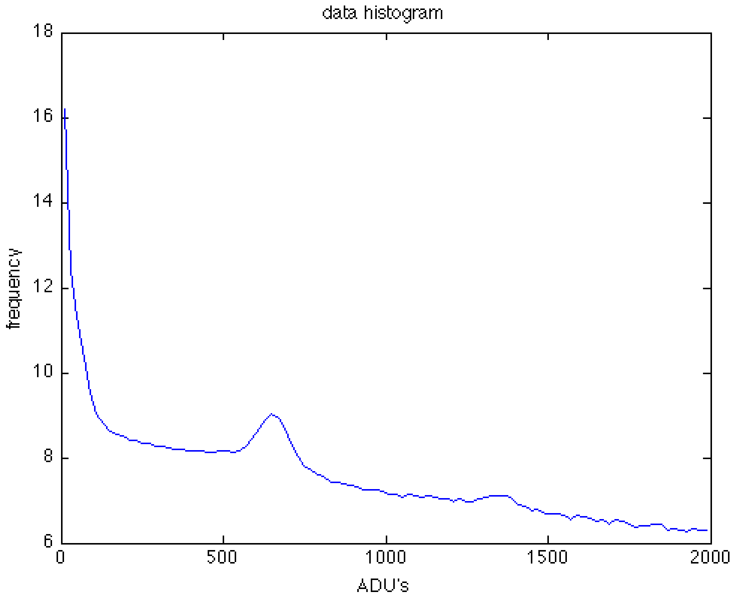

Figure 2.10: Matlab histogram of a photon count for a typical experimental data set coming from a CCD. The first photon peak is used for the noise threshold.

Even with current detector technology, the phase is destroyed in the recording process, a phenomenon referred to as the phase problem, and fundamental to CDI.

2.5.2 Resolution

Assuming post phase reconstruction (section 2.5.4), images are synthesized from Fourier inversion of the captured angular distribution of the scattered waves, hence the resolution is directly related to the maximum angular divergence (θ) to which the radiation propagates:

$$res = \frac{\lambda}{\theta}. \tag{2.39}$$

In the approximation of small angle scattering, the size of the detector D and its distance from the sample Z are used to put the resolution into units of lengths,

$$res = \frac{\lambda D}{2Z}. \tag{2.40}$$

A condition *sine qua non* to a sufficient detection aperture, is that the generated signal at high angle should contain enough photons to keep the SNR high enough. Even at synchrotron sources where the brightness is about 10^{12} times higher than lab sources, the flux may be not enough to reach satisfactory high spatial resolution.

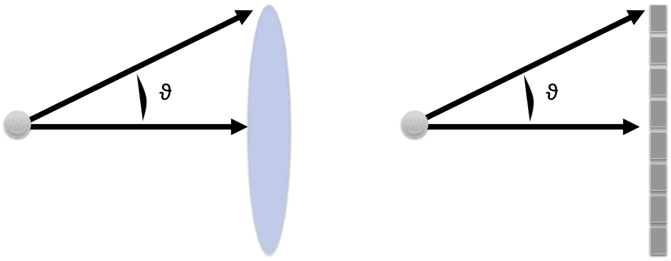

Figure 2.11: In a conventional imaging setup (left), the lens sets the numerical aperture (NA) whereas in a diffractive imaging system, the NA is recorded by a CCD (right).

Howells et al. [40] have investigated (both theoretically and experimentally) the minimal required dose for imaging biomaterials which are known to be sensitive and weak scatterers. Their starting point is the Rose criterion [41] which states that to be able to reliably detect a feature against background noise, its signal should exceed by a factor of 5 the root mean square level of noise during exposure. Taking into account Poisson shot noise, this criterion requires a minimum of 25 photons. By further proceeding with the classical electron radius:

$$r_e = \frac{1}{4\pi\epsilon_0}\frac{e^2}{m_e c^2} = 2.818 \times 10^{15} m, \tag{2.41}$$

and the complex electron density:

$$\rho_e = \frac{2\pi(\lambda + i\beta)}{\lambda^2 r_e}, \tag{2.42}$$

they found the number of incident X-rays per unit area required to scatter photons into a detector from one of sample's voxel dimensions d^3, is given by:

$$N_0 = \frac{P}{r_e^2 \lambda^2 |\rho_e|^2 d^4}, \tag{2.43}$$

and this corresponds to a dose, measured in Grays (with 1 Gy = 1 J/kg of deposited energy) of:

$$D = \frac{\mu h v}{\rho_m} N_0, \tag{2.44}$$

where ρ_m is the mass density and μ is the inverse absorption length. Finally, using a bio-material with composition $H_{50}C_{30}N_9O_{10}S_1$ of density $\rho_m = 1.35 g/cm^3$, against a water background and for X-ray energies ranging from 1 and 10 keV, the limit for imaging a single non-periodic sample at a synchrotron was found to be 10 nm [40] (see Fig.2.12).

Note that this demonstrates that the necessary flux is inversely proportional to fourth power of the desired spatial resolution. Thus, only very short and ultra intense sources have the potential to reach atomic resolution (see section 2.6).

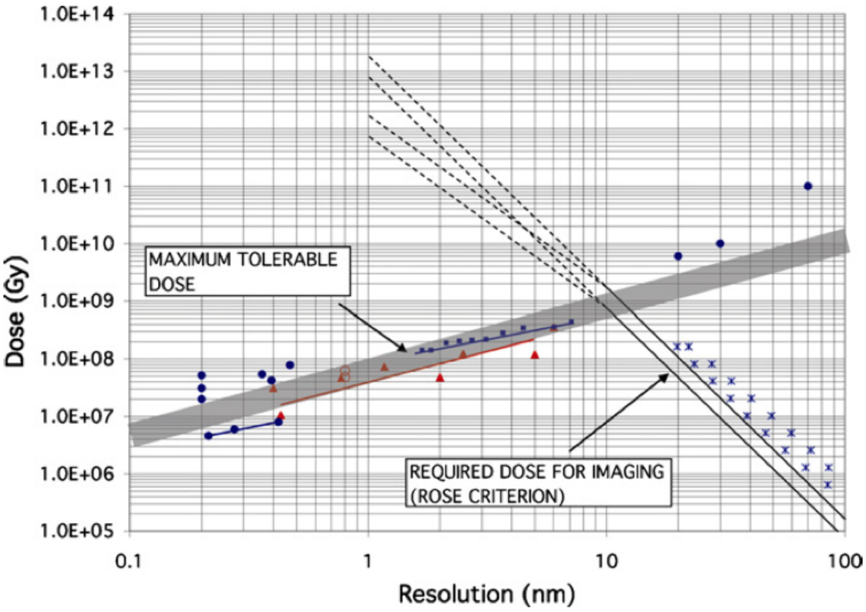

Figure 2.12: Graph summarizing information on the required dose and the maximum tolerable dose for imaging a bio-material, based on calculation from a protein of empirical formula $H_{50}C30N_9O_{10}S_1$ and density $\rho_m = 1.35g/cm^3$ against a background of water for X-ray energies of 1 keV (lower continuous line) and 10 keV (upper continuous line). The required dose is based on the Rose criterion. Measurements of the maximum tolerable dose have been compiled from experiment such as filled circles: X-ray crystallography; filled triangles: electron crystallography; open circles: single-particle reconstruction; open triangles: electron tomography; diamonds: soft X-ray microscopy (including XDM); filled squares: ribosome experiment. Image and caption from [40].

2.5.3 Sampling requirements

Having the diffraction experimentally measured on pixellated grids (to be later processed by computation), necessarily implies that a continuous real-world signal is sampled.The sampling requirements and the phase problem are closely connected, a fact primarily realised by Sayre [7]. Thus, a Fourier transform becomes discrete (DFT), still periodic but with circular boundaries that wraps up frequencies that exceed the Nyquist frequency (or limit), a phenomenon called aliasing. Bates [42] extends this argument and states that in order to avoid aliasing and rather have edges that smoothly falls to zero, the autocorrelation of an image, which is given by the inverse FT of the recorded intensity, must not overlap itself through the boundary conditions. This is known as the oversampling criteria and can equivalently be reached with an equation counting argument of the degrees of freedom [43]. Re-writing the recorded intensity at the detector of a propagated wavefield as:

$$I[q_x, q_y] = \left| \sum_{x}^{N_x} \sum_{y}^{N_y} \psi(x, y) \exp\left(-\frac{i2\pi}{N}(x.q_x + y.q_y) \right) \right|^2, \tag{2.45}$$

where $N_{x,y}$ is the width of the array, x, y are discrete real-space coordinates and q_x, q_y are discrete reciprocal-space coordinates, implies to solve $N_x.N_y$ coupled non linear equations. As the exit wavefield or real space function is a complex quantity, the number of unknowns becomes $2N_xN_y$ and explains why the object must not occupy a box of half size the array to reduce the number of unknowns. In fact this mathematical demonstration formulates Sayre's original proposition (1950's) that the methods of crystallography might be adapted for imaging general non-periodic objects provided sufficient sampling of its reciprocal space diffraction [7]. From this equation counting argument, Miao [44] and Sayre refer to a constant named the oversampling ratio, σ, and defined as the number of points in the field of view divided by the number of points in the extent of the object:

$$\sigma = \frac{\text{Field of view}}{\text{Extent of sample}}. \tag{2.46}$$

These results can also be qualitatively understood from the fact that a fringe must be recorded with more than one pixel to accurately record the minima between fringes [45, 18].

The relation between pixel resolution of the object and the pixel size of the detector are deduced, based on the Fourier transform relationship and geometri-

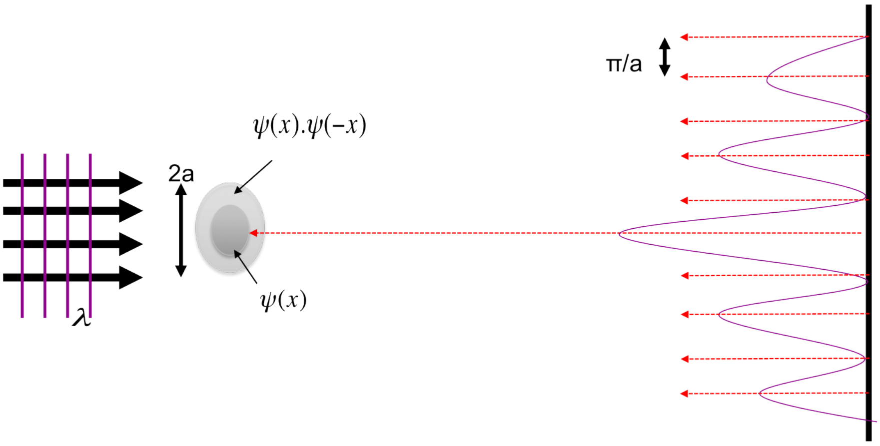

Figure 2.13: Coherent diffraction measurement of a continuous fringed intensity propagated from a single isolated object of size a. The sampling of π/a and the zero-density region of $2a$ around the object, ensures a unique reconstruction. Caption and figure derived from [17].

cal considerations. Equating a continuous Fourier transform with its discretized approximation, given a real space grid spacing, Δr show that:

$$\Delta r.\Delta q = \frac{2\pi}{N}, \tag{2.47}$$

where Δq is the reciprocal-space spacing. A far field diffraction pattern from a finite size object a, has a fringe period or smallest period in reciprocal space of $\Delta q = 2\pi/a$ and corresponds to a maximum sampling distance (see Fig.2.13). Using the geometrical parameters such as the small angle approximation $(\Delta q\text{‘}|k|\Delta_d/z)$, the distance z (where the approximation is legitimate) and the detector pixel size Δd, the real space sampling rate is finally:

$$\Delta x = \frac{\lambda z}{N\Delta d}. \tag{2.48}$$

These derivations have an important implication, the object must be contained within a band limited support which consequently places an upper limit to its size when the geometry of the experiment cannot fulfil critical oversampling. Using a beam smaller than the object and the ptychographic technique overcome this problem, as will be demonstrated in later sections.

2.5.4 Phase retrieval algorithm

Having set the necessary background to 'properly' prepare fringed patterns, our attention is now focused on the iterative mechanism whereby the remaining task of finding numerical solutions to the phase problem can be tackled. The phase retrieval problem being widespread in the optics and crystallography community, the diffraction imaging benefits from ground work of both communities. To solve for the lost phase, the reconstruction algorithms share a common strategy, which is to enforce constraints in both real- and reciprocal -space. In the latter, the algorithm takes information from the measured diffraction amplitudes and in the former, the information is derived from *a priori* knowledge on the nature of the object or experimental method. When the constraints are satisfied, convergence of the algorithms is reached and the phased diffraction can deliver (after inversion) a complex representation of the object. Even though the term algorithm is employed, this is perhaps not entirely appropriate as formal convergence is not guaranteed as with a true algorithm which provides a completely deterministic solution in a fixed number of steps [14]. The first diffraction algorithm was formulated by Gerchberg and Saxton (GS) but for example suffer stagnation (see Fig.2.15), and a variety of other algorithms were developed to circumvent such problems like the Hybrid Input-Output (HIO) of Fineup [46] or the difference map of Elser [47].

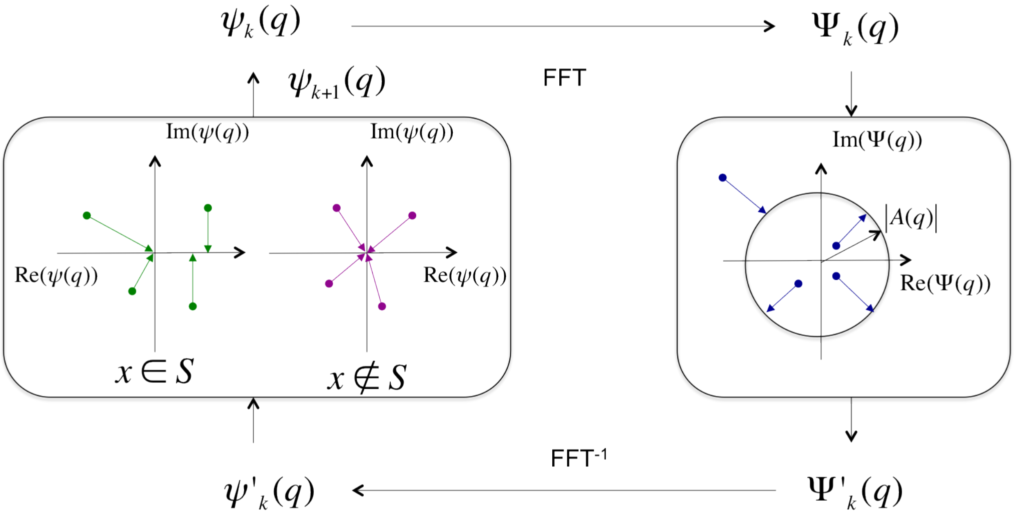

Figure 2.14: Common flow chart to diffraction imaging phase retrieval algorithms. A approximation of the real space object is propagated to the reciprocal space by mean of a Fourier transform where the measured intensity is projected. The newly constrained reciprocal space is then inverse Fourier transformed back to real space where constraints such as positivity (real object) and tight support are applied, completing one iteration. Figure and caption derived from [48].

The original iterative GS algorithm is composed of the following steps:

1. As starting point, an object guess $\psi(r)$ is formed from *a priori* knowledge.

2. The current object guess is propagated to the far-field by means of a FFT.

3. The computed diffracted wave amplitude is replaced by the measured amplitude, whilst preserving the calculated phase. It is the so-called modulus constraint and adopting operator notation [14], is defined as:

$$\Pi_m \Psi(q) = \frac{\Psi(q)}{|\Psi(q)|}\sqrt{I_m(q)}. \tag{2.49}$$

   The operator can also encapsulate the backward propagation (propagated modulus constraint):

$$\Pi_m \psi(r) = F^{-1}\Pi_m F\psi(r). \tag{2.50}$$

4. A real-space support constraint is enforced (or projected) on the updated object guess $\psi'(r)$ by,

$$\psi^{k+1}(r) = \begin{cases} \psi'(r) & \text{if } r \in S \\ 0 & \text{if } r \notin S, \end{cases}$$

   where S defines the area of the support .

5. The cycle is repeated for a sufficient number of iterations or steps, necessary to reach data convergence.

Finally, a more comprehensible way to illustrate the algorithm operation, is the projection language adopted by Veit Elser [47]. Thus, the simple GS iterative scheme can be generalized as:

$$\psi^{k+1}(r) = \Pi_S \Pi_m \psi^k(r). \tag{2.51}$$

The Gerchberg-Saxton algorithm was later classed as a steepest descent algorithm [46, 48], meaning that its 'action' either reduces or leaves the error metric unchanged, in any case not worse. This is quite a serious problem as the error metric very often reaches plateaus or is trapped into local minima. Fienup [46] went on and generalized the GS algorithm by proposing the hybrid input-output algorithm, known as the HIO, which can alleviate the stagnation problem of ER by avoiding local minima (see Fig.2.15). This is due to an ability to explore the vicinity of local minima in the solution space owed to the non linear feedback control provided by the mixture of current estimate and semi-updated estimate:

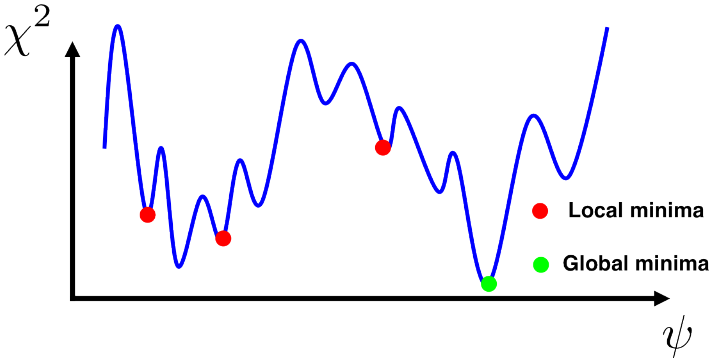

Figure 2.15: Error metric showings local minima and a global minimum.

$$\psi^{k+1}(r) = \begin{cases} \Pi_m \psi(r) & \text{if } r \in S \\ (1 - \beta \Pi_m)\psi(r) & \text{if } r \notin S, \end{cases}$$

where β is a feedback parameter, selected to be between 0.5 to 0.9.

To monitor the algorithm's convergence, the difference between calculated and measured diffraction intensities, mean square error in reciprocal-space:

$$\chi = \frac{\sum_q \left(\sqrt(I(q)) - |\Psi(q)|\right)^2}{\sum_q I(q)}. \tag{2.52}$$

The size of the support can be deduced from autocorrelation or the fringe spacing, and can be later refined with the shrinkwrap method [49]. A variety of constraints for the real-space can be employed such as constraining the range of phase values [50], the density, and in the formulation of their update. Adaptation of Fourier modulus although less ubiquitous, can be realised to account for experimental realities such as photon noise, missing data under a beam-stop [51, 52] or by the difference map algorithm which takes two instances of the Fourier modulus update. The difference map algorithm was introduced by Elser and for simplicity is written with projection operators:

$$\psi^{k+1}(r) = [1 + (1+\beta)\Pi_S\Pi_m - \Pi_S - \beta\Pi_m]\psi^k(r). \tag{2.53}$$

Using the formalism of projection operators in a feasibility problem, Garth Williams in his thesis [48] has analysed the convergence success rate of the different algorithms along with their trajectories. A similar analysis and in-depth review of phase retrieval algorithms has been presented by Marchesini [53]. These algorithms are at the root of the ptychographical algorithms, even though the support regime adopts a more complicated form.

2.6 Advances in Coherent Diffractive imaging

While the proposal of diffractive imaging was suggested 50 years ago by Sayre [7], it was not until advances in x-ray source and detection technology were introduced over the past 10 years or so, that CDI became a topic of considerable importance [54]. It was only in 1999 that the first successful experimental demonstration of a non-periodic pattern of gold dots (100 nm), took place conducted by Miao [44]. In parallel and as opposed to transmission, Robinson used the CDI technique to image gold nano-crsystals in reflection geometry by collecting diffraction pattern around a Bragg point [55] (subject of chapter 6). Seminal experiments by Miao on three dimensional imaging [56] were then surpassed by Chapman's convincing reconstruction of a buried test object composed of a pyramid of 50-nm gold spheres [57], Fig.2.16. In 2008, three dimensional reconstructions reached a new peak with the determination of structural deformation mechanism of a ceramic nanofoam, performed by Barty et al. [58].

Although more difficult and challenging to investigate, biological materials are not precluded from the CDI technique and efforts are being made to image unstained, thick and unsectionned mesoscale samples like cells [59], chromosomes [60], viruses [61], in conditions close to their native environment. The first biological images were obtained in 2003 by Miao, with a reconstruction at 30 nm resolution of the bacterium E.Coli [62]. As opposed to radiation hard material, biological materials impose limits on the absorbed dose, which one is firmly linked (even with freezing) to a minimum achievable resolution of approximately 10 nm [40]. Fig.2.17 shows the work of Nishino et al. [60] on chromosomes.The necessary conditions, limitations and technical aspects of imaging biological materials with X-rays are discussed at length in Laura Shemlit's thesis [63].

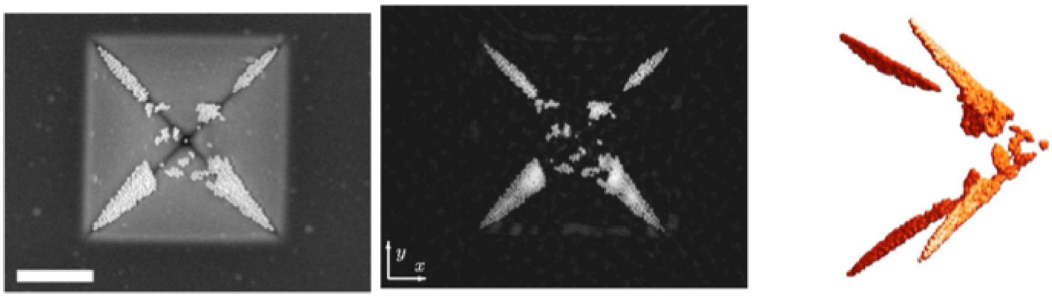

Figure 2.16: Three dimensional reconstruction of a buried sample consisting of 50 nm gold balls on a Si3N4 pyramid. Images from [57].

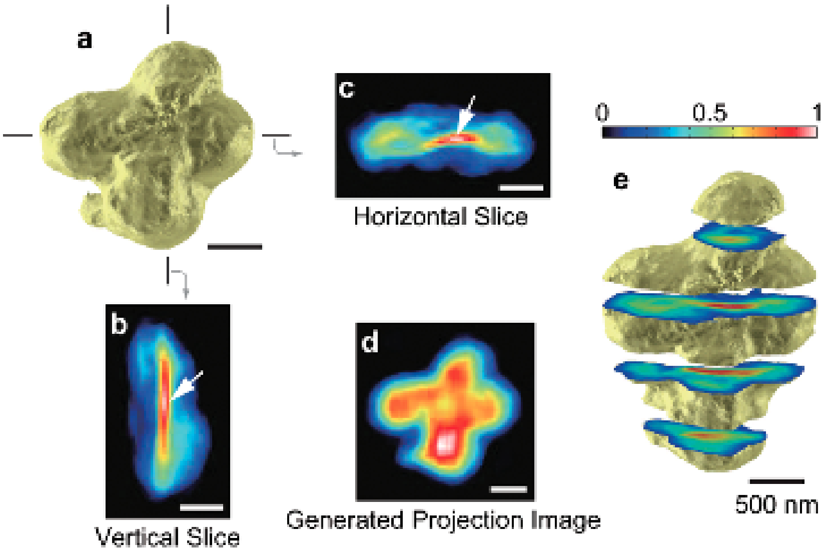

Figure 2.17: 3D reconstruction showing isosurface of the chromosome. The tomographic reconstruction is enabled by the 2D slices data taken at different projections and stitched together. Figures and caption from reference [60].

The X-ray CDI method is hopefully not restricted to photons and taking on a broader view, has its roots in coherent electron microscopy. Electrons are also described by wave mechanics and their stronger interaction with matter (10^4), benefits a higher flux at high scattering angles than X-Rays. The drawback of the strong interaction is multiple scattering, which limits the thickness of samples to 0.5-0.6 microns [40] with a size presently limited due to the short coherence lenghts (about 10's of nanometres) of typical electron beams. However, electron CDI can tackle Fenymann's 1959 challenge to make electron microscope more powerful in order to make easy analyses of any complicated chemical substance by considering its individual atomic position [64]. More recently, Howells claimed that electron CDI has the exciting potential to highlight the function of proteins in molecular machines [40]. Fig.2.18 shows the image of a reconstructed single-wall nanotube at a resolution of 1Å[65].

Progress is also being made so that large-scale facilities do not stay the only 'soundbox' for CDI, with alternative bright x-ray sources such as compact synchrotrons [66] or high harmonic Generation [67]. After Sandberg [67] first demonstrated the use of CDI from a table top HHG was possible, Dilanian [68] extended the use to more than one harmonic. Considering the implicit wasteful of photons in the coherent diffraction process, a CDI reconstruction procedure modified to include the known incident spectrum is highly efficient and together with a greatly reduced data acquisition time while providing higher resolution (over with an associated increase in computing power), small-scale facility x-ray microscopes will broaden the use of CDI in nano-science and biology.

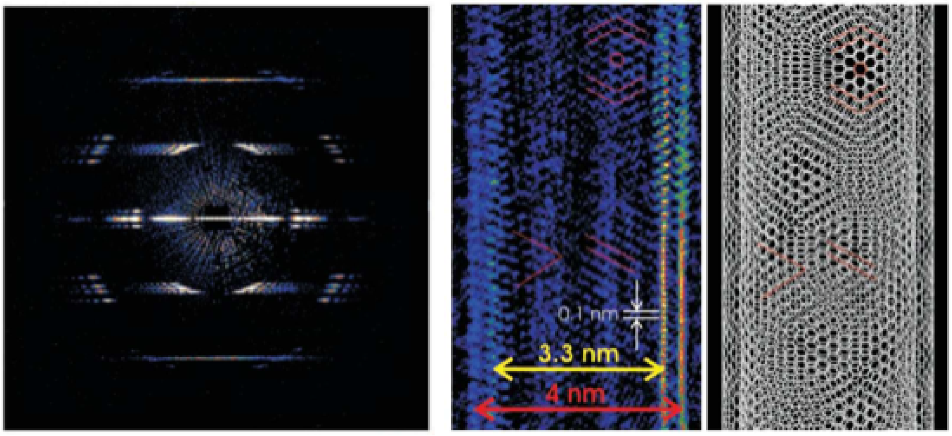

Figure 2.18: A. Measured diffraction pattern from carbon nano-tubes irradiated with electrons. B. Part of the reconstructed nano-tube. C. The structural model. (the inner and outer wall diameter are indicated by the yellow and red arrows respectively). Images from [65].

Extension of CDI research to the emerging X-ray Free Electron Lasers (XFELs) has the truly important potential for turning these extremely bright light source into discovery machines [69]. While the very high peak brilliance will allow for atomic resolution of nanostructures such as bio-molecular complexes and crystal defects, the femto-second pulse duration will allow the study of their dynamics [70]. The situation for organic matter seems at a first glance paradoxical, i.e., how a pulsed beam with a dose exceeding by more than 5 orders the maximum allowable dose of radiation can be a remedy. The key is that the sample remains intact during the very short duration of the pulse and the useful data collection at high scattering angle has been performed before a rapid photo-ionization cascads into an ultimate Coulomb explosion. Recent studies have indicated that the underlying mechanism of damage takes place between 20 to 200 femto-seconds [70], which confirmed the first theoretical consideration done on a single molecule by Janos Hajdu et al. [71]. The ability to image single bio-molecules will be of enormous benefit for structural biology and especially to the protein difficult to crystallize, e.g., the vital membrane proteins, target of future drugs [72]. Even though an XFEL has a high peak intensity, "fresh" copies are individually introduced to accumulate the homeopathic speckles. This is done with a so-called spraying technique but is challenging as it presumably involves random orientation through the beam. However, by considering a large ensemble of scattering images, the application of clever procedures can almost miraculously rearrange and classify *ex post facto*, the accumulated data and build the correct 'to be phased 3D volume' (see Fig.2.19). The pressing scientific challenges (of benefit to society) that will be addressed by XFEL's, are reviewed in the excellent SwissFEL science case [69].

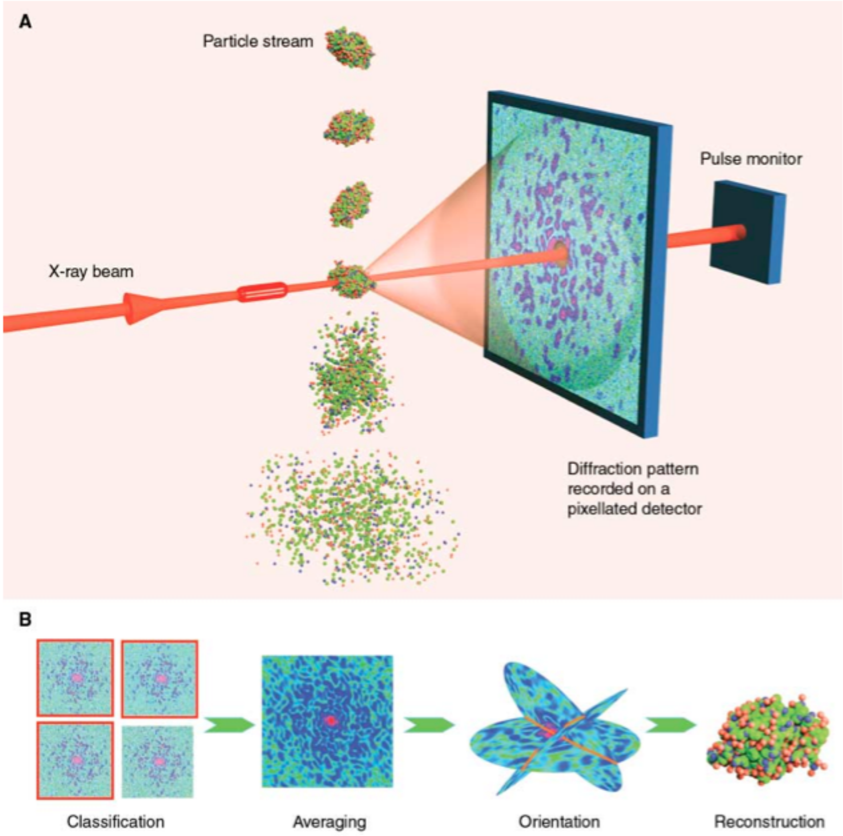

Figure 2.19: Illustration of a single-particle CDI from an XFEL pulse. (A) The intense x-ray pulse scattering off the object forms an intensity pattern at the detector. However, the intense pulse photo-ionizes the sample leading to plasma formation and followed Coulomb explosion, leaving time to record only one diffraction pattern of the particle. Thus, a jet of fast traveling identical particles is needed to record many individual diffraction patterns from single particles (the detector must be able to capture just as quickly). (B) The large ensemble of noisy diffraction patterns arising from the random and unknown orientations full is assembled into a 3D diffraction data set in reciprocal space (i.e., patterns are classified to group patterns of like orientation, averaged within the groups to increase signal to noise, and finally oriented with respect to one another). The image is then obtained by phase retrieval. Images and caption from [57].

Chapter 3

Ptychography

Coherent Diffraction Imaging (CDI) suffers from an experimental drawback, which is the required size of the sample for satisfying the oversampling criterion, thus can lead to aggressive sample preparation. Ptychography can examine any particular region of interest by shifting the probe in small steps to record diffraction patterns from overlapping regions. Ptychography is an elegant synthesis of CDI and scanning transmission x-ray microscopy (STXM), two techniques that use coherence and a detector but have developed separately. While the former has the prospect of very high resolution but is limited to isolated object, the latter easily provides a transmission map of an extended specimen by use of a scanning probe but its resolution is limited to the extent of the focal spot size. Thus for a given STXM setup, such a marriage of methods provides at least a five fold increase in resolution. Ptychography also leverages the problems encountered in single-measurement CDI methods, such as convergence difficulties for strong phase objects [73]. Its intrinsic quantitative character makes it a successful microscopy technique for nano-materials as well as biological objects [74] in 2D and in 3D [75]; as will be shown in section.3.6.

Improving the algorithms, to deal with experimental problems such as vibrations [76], partial coherence [77] and uncertainties in scan positions [78] is the subject of this chapter.

3.1 Ptychographic Iterative Engines

The translation-diverse phase retrieval approach of ptychography was brought to maturity by Rodenburg and Faulkner in 2007 with the introduction of the ptychographic iterative engine (PIE) [79]. Ptychography finds its roots in structure solving by overlapping Bragg peaks in reciprocal space by Hoppe and later implementations by Nellist et al. for electron microscopy [80].

In ptychography, an unknown specimen is scanned by a localized illumination with known displacements. For the mathematical description, the complex-valued probe and object are defined as two dimensional fields $p(\mathbf{r})$ and $o(\mathbf{r})$ with $\mathbf{r} = (x, y, 0)$, while the different positions are given by a single vector $(\mathbf{r_j})$. Each of the j-th scan points generate an exit field that is measured in the far field:

$$I_j(\mathbf{q}) = |\mathcal{F}[p(\mathbf{r} - \mathbf{r_j})o(\mathbf{r})]|^2. \tag{3.1}$$

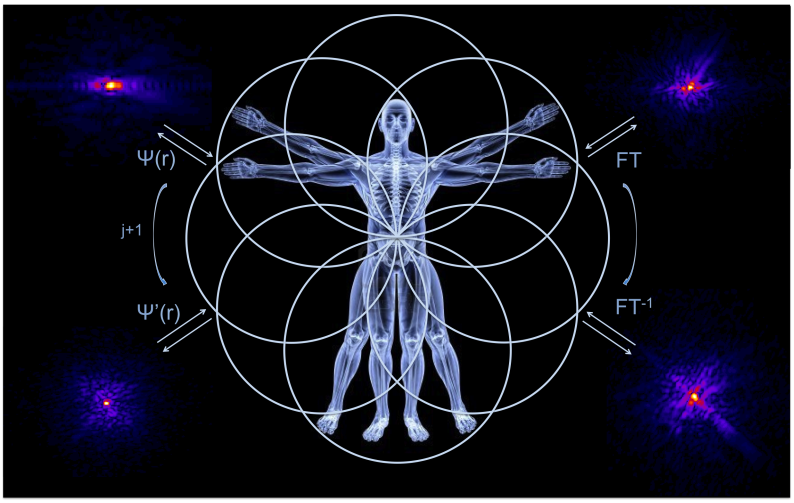

Figure 3.1: Ptychographic scheme. The circles indicate the partially overlapping positions and the arrows indicate how the desired input-output information is taken from Fourier inversion at each position stepping.

Given as inputs, $p(\mathbf{r})$, $\mathbf{r_j}$ and the corresponding measurements I_j, a ptychographic reconstruction entails finding a single object field $o(\mathbf{r})$ that agrees with all the measurements. The overlap constraint between positions implies a multiple update of the different field realizations within a single iteration, and thus dramatically increases the success of converging efficiently to a unique solution. Obviously, the relative strength of the overlapping constrained illumination is the ingredient that favours the convergence.

PIE sequentially generates views that agree with the measurements; the procedure is detailed here:

1. A current object transmission function from a shifted position $\mathbf{r_j}$ becomes after multiplication with a localized probe function: $f_j(\mathbf{r}) = o(\mathbf{r} - \mathbf{r_j})p(\mathbf{r}) = \psi_j$. Then, this complex function evolves (or propagates) to the far field by use of a computational FFT:

$$\Psi_j(\mathbf{q}) = |\Psi_j|e^{(i\hat{\phi_j})}| = \mathcal{F}[\psi_j(\mathbf{r})]. \tag{3.2}$$

2. Next, the modulus constraint is applied while preserving the computed phase:

$$\Psi'_j(\mathbf{q}) = \sqrt{I_j}.e^{(i\hat{\phi_j})}. \tag{3.3}$$

3. The inverse Fourier transform of $\mathcal{F}^{-1}[\Psi'_j(\mathbf{q})]$ updates the current view which is in turn used to estimate a new object:

$$o_j^{n+1}(\mathbf{r}) = o_j^n(\mathbf{r}) + \frac{|p(\mathbf{r}+\mathbf{r_j})|p^*(\mathbf{r}+\mathbf{r_j})}{|p_{max}(\mathbf{r}+\mathbf{r_j})||p(\mathbf{r}+\mathbf{r_j})|^2 + alpha}.\beta(\psi'_j(\mathbf{r}) - \psi_j(\mathbf{r})), \tag{3.4}$$

   where α is a term used to avoid numerical problems when $p(\mathbf{r}) \approx 0$ and β is a feedback parameter usually adjusted between 0.5 and 1.

   Operation 1-3 can be resumed into a single operator $\Pi_F \rightarrow \psi'_j = \Pi_F[\psi_j]$.

4. The above steps are repeated for each of the j diversity images all over the positions $\mathbf{r_j}$ to update for the object field. Completion is realised after n iterations, with one iteration being interpreted as one pass over all scan positions (The PIE scheme is summarised in Fig.3.2).

A few years later in 2008, Guizar-Scicarios highlighted in [81], the relation of the PIE algorithm to a steepest descent algorithm. In fact, PIE is an ordered subsets steepest descent algorithm as the whole data are divided into several subsets (in this case, one subset = one diffraction pattern) with the object updated serially. Steepest descent means that each sub-iteration consists in minimization of a cost function. The mathematical steps and analytical expression are derived in Guizar's paper but more generally, it can be more readily seen by rewriting Eq.3.20 as:

$$o_{new}(\mathbf{r}) = o_(\mathbf{r}) + \beta' \frac{\partial L_{PIE}}{(\partial o^* + \partial o)}\{o(\mathbf{r}); I(\mathbf{q}))\}, \tag{3.5}$$

where the gradient of the metric $L_{PIE} = ||\sqrt{I_j} - \Psi'(\mathbf{q})||_{l^2}$ is taken with respect to the real and imaginary part of the object. The spatially variant step size in the direction of the steepest descent are given by:

$$\beta' = \frac{|p(\mathbf{r}+\mathbf{r_j})|}{|p_{max}(\mathbf{r}+\mathbf{r_j})||p(\mathbf{r}+\mathbf{r_j})|^2 + alpha}.\beta, \tag{3.6}$$

and are proportional to the weight of each pixel in the normalized illumination function, thus emphasising the object update where the beam amplitude is significant [81]. Recognizing that other gradient search algorithm, e.g. conjugate gradient, are superior to steepest descent, Guizar suggested the use of a non linear optimization algorithm to jointly optimize over the ptychpgraphic entries, i.e. the object, the illumination beam and the translation parameters. For an efficient implementation of the algorithm, the analytical expressions with respect to each of the entries are provided in [82, 81]. The advantage of such an approach is that any other non ideality in the measurements can be included , i.e., transverse coherence, detector misalignments, finite pixel size, etc.. Even though the algorithm was found to achieve superior image reconstruction over PIE when the system is not accurately known i.e., $p(\mathbf{r})$ and $\mathbf{r_j}$, it was 'eclipsed' by an algorithm with better performance: the difference map adapted to ptychography.

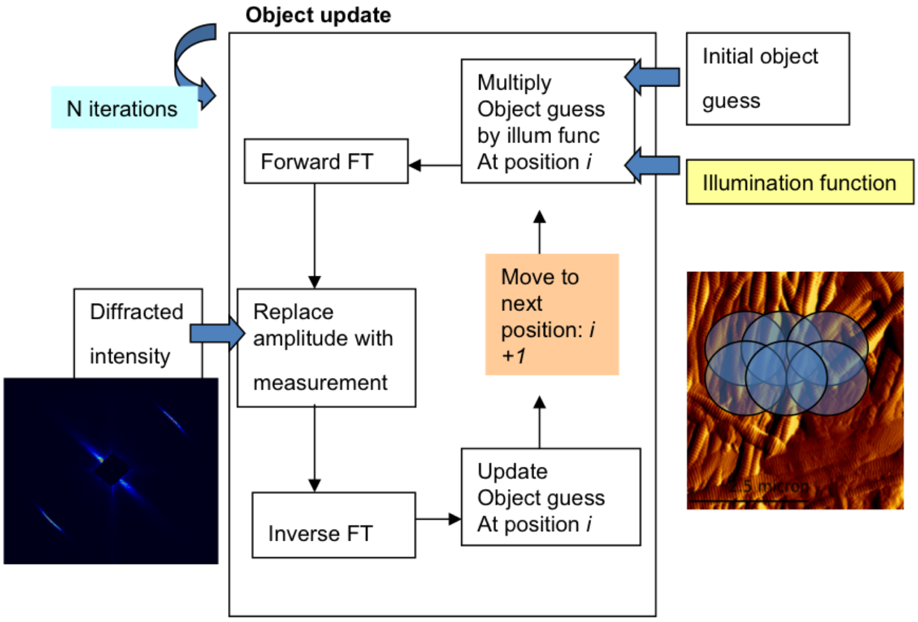

Figure 3.2: PIE scheme.

3.1.1 Difference Map

Elser found that many of the already established phase retrieval algorithms can be readily described by the formalism of projection onto constraint sets [47]. A solution is then obtained when a point has reached an intersection between two subspace constraints. Thibault in 2009 [83], has adapted the formalism of difference map to ptychographic data where the constraints are in this particular case, the

Fourier projection and the overlap projection.

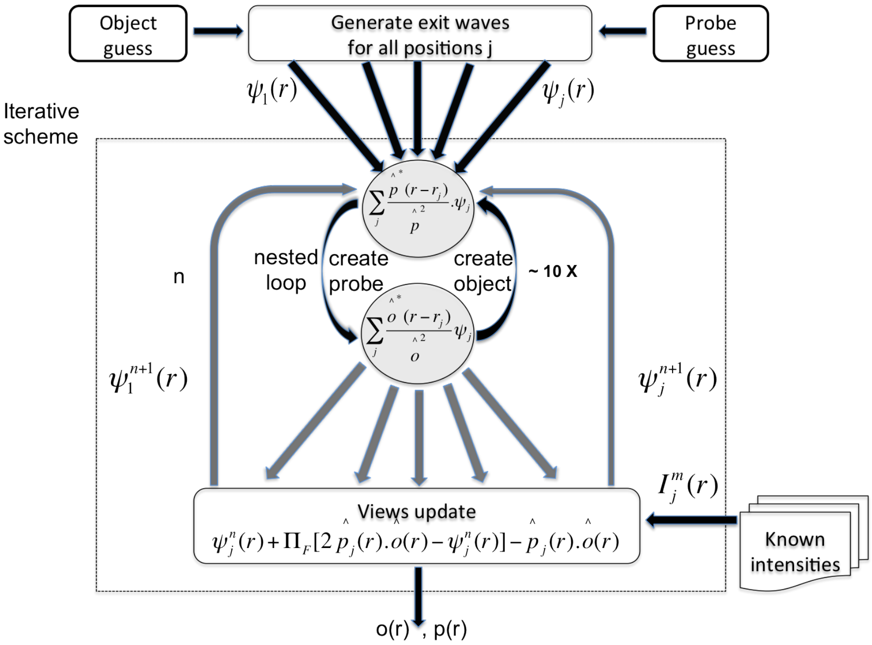

Figure 3.3: Difference map scheme: the arrow represents where the measured diffraction patterns enter. The update of the object and probe functions are computed from the entire set of views simultaneously, and the Fourier projection can be calculated in a parallel fashion. In the PIE algorithm these updates and projections are calculated serially as the algorithm loops over the individual views.

In the adaptation of DM to ptychography, a state vector formed from the multiplication of each view ($\Psi = (\psi_1(\mathbf{r}), \psi_2(\mathbf{r}), ..., \psi_N(\mathbf{r}))$ must simultaneously satisfy two constraints: the Fourier constraint and the overlap constraint. The projection onto a constraint is the element that satisfies the the constraint while minimizing the distance $||\Psi - \Pi(\Psi)||^2$. While the Fourier projection Π_F that applies to each view, has been described earlier, the overlap projection Π_0 can be computed from setting the derivative of the distance-minimisation $||\Psi - \Pi_0(\Psi)||^2$ to zero with respect to overlap constraint to give:

$$o_{new}(\mathbf{r}) = \frac{\sum_j p^*(\mathbf{r}+\mathbf{r_j}).\psi_j(\mathbf{r})}{\sum_j |p(\mathbf{r}+\mathbf{r_j})|^2}, \tag{3.7}$$

and

$$p_{new}(\mathbf{r}) = \frac{\sum_d o^*(\mathbf{r}-\mathbf{r_j}).\psi_j(\mathbf{r})}{\sum_d |o(\mathbf{r}-\mathbf{r_j})|^2}. \tag{3.8}$$

These equations need to be solved simultaneously as the system cannot be decoupled analytically and this is the reason for the built nested loop seen in Fig. 3.3 which iterates a number of times. While the ePIE uses only the overlap constraint to derive a probe, the additional step of overlap projection here, makes the probe derivation more formal.

The main difference is in the update of the state vector, which in ePIE takes a simple replacement form and is incorporated within the object and probe update whilst in the difference map algorithm the update function takes a more complicated form which is more similar to the HIO (Eq.2.53) equations of Fineup for single-shot CDI:

$$\Psi_{n+1} = \Psi_n + \Pi_F(2\Pi_o(\Psi_n) - \Psi_n) - \Pi_o(\Psi_n). \tag{3.9}$$

The convergence is monitored by the squared absolute difference between the current and previous iterations [84]:

$$\epsilon_{n+1} = ||\Psi_{n+1} - \Psi_n||^2. \tag{3.10}$$

Projections: In the supplementary info of Thibault's paper were DM is presented, the validity of the multiplicative projection is also assessed with real space argument whereas Rodenburg and Bates had first developed their argument as Reciprocal-space argument [86]. Thus, for the multiplicative relation of probe and object to be true, a maximum depth of the sample is given as a function of the resolution of the system, R, the spatial extent of the probe wave-field, and the wavelength by $Z = Ra/\lambda$. Consequence of the overlap, stems a large a, and so allows the assumption that the probe is always constant within the sample. Under these conditions, reconstructions are possible independently of the scattering regime (whether weak or strong) and even not compromised with strong dynamical diffraction [83].

Other techniques

Phase modulator scanning : This method takes a similar approach to phase retrieval but using the essence of the wave-front sensing technique. This uses a known phase perturbation (coming from a manufactured plate) in the recording of intensities from which the phase can be derived. This method can also be used to image extended objects where the support cannot be defined by the sample. The technique has been developed by Zhang et al. [87]. As with other forward scattering methods the sample must have sufficient transmission in order to capture diffraction with sufficient statistics.

Marchesini: Marchesini in his 2011 paper reviews some of the existing meth-

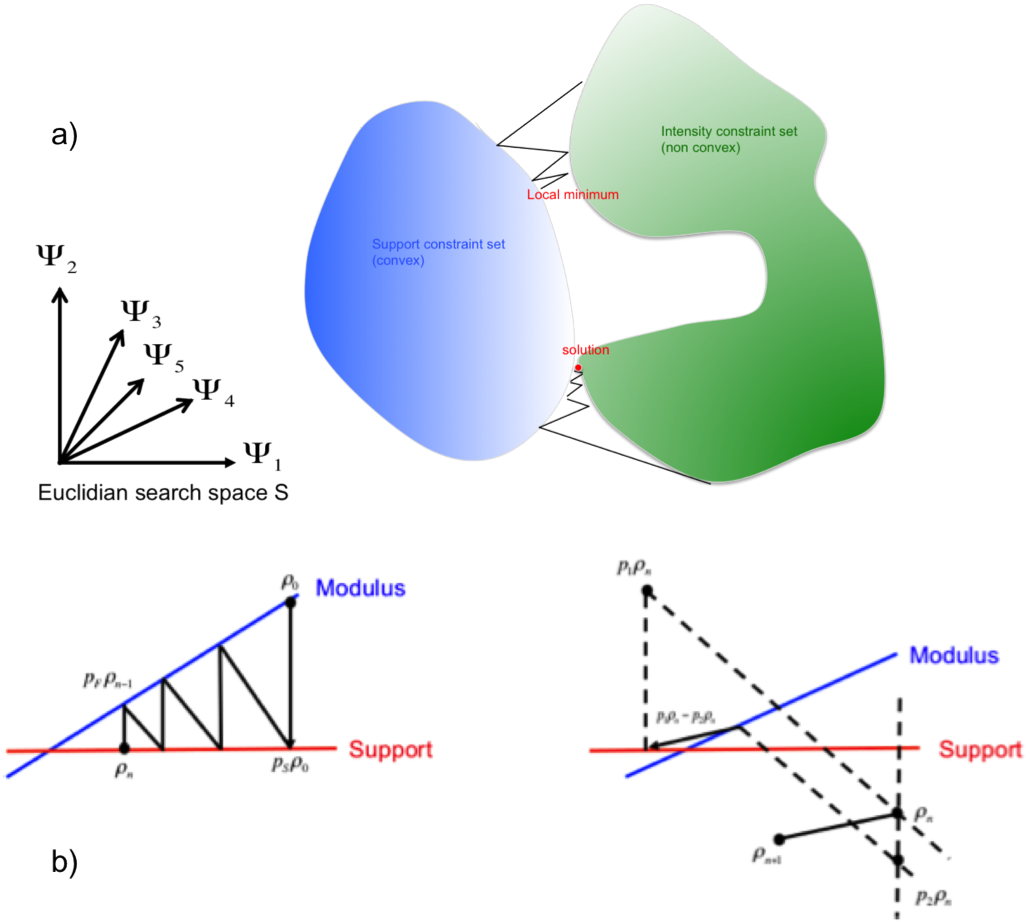

Figure 3.4: Sketch of the behaviour of ER and DM algorithms as projections onto constraint sets. The modulus constraint set is shown as a blue line and the support constraint as the red line, the solution is at the point where the two lines intersect. From these geometrical representations, it is understood that the difference between the ER and DM algorithms lies in the paths taken to reach the solution (which is not always on the constraint set), e.g., the DM algorithm works by taking the difference between two projections labelled here as $p1$ and $p2$. Caption and figures derived from [53, 85, 63].

ods for solving ptychographic phase retrieval problem from a numerical analysis approach, and proposes a solution to the problem by alternative methods that are standard in the numerical optimization community [88].

3.2 Simulation and experimental parameters

A common practice when extending the algorithms tools is to perform numerical tests (or simulations) to assess their performance. An arsenal of tools has been developed in the CDI field to correct for imperfections in data and next sections cover their implementation within the difference map method as to reach satisfactory results under departure from a controlled environment. The following scenarios are considered: uncertainties in scan positions, degraded beam coherence, illumination drifts, vibrations. To be more realistic, all scenarios are tested with different degrees of noise (the procedure to add Poisson noise counting statistics diffraction data is explained later in this section). As the effects of realistic parameters can be studied separately, simulations aim to give us a better understanding of the correcting mechanisms and their respective limits. However, real world experiments usually involve all the scenarios during acquisition of a data set; then, it will be assumed that the large amount of redundant data allows the combination of refinement methods to work together in an efficient manner.

Simulations and reconstructions share the discrete pixel units of the computer whose sizes are related to experimental 'real world' units by the sampling relationship of real and reciprocal space of the DFT:

$$\Delta r \Delta d = \frac{\lambda L}{N}. \tag{3.11}$$

Thus, the translation for each of the j^{th} illumination positions during numerical reconstructions are set by this equation. However, this should be understood as the pixel size for the numerical calculation as opposed to a measure of resolution.

Simulations were designed with Matlab (short for Matrix laboratory), a computer language where the fundamental units are matrices. It is thus perfectly suited for numerical imaging problem in two and three dimensions, as a range of arithmetic operations can be performed on arrays. The language is interpreted by and also contains a number of built-in computational and graphical procedures.

At the root of the ptychographic simulations lies the transformation of a feature rich (jpg or png) image into a complex-valued matrix. The following sequence of Matlab functions is used:

1. Transformation into a Matlab matrix using the function:
   image = imread('image.jpg').
2. The RGB image is merged into a single matrix with:
   image = rgb2gray(image).
3. Normalisation of the image to have an amplitude [0-1] :
   object = image-min(min(image)),
   object = object / max(object(:)).
4. The object is embedded into a larger field of view,
   object = padarray(object, [300 , 300]).
5. Finally, the object is rendered complex,
   object = exp($-k * \delta *$ object). * exp($-i * k * \beta *$object).

For the effectiveness of simulations, the projection of a single material sample is considered, with a convenient ratio β/δ of approximately [6-8], to avoid the situation of a pure phase object or a purely absorptive object. The computational sensitivity of CDI with regard to the integrated phase does not decrease as a function of the object thickness but rather curl the signal around the origin due to the limited interval $[0 \leftarrow 2\pi]$, a phenomenon called phase wrapping. Then, simulations are produced with a phase retardation of maximum 2π, otherwise the reconstructed phase images need to be unwrapped, and this could provide a difficulty for 'noisy' images (the Goldstein method [89] which uses spatial correlations in the image, is a reliable way to this end). Extension to multi-materials has not been considered but should be straightforward, for example the object field could be divided into regions with different ratios along with sub-regions that are formed by union of these different regions.

Once a complex-valued object is created, the type and size of the localised illumination must be considered. Simulations presented in the next sections are based on a pupilar function, meaning a circular aperture filled by ones generated on a background array of zeros. To 'smoothen' its sharp edges, the pupilar function will either be convolved with a Gaussian function (of few pixels) or be propagated slightly using the angular spectrum method (Equ.2.6). To avoid aliasing and also generate oversampled diffraction pattern, the substantially localized illumination must not fill more than half of each of the array dimensions. The illumination array size and therefore the size of the computed diffraction patterns is set to power of two in each dimension (e.g.2^8, 256 pixels) for computational efficiency of the FFT. In later sections of the thesis, it will be shown that ptychography can cope with illuminations that are more 'structured' or present astigmatism with an initial model strongly dissimilar from the wavefront to be recovered.

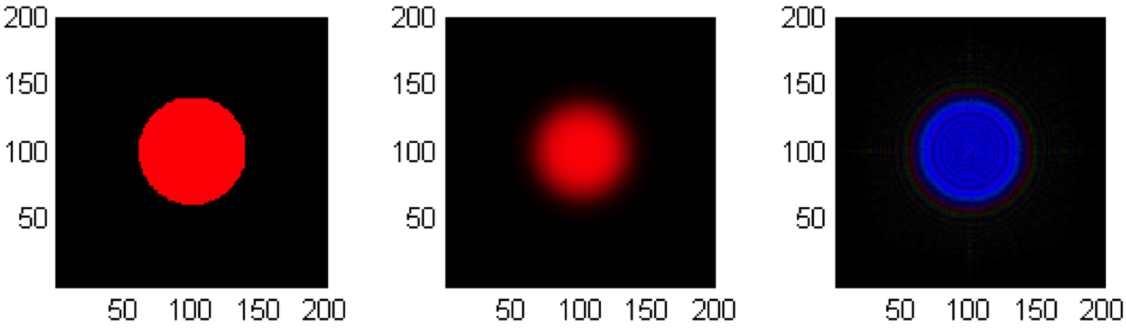

Figure 3.5: HSV plot of a pinhole, a pinhole with smooth edges and a pinhole propagated using the angular spectrum approximation to $z = 5$ mm. Pixel size is 50 nm

No 3D simulations were performed. Nonetheless, considering the previous assumption that the beam wavefront function stays constant inside the sample, a three dimension illumination is simply created by expanding the 2D array into the third dimension z. For more realistic simulations, an exponential term based on calculation of the absorption length as a function of the beam interaction with the material, should be imparted in the amplitude term. 3D simulations were investigated in Bean's thesis [52] with the findings that convergence is only reached if a relatively tight support is applied to the object's third dimension.

3.2.1 Error assessment

In the case of simulations, the error in reconstructions can be reliably computed by a suitable metric such as the one provided by Fienup [90]:

$$E_n = \frac{\sum |O_n|^2 + \sum |O|^2 + \sum \sum OO_n^*}{\sum |O|^2}, \tag{3.12}$$

which in this form, is insensitive to constant global phase factors. As the the probe is allowed to float during ptychographic reconstructions, the object will also consequently move. Thus, the term $\sum \sum OO_n^*$ should be replaced with the maximum of the cross-correlation to render the metric insensitive to translational offsets.

However, assessment of error for real reconstructions is less absolute and the reliability of the reconstructions will be mainly monitored (or analyzed as for real data) with difference map error metric Eq. 3.10 and the R-factor [83] which quantifies the agreement with the measured data and calculated as:

$$R = \frac{\sum_j^J \sum_q^Q (||I_{obs}^j(q)| - |I_{calc}^j(q)||)}{\sum_j^J \sum_q^Q |I_{obs}^j(q)|}, \tag{3.13}$$

where the summation is over the reciprocal-space coordinate q and the j^{th} measured diffraction patterns.

3.2.2 Scans

Simulated and real data were acquired using a 'spiral' scan pattern or more precisely, the Round-ROI-scan. This scan, which follows concentric trajectories, eliminates grid artefacts in ptychography [75] that are due to a 'pathological' symmetry. Its ability to break down translation symmetries has also proven to improve data convergence and to reduce ambiguities in data reconstructions [83]. Explanation given in [75] are repeated:

" If $p(\mathbf{r})$ and $o(\mathbf{r})$ are the solutions to a ptychograpic dataset then so are the functions $o'(\mathbf{r}) = f(\mathbf{r})o(\mathbf{r})$ and $p'(\mathbf{r}) = [f(\mathbf{r})]^{-1}p(\mathbf{r})$ if and only if $f(\mathbf{r}) = f(\mathbf{r}+\mathbf{r_j})$ for all positions j. This has only the trivial f = Cte solution unless the scan positions lie on a regular grid. Implementations of this in use are adding a random offset to a set of 'grid' positions. One benefit of the round-ROI scan is that while breaking the translational symmetry, an analytical description of the scan positions can be preserved ".

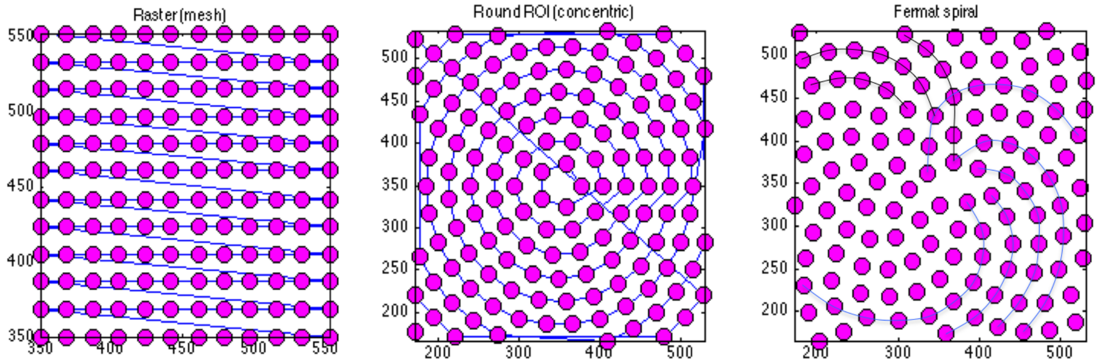

Figure 3.6: Scan positions for ptychography: Left: periodic pattern. Middle: concentric pattern. Right: Fermat spiral pattern containing two sets of equiangular spirals following clockwise (black curves) and counterclockwise (blue curves) path [91]. They are two consecutive Fibonacci numbers.

The scan pattern is defined by the following equations:

$$x = \Delta r.n \cos((m-1)\frac{2\pi}{N_\theta n}), \tag{3.14}$$

and

$$y = \Delta r.n \sin((m-1)\frac{2\pi}{N_\theta n}), \tag{3.15}$$

where x and y are the coordinates of the object position, Δr is the step size, n is the schell number, N_θ is the number of points in the first shell and m is the m^{th} point in the n^{th} shell (whilst still sampling evenly).

This scan has been widely used, but a promising scan that presents a lack of symmetry while featuring a uniform coverage has been presented very recently by Huang [91]: a Fermat spiral pattern. This scan presents better reconstructing performance, especially towards low overlapping conditions. Inspired by plants in nature (daises, sunflowers, pineapple) where arrangements of branches are 'space-optimized' as to provide equal exposure to pollinators (or even to the Sun). The analytical expression proposed by Vogel [92] to construct the tightly packed sunflower seeds is given in polar coordinates:

$$r = c\sqrt{n},\ \theta = n.\phi_0, \tag{3.16}$$

where c is a constant scaling factor for the radius r, n is the index number of the seed, and ϕ_0 is the divergence angle, known as the golden angle ≈ 137.508 . Due to its recent introduction, the scan has not been used in this thesis but should be used for future experiment has it has proven to improve SNR of reconstructed images by a factor $\approx 5\%$

Fig 3.6 c) shows a Fermat spiral pattern, with the factor c adjusted to give a total number points that matches with that of the other scans over the same area. Some of the clockwise and anticlockwise lines are drawn to depict the capitulum of a sunflower. Its superior performances is explained by the fact that the scan distributes more power to high spatial frequency (through the Fourier transform of the overlap maps). It has then been concluded that: 'the Fermat spiral pattern indeed represents more randomly arranged points while providing more uniform coverage' [91].

Simulated diffraction

Once a scan regime has been chosen, a ptychographical set of 2D diffraction amplitudes is generated from a complex-valued object and illumination, using the following procedure (script 'diff.pattern.sim' in appendix) which is also given in Bean's thesis [52]:

1. Generate the vector position $\mathbf{r_j}$ (pixel units) from the scan regime (raster or Round-ROI) and its respective parameters.
2. At each of the $j-th$ positions, cut a region defined by the size of the illumination function array to form the sub-images, $(o(\mathbf{r}-\mathbf{r_j}))$.
3. Multiply each sub-images with the illumination array $p(\mathbf{r})$ to yield the views $\psi_j(\mathbf{r})$.
4. Propagate the views to the far field using an FFT as for propagator.
5. Square the propagated views,$|\Psi_j|^2$, to remove the phase information and generate the intensity recorded as in an experimental diffraction experiment.
6. Stack the intensity patterns in .mat structure as input data for the ptychography algorithms.

In an experimental measurement, the number of arriving photons follows a Poisson distribution, so even a perfect measurement inherit of some uncertainty which follows $\sqrt{M}$, with M being the number of photons measured at each pixel. The procedure to make realistic simulations is given in Garth Williams' thesis [48]:

- Select the density projection of the object
- Compute the FFT to simulate a diffraction pattern
- Estimate or select the number of photons M
- Calculate the intensity for use as a probability for determining the location of photons
- Based on the integrated intensity and the number of photons, calculate the average intensity per photon drawn from a random distribution with mean given by the intensity in that pixel divided by the average intensity per photon.

In Matlab language the process can almost can be condensed into one line using the implemented poisson distribution function:

Pattern= $poissrnd((Intensity/sum(Intensity(:)))*M)$

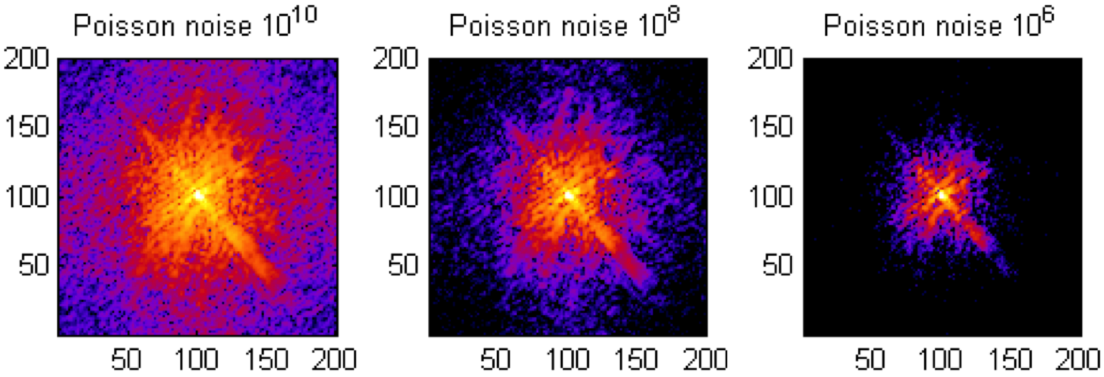

Figure 3.7: Left to right: A typical diffraction pattern with its number of photons and hence SNR decreasing.

Figure.3.7 shows the effect of different level of photons on the diffraction patterns.

Fortunately, the ptychography has been shown from its early days to be robust with respect to noise [93], nonetheless for low counting statistics, techniques like maximum likelihood can be implemented for even better performance of the algorithms [94, 95]. The degrees of partial coherence and scan errors are set optionally in the simulation code.

3.3 Positions determination

If robustness is the consequence of the translation diversity, in counterpart, this latter couples the reconstruction resolution to the accuracy requirement in translation. Indeed, it was quickly realised experimentally that the achievable resolution could not surpass the scan accuracy [96]. Moreover, the degradation increases drastically at short wavelength as the instabilities and inaccuracies of translation stages become significant with the desired resolution [97].

Based on the premise that thermal drifts and mechanical instabilities are integral parts of real-world experiments, Takahashi in his quest for high resolution [97], developed an *in situ* technique to suppress position errors but it is quite tedious a method (before measuring a diffraction pattern at each focused beam position, an isolated particle has to be scanned with a dark-filed knife-edge method, then the peak of the fitted intensity profile is used as a reference point to precisely measure the drift). An *a posteriori* method that relaxes the sensitivity to positional errors while improving the quality in images, is a better tool being able to also correct for camera length and misalignment inaccuracies.

Guizar-Sicarios in 2008 [81] was in fact the first to address such a numerical challenge as his metric minimization approach (using conjugate gradients) allows each ptychographic entry to be optimised simultaneously. This method was not shown to operate robustly using experimental data [96] as it easily becomes trapped in local minima. However, keeping the conjugate gradient descent approach to correct for insufficiently known position while updating the object and illumination functions with ePIE or DM has shown (very recently) to be a scheme that operates robustly, even for large critical scan positions errors [98].

Rodenburg and coworkers developed a genetic algorithm [99] but it did not prove to be robust either, so they came to settle upon another method that is simpler in its implementation while providing a promising solution, an annealing approach based on a trial and select strategy at each single position of the diversity field [96]. While the annealing method is based on optimization of each single exit wave's Fourier space, it was followed thereafter by an alternative method based on a model of position errors, which instead optimizes the summed-square error. In the latter method, randomly distributed linear drifts are applied during reconstructions until a global coefficient has been found within the applied parameter space of error distribution (see Fig.3.8). Considering that the method requires to first correct for the linear drift and then to switch to a conjugate gradient search to correct for non linearities left, the flexibility of annealing method will be preferred.

In contrast to these methods that explore various ways of finding some configurations of scan positions that minimize a reciprocal-space error metric, the solution that came very recently to existence, is a real-space sub-images cross-correlation method proposed by Fucai Zhang [78]. It is a very promising technique that has shown to achieve sub-pixel correction accuracy within several tens of iterations.

This section describes the annealing and cross-correlation strategies and explain how they can be adapted to DM together with the use of a simulated test object to explore the capabilities of the algorithms. A rigorous comparison of the performance of ePIE and DM regarding positions refinements is not the purpose here; rather DM is targeted because it performs better on non-extended objects. Moreover, the ability of position correction method to retrieve global tilt through a transformation matrix $T(\theta_x, \theta_y, \theta_z)$ reveals similarity to the transformation matrices needed in the Bragg ptychography geometry, thus will be used to reinforce the success of reconstructions regarding this challenging geometry.

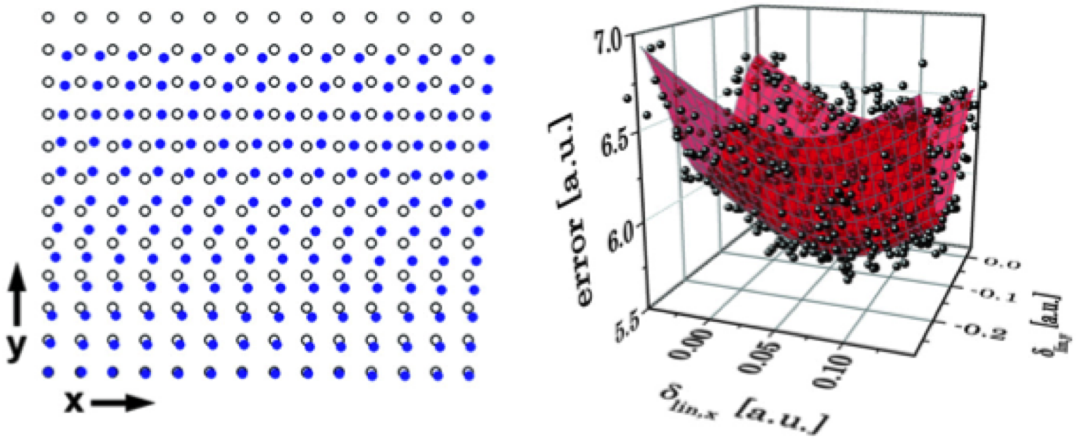

Figure 3.8: Left: scan positions before drift correction (black circles) and after linear correction (blue dots). Right: the error distribution of individual reconstructions after many randomly distributed linear drift founds a minimum (polynomial fit, red surface) providing the adequate set of corrections in x, y. Image and caption taken from [100].

3.3.1 Annealing based algorithm for ptychography

The trial and select method known as the annealing method is an obvious choice for an algorithm that proceeds in a serial manner, such as the ePIE. At each single sub-iteration the modified ePIE algorithm (epcPIE) takes iteratively update its corresponding position correction vector $\mathbf{r_j}$ through the following sequence, reported from [96].

1. Form an estimate of the wavefront at position $\mathbf{r_j}$, $\psi_1(\mathbf{r}) = p(\mathbf{r})O(\mathbf{r} - (\mathbf{r_j} + c_j))$ along with a set of m=1..M further estimates of wavefront, each with a different trial offset $c\Delta_m$:

$$\psi_{guess,j}(\mathbf{r}, R) = p(\mathbf{r} - (\mathbf{r_j} + c_j + c\Delta_m)).o_{guess,j}(\mathbf{r}), \tag{3.17}$$

   where $\Delta_m = c[\delta_{x,m}, \delta_{y,m}]$ is a vector of two random numbers between [-1 1] and the variable c is a function of the iteration numbers. (c_j is set to zero to start).

2. Next, each output exit wave will now travel to the far field using an FFT to give M+1 estimates at the detector plane:

$$\Psi_{n,m}(q, R) = \mathcal{F}[\psi_{guess,j,m}]. \tag{3.18}$$

3. The modulus of each of the trial exit waves ($[\psi_{guess,j,m}]$) is compared to the measured diffraction pattern ($\sqrt{I_j}$):

$$E(m) = \sum_q (||\Psi_{guess,j,m}| - \sqrt{I_j}|^2). \tag{3.19}$$

4. The index of the minimum value of E_m is labelled n, so that $m = \min E_m$. If one of the trial offset has resulted in a lower error, the current vector c_j is updated with $c_j = c_j + c\Delta_m$ and stored until the next iteration, in which it will used as the centre-point for the M trial offsets.

5. The projector operator Π_F is applied to the wavefront that resulted in the lowest error metric value, $\psi' = \Pi_F(\hat{\psi_m})$.

6. Then Eq.3.20 applies for the object update, followed by the probe update:

$$p_j^{n+1}(\mathbf{r}) = p_j^n(\mathbf{r}) + \frac{|o(\mathbf{r}-\mathbf{r_j})|o^*(\mathbf{r}-\mathbf{r_j})}{|o_{max}(\mathbf{r}-\mathbf{r_j})||o(\mathbf{r}-\mathbf{r_j})|^2 + alpha}.\beta(\psi_j'(\mathbf{r}) - \psi_j(\mathbf{r})), \tag{3.20}$$

7. The procedure is repeated for each of the j sub-iterations.

The 'epcPIE' has been reported [96] to give good results for simulated and experimental data (optical and x-ray) with a mean error under a single pixel for diffraction patterns with reliable photon counts and with initial position errors $<$ 20 pixels . The manner used to 'corrupt' the translation positions is quite original: the specimen was loosely coupled to the scanning stage during the data collection (from an optical bench). The reconstructed complex-valued images, are reported from [96] in Fig.3.9.

Implementation into difference map

The common feature to ePIE and DM is the the Fourier projection (Π_F) operation, so the minimization of a reciprocal-space error metric can be also applied to each wavefront of the diversity field. If we express the the Fourier projector inside the DM equation as:

$$\Pi_F^m \left[2\hat{p}(\mathbf{r} - (\mathbf{r_j} + c_j + c\Delta_m))\hat{o} - \psi_j\right] \tag{3.21}$$

this operator resumes operation 1-6 in section 1.6, in which the modulus of each of the M trial exit waves at each position j is compared during the Fourier operations to the measured diffraction pattern ($\sqrt{I_j}$) and the exit-field which provides

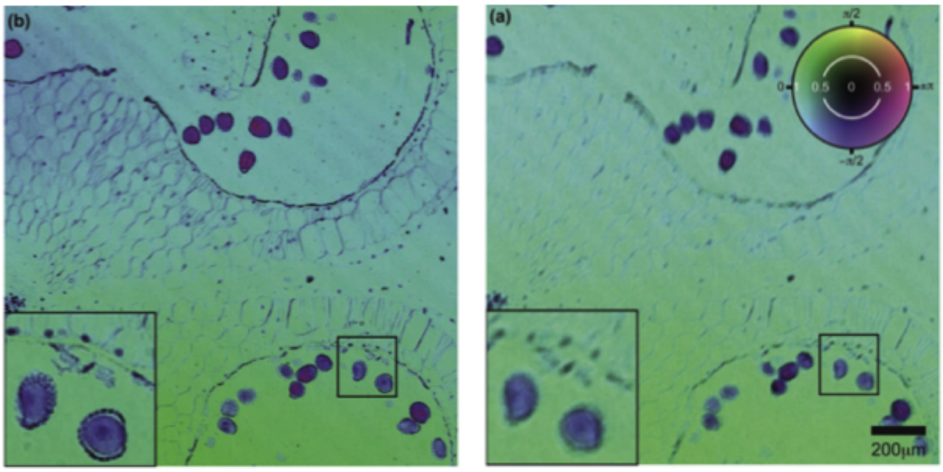

Figure 3.9: Reconstructed complex-valued image of a Winter Jasmine flower bud using data collected from the optical bench with the specimen insecurely fastened to the translation stage. (a) ePIE reconstruction, (b) pcPIE reconstruction, both after 500 iterations. The insets show the areas in the black boxes bottom right of the respective figures. The colour wheel scale shows how phase is represented by hue and modulus by brightness; the same scale is used throughout for the colour reconstructions. Images and caption reprinted from [96].

the best metric is kept so to update a view along with its corresponding position. Below, a sketch of the implementation of annealing for DM is given in Fig 3.10 with parallelization of the annealing process seen as a direct advantage over ePIE.

To explore the ability of the annealing method implemented for DM, a simulated ptychographic experiment was performed. A complex object is derived from the image found in Fig.3.1 with a modulus comprised between 0.1 and 1 and a phase from 0 to π. A pupil function and 128×128 pixel array detector with 20μm pixels placed 1 m downstream of the object gives a Fourier pixel scaling of 28 nm in the real-space for x-ray energy of 9 keV. A round-roi scan of 200 points is selected with a corresponding beam-overlap of $\sim$ 70%, (previous work situates the optimum beam overlap around this value [SLS]). The errors introduced in the translational positions were of Gaussian distribution within an interval of [-5 5] pixels for a mean difference in position vectors of 20 pixels.

The reconstructions with and without position corrections are shown in Fig 3.11 with inclusion of Poisson noise with total counts in the probe set to 10^8. It can be noticed from Fig 3.11 c) that the annealing method has largely improved the difference-map error metric and hence is robust to noise. 150 iterations of the optimisation procedure appears to be enough to reach a plateau as no oscillations are observed at the end of the annealing cycle. The mean error was less than one

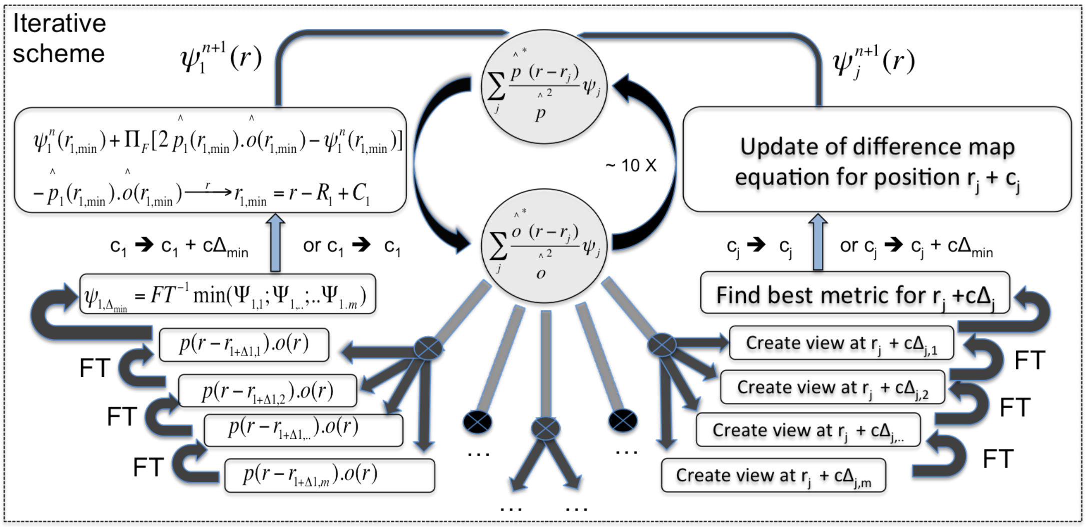

Figure 3.10: Schematic representation of the position-correcting algorithm. At each positional entry, a set of corrections are tested. If one those trialled positions is the source of a better diffraction pattern, it is kept and become itself the source for the trial correction offsets in the following iteration; as in the epcPIE of Maiden [96].

pixel for this simulation and investigation as a function of noise as a function of noise is reported by Maiden for epcPIE in [96] and it is believed that the present adaptation of annealing to DM should in principle reproduce similar results, under the same experimental conditions.

Sub-pixel shift implementation: As in 'real-world' applications the scan step sizes happen to be non-integer multiples of the calculated pixel size, the use of sub-pixel shift is necessary to obtain high quality reconstructions. A small displacement in real-space is realised by application of a phase ramp in the Fourier space (but direct linear interpolation can also in principle be performed). The simulation was performed without the usual rounding of the position errors that is usually administered to the numerical scan positions. To reduce the computation time, the sub-pixel shift correction should obviously be applied to the probe instead of the entire field of view and only employed towards the very end of the iterations. In Fig.3.12, it can be observed that the majority of the points have found their respective 'nests' but to improve the chances of getting a 'full' nesting, the overlap should probably be increased along with the trial of different parameters for the decrement of $c\Delta_m$.

To further understand the kind of uncertainty, like global rotation and scaling, the position errors can be decomposed during the iterative process through transformation matrices [78, 96].

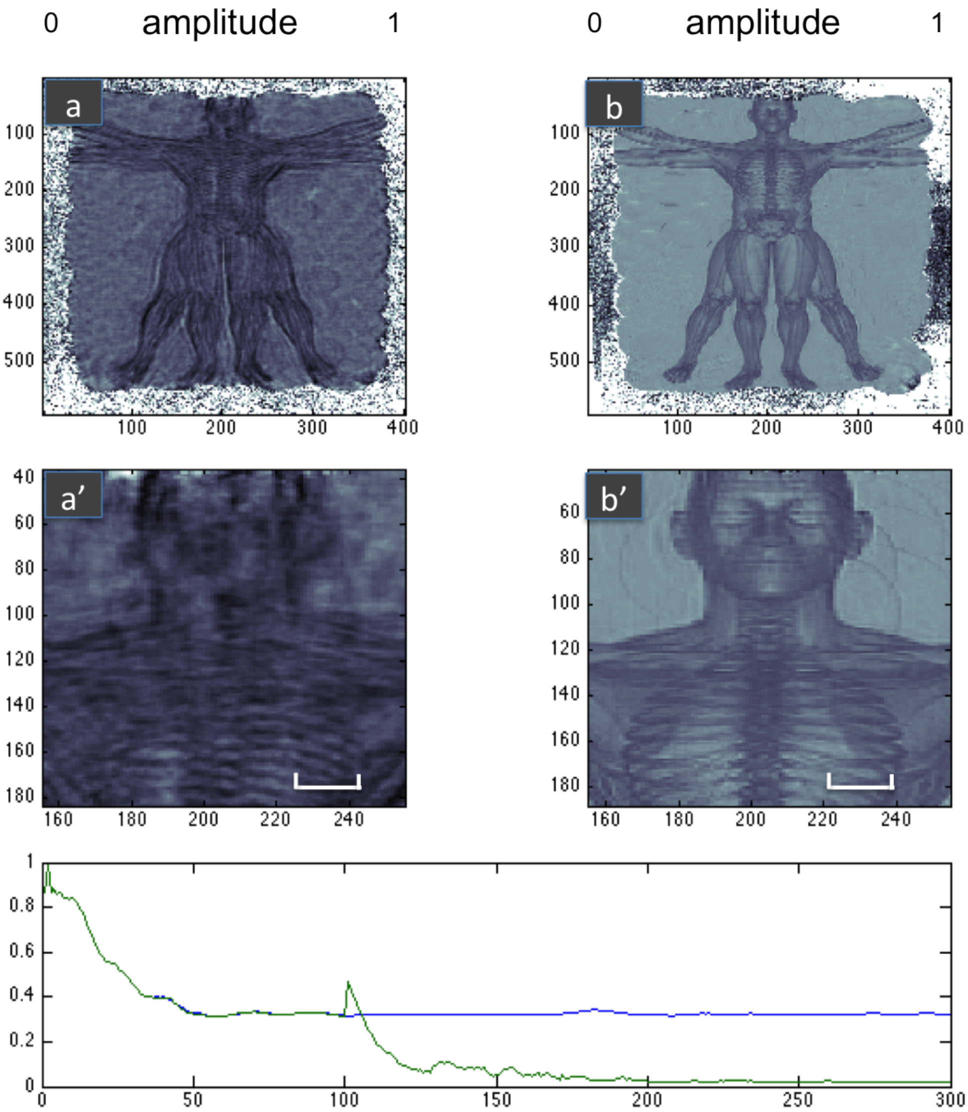

Figure 3.11: Comparison of simulated objects reconstructed in amplitude without and with position corrections, for positional errors of Gaussian distribution in an interval $[-5 \rightarrow 5]$ pixels. Middle row: zoom over the reconstructed objects. Down: Difference in error metric for reconstructions with (green) and without (blue) the annealing method. The annealing scheme is launched after 100 iterations for a cycle of 200 iterations with $M = 5$. Scale bar, 1μm.

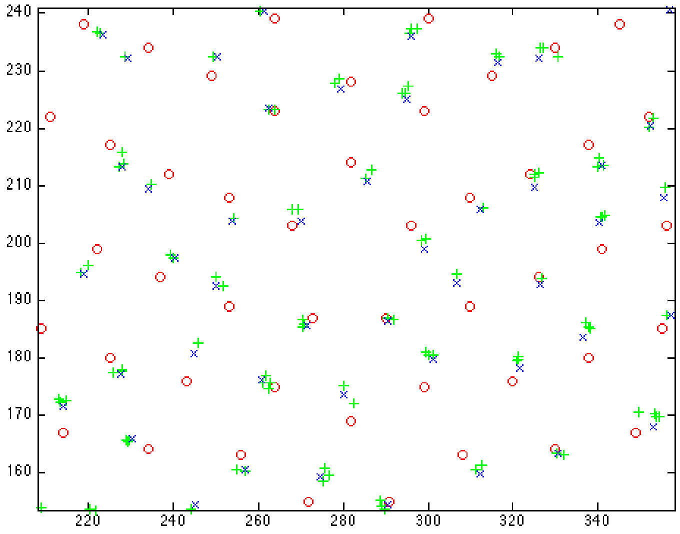

Figure 3.12: Zoom over the central region of the scan used for the ptychographic reconstructions shown in Fig.3.11. Initial positions in red (circle), positions to retrieve in blue (cross) and in green the annealed positions which have in majority, found their respective nests. The added positional errors are of Gaussian distribution in an interval $[-5 \rightarrow 5]$ pixels External regions of the scan usually result in the largest remaining position errors as the image is the not feature-rich. Pixel size is 28 nm.

'Cardinal correction' method : Using the same principle of trial and select described but even simpler in its implementation, would be a method 'using' the 4 cardinal neighbours to guide the search for true positions at each of the scan position. This was not tested but should be in principle equivalent.

3.3.2 Cross-correlation based position determination

The recent scheme for position determination developed by Fucai Zhang [78], is 'radically' different from methods that are based on minimization of an error metric as the correcting mechanism involves the cross correlation of sub-images in the real-space. It is such a powerful method that in the case of perfect simulated data, all the positions can be initiated at the origin of the numerical scan (0,0). It is reported that the algorithm gives a mean residual error well below 0.004 pixels for a total count in the probe set to 10^7 with Poisson noise and a mean start error less than about 20 pixels.

At the genesis, Zhang observed that in the presence of translation positions errors, the individual objects estimate $O_{new}(\mathbf{r}-\mathbf{r_j})$ have a 'natural' tendency to move towards its correct position after the modulus constraint and the overlap constraint have been enforced. This relative shift (e) is indeed tiny but can be injected into a position error c_j feedback mechanism:

$$c_j = c_j + \beta e, \tag{3.22}$$

where β is a constant or a function of the iteration number. The small shift error e is from the peak of the following cross correlation function:

$$e(t) = \sum_r o_{n+1}(r, c_{j;n}) \prod_m (r) o_n(r-t, c_{j;n}) \prod_m (r-t), \tag{3.23}$$

with $\prod(r)$, a window that defines an area over which the light contributes significantly. This equation is computed through an image registration algorithm, commonly used in image processing, such as the matrix multiplication method developed by Guizar-Sicairos [101] and which largely reduces computational time.

implementation to difference map

In DM an object is created as a whole using all the updated exit-fields (or views) and so the sub-images are stitched together in a single process. However, it is suggested to perform the cross correlation between the newly updated exit fields with DM

(Eq.3.9) and the previous ones, in order to extract the shift information. Thus Eq.3.23 adapted to DM becomes:

$$e(t) = \sum_r \psi_{j,n+1}(r, c_{j;m}) \prod_m (r) \psi_{j,n}(r-t, c_{j;m}) \prod_m (r-t). \tag{3.24}$$

However, as the accuracy of the feedback parameter (and thus of the algorithm, see Fig.3.13) is reliant on the performance of the cross-correlation which one is determined by the degree of overlap and update in the illumination and object function, the adaption of the method to the difference proved to be more difficult than for the annealing. More care in the weight of the function Π_m together with implementation of a generic adjustment of the β parameter, should overcome the difficulties encountered.

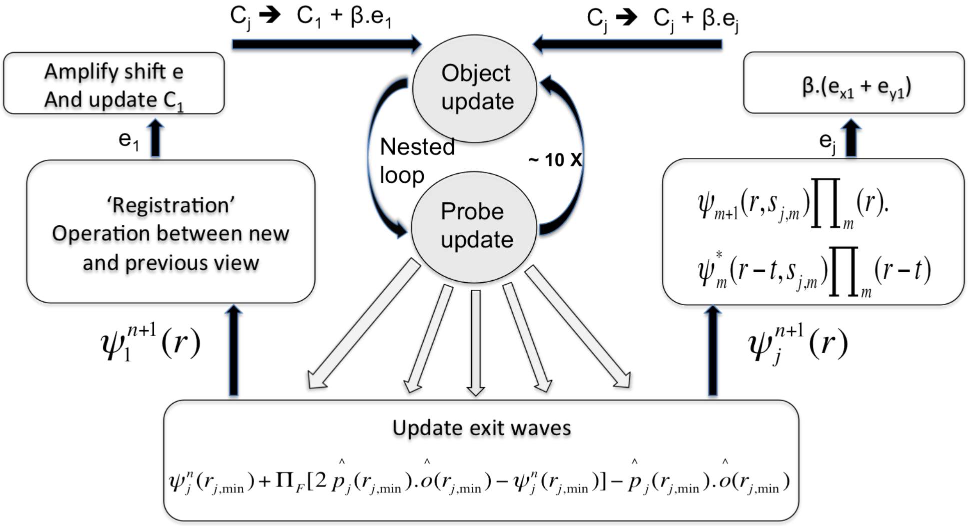

Figure 3.13: Difference map scheme for cross-correlation based position determination. After a view has been updated, it is cross-correlated with the previous view to extract the small shift e, which updates c_j through a feedback mechanism.

3.4 Partial coherence correction

The confidence of both CDI and ptychography in reconstructing images is entrusted on the high degree of spatial coherence of X-ray illumination. Nonetheless, even a third generation synchrotron presents a certain degree of partial coherence, leading to reduced data quality and less coherent diffraction pattern speckle contrast that could compromise the authenticity in recovered images [102, 103]. It manifests as spurious spots or reconstructions that completely fail. Whitehead [?] in 2009 has lifted the need for full coherence by suitably incorporating its characteristics into reconstructing algorithms like HIO. But a full determination of the spatial coherence can be time consuming [104, 105, 106], and once more, *a posteriori* methods that improve image interpretability are needed. Jesse Clark [107], using convolution rather than modal decomposition, was the first to demonstrate that coherence can be recovered from the sample diffraction data alone. His method was later cast as a blind deconvolution problem as the effects of fluctuation in probing radiation, random vibration of components and sample dynamic are unmitigated [108]; even though beamlines are constructed as to drastically reduce these unwanted effect. It is assumed in this section that all the decoherence effects are contained within the illumination (Babinet principle) [21].

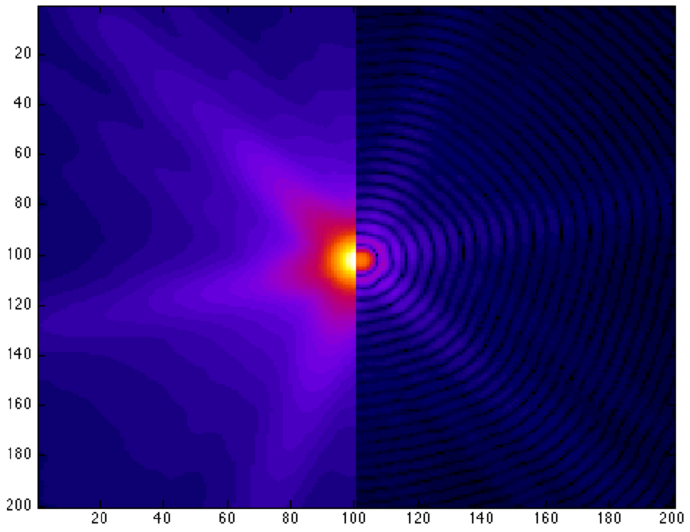

Figure 3.14: A source of decoherence affects the measured intensity distribution by reducing the visibility of the fringes (here on the left side, the blurring is exagerated).

3.4.1 Theory behind partial coherence correction

The scattered far-field intensity from a sample's complex electron density, was developed for the ideal case of coherent illumination, in section 2.1 . The diffracted intensity under effect of partial coherence and quasi-monochromaticity in the illumination, can be described by introducing the mutual optical intensity (MOI) [21] at two points in space $\mathbf{r_1}$, $\mathbf{r_2}$:

$$I\mathbf{q}) = \int\int J(\mathbf{r_1},\mathbf{r_2})\rho(\mathbf{r_1})\rho^*(\mathbf{r_2})\exp\left[i\mathbf{q}.(\mathbf{r_1}-\mathbf{r_2})\right]d\mathbf{r_1}d\mathbf{r_2}, \tag{3.25}$$

where

$$J(r_1,r_2) = \sum \mu_k P_k(r_1)P_k^*(r_2), \tag{3.26}$$

and P_n is the illuminating wavefield. Instead of a sum of mutually incoherent modes, the Schell model describes an equivalent estimate for $J(r_1,r_2)$, where the MOI is treated as a statistically stationary Gaussian form separable in x and y:

$$J(r_1,r_2) = I_o \exp\left[\frac{-|x_1-x_2|^2}{l_x^2}\right]\exp\left[\frac{-|y_1-y_2|^2}{l_y^2}\right], \tag{3.27}$$

with respective coherence lengths l_x and l_y. The recorded partially coherent intensity takes now the form of a simple convolution:

$$I_{pc}(\mathbf{q}) = I_{fc}(\mathbf{q}) \otimes \hat{\gamma}(\mathbf{q}), \tag{3.28}$$

where $I_{fc}(\mathbf{q})$ is the fully-coherent intensity obtained through the usual Fourier transform of the wavefield exiting the sample, $\hat{\gamma}(\mathbf{q})$ is the Fourier transform of the complex coherence function, and $\otimes$ denotes convolution. As $\gamma(q)$ blurs the coherent intensity (Fig. 3.14), artefacts or even non-uniqueness will result in the reconstructed images as no object will satisfy both constraints [**?**].

The method developed by Jesse Clark [107] that accommodates for partial coherence, can simultaneously retrieve the object and the MCF (or complex coherence function) of the illumination from a single diffraction pattern, as opposed to tedious interferometric measurements [104, 105, 106]. The simple reciprocal-space projection assumes illuminating x-rays are fully spatially coherent, ignoring any imperfection of coherent X-ray sources that might introduce complexity of recorded Fourier-space diffraction intensities. The projector associated to the Fourier constraint Π_F in the difference map update (Eq.3.9) is thus modified to account for partial coherence at each iteration k, $\Pi_F \rightarrow \Pi_{pc}$:

$$\Pi_{pc} = \mathcal{F}^{-1}\left[\mathcal{F}(2\Pi_o[\psi_j^k(\mathbf{r})] - \psi_j^k(\mathbf{r})).\left(\frac{\sqrt{I_m^j(\mathbf{q})}}{\sqrt{|\mathcal{F}(2\Pi_o[\psi_j^k(\mathbf{r})] - \psi_j^k(\mathbf{r}))|^2 \otimes \hat{\gamma}(\mathbf{q})}}\right)\right]. \tag{3.29}$$

Notice that the overlap projector Π_0 that computes for an object $o(\mathbf{r})$ and a probe $p(\mathbf{r})$ from all the subsets together (Eq.3.7 - Eq.3.8), does not need modification. Prior to the application of the intensity constraint (Eq.3.3), it is suggested [107] to update the numerical estimate of $\hat{\gamma}^k$ by employing a Richardson-Lucy (RL) algorithm:

$$\hat{\gamma}^{k,i+1}(\mathbf{q}) = \hat{\gamma}^{k,i}(\mathbf{q}). \left(I^{\Delta k}(-\mathbf{q}) \otimes \frac{I_m(\mathbf{q})}{I^{\Delta k}(\mathbf{q}) \otimes \hat{\gamma}^{k,i}(\mathbf{q})} \right), \tag{3.30}$$

where $I^{\Delta k}(\mathbf{q})$ is formed by a combination of the previous and current iterates estimate of the coherent intensities. Straightforward adaptation of the RL refinement algorithm to ptychography is realised by using:

$$I^{\Delta k}(q) = 2|\mathcal{F}(2\Pi_o[\psi_j^k(\mathbf{r})] - \psi_j^k(\mathbf{r}))|^2 - |\mathcal{F}(2\Pi_o[\psi_j^{k-1}(\mathbf{r})] - \psi_j^{k-1}(\mathbf{r}))|^2, \tag{3.31}$$

while i in Eq.(3.30) is referring to a sub-iteration, $\hat{\gamma}^{k,i+1}(\mathbf{q}) \rightarrow \hat{\gamma}^{k,j+1}(\mathbf{q})$ will be now referring to the index j of each ptychographic data subset. To reduce computation time, the RL algorithm is applied each 10 iterations. Alternatively, minimisation of the reciprocal-space quantity:

$$E_j = \int |I_m^j(\mathbf{q}) - |\hat{\psi}_j^k(\mathbf{q})|^2 \otimes \hat{\gamma}^{k,j}(\mathbf{q}, \hat{\sigma})|^2 d\mathbf{q}, \tag{3.32}$$

with respect to the free parameter $\hat{\sigma}$ or to the free parameters, l_x and l_y can be used to update $\hat{\gamma}^{k,j}$.

The work of Clark et al. [107] reported in Fig. 3.15, shows a typical image of a reconstructed gold nanocrystal comparing data assuming perfect coherence and accommodating partial coherence. To degrade the coherence, coherence defining slits (beamline 34 ID-C, APS) were opened (50 μm) beyond the nominal size of coherence (30 μm).

The findings are clear, a reconstruction not accounting for partial coherence produce an image that suffers from significant unphysical density modulations (Fig. 3.15 (c)) while a reconstruction that corrects for partial coherence generates an image of a defect-free nanocrystal of uniform density (Fig. 3.15 (d)). Certainly, data for the same nanocrystal were taken with a high degree of coherence at the beamline (slits opening of 12.5 μm) in order to demonstrate that correcting for partial coherence gives the same results. However, Clark did not investigate the limit for the partial coherence correction.

3.4.2 Simulations

The partial correction method adapted to ptychography was tested on a simulated crystal derived from Fig. 3.15, with comparable size and electron density on a 128 ×

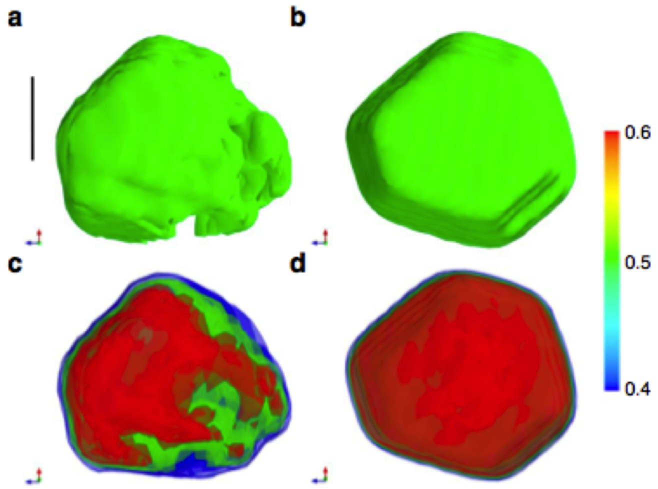

Figure 3.15: Comparison of reconstructions of a nanocrystal taken under partially coherent illumination, shown in isosurface. (a) assuming full coherence, and (b) using the modified modulus constraint that accommodates partial coherence (b). Figure and caption taken from [107]

128 pixel size but a strong phase of 7π of spherical curvature is added, and a simple soft edge pupil function is used a scanning probe. To introduce a partial transverse coherence function that acts as a point-spread function that causes fully coherent diffraction intensities to be blurred, one can simulate spatially partial coherent X-ray illumination using a two-dimensional Gaussian function with standard deviation σ as complex coherence function, the same approach as in the previous study of Parks et al. [109]. Here, a simulated ptychography data reconstructions with transverse partial coherence of $\sigma/L = 0.75$ where L is the size of the probe array (when $\sigma/L > 1$, perfect coherence is assumed).

The reconstruction shows that the ptychography is relatively robust to a reasonable amount of partial coherence (Fig.3.16 b-b')) and that the correction of partial coherence (Π_{pc}) certainly amounts to same reconstructions as with perfect calculated coherence. This proof of concept could have been stopped with this simulation but a recent study [109] has performed systematic analyses on both simulated and experimental CDI data and concluded that for strong-phase objects, applying partial coherence correction has very little improvement in reconstructed results comparing to improvement of partial coherence correction of samples of flat or weak-phase structures. And so in conclusion, they suggested: " in CDI, the best strategy for study of strong phase objects is to maintain high degree of coherence of illuminating X-rays due to broadening of solution space due to high phase structures in the

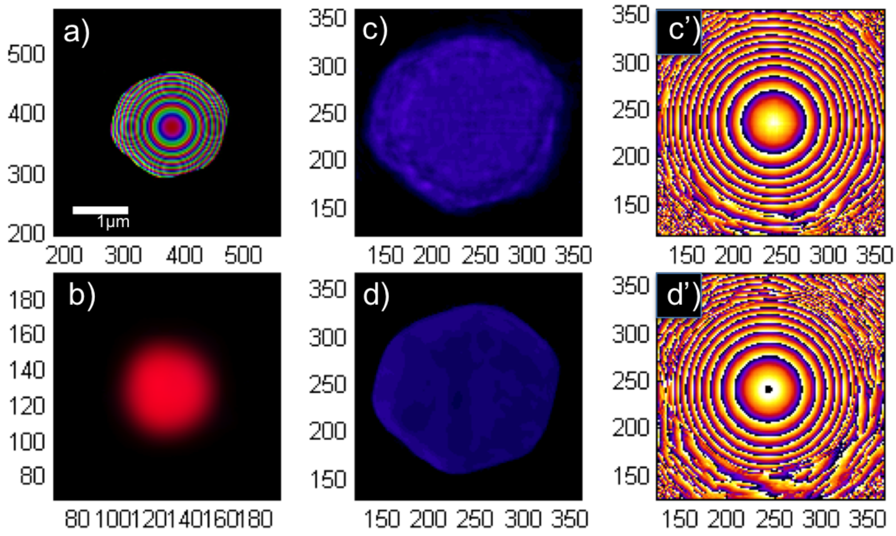

Figure 3.16: (a) Simulated crystal with 5 π of quadratic phase. (b) Gaussian probe used for the simulations. c-c') Zoom over amplitude and phase of the reconstructed crystal without partial coherence correction. d-d') Zoom over amplitude and phase of the reconstructed crystal with partial coherence correction.

sample ".

In order to gain in understanding of correction of partially coherent light source in X-ray ptychography, further analyses on simulated ptychography data are performed, varying both degree of coherence properties of X-rays and sample phase structure complexity

To be comparable with previous study of Parks et al. [109], a Lena object was used to generate the numerical experiment (see Fig.3.17). Also, for the same reason of minimizing of correlation between the magnitude and phase components of the real- space complex wave-field, the same image for both amplitude and phase component with 90-degree rotation to each other is used. The Lena image used in simulation has 512×512 pixels. To minimize the factors contributing ptychography reconstructions, a simple probe, the same soft pupil probe as in Fig.3.5 b) is used.

Initial random seeding of both amplitude and phase was used for fully-coherent (FC) reconstruction step; partially-coherent (PC) projection was applied after data difference map metric reached a plateau after 60 iterations of FC projection. The definitions of FC (Π_F) and PC (Π_{pc}) are illustrated in Eq.3.9 and Eq.3.29 respectively. Refinement of the complex coherence function parameter sigma was not performed at this stage, Π_{pc} projection step uses a single convolution of reciprocal-space complex wavefield of the exact coherence function parameter σ_0.

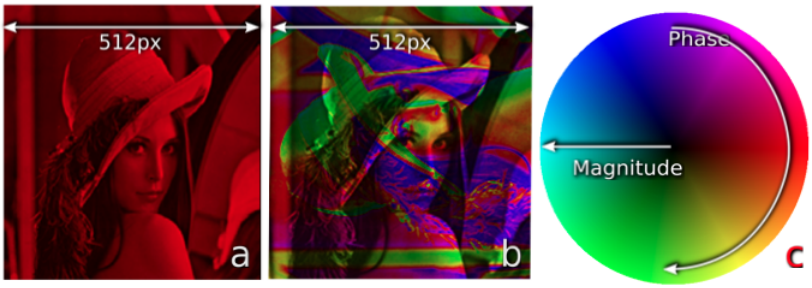

Figure 3.17: Object used in reconstruction simulations. (a) a real- valued object with max phase $= 0$; (b) a complex- valued object with max phase $= 2\pi$

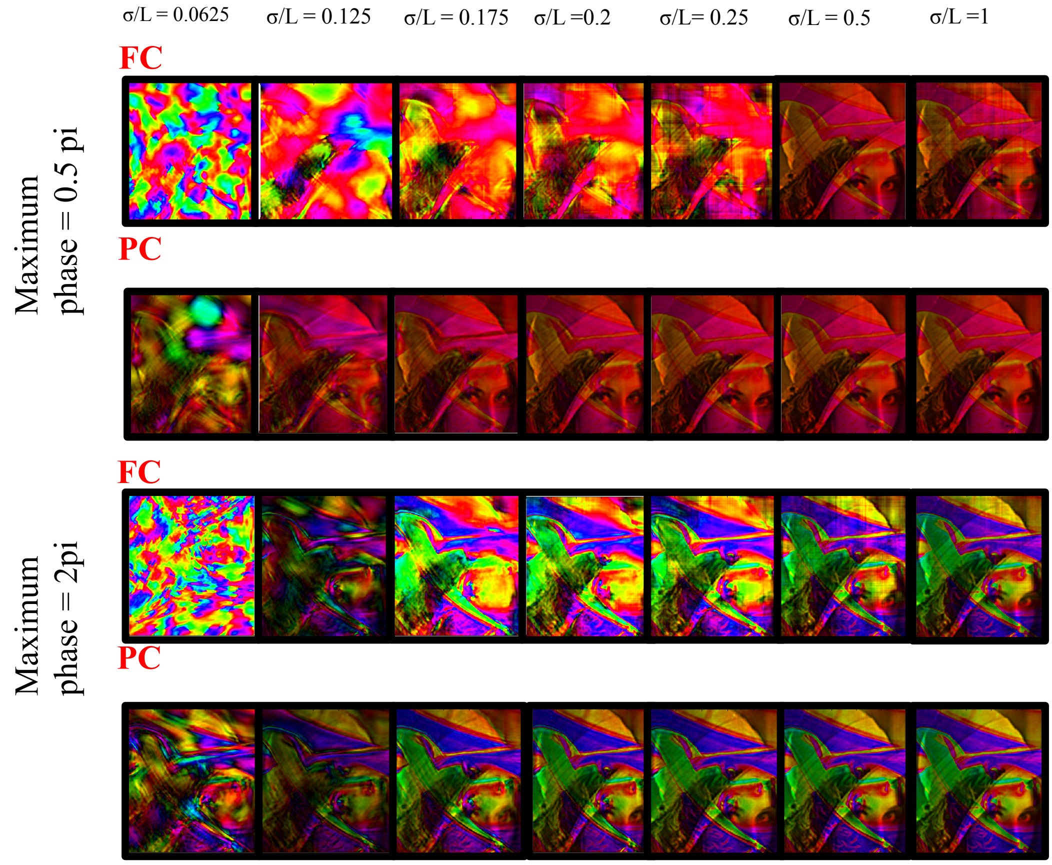

Figure 3.18: Results of reconstructions using both the PC and FC projections for real-valued and complex valued (max phase$= 2\pi$) samples at several degrees of coherence σ/L. The reconstruction of the real- valued sample always receives a bonus from the PC projection vis-a-vis the FC projection, but the complex-valued sample is sometimes penalized. All reconstructions were performed with overlap of 80 % in ptychographic simulations. Probe used here is simple Gaussian function as in [109, 110].

3.4.3 Interpretation of reconstruction results

One expects that with robust overlap constraint in real-space, ptychography is much more tolerant to imperfections in X-ray illumination, reaching better data convergence compared to that of conventional CDI. The reconstructed simulated results support this claim (published by Burdet, Shi and Parks [110]). It is observed better quality of reconstructed data with same coherence properties for ptychography than CDI. This improvement of data reconstructions occurs in the coherence definition parameter σ/L from 0.25 to 1, however, there has been no significant improvement of reconstruction results for σ/L values that are outside of the selected range (see Fig.3.18).

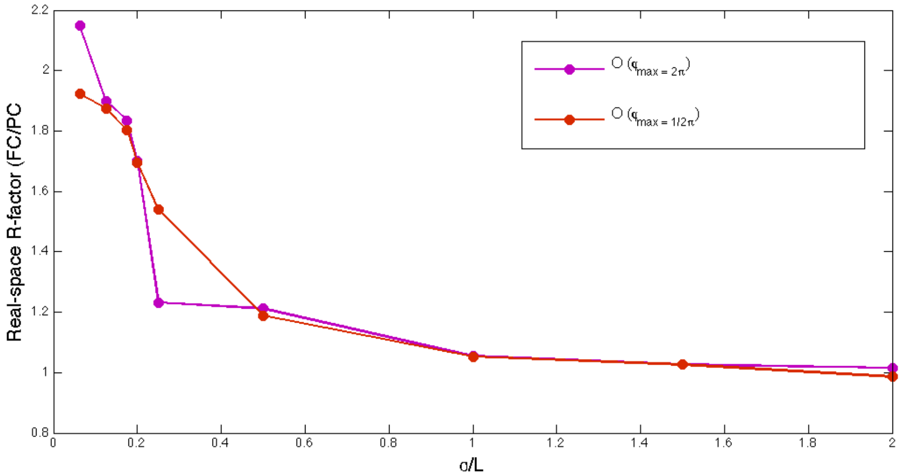

Figure 3.19: R_{real} (PC/FC) Vs σ/L for 9 σ/L used in simulations, for maximum phase $= 2\pi$ and 0.5π. Two sets results are done with 2D Gaussian probe in simulations. This figure is for investigation of cut-off σ/L for phase $= 2\pi$ and phase $= 0.5\pi$ of objects. We have result which show that the cut-off σ/L for good reconstructions is higher for max object phase $= 2\pi$ than that of 0.5π. In other words, better coherence is needed for highly complex objects. All simulations were performed with 70 % overlap. Reconstructions performed in collaboration with Shi and Parks, [109, 110].

It is very convincing that by incorporation of partial coherence correction in the ptychographic iterative algorithm, reconstructions are improved significantly in a wide range of degree of coherence σ/L values. It was found that the ptychography reconstructions with partial coherence correction converge well with σ/L value at or above 0.25. Moreover, the real-space metric analyses, proves that ptychography with partial coherence correction works well for maximum object phase equals or bigger than $\pi/2$, suggesting that the method is a very robust technique for complex real condensed matter physics materials that usually exhibit high phase structures.

For a better understanding of how well the partial coherence correction performs for the usually unknown parameter sigma, a ratio of $\sigma/\sigma_0 = 1.5$ was introduced as initial parameters for the reconstructions. The rationale behind this analysis is the fact that we would never know the exact complex coherence function for experimental data, owing to the experimental complexity and instrumental instabilities in real world synchrotron beamlines. Ptychographic reconstructions were performed with the RL approach of Eq.(3.30), initiated at iteration 80 and performed each 10 iterations only.

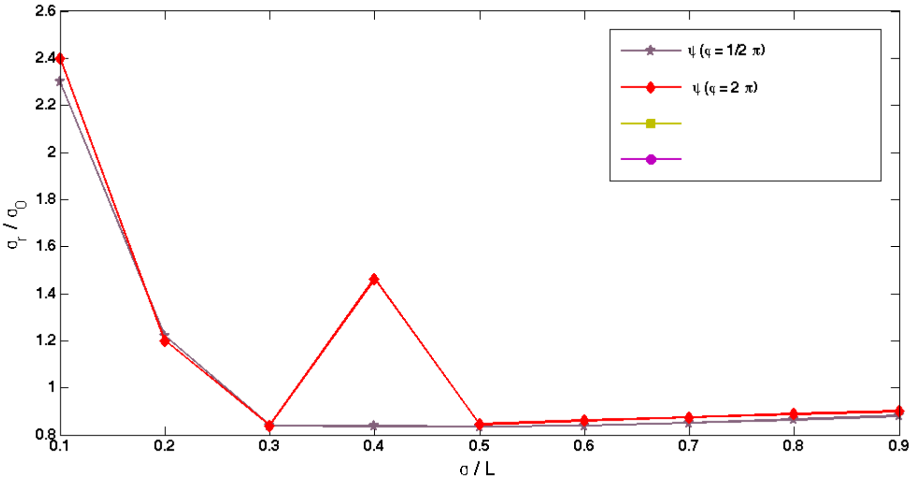

Figure 3.20: Results of reconstructed coherence function, parametrized by σ/L, the results are plotted as ratio of reconstructed σ to simulated σ_0 for various degree of coherence, sample complexity with 70% overlap in simulated dataset. Performed in collaboration with Shi and Parks, [109, 110]

X-ray ptychography is then envisaged has an overwhelming advantage over conventional CDI for investigation of complex objects of scientific interests, and suitable samples for ptychography can be relatively of large area, ranging from hundreds of nanometers to microns.

3.4.4 Multimodal decomposition

Thibault and Menzel [108] have recently demonstrated the feasibility of incorporation of multi-modes of X-rays into ptychographic reconstructions, and this particular approach accommodates arbitrary complex coherence function in the iterative algorithms. In the previous section, a two-dimensional Gaussian-Shell model (Eq.28) was employed to approximate possible arbitrary complex coherence function (Eq.27), as suggested by K.A. Nugent [111]. However, studies of multi-modes of X-rays in ptychography is becoming a subject of intense studies considering its promises of high-resolution diffraction imaging of extended objects. Starting with Eq.27, the

In the case of a mode specific illumination (Eq.27), a set of mutually incoherent exit waves $\psi_j^{(k)} = P_j^k(\mathbf{r}).O$ propagate in concert to the detector:

$$I_{j,q} = \sum_l \mu_l |\mathcal{F}[|\psi_j^{(k)}]^2 \tag{3.33}$$

In order to decorrelate the incoherent set of diffraction patterns from the recorded data, a parametrization of the Fourier projector $\Pi_F(\psi_j^{(k)} = P_j^k(\mathbf{r}).O)$ becomes the key ingredient:

$$\Pi_{ms} = \mathcal{F}^{-1}\left[\sum_l \mathcal{F}(2\Pi_o[\psi_j^{k,l}(\mathbf{r})] - \psi_j^{k,l}(\mathbf{r})).\left(\frac{\sqrt{I_m^j(\mathbf{q})}}{\sqrt{|\sum_l \mathcal{F}(2\Pi_o[\psi_j^{k,l}(\mathbf{r})] - \psi_j^{k,l}(\mathbf{r}))|^2}}\right)\right], \tag{3.34}$$

together with the real-space projection probe update operation Π_0, similarly augmented to incorporate the multi-modes:

$$P_l(\mathbf{r}) = \frac{\sum_j O^*(r + r_j).\psi_j(r)^{(k,l)}}{\sum_j |O(r + r_j)|^2}, \tag{3.35}$$

and

$$O(\mathbf{r}) = \frac{\sum_l \sum_j P_{k,l}^*(r + r_j).\psi_j(r)^{(k,l)}}{\sum_k \sum_j |P_{k,l}(r + r_j)|^2}. \tag{3.36}$$

Since the relative weighting of each illumination mode is generically computed from Eq.3.33 , their orthogonal combination allows for an *ab initio* a recovery of the coherence property of the illumination wave-field [112]. The modes can easily be made orthogonal with the Gram-Schmidt orthonormalization. The number of reconstructed modes should in principle scale with the ptychographical prescription, although no rule has been clerly formulated yet.

A model calculation was performed on the simulated Lena object by mean of four illumination modes. The choice of Gaussian transverse modes (TEM) was rather an arbitrary choice and a formal comparison between arbitrary complex coherence function and two-dimensional Gaussian-Shell function should be perfomed at a synchrotron beamline, as will be discussed in section 4.3.1 The amplitude modes were converted to phase modes, with the Gaussian shape for the amplitude parts. Thus, the amplitudes for the selected modes were, TEM00= 50%, TEM11= 20%, TEM22= 5% and TEM33= 2.5% respectively. For the reconstructions, the initial

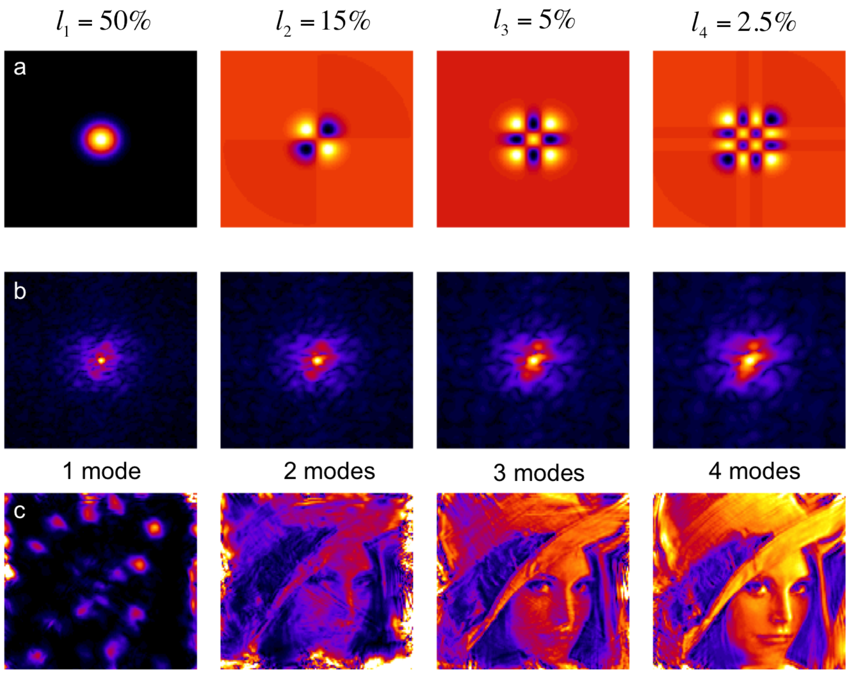

Figure 3.21: Results of reconstructions using multiple modes in the illumination (simulation of a low coherence x-ray experiment). a. The four modes (l = 1,2,3,4) modes used for the simulation realised on a static object. b. Diffraction patterns as a function of accumulated modes. c. Reconstructions as a function of modes inserted into the extended difference-map algorithm

modes were altered from the original probes amplitude by +/- 10 %, and multiplied with a random phase array of values. The reconstruction taking into account only one mode (l_1) totally fails, as displayed in Fig.3.21 and comes to an acceptable level only with 3 modes.

The method seems to be so powerful that the vibrating modes of a sample can be absorbed by the modes in the probe [112]. Moreover, Batey et al. have demonstrated that the states of the object can be also concurrently reconstructed. These pioneering works on the reconstruction of discretized dynamics will possibly venture the ptychography into the universe of quantum physics [108].

3.5 Towards real-time ptychographic reconstruction

With the ever increasing performance of computing - thanks to a proliferation of multicore machines and hyper-threading technology -, real time ptychography is becoming a reality. An online analysis process, synchronized with the data acquisition will be made possible without the need to go offline to a 'dark chamber' to develop a ptychographic image, essentially turning it from an offline to interactive job [113].

Graphics Processing Units (GPU's) were first used for graphics but then their computing power used to leverage Matlab calculations and applications while requiring minimal programming effort, thus it has been in use for the reconstructions found in this thesis. But to be able to reconstruct the images in real time, a parallelization of the ptychographic algorithms over many GPUs can be adapted to take advantage of parallel hardware. In fact, computationally intensive problems such as data analysis, image and signal processing applications including communications systems and computational finance are made easier with the Matlab Parallel computing tool box (PCT) [114] where scaling a code does not require investment in CUDA programming (high level constructed parallel for loops are already built). Hence changing the ptychographic code is done with quite trivial changes with no major trouble as such, leading to drastically increased performance [114] .

A Matlab benchmark as a function of number FFTs performed is reported in Fig.3.22 with a speed increase up to 50 times with a GPU cluster. The number of FFTs performed (2.5×10^5) more or less corresponds to those needed to reconstruct a single ptychographic image. When there is cost of transferring data between the CPU and GPU, and the time it takes to create a matrix, or other parameters, the increase in speed is rather poor. For example, to prevent unneeded data transfer, the variable that goes within the body of a *parfor* loop should be sliced (hopefully, Matlab tutorials highlight the main challenges that one might encounter like independence, globals and transparency, classification and uniqueness [115]).

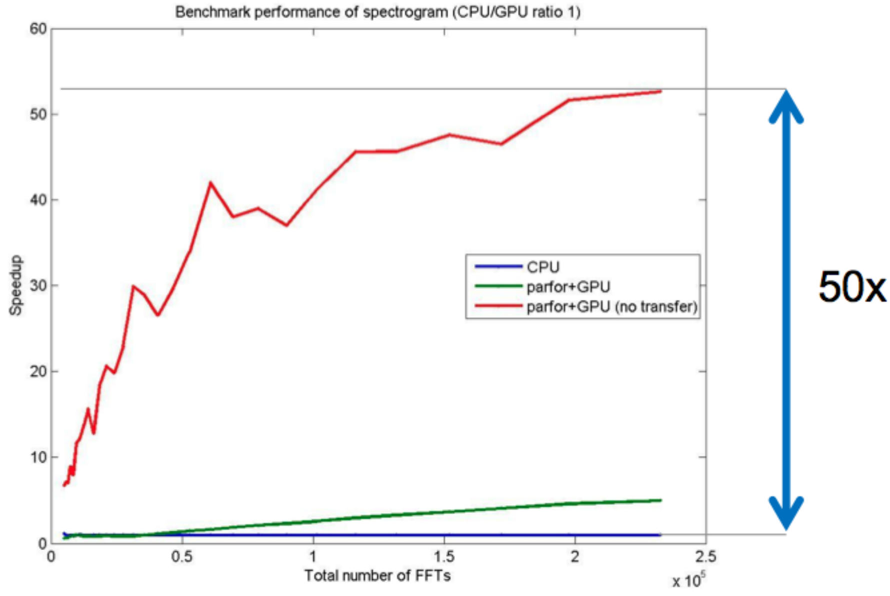

Figure 3.22: A Matlab benchmark as a function of FFTs performed with and without transfer between CPU and GPU. The ratio GPU/CPU time is indepedant of matrix size.

In general, taking full advantage of a code requires careful programming but parallelization is responsible for the major improvement in speed. Parallelization will be essential to ptycho-tomographic technique which requires the assembly of at least 180 ptychographic images. Moreover, to reduce upfront cost, Amazon Elastic Compute cloud offers to run Matlab programs on its high computing performance GPU's. This approach could be a growing trend in the ptychographic community because users get instant access to large memory GPUs [116].

3.5.1 Parallelisation strategy

Starting with the serial program of DM ptychography, it is explained here how it can be parallelized (and optimized). The first obvious candidate for parallelization is the difference map equation (3.9), whereby a subscript inspection directly reveals that the views update (through phasing operation), does not depend on previous positions or sub-iteration calculations. Thus Eq.3.9 should be sent to as many cores (or nodes) as possible. It is regarded that this has a better advantage over ePIE, where the views update is dependant on the previous sub-iteration.

Although, due to the DM overlap constraint projection requirement in real-space, the object and illumination update requires all the updated views altogether (see

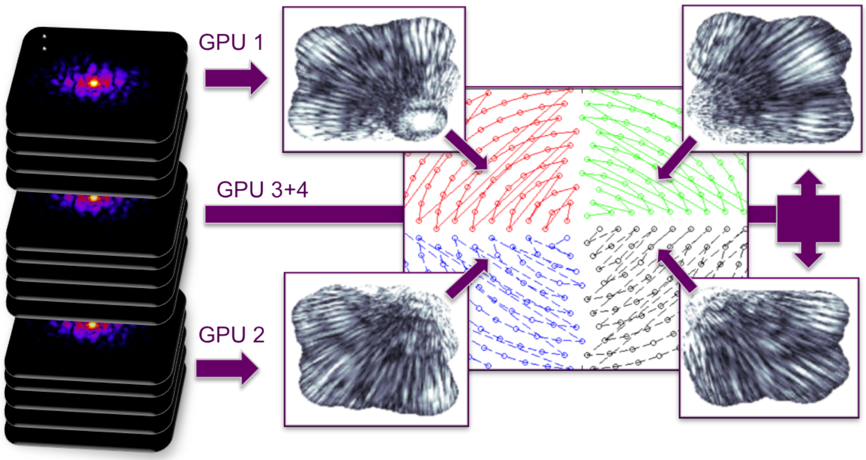

Figure 3.23: The ptychography frame stack is sent to four GPU's to reconstruct the four quadrants of an image independently. The full image is recombined at the end.

Eq.3.7 and Eq.3.8) and so has to be classicaly calculated (or processed) in a serial fashion. However, to increase the computational efficiency, the numerical scan area can be broken into smaller pieces. For example as Matlab can easily manage up to 4 Tesla GPUs inside a personal computer, the scan area together with ptychography frame stack is divided into four 'quadrants' where the regions are independently reconstructed, as can be seen in Fig.3.23.

This solution obviously applies to both ePIE and DM and requires either a substantial amount of recovery in between the image 'sub-pieces' (if there are no communication between iterations) or a stitching operation at each iteration in order to avoid ill-conditioned boundaries areas. A more appropriate way to take advantage of the Round-ROI scan is to decompose it into concentric ring domains and 'recombine' the pieces at each iteration.

The performance improvement provided made the refinement methods computationally reasonable but unfortunately, a 'complete' parallelization of combination of refinements method is not yet possible considering that Matlab cannot manage yet, the double or even triple *parfor* loop required (although researchers like Philipe Maia et al. [113], have used advanced programming techniques to optimize triply nested loop).

3.5.2 Dynamical probe reconstruction

One of the fundamental assumptions in ptychography is that probe structure is assumed to be constant during the scan [79]. However, beside the computational advantage of a real-space parallelization, it was realised that real object reconstructions could be improved by assigning a probe to each of the 'decomposed' scan areas. This is explained by the unavoidable oscillations and drift in the illumination structure that occurs during the time to perform an entire ptychographic scan, which ranges from several minutes to several hours [63]. To this effect, the overlap projection equations (Eq.3.7) that computes the real-space update of object and illumination are modified:

$$O_{new}(r) = \frac{\sum_{d=1}^{D} \sum_{j=(d-1)\frac{N}{D}+1}^{d\frac{N}{D}+1} P_d^*(\mathbf{r}+\mathbf{r_j}).\psi_d(\mathbf{r})}{\sum_{d=1}^{D} \sum_{j=(d-1)\frac{N}{D}+1}^{d\frac{N}{D}+1} |P_d^*(\mathbf{r}+\mathbf{r_j})|^2}, \tag{3.37}$$

and

$$P_d(r) = \frac{\sum_{d=1}^{D} \sum_{j=(d-1)N/D+1}^{(d)N/D} O_{up}^*(\mathbf{r}-\mathbf{r_j}).\psi_d(\mathbf{r})}{\sum_{d=1}^{D} \sum_{j=(d-1)N/D+1}^{(d)N/D} |O_{up}(\mathbf{r}-\mathbf{r_j})|^2}, \tag{3.38}$$

where D is the number of reconstructed illuminations and N the number of scan points.

To illustrate the concept, ptychographic simulations are conducted on a complex image with a probe drifting of 50 μm incremental steps along z (between each scan point). In a real world experiment, the illumination drift is rather pseudo-continuous, thus this simulation is based on an illumination that is continuously drifting from the sample (z direction only with its evolution calculated with a Fresnel propagator); see Fig.3.24. The simulation parameters for a simulated 9 keV x-ray beam are resumed below.

Properties	beam size	pixel resolution	scan range	scan step size	degree of overlap
value	$1_H \times 1_V$	50	15x15	300	70
unit	μm	nm	μm	nm	%

. As the algorithm requires a minimum of overlapped illuminations, the presented reconstruction is performed with $D = 10$ dynamical illuminations, which represents about 20 illuminations projected (or averaged) into a single one. Even though the drift is exaggerated, the assumption that the probe is constant over $\sim$ 20 scan postions is consistant with experimental findings [63].

As expected, the resolution of the classically reconstructed ptychographic image is affected whereas the image reconstructed with a set of 10 dynamical probes retrieves a high resolution (see Fig.3.25). A drawback when "linearly" decomposing the Round-Roi scan is that the probes overlap is constrained in one direction only

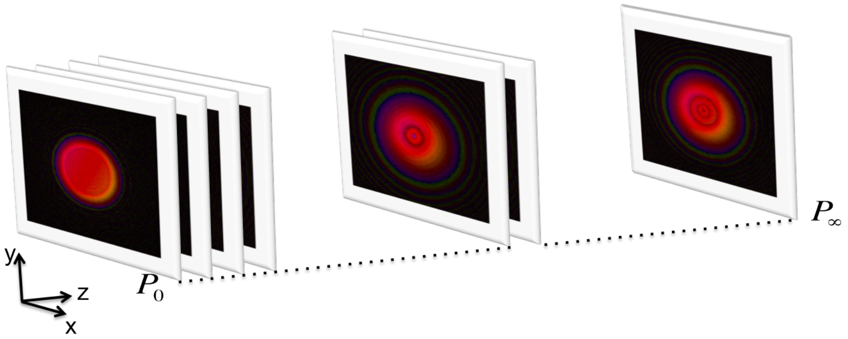

Figure 3.24: Pupilar function propagated along the z direction. The starting illumination at the first scan position is a pupilar function. Then this function is propagated by increment of 50μm using a Fresnel propagator.

for some regions of the scan. Thus different manners of decomposing the Round-ROI scan should be considered for next experiments at coherent beamlines.

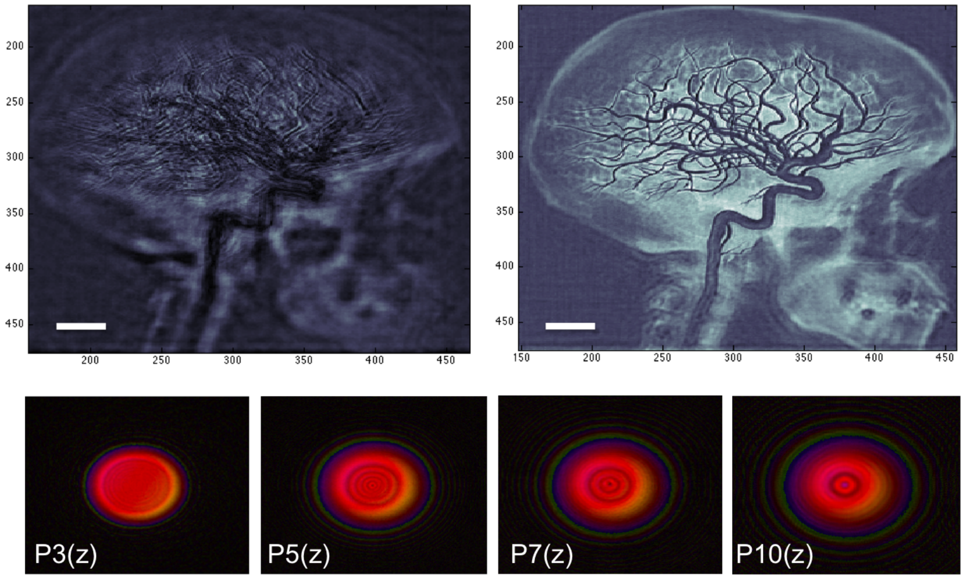

Figure 3.25: Reconstructed images with and without dynamical probe correction. Lower row: reconstruction of the probe as a function of its evolution. Scale bar, 2μm.

In the experimental section, the dynamical probe method will be combined with cycles of illumination positions corrections as both of these drift incertitudes are rather entangled (this to enhance chances of getting better averaged dynamical probes). For more 'completeness', this method could be extended to the multimodal decomposition.

3.6 Ptychography-tomography

As ptychography-tomography is expected to become an inescapable tool of nanoscience, this chapter ends with examples of work from participation with members of the Research Complex of Harwell. Tomography from Ancient Greek $\tau o \mu o \zeta$ (tomos, 'section, slice') is a generic term for methods that aims at visualizing virtual sections through a specimen [117]. Since its inception in the 70s, computerised tomography (CT) is a well established technique in the field of medical engineering that aims to reveal high resolution features within biological specimens [118]. In CT, an algorithm 'fuses' projectional images taken at different angles, to access the third dimension, thus overcoming many limitations of plain radiographs. While this sophisticated method is considered to be the the greatest marvel since Rontgen's discovery of x-rays, it is not limited to this portion of the electromagnetic spectrum but extends from Gamma ray to radio-waves, and also extends to particles like electrons, positrons, neutrons. The spatial resolution achieved in medical applications is just < 1 mm^3 from attenuation maps. Combining the sets of projection in the real space is owed to the Fourier slice theorem, which states:

The Fourier transform of a parallel projection of an object, $\mu(u,v)$, taken at an angle ϕ, gives a slice of the two-dimensional transform of $\mu(u,v)$ subtending an angle ϕ with the u-axis.

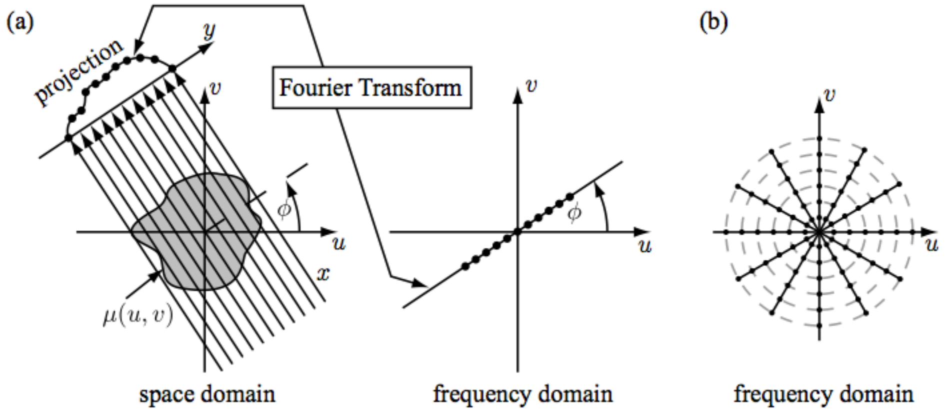

Figure 3.26: (a) The Fourier Slice Theorem. A projection measured in space domain is connected by a Fourier transform to a slice of the frequency domain. (b) The frequency domain is filled by recording tomographic projections from many angles. Illustration taken from [119].

The Fourier slice theorem is illustrated in Fig 3.26. Once the Fourier space is filled with the transformed projectional images measured at different angle ϕ, an object is in principle simply retrieved after an inverse Fourier transform has been performed. However, Fourier transforms are performed onto rectangular grids while the rotational angle ϕ calls for polar grid, thus an extra step is involved to switch between the two systems of coordinates prior to calculating the inverse Fourier transform. The Filtered Back Projection (FBP) is the most popular answer to this problem as the Jacobian determinant for the coordinate transformation, is a multiplying factor which acts as a frequency filter (visualized as ramp that accentuates large frequencies) that ensures equal contribution for all of the measured values. Central to tomography is also the question of how many angular projections are needed to appropriately sample the Fourier space [119].

CT is also used in other fields, such as nondestructive materials testing but requires the addition of phase-contrast mechanisms [120]. The two major drawbacks of x-ray phase contrast tomography are a difficulty to quantify physical quantities and to scale down the resolution below μm^3. It was found that the diffraction contrast in CDI leverage these difficulties by providing quantitative maps at nanometer resolutions without reverting to weak phase object or negligible absorption [120] and has been successfully applied to materials such as ceramic nano foam [58]. Slice-and-image methods that uses electron microscopy [121] can also reveal the nanostructure inside macroscopic objects but to the risk of spoiling the original structural features.

It is thus to the great interest of the CDI community to combine high-quality projectional images as to 'project' tomography into the nanoscale world [120]. Some of the CDI reconstruction schemes considered up to now were inspired by crystallography where phase retrieval is carried out in 3D space directly after assembling the diffraction measurements as done by Jiang in 2010 [122], who conducted tomography of biological samples too thick for electron microscopy [123, 8] (using projections from CDI at nanometer scale). While this approach works only for samples that have been totally isolated, x-ray ptychographic tomography propose to to image the structure of entire organisms, in conditions close to their native environment [1].

The 3D images reported in this section were reconstructed from data collected at cSXAS beamline, thus the experimental and data processing procedures for tomography are resumed from the papers of the dedicated beamline scientists, which are Guizar [1], Diaz [124, 125] and Holler [126, 127]

Tomographic measurements: The collection of diffraction data for a number of angular projections is resumed in Fig. 3.27. A ptychographic tomography measurement could prolong time to several hours due to the large number of accumulation necessary at high diffraction angles. Keeping the axis of rotation and sample

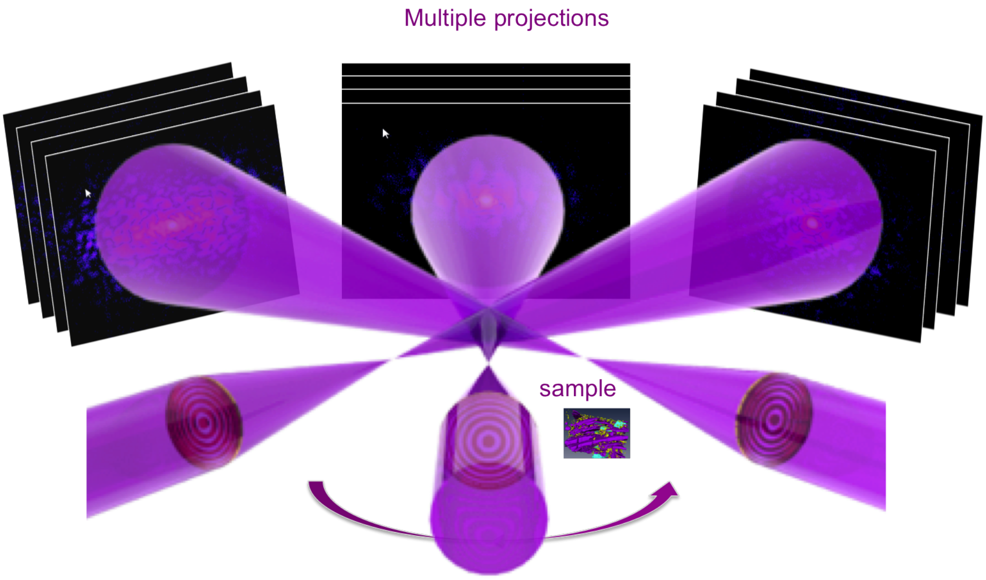

Figure 3.27: Schematic of data collection in a ptycho-tomo experiment for three angular projections. Experimentally the sample is rotated to obtain different projections, while the optics, illumination, and detector positions remain constant. Figure and caption derived from [14].

position stable during such enduring time, is technologically challenging when targeting nanoscale tomography. A precise extroceptive metrology measurement with laser interferometry was then developed at SLS [126, 127] to control the degrees of liberty of the different parts within tens of nanometers while rotating. The differential measurements are used as feedback to compensate thermal drift and position stabilities to better than 10 nm standard deviation.

Post processing the data: When a sample had no fiducial or salient features in the projectional images to allow fiducial marker tracking [1], alignment of tomographic phase projections are done by the following algorithm developed by Guizar et al. [1] sample had no fiducial or salient features in the projectional images to allow fiducial marker tracking

The algorithm developed by Guizar *et al.* [1] can realise an alignment of the tomographic phase projections from samples presenting neither a fiducial nor salient features. After proper phase removal and unwrapping, an iterative procedure allows to find the center of mass from maximizing the correlations of transversal variations in mass (it is worth noting that mass is understood here as the integral of the projected phase). The processing steps are resumed in Fig.3.28.

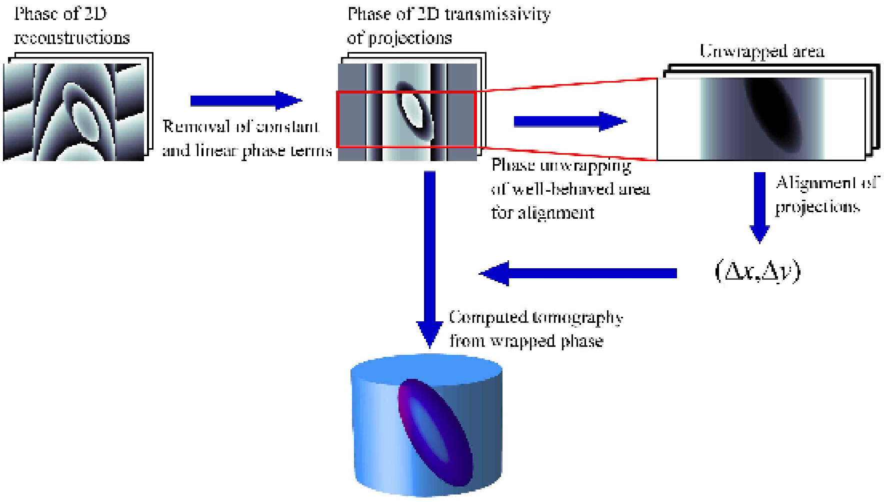

Figure 3.28: Scheme used by Guizar for ptychography tomography [1]

3.6.1 3D spatial structure of aluminium epoxy anti-corrosive marine coatings

The 'ptycho-tomo' method was applied to a relevant industrial material, a marine coating, and provided ground for further analysis by modelling its protective function with regard to corrosion and fouling of ship hulls. The work been highlighted by the London Centre for Nanotechnology as: "a fine example of the modern scientific method, teamwork between industrial hi-tech materials development, international characterisation facilities and university-based theory and modelling" [128]. The full experimental details are reported elsewhere [129] and here, partially. [1]

Marine coatings provide outstanding corrosion protection to substrates. The crucially functional component is made from aluminium flakes, whose lamellar shape and alignment are parallel to the surface improve the barrier properties of coatings by decreasing the transportation rate of corrosive substances such as ions, water (vapour) and oxygen through the coating layers. While Chen [130] could not effectively visualize the aluminium flakes by using transmission X-ray microscopy methods, the ptychographic X-ray tomography has produced 3D images with sufficient phase contrast. Moreover, the quantitative x-ray refractive data allowed, through the automatic identification of the main components of the coatings; to build a de-

---

[1] x-rays of 6.2 keV with a 3 μm diameter pinhole placed 4 mm upstream of the sample along the x-ray propagation direction were used to partly illuminate the sample which was rotated 180 degrees with 0.5 degree intervals to obtain 361 orientations (and projections), during the measurements. At each orientation angle, a Round-Roi scan of 1.4 μ m radial step (0.2 s exposure) generated 487 different scan positions.

tailed modelling of the paint's function. By plugging the modelling in the COMSOL simulation software, important physical key insights such as the relation between the orientation and morphology of the aluminium component to the permeability of the material to ions, were enabled. Fig.3.29 shows the work of Bo Chen [129] on segmentation and rendering of a 3D spatial structure image of the sample.

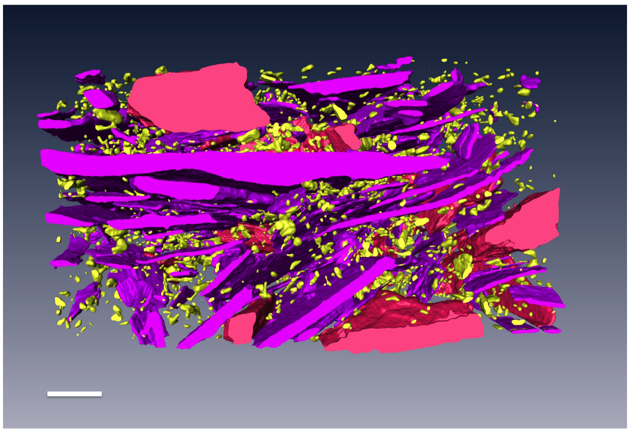

Figure 3.29: 3D ptychographic X-ray tomography of an aluminium epoxy marine coating: rendering of the segmentation of the 3D spatial structure. Purple parts are aluminium flakes, red objects are talc fragments and yellow particles are iron oxide. Image and caption taken from Bo Chen [129]. Scale bar, 1μm.

3.6.2 3D spatial structure of virus crystals

As the 'ptycho-tomo' provides sufficient phase contrast even for transparent biological specimens, another tomographic experiment was performed at SLS c-SAXS beamline on biological crystals (0.1-5micron in size) armouring viruses [131, 132], in collaboration with Colin Nave from Diamond Light Source, England. In fact, this is the viruse itself that encode for proteins, polyhedrin, thus building large proteinaceous crystalline occlusion bodies or polyhedra which isolate them from harsh environmental conditions. The experiment aimed at imaging the virus particles inside the polyhedra crystals and determine whether there was a preferred orientation of the cylindrical virus particles with respect to the crystal lattice. In addition, the relatively robust crystals are useful for developing and comparing x-ray imaging methods for low contrast biological objects.

The same c-SAXS beamline set up was used to the exception of a zone plate which, while retaining a fully coherent beam, provided approximately a 40 times increase in flux compared with the pinhole previously used. Considering that biological materials are weakly scattering, the increase in flux was considered essential.

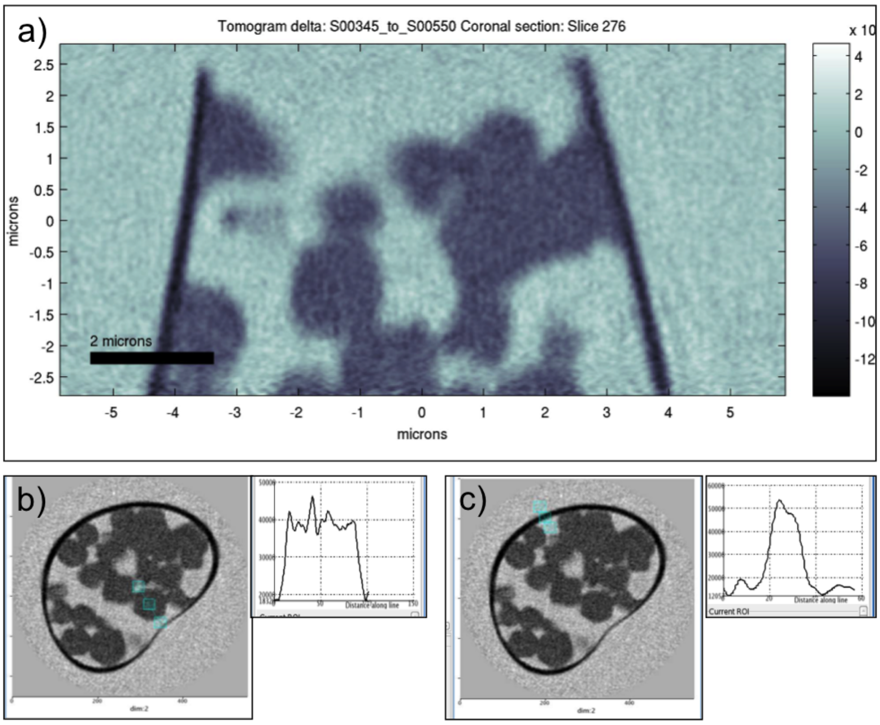

Figure 3.30: Slice of a tomogram showing a slurry of dried crystals inside the tip of a capillary. b-c) line scans through a crystal and the capillary.

A slurry of crystals were allowed to dry in the ends of capillaries which had a diameter of approximately 8 microns (the cubic shape of the 1-2 microns size crystals are easily visible in the projections from the ptychographic scans, Fig.3.30). A typical slice through one of the tomograms, together with line scans through the crystal and capillary are shown below.

The presented tomographic reconstruction was performed in collaboration with Manuel Guizar during the beamtime, and the following discussion is based on the experimental report. While the tomographic reconstruction was carried out with minimal smoothing in order to maintain the best resolution, this latter is of no better than 100nm, and the noise levels appear rather high. Although extra smoothing might reduce the noise level, it would degrade rather than improve the resolution, therefore it appears to be unlikely that the presence of single virus particles can be identified. The reasons for the poor resolution can be due to remaining instabilities in the probe beam or by the low contrast object. These unfavourable circumstances that preclude sufficient resolution, thus call for robust solutions in each ptychographic projection, such as probe fluctuations correction, the maximum-likelihood technique, modification of ptychographic algorithm for weakly scattering sample.[2]

---

[2] Fig.3.31 shows the presence of streaks presumably coming from scattering by the edges of

Therefore, the code required for further analysis was impossible to realize in the frame of this thesis.

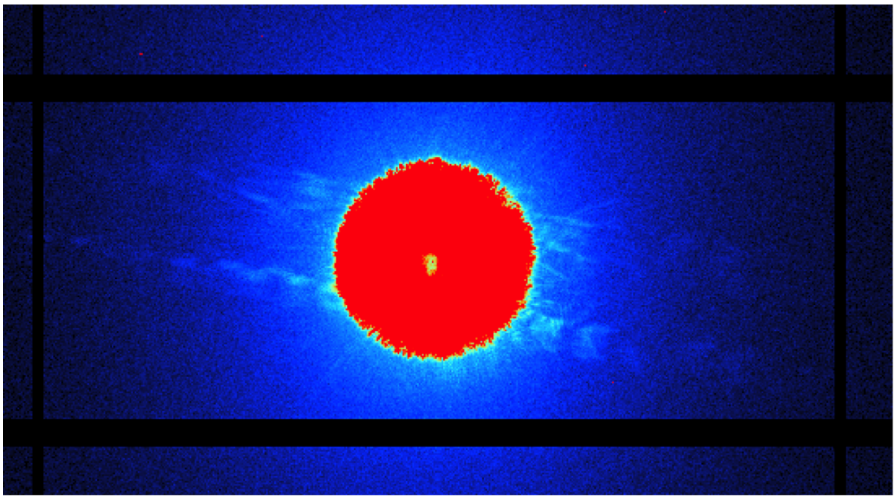

Figure 3.31: An image of one of the raw diffraction images which went in to the ptychographic reconstructions

---

the capillary, these streaks extended to a Bragg resolution of approximately 35nm, a significantly better resolution than obtained from the reconstructions. The raw data also includes an intense central annulus produced by the zone plate in combination with the order sorting aperture. The beam scattered from the specimen interferes with this incident beam as in the production of a hologram. The outer radius of the annulus corresponds to a Bragg resolution of approximately 130nm, similar to the resolution obtained in the tomographic reconstruction. It is possible that the ptychographic reconstructions are dominated by this holographic component.

Chapter 4

Experimental realisation at APS

This chapter will examine the implementation and optimisation of the experimental parameters for the set-up developed for ptychography under the partner user proposal (PUP) at beamline 34 ID-C of the Advanced Photon Source (APS) located on the site of Argonne National Laboratory (ANL) in Argonne, Illinois. This beamline has been developed for Bragg coherent diffraction experiments, thus, the very specialized requirements with respect to beam optics, sample environment with ability to easily mount and optically observe samples in beam position with the confocal microscope, large working distance and photon detection (which are similar for ptychography in transmission and Bragg geometries) were already optimised for this geometry. The high coherence capabilities of the APS have been developed considerably and are needed for CDI as the high brilliance and tunable energy. Parallel to the development of such sources, has been those of monochromators capable of providing sufficient temporal coherence while withstanding the high heat loads implicated.

The successful developments of CDI at this beamline constituted in several thesis from PhD students of Prof. I.K.Robinson [133, 134, 48, 135] e.g., high-precision slits to create apertures of only a few micrometers, necessary for achieving spatial coherence and convenient to use, etc.. Thus, the development of this section is built upon their work.

The motivation for the PUP application was to develop new imaging capabilities for 34-ID-C that will expand the existing one from imaging of small isolated objects to large field of view. The 'long term' goal is to develop the imaging capability to the 'black box' level where users can walk away with completed images. The plan for this PUP is to develop the method by testing a range of different variations of the method. It was proposed that UCL would contribute to the piezo scanning hardware needed to make precise scans of the probe position with respect to the sample. X-ray ptychography, both Bragg and in-line versions, will be available as a 'user' technique.

The high degree of coherence of 34 ID-C and high brilliance at 8.9 keV photon energy, combined with the standard KB focusing system were used to create a suitable probe without loss of coherence and high photon density at the sample to produce enough photon statistics at high diffracting angles. The diffraction has been recorded in the far field using a CCD detector compatible with KB focused mode and optimised (quantum efficiency [37]) for hard x-rays of 8.9 keV energy. The high dynamic range of the detector used, means the diffraction can be measured in the forward direction without a beam stop, allowing even the lowest orders of diffraction to be measured. Having a focused beam results in the recorded diffraction pattern from the extended object being oversampled. A photon with energy of 8.9 keV also means that its wavelength (~ 1.4Å) is comparable with the interatomic distances in crystalline samples and has enough momentum to reach reciprocal lattice vectors for experiments performed in Bragg geometry (see Ewald sphere construction, section.5.1).[1]

4.1 Experimental set-up

The x-rays employed at sector 34 ID are produced by an APS undulator A [137]. Before the experimental hutch, a liquid nitrogen cooled mirror filters out the high harmonic to leave a 'pink' beam which then passes through a double crystal Si(111) monochromator that selects only a narrow band of frequency. The beam size coming inside the hutch is determined by the synchrotron with the half width at half maximum (HWHM) transverse coherence lengths given by $2\lambda Z\sqrt{ln2}/(\pi\sigma)$ [111] (where Z refers to the 54.5 m distance away from the center of the Undulator A and σ to the X-ray beam source size, i.e., $\sigma_v = 26\mu$m [137]). Thus, to control the transversal coherence properties a pair roller slits with gap settings linearly tuneable between in the range 0-200 microns [134] are used, see Fig.4.1. Each slit consists of two polished molybdenum cylinders made from brass material, to produce very smooth aperture edges. A flexural-pivot design allows good reproducibility of the gap setting and positioning to a precision better than 250 nm. Although the possibility to increase the horizontal coherence length, is given by selecting a 100 μm wide beam by horizontal slits in front of a mirror, placed 27.5 m in front of the coherence-defining entrance

---

[1] A severe increase of the hard x-rays energy would allow for the simultaneous mapping of the small angle scattering and several Bragg peaks on the detector, to reveal nano structured materials with atomic resolution [136]. However, in practice it is very difficult to realise as the photon energy required is in the range of 100 keV.

slits; as was done in the experiments performed with Huang [138].

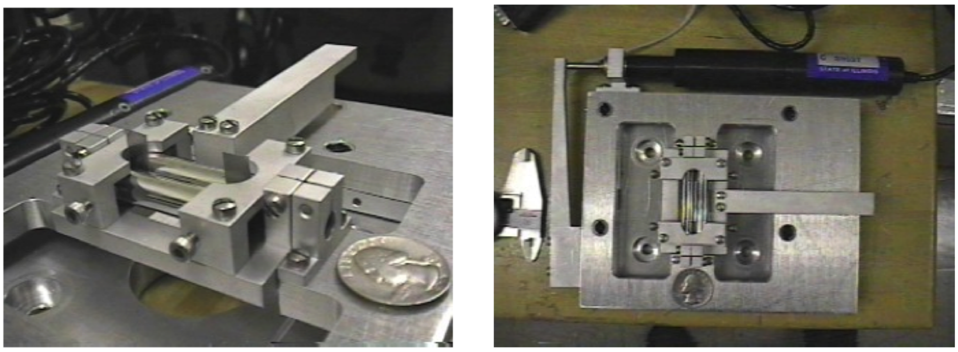

Figure 4.1: Picture of the Roller-blade slits made of polished molybdenum cylinders and separated by 200 μm shims. A first actuator allow them to be rotated thanks to flexible pivots. A second actuator translates the slit assembly on another set of flexural pivots with a 4:1 reduction. Images and caption taken from [134]

The flux of X-ray impinging on the optics is simply increased by bigger slit openings but this has the consequence of introducing additional wavefields modes, hence partial coherence effects with reduced visibility in fringes of recorded diffraction patterns. In the opposite, for narrow slits opening (1-5 μm), the illumination become asymmetric due to a parallax effect [134]. As the CDI single-shot method assumes a plane wave as illumination, any departure from this ideal condition will lead to misinterpretation of the reconstruction. In ptychography this has no importance but for a better idea over the focused spot, beam propagation was simulated. Here are the necessary elements for the simulation:

- The incoming field is a plane wave with a Gaussian intensity profile.
- The slits are simple steps function (heavy-side function in mathematical terms).
- The KB mirror which is a one dimensional parabola is treated as a lens.

The beam is first propagated until a 1-D focusing lens using a Fresnel propagator (Eq.2.5) then, as the high frequency term of the lens cannot be sampled finely enough, another form of the Fresnel diffraction is used for further propagation (section.4.2.1). The finding is that the focusing spot distribution is only asymmetric for narrow slits opening ($< 5\mu$m) but for larger openings, the distribution is relatively symmetric. More details on the distribution of the focal spot for usual slits opening of ptyhographic experiment are provided in next section (section.4.2.2).

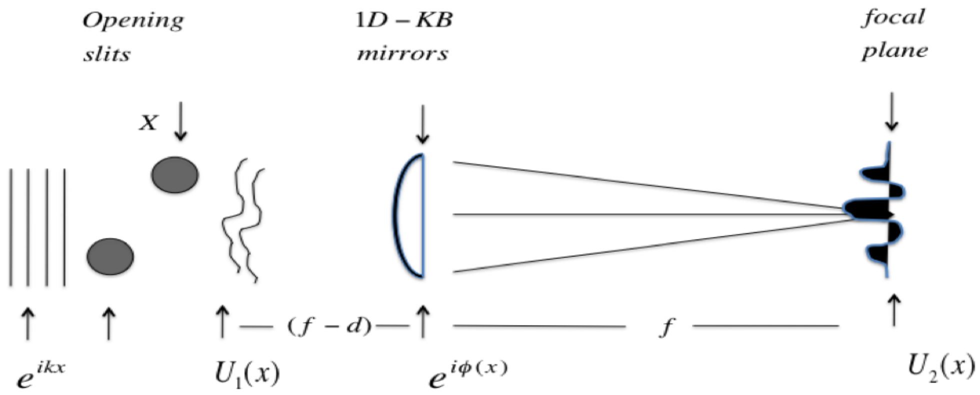

Figure 4.2: Slits and KB mirror at APS: A Si(111) channel-cut single crystalline monochromator is used to define the energy and monochromaticity of the incoming synchrotron radiation then followed by roller-slits used to preserve incoming coherence and quality of the X-Ray spectrum, then finally passing through the 'lens'.

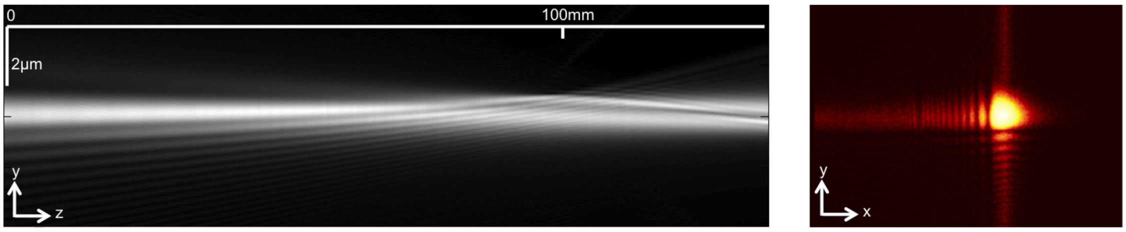

Figure 4.3: 2D simulation of the KB focus for asymmetric slits setting

4.1.1 Focusing optics

Once the coherence area is defined by the slits, the beam (after propagation) can either directly impinge on the sample or illuminate a focusing optics. Focusing can be used to overcome space limitations, a large detector pixel size or to match the needs of the sample, i.e., nanoscale objects that are smaller than the coherence volume. KB mirrors as focusing elements for CDI were first introduced at APS 34-ID-C to compensate for the reduction in signal brought by the reduced dimensions of nanocrystals [139] (focusing is also serves in isolating particles from other in a field of nanocrystals [140]). It is explained by the broadening of reciprocal space which thus calls for a maximisation of the coherent photons involved in scattering. So to use the whole coherence volume of the beam KB mirrors are employed with the property that the coherence area is reduced (without affecting the coherence) while the demagnification of the beam is increased, a consequence of Liouville's theorem. Moreover, focusing optics such as KB mirrors or diffractive optics, create almost no scattering artefacts [139].

At 34-ID-C, the focusing is administered by a set of KB mirrors of Peter Eng design [141], see Fig.4.4. The KB mirrors are designed with two shaped highly reflective silicon crystals, each held in a carriage. The focusing power is provided by applying force at both end of the tapered mirror [52, 134]. As the mirrors are implemented in a row along the x-ray propagation direction, a longer focal length for the downstream mirror is necessary to get the focus at the same position (ie., $f_v = 200$mm and $f_h = 100_h$ mm). The bendable KB mirrors are coated with 50 nm platinum on top of a 10 nm chrome under-layer. To measure the size of the focused beam, a tungsten wire is scanned across at the sample plane.

4.1.2 Experimental data handling

The different types of scan patterns seen in section 3.2.2 are realised experimentally thanks to an nPoint NPXY100Z25A dual-axis piezo stage, which one is mounted on the top of a set of XYZ stepper-motors for larger range movements [138]. Then, diffraction patterns are collected using the Princeton Instruments CCD and its native WinView software (.SPE format). This program controls the number of accumulations at a constant exposure time and group it into a single frame. As long exposures saturates the detector, instead many short exposures are taken at a particular data point. The transistor-transistor logic (TTL) pulse provided by the controller is used to command a shutter event and also to control when to (automatically) move to the next scan point. Once the ptychographic scan is completed,

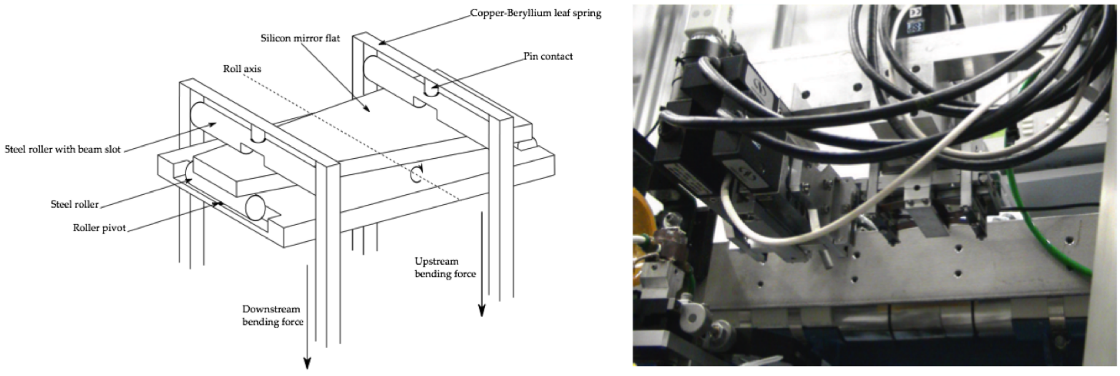

Figure 4.4: Left: schematic of a silicon KB mirror bender. The flat mirror is suspended between steel rollers placed on pivots where the bending force is applied through a pin contact and CuBe leaf springs. The dashed line represents the pivot axis for the roll adjustment. Translation is parallel to the bending force direction. Motors are omitted for clarity. Right: bottom view of the KB unit assembly. The position of the mirror is adjusted by a first motor while its orientation is adjusted by a second one. Two more motors apply their force at each end of the silicon mirrors to bend them in order to focus the reflected beam. The vertical focusing is done first (right) followed by the horizontal focusing (left). Picture and caption taken from [52].

a series of 3 dark current CCD exposures with the beamline shutter closed using the same exposure time are recorded (to ensure as close as possible conditions between the measurements). The WinView program stores the data and the experimental parameters in a file whose structure is 'publicly' available. It is then used in conjugation with a Matlab data preparation (appendix) code needed to feed ptychographic algorithms, and from which the steps are resumed here:

- Both experimental diffraction and backgrounds files are converted to Matlab matrices using a .SPE read file and all the 2-dimensional data stacked into a third dimension (representing the probe positions).
- The average dark counts from the background exposures are subtracted from the all the experimental diffraction patterns and values.
- A threshold value for the noise is given from the first photon peak statistics found in the data histogram.
- The centre of mass is automatically found from the first diffraction pattern and used as centre for the rest of the data stack.
- The user decides on the size of the frame ROI based on the maximum extent of the diffraction.

- The code thus pad an extra 20 percent to the size of the ROI with zero's in order to avoid aliasing when performing the FFT (with rounding to the next power of two for more computational efficiency.)
- The user possess the choice over data binning in x, y (this speeds out FFT calculation if data are oversampled).
- Square root the intensity values to give diffraction amplitudes is performed over the 3d stack.
- Finally, the code will generate a .mat parametric structure to feed the a ptychographic algorithm.

4.1.3 Test pattern for APS

An array of test patterns was designed for use in x-ray imaging. Dr. Graeme Morrison orchestrated the design and choice of materials for the pattern arrays that were later sent to Zoneplates Ltd (see www.zoneplates.com) who replicated them in tungsten films supported on silicon nitride membranes [142]. Small Siemens stars were drawn with 36 open spokes etched into the tungsten support film, with equal mark-space ratios, so the angular width of each spoke will be 5 deg. The spatial period d of the spokes at a distance r from the centre of the star is $d(r) = \pi r/18 = 0.1745r$. There are of unetched tungsten film at the centre of the star.

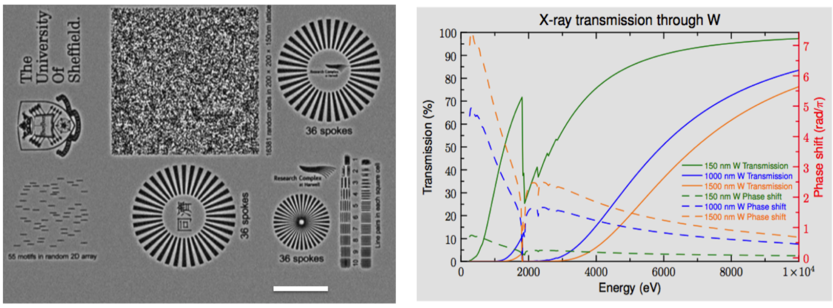

Figure 4.5: Left: SEM images of the test patterns replicated in 1.5 μm thick W film. b) X-ray transmission and phase shift as a function of energy for 3 different thicknesses of tungsten.

Tungsten was chosen as the material from which the test patterns would be fabricated. Its chemical and mechanical properties allow it to be prepared in uniform thin films, films that can be etched anisotropically using Reactive Ion Etching (RIE) so that nano-patterned structures can be reproduced in the tungsten film. It has a high atomic number so a relatively modest thickness of tungsten can absorb a significant fraction of an x-ray beam, giving good absorption contrast in an x-ray image. The real part of its refractive index means that phase shifts that are a significant fraction of π can also be achieved with thin tungsten films. The test patterns were intended for use on both hard and soft x-ray beamlines, for which different thicknesses of material are required. The percentage x-ray transmission and phase shift as a function of energy is plotted for 3 different thicknesses of tungsten in Fig.4.5 b). The pattern used in the experiments of Burdet and Huang [138, 143] was prepared in 1.5 μm thick tungsten film evaporated on to a 1 μm thick silicon nitride window, to provide about 70 % intensity transmission and about 0.9π phase shift when illuminated by a 9 keV ($\lambda = 0.138$ nm) X-ray beam.

4.2 Wavefield characterization

4.2.1 Intro

The ability to characterize wavefronts opened a new dimension for ptychography as the recovered information is used as *in situ* feedback over optics fabrication and x-ray imaging where optical quality and alignement between elements are critical to achieve small focus spot size [144]. Alignment will be even more critical when compound optics will be required to achieve sub-5nm focus size.

A major concern at the beginning of this thesis was the motivation for better approximations of the beam for input to the ptychographic algorithm and thus to finding a door to a general wavefront characterization procedure [145, 146, 147, 148]. Even if it will be demonstrated that ptychography is able to accurately characterize a wavefront from very simple model, methods to provide an a priori knowledge of the illumination function such as simulations and the Quiney method [148] were investigated. The latter has proven to be useful for the characterisation of x-ray beam focused by Fresnel Zone Plate. It is evident that when complicated experiments like for example: focused beam Bragg geometry ptychography studies on Silicon-On-Insulator nanostructures [149] are envisaged or experiments on weak scattering samples, the difficulty of retrieving a highly complex object is relaxed by a good knowledge of the focused beam.

Fresnel Zone Plate characterization

Numerical and experimental approaches were used to understand the focusing behaviour of partially illuminated FZP (Fig 4.7 (a)). The partial illumination results from the coherence length of the x-ray beam which possess a limited extent, typi-

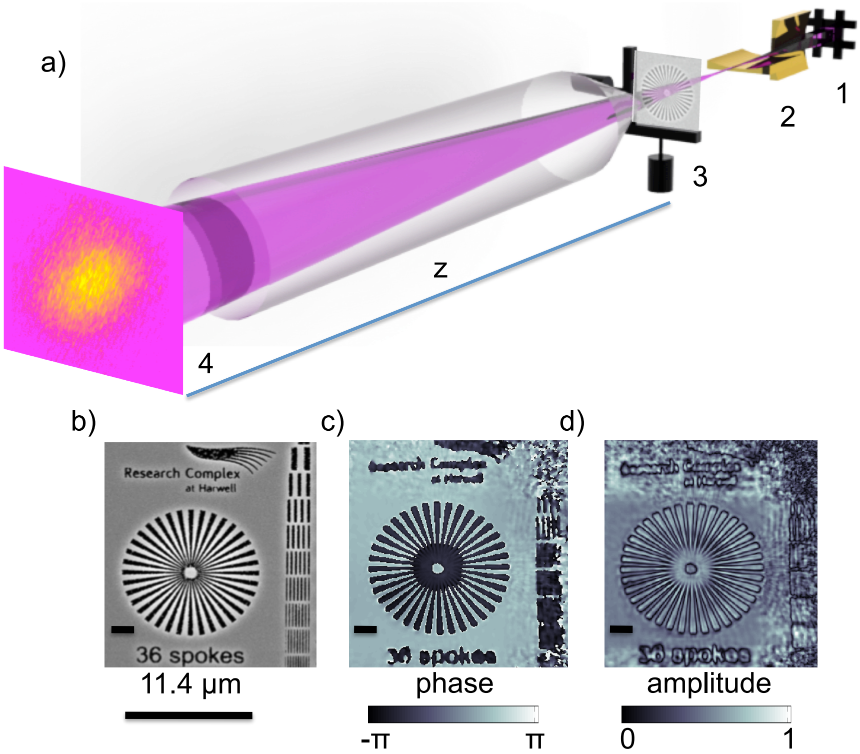

Figure 4.6: (a) Sketch of the experimental setup at 34-ID-C with entrance slits (1), KB mirrors (2), piezo-stage (3) and camera (4). (b) SEM image of the test pattern. (c)-(d) reconstructed phase and amplitude images using data measured at z =2.3 m. Scale bars, 2 μm.

cally $10 - 100\mu$m. A good compromise between working distance and loss of photon flux is obtained in this manner but as the resulting focused x-ray beam necessarily represents a noteworthy departure from the focus of a fully illuminated FZP; the wave-field behaviour is investigated here. The important question to whether the Quiney algorithm can converge under partial illumination has been assessed elsewhere [150]. The initial wave-field $\psi(x, y, 0)$ at the pupil just after the pupil function is defined as:

$$\psi(x, y, 0) = P_1 = exp(-\Phi_{FZP}(r_n)).M_1(x, y), \tag{4.1}$$

where the zone plate phase profile $\Phi_{FZP}(r_n)$ is function of the radius $r_n = \sqrt{n\lambda r}$ with n the number of zone. The mask $M_1(x, y)$ defines the illuminated area. For initial simulations a shifted 'logical' square pupil was employed but for more refinement, propagation of the beam from the coherence defining slits to the FZP was used. [2]

The Quiney method: In principle, a single step calculation between the pupil plane to the detector should be possible using the Fresnel free-space propagator but sampling of the quadratic phase factor makes it a difficult task. Quiney [148] derived a new formalism of the Fresnel equation which extend the process of phase retrieval algorithms to a three plane iterative method that provides stability to the algorithm, through removal of the highly oscillatory terms. Since the focal distribution is theoretically of infinite extent it is by definition it is not possible to impose a well defined support in this plane, his key idea was then to use the known support in the pupil plane as opposed to the object's plane.

For the calculations, the FZP is assimilated to a complex pupil function of a thin lens $P(\rho)$ of focal length z_f. As the detector is placed in the far field the propagation from $z_3 \mapsto z_2$ requires only the Fourier transform of the slowly varying function $D(r_3)$, rather than of the complete rapidly oscillating wavefield $\psi(r_3, z_3)$. The stability of the phase retrieval is maintained by simplification of the Fresnel terms seen in section 2.1 and summarized by the following steps:

1. Propagate from Pupil to focal plane : $\psi(r_2, z_2) = Q[\frac{1}{\Delta Z_{12}}, r]\mathcal{F}[P(r_1)]$.

2. Propagate from focal plane to detector : $\psi(r_3) = \alpha[\frac{1}{\Delta Z_{23}}, r]\mathcal{F}[Q[\frac{1}{\Delta Z_{12}}, r]\psi(r_2, z_2)]$.

3. Impose modulus constraint π_m on $D(r_3)$.

---

[2] When it is not possible to image where the beam is hitting the circular plate, e.g. because of a vacuum chamber, a method like the shrinkwrap [49] invented by Marchesini should be used to refine iteratively the support of the 'pupil' function which is realised by smoothing and thresholding the current iterate

4. Propagate from detector to focal plane $\psi(r_2, z_2) = Q[\frac{1}{\Delta Z_{12}}, r]\mathcal{F}D(r_3)]$.

5. Propagate from focal plane to Pupil : $P(r_1) = \alpha[\frac{1}{\Delta Z_{23}}, r]\mathcal{F}Q[\frac{1}{\Delta Z_{12}}, r]\psi(r_2, z_2)]$.

6. Impose support constraint π_s on $P(r_1)$.

Propagation of the phase-retrieved foucs to the pupil plane gives insight about deviations from a perfect spherical wave, thus a decomposition of the wave-front into Zernike polynomials [16] can give quantitative information about the kind of aberrations present in the optics.

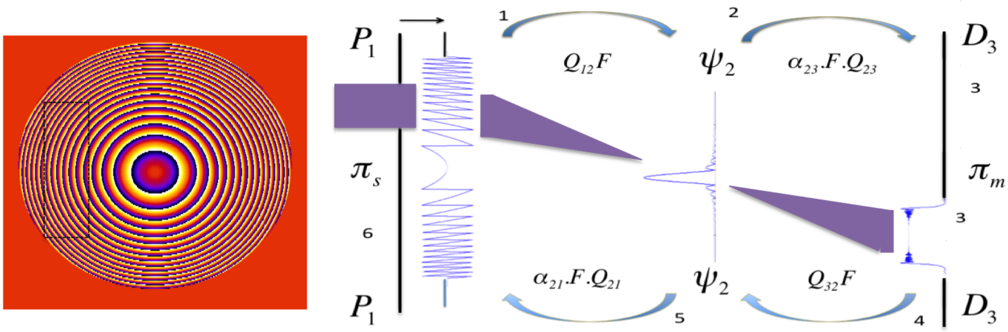

Figure 4.7: Left: A partially illuminated zone plate matching the coherence lengths of the x-ray beam. 2D schematic of the propagation wavefield produced the partially illuminated FZP along with the Quiney cycle.

Experimental[3]: to simulate the focusing performance of the FZP, the FZP fabrication details together with the experimental setup parameters (Fig.4.8) were introduced into the Quiney algorithm. To calculate the function $M_1(x, y)$, a plane wave was assumed at the the plane of the beam defining slits set to $30_h \times 100_v \mu$m which was then propagated 286 mm downstream until partially illuminating the FZP with an offset of 35 μm in the horizontal direction. After passing through the FZP, the modified wavefront continued to propagate by 85 mm, where the outer

---

[3] The FZP we used in this work contains 2 μm thick alternating gold and diamond zones [151]. The diameter is 180 μm with 80 nm outer-most zone width and a 30 μm diameter central stop. For X-rays with energy of 9 keV, the first-order focus length is found at 104.5 mm. It was fabricated using ultra-nanocrystalline diamond (UNCD) as the dielectric mold material into which Au is electroplated. UNCD is a chemical vapour deposition (CVD) diamond composed of 2-5 nm grains of diamond bonded together with graphitic type bonds [152]. A 2-μm-thick layer of UNCD was prepared on 40 nm of tungsten and 1μm of Si_3N_4 supported by a Si substrate. These layers were released to form a membrane by back etching the Si substrate. The sample was then coated with hydrogen silsesquioxane (HSQ) acting as the resist material and exposed using a 100 keV e-beam lithography system. After development, UNCD was etched with oxygen plasma designed for high anisotropy and selectivity. The resulting mold was filled by electroplating gold using tungsten as the conductive base. The HSQ was removed and the resulting FZP consists of alternating Au and UNCD zones.

wavefront was masked out by an optical sorting aperture (OSA) of 30 μm diameter. The wavefront propagated a further 19.5 mm until the focal plane z_f.

A 10 × 10 μm Round-ROI scan, with 0.5 μm radial increments, produced 323 far-field diffraction patterns from the ptychographical measurement performed at the plane of focus z_f. The simulated focused probe was used to initiate the DM. A typical reconstructed test sample image is shown in Fig 4.8 c).

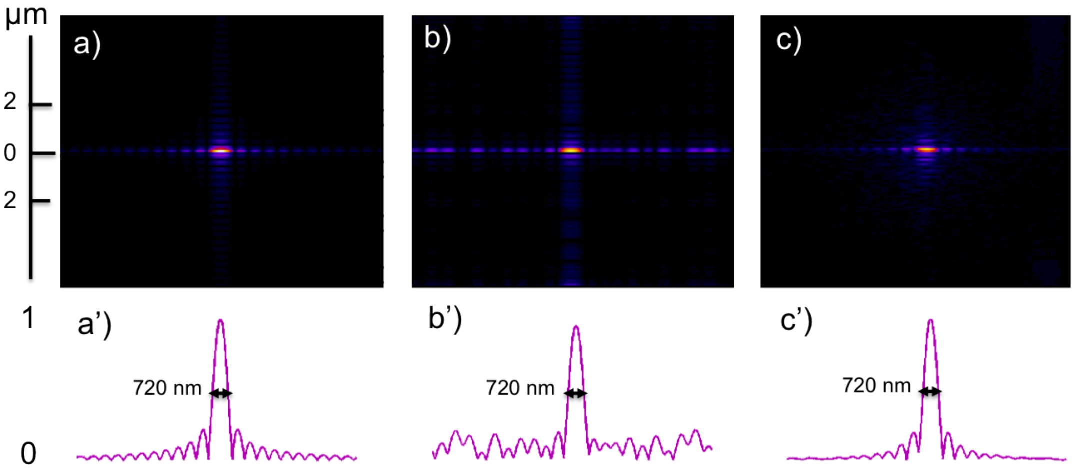

Figure 4.8: Comparison between the simulated probe (a), the probe obtained using the Quiney method (b) and the ptychographic probe (c).

As the same ptychographic experiment was performed on a bounded object (a tungsten pin), the main input for the Quiney method - a diffraction pattern coming from the free propagation of the beam to the detector- was taken from the last point of the scan region (where the beam is the least perturbed). For better performance of the three plane method, a diffraction pattern should be taken with object removed. This probably explains why the ptychographic measurement has given perfect agreement with the simulated beam as compared to the three plane method.

The retrieved focused beam Fig 4.8 c) was propagated along z as ptychographical measurement were repeated at 2 different defocus positions with $z = +6.0$ mm and $z = -12.32$ mm, respectively, while the positive z points the downstream direction of the X-ray beam. A half-pixel size sampling interval was used in the Fresnel propagation calculation, upon FFT in an array of 1024×1024 pixels. Fig.4.9 shows how the beam propagates between the planes of measurement. The recovered wavefront are not analysed in this section but are reported in the publication of Huang [138] as KB mirrors were exclusively used for the results throughout the thesis, hence are the main interest of this section.

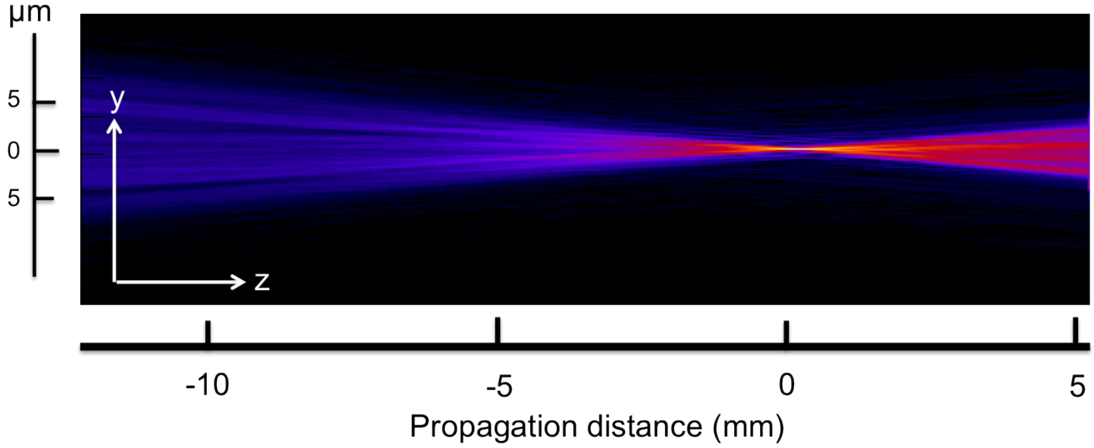

Figure 4.9: Propagation of the probe retrieved at the focus z_f.

4.2.2 KB mirror

Kewish et al. [144] used the ptychographic method to do comparison of phase-retrieval results with projected metrology data. They propagated the phase-retrieved probe to the exit plane of the KB mirror and the optical wave coming from surface metrology to this very same plane and reached very good agreement. As the lack of metrology measurement of KB mirrors at APS prevents numerical simulation of their focusing behaviour and in analogy to three plane method explained earlier (which appears to be hard to adapt for a pair of mirrors) the idea of performing measurements at three different planes around the focus came as a self-imposing method.

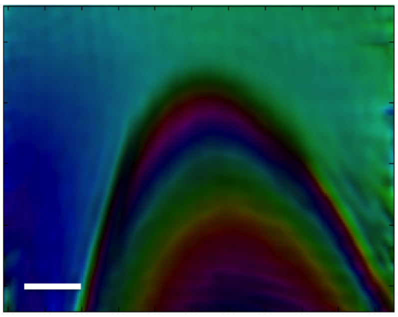

Figure 4.10: Reconstructed tungsten pin with difference map. Scale bar, 1μm.

As recovered wavefronts are related to each other by Fresnel propagation, an agreement with numerical propagation to a plane of interest, is a means for convincing self-verification [138].

Experimental: A tungsten pin (Fig.4.10) was placed at the focus of KB system, which was set at an incidence angle of 3 μrad. The coherence defining slits were set to an opening of 20×20 μm for full coherence of the x-ray beam. Ptychographical measurements were performed at the the focus plane $z = 0$ and at two other planes, almost symmetrical to the latter, $z = -10.0, +10.5$ mm respectively. The scan range of the usual Round-ROI scan was set to 10×10 μm with radius increment of 0.75 μm. The detector region-of-interest (ROI) was set to $N = 512$ pixels.

The results presented here are complementary to the study of Huang [138], as they concern the reconstruction of a probe from an non-extended sample. This was of major importance for later implementation of Bragg projection ptychography for crystals (chapter 5). The pin sample (Fig.4.10) could be reconstructed with the difference map algorithm alone, meaning without constraining the probe update with a diffraction pattern coming from the direct beam. The lower of Fig.4.11 displays the reconstructed KB probes, while the upper row displays the central numerically propagated to the computed from the Fresnel propagator (Eq.(2.5)) to the the -10 mm and +10.5 mm planes. The recovered probe at the focal plane was propagated backward and forward to the other two planes as they relate by free space Fresnel propagation. Good agreement with the retrieved probes validates the ability of ptychography to recover wavefronts.

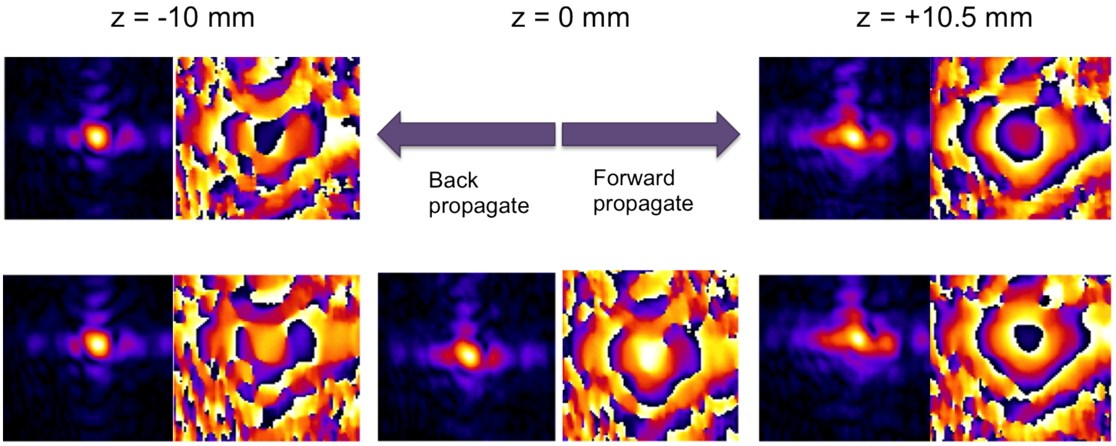

Figure 4.11: Lower row: the reconstructed probe of the KB mirrors with the sample placed at -10 mm, 0 mm and 10.5 mm, respectively. Upper row: the simulated probes propagated from the focused probe matches the reconstructed probes at -10 mm and 10.5 mm as in [138].

The reconstructed probe was propagated in a range of 100 mm with 100μm propagation step size. To avoid aliasing, the Fresnel propagator was calculated with a a half-pixel size sampling interval, upon FFT in an array of 512×512 pixels. The horizontally and vertically integrated intensities at different planes are shown in Fig

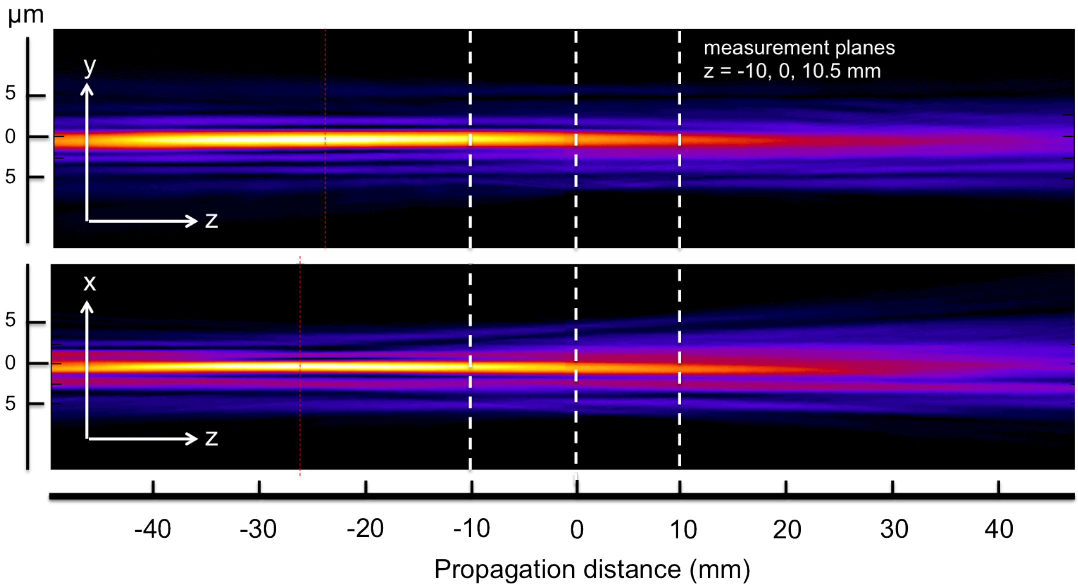

Figure 4.12: a)b) The integrated vertical and horizontal amplitude through focus from the central probe of Fig 4.11

4.12 (f) and (g). The vertical focal plane was located at $z = -18.6$ mm, while the horizontal focal plane was at $z = -27.8$ mm.

The horizontal and vertical focal sizes were estimated to be 0.9 μm and 1.3 μm, respectively, as shown in Fig 4.13.

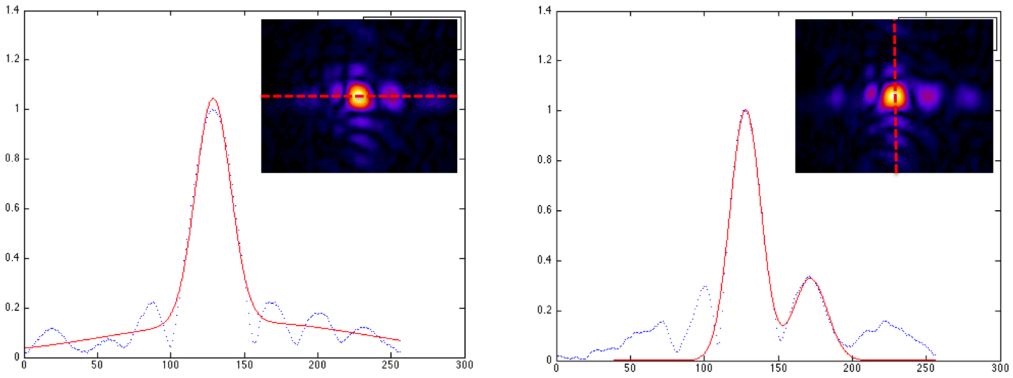

Figure 4.13: Horizontal (a) and vertical (b) focal sizes of the Kirkpatrick-Baez (KB) mirror system at their corresponding focal planes. Respective size are 0.9 (V) and 1.3 μm (H) from fitted Gaussian HWFM.

The methodology of defocused planes produces a convincing self-verification of the analytical method recovering un-arbitrary wavefield structure information.

4.3 Probe bandwidth experiment

Previous chapters demonstrated that reconstructions are readily obtainable with only initial rough estimates of the probe. Exploration of what characteristics are of benefit for the the imaging resolution and convergence [153] of the reconstructions are now of very interest in the CDI community. As the scattering power for a given object is fixed, it is the probe bandwidth that amounts to changing the attainable angle in diffraction space and hence the image resolution.

Guizar et al. in 2012 [1] showed (experimentally) that a probe with a wider spatial-spectrum is beneficial for ptychographic reconstructions. They compared the illumination coming from a pinhole and a focused illumination coming from a FZP and assessed the resolution of the reconstructed images via Fourier Ring Correlation. However, the starting point of their reflection was based on previous theoretical work on Wiener deconvolution for ptychography [86]. While ptychography could be performed through Wigner deconvolution, it would be only under the unrealistic condition of data taken with sample steps finer than the desired resolution. However, Guizar [1] found from the mechanism of information encoding by ptychography that : "a limited probe spectrum does not pose a fundamental limitation in resolution but rather a disadvantage in SNR, for a faithful recovery of the object's high resolution details it helps to have a probe ambiguity function with a wide spread in reciprocal space. "

In our set-up, a smaller probe with an increased bandwidth within a CDI window is easily obtained by opening the KB entrance slits wider. According to classical diffraction theory of lenses, the size of the focus scales as the reciprocal of the entrance aperture: ($d \sim 2\lambda f/a$) where d is the focus spot size, f the focal length and a the entrance aperture size. The X-ray beam coherence is ensured within the nominal length of 30×50 μm, thus, it is considered detrimental to open the slits wider.

To study the effect of probe bandwidth with a significant change between probes within the CDI window, two entrance slit settings to provide full coherence (10×10 μm and 30×50 μm) along with three distances ($z = 0.55$, 1.0 and 2.184 m) which are representative of the available range of camera lengths were chosen. A concentric circular scan trajectory [75] with 5n points on the n^{th} ring and a radius increment of 0.5 μm within a 12×12 μm scan range, generated 460 frames of far-field diffraction patterns for each measurement. The detector region-of-interest (ROI) was set to $N = 256$ pixels, which respectively gave the real-space pixel size of Δx =14, 24 and 55 nm for the three detector distances used. As the focal length of the KB mirrors are 100 mm and 200 mm in the horizontal and vertical directions respectively, the slits settings give a nominal focus size of 2.7×5.4 μm and 0.9×1 μm.

The difference map approach was used to retrieve the complex sample and illumination functions from the measured diffraction data. As initial input for the algorithm, a random guess of the sample image and a 1×1 μm square aperture for the illumination probe were used. For the first 10 iterations, only the object was updated, while the illumination function started to update after 10 iterations until the final number of 100 iterations.

In Fig.4.14, we can clearly observe that for a given distance, sharper edges, improved contrast are given by reconstructions with the smaller probe that has a larger bandwidth. We observe as well that for longer distances, the 36 spokes legend' written on the sample becomes visible along with the grid pattern. To explain these results, we can define a quality criterion, by coupling into a single product (Ω) the two fundamental quantities of ptychography, which are the overlap (Θ) and the sampling (S) as both are varying in this experiment. The overlap in 2D is given by: $\Theta = (d_x - dr)/d_x + (d_y - dr)/d_y)/2$, where d_x and d_y defines the beam size in x and y and dr is the scan radius increment. The sampling S, defined here by dividing the CDI window by then beam area ($d_x \times d_y$). We define the quantity $\Omega = \Theta.S$ as an aggregate measure of the overdetermination of the phase problem. In principle, the value Ω should be ≥ 1 as the respective entities taken alone should be ≥ 0.5 for the overlap Θ [154] and ≥ 2 for the sampling S. From the numbers that are reported in Fig.4.14, it seems that Ω needs to be an order of magnitude higher to obtain good reconstructions.

It is concluded that probes with increased divergence show higher quality reconstructions despite a reduced degree of overlap. This demonstrates that probe bandwidth is a complementary factor to the overlap. Another factor which seems to surpass the effect of overlap, is the sampling of the probe, where the majority of the power gradually fits within the field of view when the camera distance is increased. The increased divergence also allows more flux, so has a double benefit due to the enhancement of high photon signals at high-angle scattering.

The obvious solution to increase the resolution is to reduce the scan steps, but the number of points in the scan would require more stability from the instrumentations, sample drifts and also humidity (except for smaller field of view, such a compromise on time of measurement is not necessary and the overlap could be increased followed by a drastic increase in the overdetermination factor S).

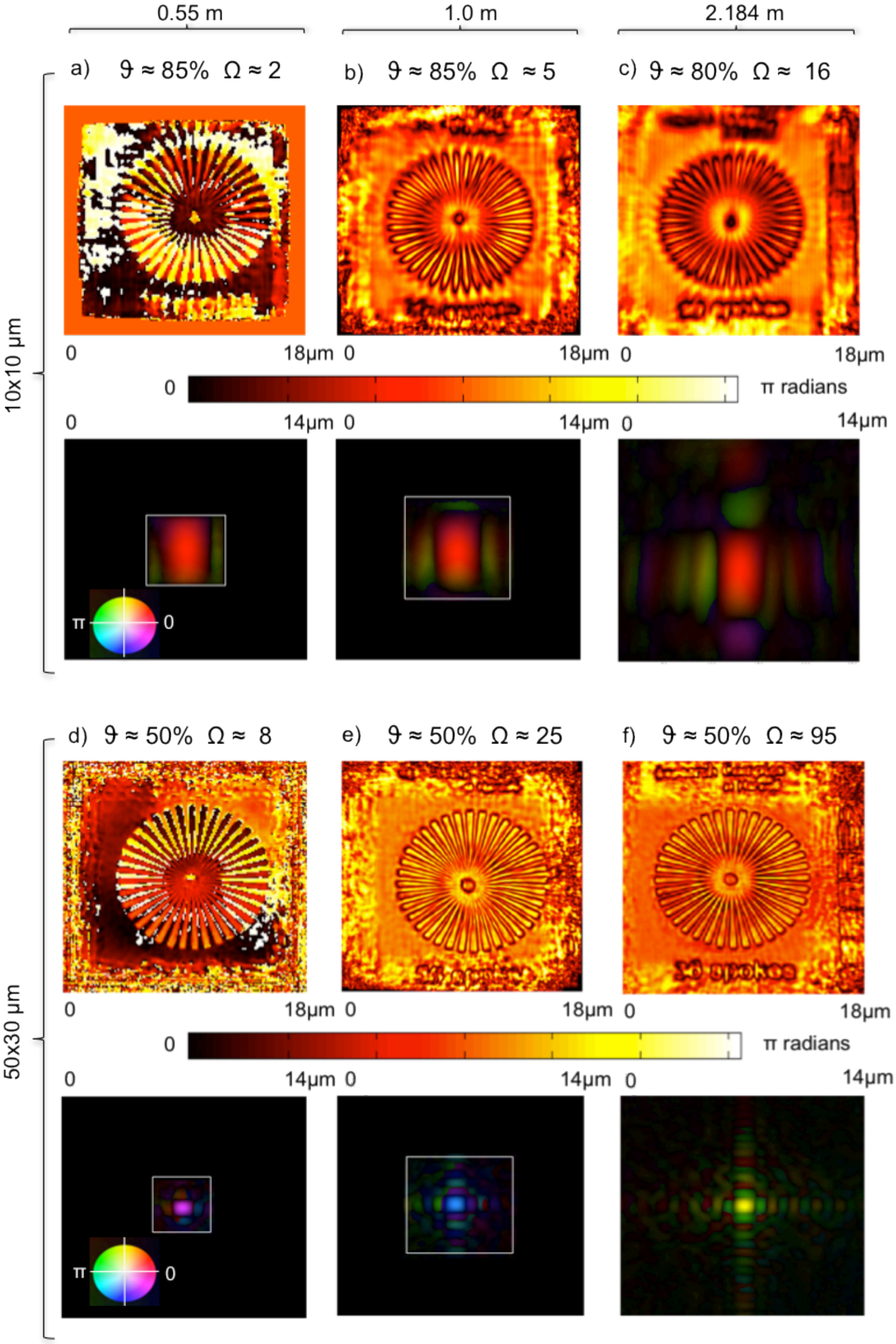

Figure 4.14: From left to right: reconstructed objects and probes for detectors located at distance $z = 0.55$, 1.0 and 2.184 m from the sample. Top half part: reconstructions for slit openings of 10×10 μm. Lower half part : Reconstructions for slit openings of 30×50 μm (note: the horizontal KB mirror has one half the focal length of the vertical). The probes are shown on a common array scale but a white frame has been drawn to represent the original size of the CDI window. The amplitude of each probe is mapped to the image brightness, and the phase is mapped to Hue. The beams sizes are in good agreement with what predicted from diffraction theory.

4.3.1 Probe diversity: simulations

It was seen in the previous sections that the ptychography unquestionably disentangle the probe features from these of the objects. The probe bandwidth experiment also suggested that finer features in the probe could maximise the diffraction data. Thus, to further understand the impact of the probe structure and phase diversity over resolution, a numerical experiment is performed. The study also aims at decoupling the effects of probe structure (the lobes) and phase structure (diversity). To do so, a reconstructed probe coming from the KB mirror system is used to create four different types of illuminations:

1. A first probe where only the amplitude structure remains but its typical phase structure is suppressed, Fig.4.16 a).
2. A second probe that is made by filtering the oscillations surrounding the central spot of the first probe with a Turkey window, Fig.4.16 b).
3. A third probe is created by multiplying the second probe with a complex phase valued array, Fig.4.16 c).
4. A fourth probe is generated by using the first probe amplitude structure but multiplied with the complex phase valued array of the third probe, Fig.4.16 d).

To generate the phase diverse array, a gently varying landscape of valleys and troughs is generated by convolving a uniformly random distributed array of numbers [0-1] over with a Gaussian kernel of 10 × 10 pixels. Simulation were based on a simulated siemens star (see Fig.4.15) and the usual Round Roi scan used to generate 565 diffraction patterns. Different level of Poisson noise were used from 10^6 to 10^{10}.

Properties	Value	unit
Energy	9	KeV
Array size	256	pixels
λ	1.4	A
beam size	$\sim 1.5_H \times 1.5_V$	μm
detector distance, L	1	m
pixel size	20	μm
pixel resolution	27	nm
scan range	8x8	μm
step size	0.3	μm
Number of positions	565	
Noise level	$10^5 \mapsto 10^{10}$	

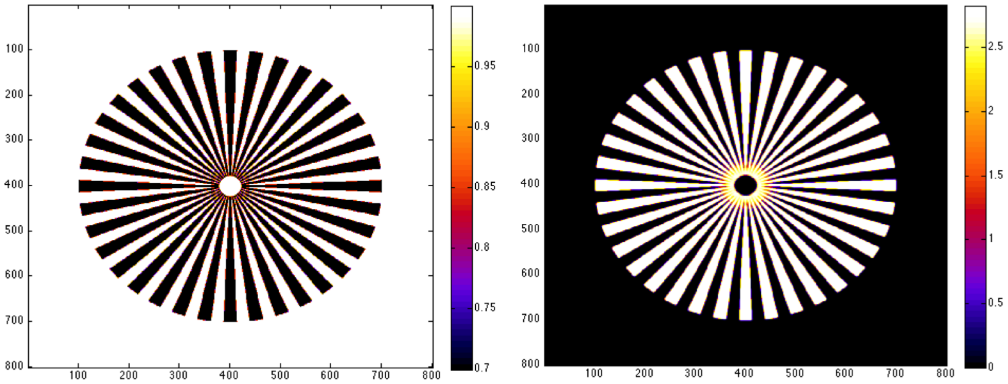

Figure 4.15: Simulated Siemens star of size,11.4 μm

Results on preliminary study: The quality of the reconstructions was examined using two quality criterions. The first one, the difference map error ϵ that takes place in the real space and measures the difference between subsequent iterations (Eq.(3.10)) whereas the second takes place in reciprocal-space and is based on the difference between the generated and calculated intensities (Eq.(3.13)). The difference map error analysis reported in Fig.4.18 indicates that a KB probe cleaned of its structure (whether phase or amplitude) gives better reconstructions, meaning that the side fringes have a 'detrimental' impact on the quality of the reconstructions. The R-factor analysis is more mitigated as the level of noise seem to play a role regarding the role of the structure in the quality of the reconstructions. A visual inspection is not possible when the level of photons is $> 10^8$. Interesting behaviour at lower photon count which suggests that phase diversity will be useful for biological sample (like the human metaphase chromosome imaging project [63]) where lower dose are required.

The results on the filtered KB probe converge with the analysis on X-ray ptychography of a weakly scattering object (still a daunting task) done by Takahashi [97] where a spatial filter at the KB focus provided a better solution with this kind of illumination optics, to measure the slight object phase-shift.

4.3.2 Discussion

A real object presenting more diversity could also help at identifying the pros and cons of phase structured illuminations. A set of irregular test patterns made of polycrystalline tungsten could be used for future experiments. For simulations with both phase diverse objects and probes, the problem that could arise is that the high frequency in the Fourier data will wrap-around across the edge of the compu-

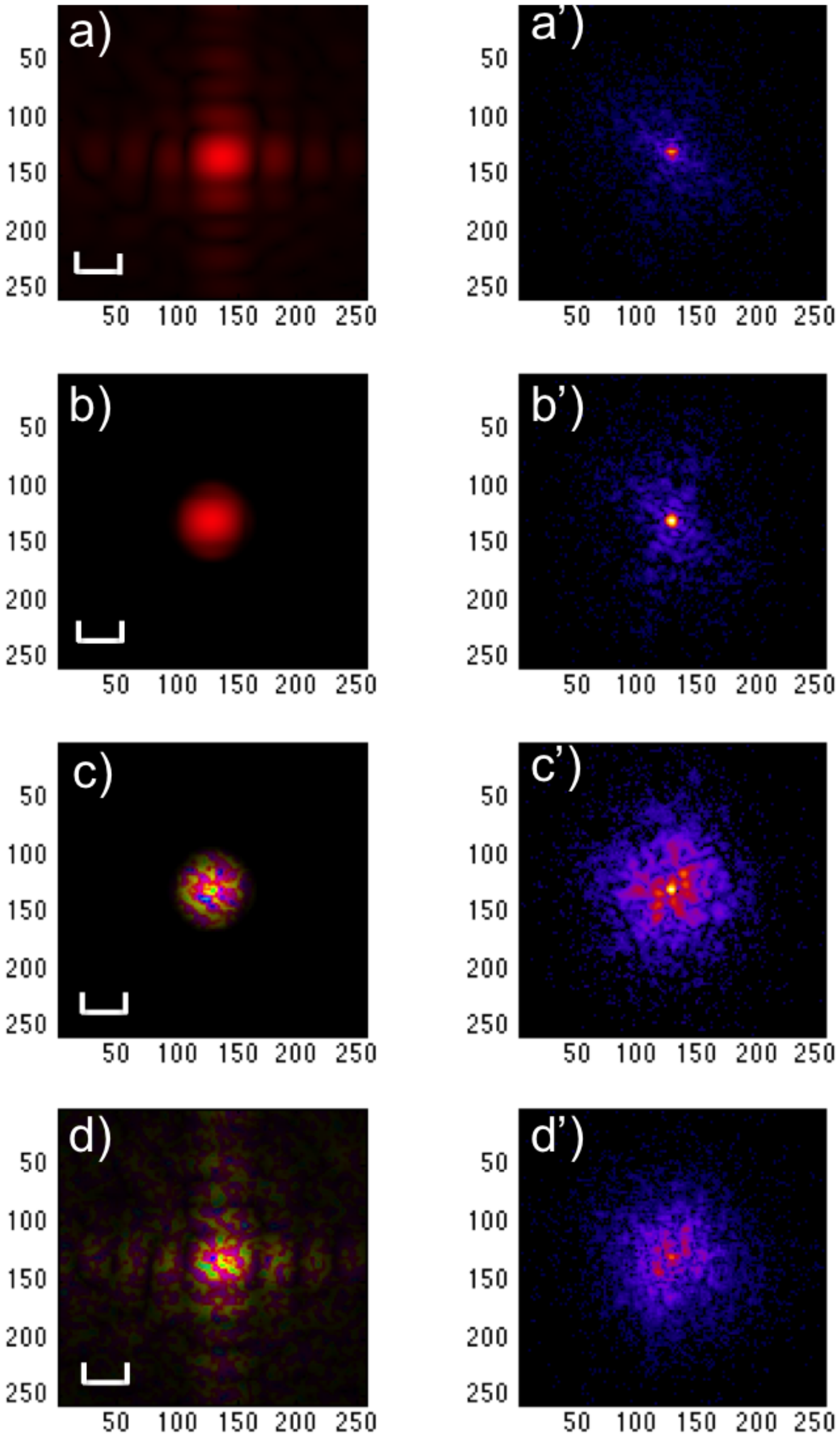

Figure 4.16: Left column: 1) Original probe with amplitude structure only. 2) Probe with central spot left. 3) Central spot with phase diversity. 4) Original probe with phase diversity. Right column: Respective Fourier Transforms from the product of the corresponding illumination pattern and the simulated Lena object (for better diversity in features). Scale bar, 1.5μm.

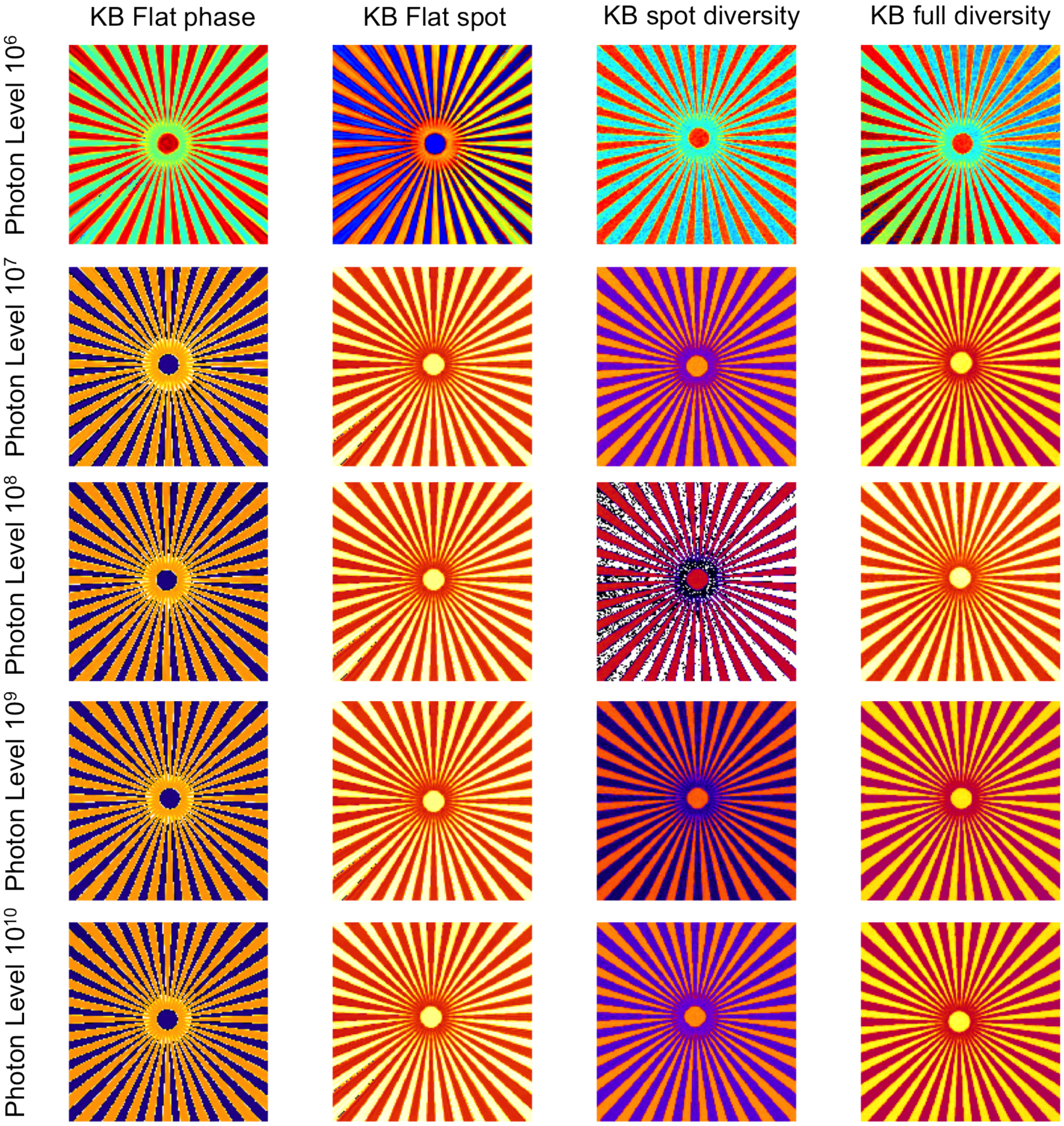

Figure 4.17: Reconstructed objects from the diverse probes as a function of photon counting in the simulated data. The difference in colours indicates the presence of phase offsets in the reconstructions (also, one of the reconstructions reveals a transfer of the probe diversity onto the object).

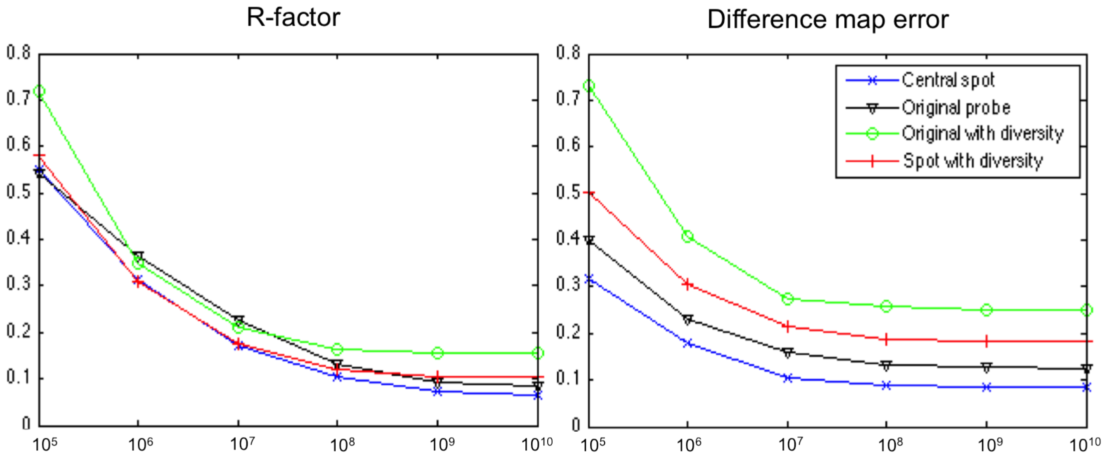

Figure 4.18: Metrics comparison for the reconstructions with different level of noise. Left: Comparison using the R-factor. Right: Comparison using the difference map error.

tational window; as pointed out in Guizar's thesis [82]. The use of this continuous extra wrap-around intensity pattern for image reconstructions, though non-physical, is not a cons for simulations. However, in a real-world experiment, care must be taken that the propagated radiation resulting from such a diversity does not fall outside the detector area as it would cause discontinuity at the edge of the computational window. Such truncation would translate into aliasing of the reconstructed image. Although, it is possible to overcome this limitation by implementing the super-resolution method developed by Maiden and Rodenburg, which extrapolates the information outside the detector (and thereby improving the image resolution) [155]. Furthermore, recent developments at 34-ID-C enlarge both the space available between samples and detector and the pixels size of the latter, the medipix [38], to enable resolving much finer reciprocal space speckle diffraction patterns.

Moreover, a systematic study on transmission-geometry ptychography as a function of X-ray probe phase diversity and degree of partial coherence properties at beamline 34-ID-C at APS should be performed. Previous researchers [109] have suggested that incorporation of phase diversity improves CDI reconstructions significantly. The previous studies have suggested that, according to the numerical simulations, introduction of a high degree of phase diversity to X-ray illumination improves ptychographic reconstructions significantly [N. Burdet, X.Shi, et al, submitted to optics express 2014]. The theoretical predictions should be tested with experiments, which would be an important precursor to X-ray coherent diffraction imaging studies on real condensed matter materials.

Phase-diversity x-ray illumination means the introduction of certain phase structure in the incoming illumination function, as comparing to a typical KB focusing probe. Several random pinhole diffusers will be fabricated to this aim (a typical SEM image of a similar type of diffuser is illustrated in Fig.4.20. Higher number of random pinholes present in the diffuser can generate high phase-diversity in the x-ray probe. The phase diversity can be influenced by the number and size of the random pinholes that are illuminated by the x-ray beam, so it is possible to artificially make X-ray illumination with high and low phase-diversity. To vary the degree of coherence of illumination, both the horizontal and vertical coherence defining slits size should be varied so as to introduce extra modes in the illumination. Preliminary reconstruction on partially coherent illumination at APS demonstrates that a multimodal decomposition for a KB probe is achievable, see Fig.4.19, and will enable a thorough investigation of partial coherence correction reconstructions.

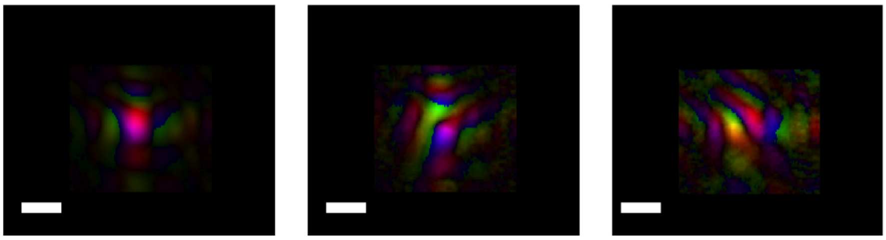

Figure 4.19: Reconstruction of three KB focus modes for the case of partial coherence. Preliminary work done with Clark [112]. Scale bar, 1μm.

The insertion of random pinhole array diffuser may cause the KB focus of X-rays to be more difficult to retrieve. Appropriate guard and standard pinholes; slits should be placed before the x-ray beam enters the KB mirrors. A guard pinhole to define the area of random pinholes that are illuminated, and that this pinhole may also affect the degree of coherence of the illumination reaching the sample.

Ptychographic data with various complexity of random pinhole diffusers, and a number of coherence defining slits sizes should be taken for investigation of partial coherence correction with X-ray illumination phase diversity introduced.

Because the numbers of variables are too many for ptychographic simulation studies, incorporation of all unknown variables of real experimental condition could provide vital information about the effects of partial coherence and probe phase diversity in X-ray ptychography, and thus help to test the validity of findings in recent numerical studies.

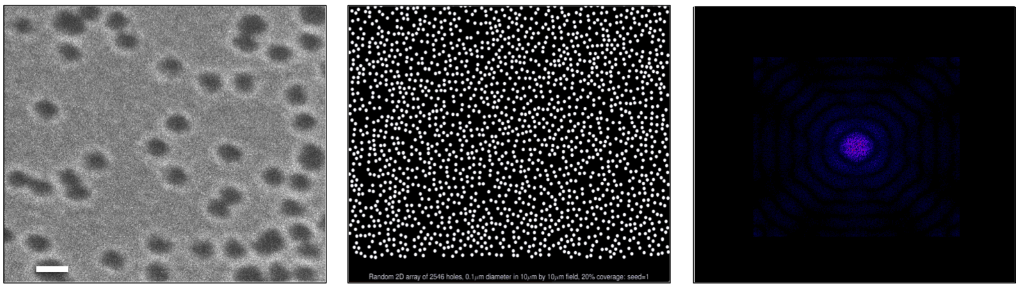

Figure 4.20: Left: SEM image of some randomly-positioned holes. The image was taken by Pambos Charalambous [156]. The holes are about 40nm diameter, and were etched into 50nm thick tungsten film, with the holes covering about 14% of the film area. The area into which random holes were drawn was about 94×94 μm microns, which is much larger than the area shown in the SEM image. Middle: field size for a generic example, with 2546 holes of 100nm diameter, giving 20% area coverage in a field size of $10 \times 10\mu$m. Right: diffraction limited spot obtained from the simulation holes (middle picture). Scale bar, 50nm.

Chapter 5

Bragg Ptychography

5.1 Bragg CDI

The foundations of the support-based CDI technique were explained in the background chapter for non-periodic objects but are also applicable to crystalline objects in Bragg geometry (originally, CDI is an emancipation from crystallography to allow for the imaging of non periodic samples). X-ray crystallography study how atoms organize in periodic arrays, but Bragg-CDI is able to investigate the atomic displacement from the ideal periodic lattice, making it a strong contender over more conventional imaging techniques such as TEM, which requires thinning of the samples. The ability of Bragg CDI to recover a quantitative map of the strain distribution is of fundamental importance to nanoscience, as strain relates to chemical, electrical, magnetic, and mechanical properties [157]. Strain engineering in nanoscale materials, includes the enhancement of semiconductor functionality, and also spatial tuning which may give rise to multiple device relevant effects, such as anisotropic magnetoresistance [158]. The extension of the Bragg CDI technique in the XFEL domain has recently demonstrated ultra-fast imaging of lattice dynamics in nanocrystals [159], and will be of great benefit for the study of pico- and femtosecond processes. Examples of systems which may be studied thus include catalysts and photonic devices.

5.1.1 Theory behind Bragg CDI

A perfect crystal arrayed on an infinite lattice and broken down into unit cells arranged on a periodic Bravais lattice [160], is first considered. The direct lattice vectors a, b, c, known as the primary lattice vectors, defines the discrete translation:

$$R_n = n_1\mathbf{a} + n_2\mathbf{b} + n_3\mathbf{c}, \tag{5.1}$$

where the $n_i s$ are integer value. Conveniently, the Fourier transform of the direct lattice is also a Bravais lattice (see Fig.5.1) with the reciprocal lattice vectors that are defined as:

$$G_{hkl} = h\mathbf{a}^* + k\mathbf{b}^* + l\mathbf{c}^*, \tag{5.2}$$

with:

$$\mathbf{a}^* = 2\pi\frac{\mathbf{b}\times\mathbf{c}}{\mathbf{a}\cdot(\mathbf{b}\times\mathbf{c})}, \quad \mathbf{b}^* = 2\pi\frac{\mathbf{c}\times\mathbf{a}}{\mathbf{b}\cdot(\mathbf{c}\times\mathbf{a})}, \quad \mathbf{c}^* = 2\pi\frac{\mathbf{a}\times\mathbf{b}}{\mathbf{c}\cdot(\mathbf{a}\times\mathbf{b})}, \tag{5.3}$$

and where h, k, l are the Miller indices. As diffraction from crystals is interpreted as the reflection from a set of lattice planes, (h, k, l), thus the convenient reciprocal lattice vector G_{hkl} locates the scattered intensity that can be probed by an experiment. This is the Laue formulation, which is equivalent to but more formal than Bragg's law (Eq.5.4), which nonetheless is at the origin of x-ray crystallography. Indeed, Bragg was the first to elucidate the fact that for diffraction to occur, the x-ray wavelength must match the interatomic distances in crystals, which led him to express the master equation:

$$n\lambda = 2d_{hkl}\sin(\theta), \tag{5.4}$$

which states that a Bragg peak is produced when the x-ray radiation from the atomic lattice planes interferes constructively (when the phase shift is a multiple of 2π). The lattice spacings d_{hkl} fulfil many realisations of Bragg peaks.

The Ewald sphere construction depicted in Fig.5.2 helps visualizing the scattering process in reciprocal-space. The initial and scattered momenta of the radiation are denoted k_i and k_f and the scattering vector q defined as $q = k_i - k_f$, with $|q| = (4\pi/\lambda)\sin(\theta)$ and θ the angle between the scattered wave vectors. Neglecting inelastic scattering process ($|k_f| = |k_i|$), the scattered wave vector sweeps out a sphere of radius $|k|$ and each reciprocal lattice point that lie in the sphere can be measured by a detector placed at the right location. In the case of a finite crystal, the physical consequence implies that a copy of the object's Fourier transform convolves around each Bragg peak (Fig.5.2).

As it was seen in section 3.6, a 3D diffraction pattern cannot be probed from all directions simultaneously, and a set of 2 dimensional reconstructed projections, spanning an angular range of close to 180 degrees is assembled into a single 3 dimen-

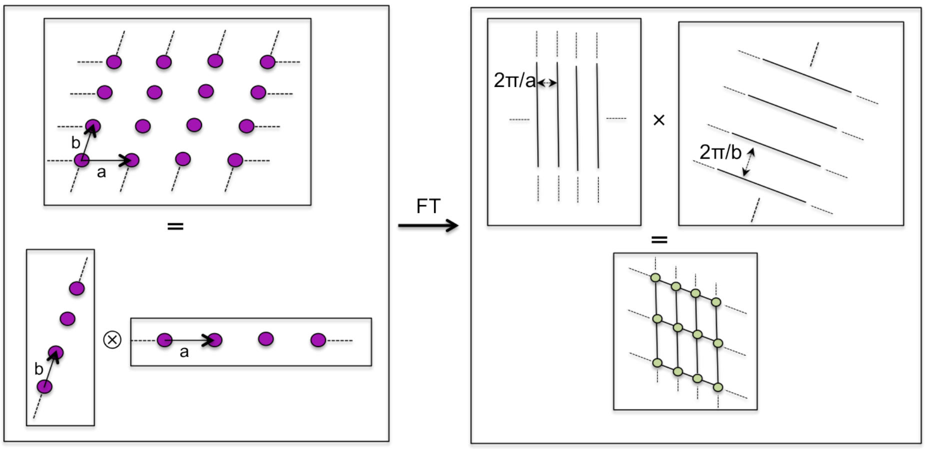

Figure 5.1: Two dimensional real and reciprocal space based on a set of infinite lattices. A lattice (top left) in the real space can be thought of as the convolution of 1D lattices (bottom left). The Fourier transform is therefore the product of the Fourier transforms of the individual 1D lattices (top right), which are sets of lines which intersects to form a lattice of points. Figure and caption derived from [133].

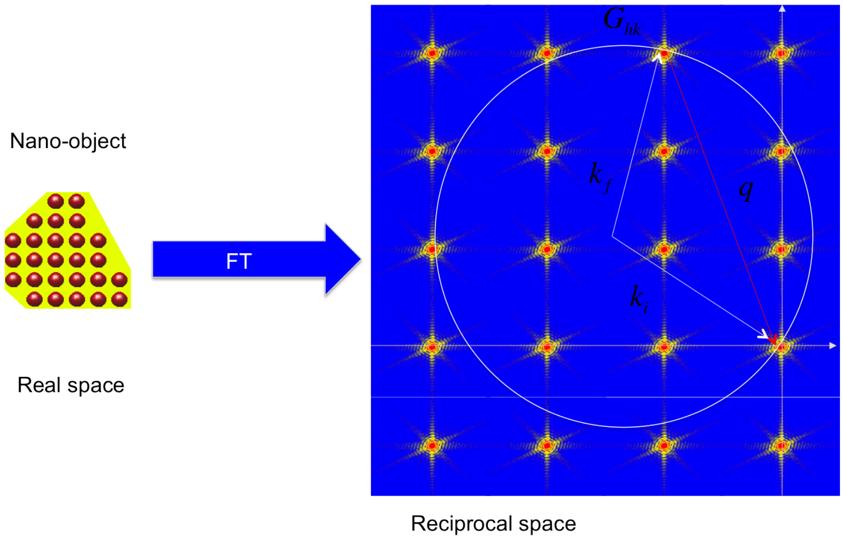

Figure 5.2: Left: a finite lattice network representing a crystal in real space. Right: reciprocal space construction in which the Fourier transform of the shape of the crystal is found to be convolved around given lattice points (red grid). In an Ewald circle representation of a constant-wavelength scattering experiment, the scattered intensity occurs at reciprocal lattice points (red grid) for which the scattering vector $q = k_i - k_f$ (red arrow) matches the reciprocal lattice vector G_{hk}. Figure and caption derived from references [52, 135].

sional diffraction by mean of the back-projection technique (tomography). However, a Bragg geometry experiment presents a major difference to its transmission counterparts as the 3D information (or diffraction pattern) is easily available via the so-called rocking curve, see Fig.5.3. Typically, a few degrees are enough to rock the entire crystal through the selected (hkl) planes to assemble the 2D projections while going through a Bragg peak, hence requiring smaller time investment in scanning. The 2D projectional slices are perpendicular to the k_f vector, although a small geometrical correction is to be applied to each of the slices [135, 133].

A less-often used way to measure slices away from the center of the diffraction pattern, is by tuning the radius of the Ewald sphere by changing the energy of the incident beam very slightly. This has the effect of changing by a small amount the position of the diffraction pattern on the detector plane [135].

A crystalline sample with no strain will show an a symmetric diffraction pattern giving information about its shape and size. Any departure from an ideal crystal (see Fig.5.4) which is represented by the displacement vector field $u(\vec{r})$ will be projected onto the transfer momentum q and result in an asymmetric pattern in the reciprocal space. Robinson [55] derives an equation that allows expressing the crystal scattering contrast as an effective complex-valued electron density:

$$\rho(r) = |\rho(r)| \exp(i\Phi(r)), \tag{5.5}$$

where $|\rho(r)|$ is the physical density of the crystal and the phase shift $\Phi(r)$, resulting from the displacement field and is given by:

$$\Phi(r) = G_{hkl}.u(r), \tag{5.6}$$

where G_{hkl} , the Bragg vector for the chosen hkl reflection, is related to the lattice spacing d_{hkl} being considered. Full three-dimensional strain tensors can be obtained from the measurement of three non coplanar Bragg reflections, as later demonstrated by Newton et al. [161]. This technique gives an overwhelming advantage for investigation of nanoscale strains in nanocrystals, nanostructures, buried structures (nm to micrometer) in native states.

All the normal x-ray imaging techniques can be applied in a Bragg geometry using a zone plate to form the image, but do not provide phase information. Some techniques could, like STXM in Bragg geometry, but all these techniques are limited by the lens-resolution, ability to manufacture good lenses, and ease of use, as well as to the fact that 3D images are very hard to obtain.

Bragg CDI has been shown to work well for objects that are smaller than the

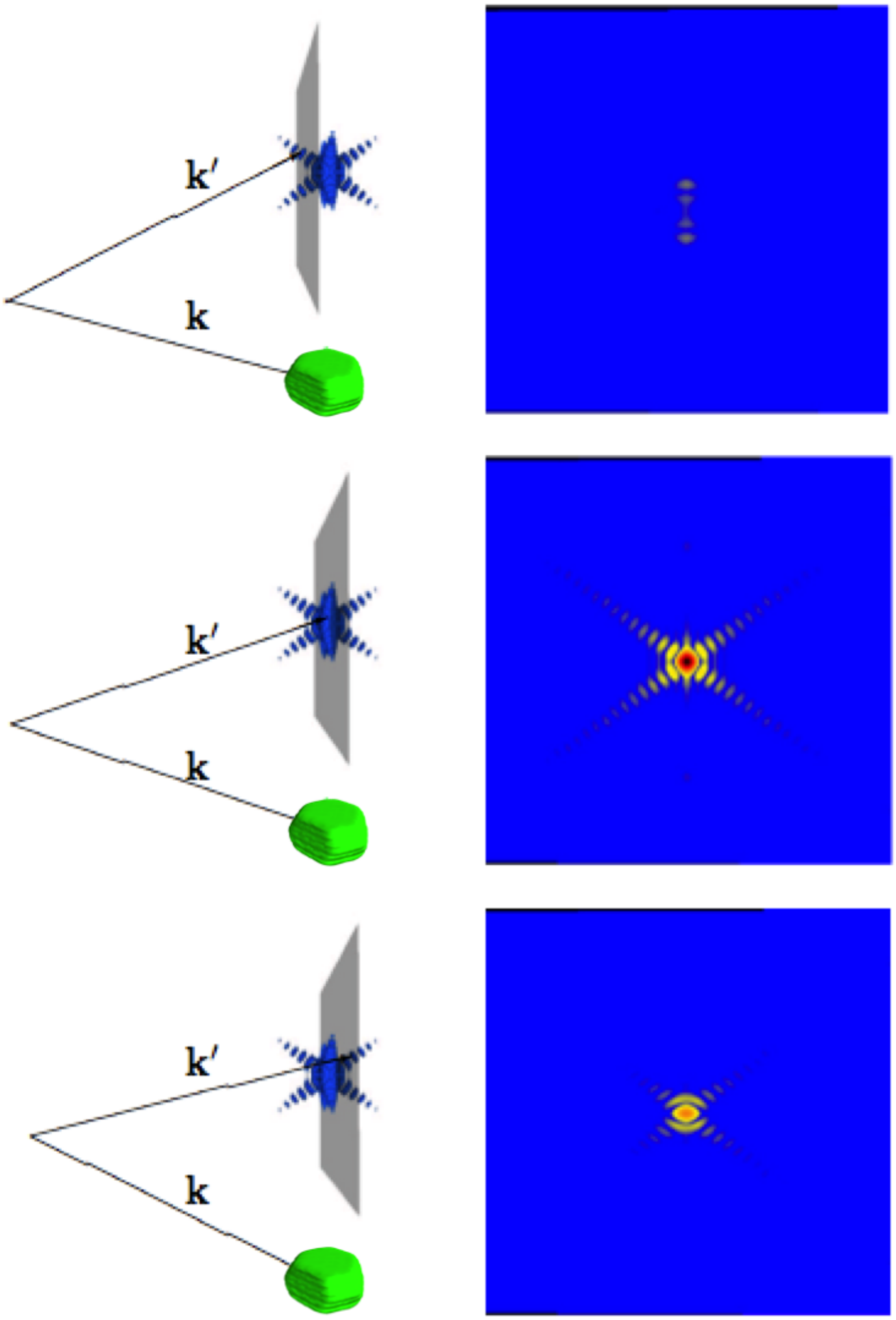

Figure 5.3: The orientation of the CXD pattern from an octahedral fcc crystal is fixed to the orientation of the crystal. Rotation of the crystal is equivalent to a rotation of the x-ray beam. A 2D detector probes slices through the CXD pattern and different slices are measured for different sample orientations. The scattered amplitude for the corresponding 2D slice is shown on the right side. Derived from [135].

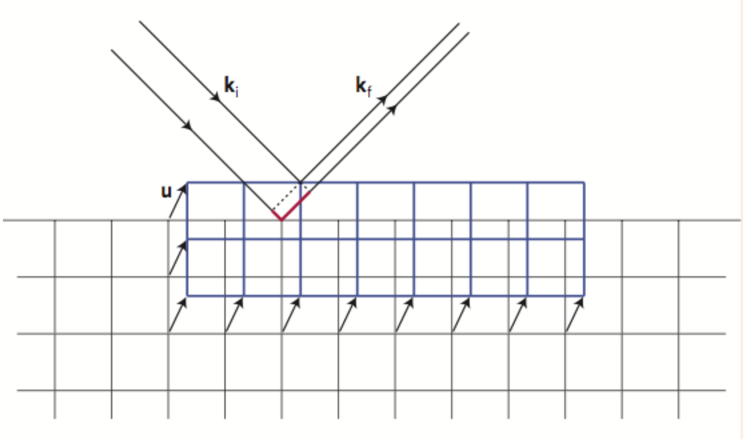

Figure 5.4: Illustration of a strained region of a crystal. A position dependent vector $u(r)$ displace a local block of material along with the phase of the scattered x-ray beams relative to that of the reference crystal by a total amount $\phi = k_f \cdot u - k_i \cdot u = Q \cdot u$. Whenever Q is set to a Bragg condition, all unit-cell corners scatter in phase, so this phase shift is manifested in the final image as a region of complex density with the same magnitude as the rest of the crystal and a phase $\phi(r)$. Caption and figure taken from [55].

beam but extended objects or structures tend to be difficult to study. This is because of the requirement that the beam coherence width should in principle be twice the lateral size of the object [162]. Highly strained objects tend to be even more difficult to study as convergence is not guaranteed, for reasons not yet fully understood [163].

Simulation studies for Test of Robustness of Conventional ER and HIO algorithms on 'highly' strained 2D objects were performed by Shi and Clark [149]. Their results show that reconstructions of a highly strained object with a quadratic phase fails, see Fig.5.5. To solve for highly strained CDI datasets (8π which corresponds to 4 phase-wraps), Shi et al. have introduced a new Guided-Phase approaches whereby knowledge of the phase structures derived from finite element calculations that are close to that of the actual objects, are used to define an allowed phase range for each pixel, thus guiding the iterative algorithm to reach data convergence [149] .

Diffractometer

To accomplish the sample orientation and detector positioning for the scattering geometry of our experiments, a 6 angles Newport kappa diffractometer is used [164], see fig.5.6. The long detector arm is necessary to achieve the desired high resolution in q space, and to support a heavy camera at a distance $>$ 2m from the center of rotation, the diffractometer has to be strong with a counterweight. To capture the outgoing Bragg diffraction in reciprocal space, the detector can be moved to arbitrary points of space by control of the δ and γ angles of the diffractometer. The

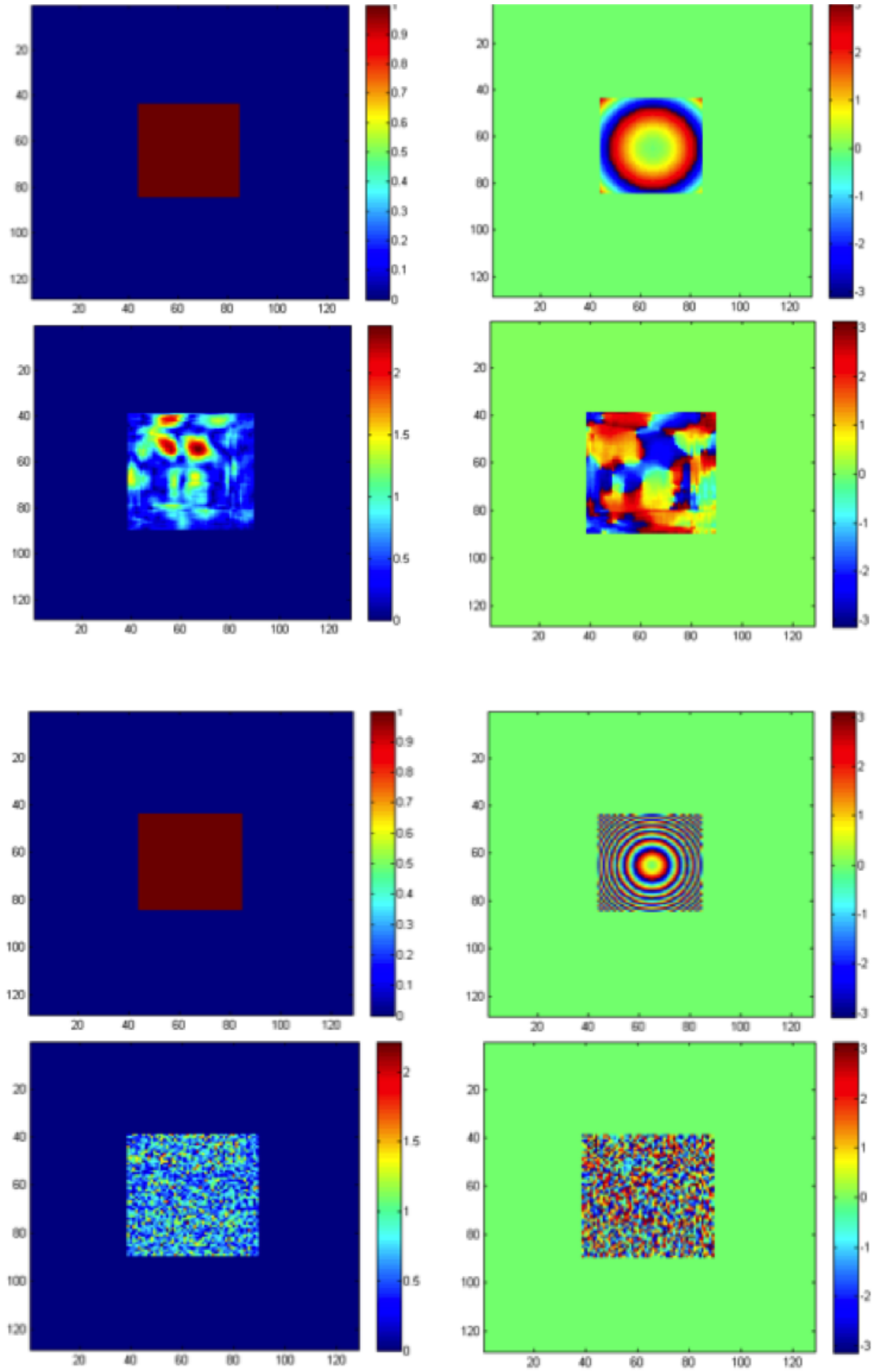

Figure 5.5: Top Panels: 2D simulations of amplitude with soft and strong phase structure (up to 5 phase wraps). Bottom Panels: Reconstructions using an alternation of ER-HIO. Courtesy of Xiaowen Shi [149].

camera distance is adjustable along an arm that is designed to hold various lengths of flight path, which are chosen for an individual experiment based on the desired resolution and field of view.

To orient the crystal to its specific Bragg reflections, the sample stage is mounted on a goniometer capable of orienting in any direction, and independently of the detector part. The precision of the angles and steps with respect to the incoming beam is high to allow oversampling in the third dimension (operated by the SPEC package). The use of a 20-micron-pixel CCD detector aims at resolving (oversampling) the fringes in the remaining dimensions.

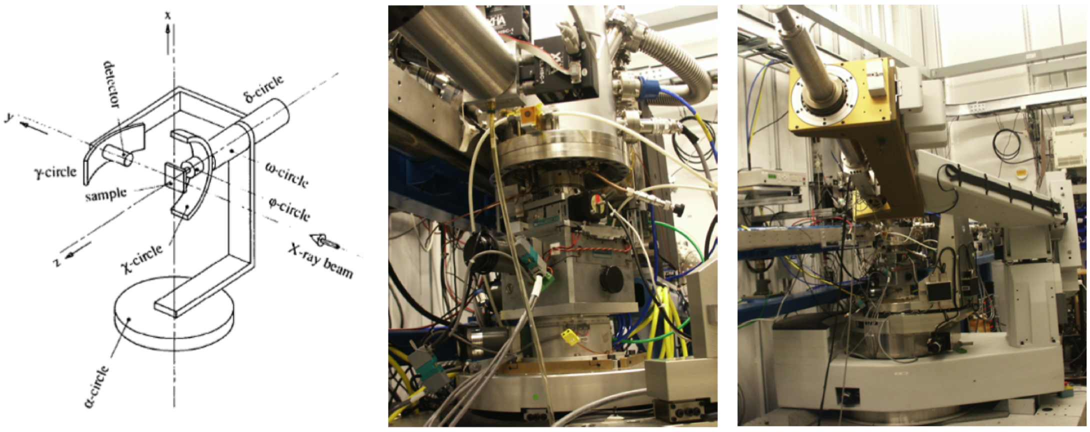

Figure 5.6: Left: A typical schematic layout of a Newport Six-Axis Kappa diffractometer (image taken from [28]). This type of diffractometer is implemented at the beamline 34-ID-C at APS. Middle: Gionometer showing altogether the θ, χ, ϕ rotation and translation stages. Right: The diffractometer arm set at a small 2θ angle and large γ angle. Derived from [133].

5.1.2 Ptychography in Bragg geometry

The limit imposed by the partial coherence and the need for concentrating the coherent beams, lead to a restriction of the specimen size to the micrometer range. Bragg ptychography comes as a solution for arbitrarily extending the field of view while keeping high resolution [73]. Huang in his 2012 paper, observed an advantage of Bragg ptychography in regards to its single-shot counterparts for ZnO crystals: improvements are seen at the image boundary where the beam can drop to a low level and prompt roughness and structural undetermination at at the edges of the crystal. Moreover, its redundant nature coupled with its better real-space constraints makes it a strong contender to overcome the problem of solving complex direct-space structures in compact or extended highly crystalline structures [149, 52]. Indeed, its robustness with regards to highly non homogeneous strain fields was evidenced by numerical analysis [73], while it was demonstrated earlier (section.5.1.1) that such problems pose a difficulty in Bragg CDI even if improvements in the technique have been made. High strain fields are to be found in a wide variety of materials like epitaxial nanocrystals, i.e, quantum dots, nanowires [73]).

The ptychographical Bragg data of crystals, presented in the following sections show encouraging results, and aim at providing subsequent developments for 3D atomic displacement fields and surface science.

Bragg geometry considerations

The Bragg scattering geometry calls for a correction of the scan positions as the apparent movement of the sample is no longer equivalent (or co-linear) with the detector. Indeed, the sample is now at an angle to the detector, and the overlap must be adjusted so that the Fourier constraint which is applied at the detector plane, keeps enforcing the consistency between the views. Thus, for computational reconstructions, a set of matrices is introduced that account for the sample angles (ϕ, χ, θ) and diffractometer angles (δ, γ). First, a translation of the scan positions to the laboratory is prepared with:

$$\begin{pmatrix} x \\ y \\ z \end{pmatrix}_{lab} = M^{-1}\theta M^{-1}\chi M^{-1}\phi \begin{pmatrix} x \\ y \\ z \end{pmatrix}_{samp} , \tag{5.7}$$

and using the following sequence of rotation matrices, as rotations are in general non commutative:

$$\begin{pmatrix} 1 & 0 & 0 \\ 0 & \cos(\theta) & sin(\theta) \\ 0 & -\sin(\theta) & \cos(\theta) \end{pmatrix} \begin{pmatrix} \cos(\chi) & \sin(\chi) & 0 \\ -\sin(\chi) & \cos(\chi) & 0 \\ 0 & 1 & 1 \end{pmatrix} \begin{pmatrix} \cos(\phi) & 0 & \sin(\phi) \\ 0 & 1 & 0 \\ -\sin(\phi) & 0 & \cos(\phi) \end{pmatrix}, \tag{5.8}$$

finally, the coordinates are further transformed from the laboratory to the detector:

$$\begin{pmatrix} x \\ y \\ z \end{pmatrix}_{det} = M\delta M\gamma \begin{pmatrix} x \\ y \\ z \end{pmatrix}_{lab} , \tag{5.9}$$

$$\begin{pmatrix} x \\ y \\ z \end{pmatrix}_{lab} = \begin{pmatrix} 1 & 0 & 0 \\ 0 & \cos(\delta) & \sin(\delta) \\ 0 & -\sin(\delta) & \cos(\delta) \end{pmatrix} \begin{pmatrix} \cos(\gamma) & 0 & \sin(\gamma) \\ 0 & 1 & 0 \\ -\sin(\gamma) & 0 & \cos(\gamma) \end{pmatrix} \begin{pmatrix} x \\ y \\ z \end{pmatrix}_{samp} . \tag{5.10}$$

The approach reported here, is well described in Richard Bean's PhD Thesis [52], with the corresponding Matlab code given in its annex part.

5.1.3 Ptychography on gold nanocrystals

Experiments at SLS

Gold nanocrystals (using Bragg CDI) have been the subject of intense study from Robinson's group [157]. The experiment reported here, which took place in February 2011, was in fact the first demonstration of ptychography adapted to Bragg geometry. The primary aim of the beamtime, however had been to record diffraction patterns while slightly rocking the sample and use X-ray ptychography in the forward direction to look at the change in effective density when the Bragg peak is excited. Upon exciting a Bragg condition, the phase shift changes and gives a detectable contrast change in the forward 'hologram' part of the diffraction pattern. Maria Civita [45] was able to measure the phase shift inside the crystals between the different rocking conditions and compare results with dynamical theory [165]

As a second detector was placed at the Bragg angle, to collect reflection intensities during the rocking curve, the possibility to image the crystal by performing Bragg-ptychography through the matrices described earlier (Eq.5.9-5.7) was granted.

The following experiment was not conducted at 34-ID-C APS but at the dedicated coherent small angle X-ray scattering (cSAXS) beamline at the Swiss Light Source, Paul Scherrer Institute. The apparatus used for ptychography is similar to the APS set-up where a FZP was used to focus the beam (section 4.2.1), to the exception that the Pilatus detector was placed at 7.2 m due to larger pixel size ($172 \times 172 \mu$m). The set-up is well described in Maria Civita's transfer report [45].

The FZP outermost zone width (100nm) sets the focus size, which is smaller than the crystal. The estimation done by analyzing the reconstructed probe profile

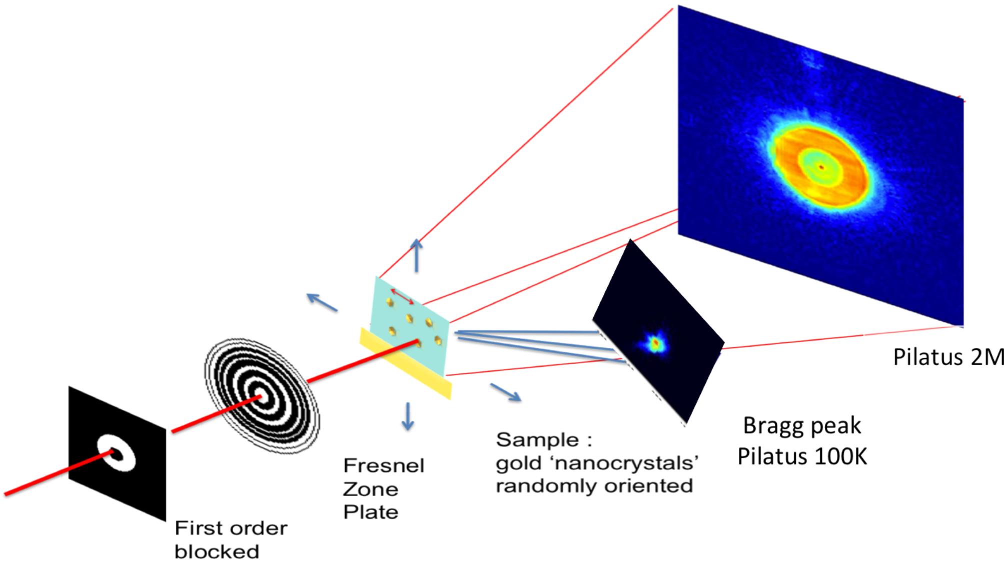

Figure 5.7: Schematic of the experiment made at SLS where it can clearly be seen that the two detectors collect the transmitted beam (Pilatus 2M) and the reflected beam at Bragg angle (Pilatus 100k) from the (111) diffraction planes. From left to right: the coherent beam goes first through a pinhole with a central part made to block the central part of the beam. Focusing optics: a high-efficiency Fresnel zone plate we used a 1mm thick gold FZP with 75 μm diameter and 100 nm finest zone width which produces a focal spot of about 100 nm. An Order Sorting Aperture has been placed between the FZP and the sample to block the higher harmonics generated by the binary phase plate. The sample is centered in the beam waist of the illumination where the phase front has no curvature. Experiment preformed in collaboration with Civita [45].

gives a beam size of around 110 nm (FWHM) with pixel size of 31nm, which is then consistent with expectation. The Bragg angle for Au nano-crystals is found at 17.65° for the (-111) plane. Once a crystal was 'picked' (xy plane scan), the exact Bragg condition was found based on the highest intensity of the spots recorded with a PILATUS 100k detector. The latter was inclined at 35 degree with respect to the axis of beam propagation z and at a distance of 1.03 m with respect to the sample. The reconstructed image of an isolated gold nanocrystal grown on thin Silicon membrane was obtained and analysed (Fig.5.9), which confirm the dimensions found from an SEM image: lateral dimension of 250nm and thickness of 150nm.

The ptychographic reconstruction shown in the lowest part of Fig.5.8, was performed on the dataset recorded at the Bragg condition. Maria Civita went further in her transfer report [45], by analysing each of the datasets collected off-Bragg, to report that the ptychographic reconstructions were only viable for those recorded in the proximity of the Bragg condition. This is explained by the weak intensity recorded off-Bragg, thus preventing correct Fourier inversion. These results have an interesting outcome: they suggest that the tomographic techniques would not work for the Bragg geometry, whereas assembling the 3D diffraction at each point and performing direct 3D FFT during ptychographic reconstructions, should lead to a full reconstruction of the 3D shape of the crystal; this has been performed by Godard in [95] and by Huang [138]. For stability reasons, it is also suggested to rock the crystal at each position of the ptychographic scan instead of performing a full scan for each of the rocking curve angles.

This small excursion primarily aims at demonstrating the sensitivity of ptychography to the shape of nano-crystals (see Fig.5.8), but also to highlight that besides the high performances of the c-SAXS beamline, the success of the Bragg reconstruction is most likely due to a beam focused on a vastly smaller scale than the object. The change in the reconstructed crystal density from transmission to Bragg conditions is studied in the ongoing thesis of Maria Civita, UCL. The main interest of the Bragg-ptychography, which is the mapping of strain pattern in nano and micro crystals is investigated in the following sections.

Experiments at APS

Another experiment on gold nanocrystals was conducted at APS 34-ID-C beamline. The nano-crystals were formed by annealing of a film of 20 nm of Au, grown epitaxially on a SiN membrane. Ptychographic data were collected at a distance of 0.7 m with a Medipix detector, set at an angle of $\gamma = 34°$. A Round-ROI scan of $2 \times 2\mu$m, with radial steps of 100 nm gave 360 scan points with 30s accumulation

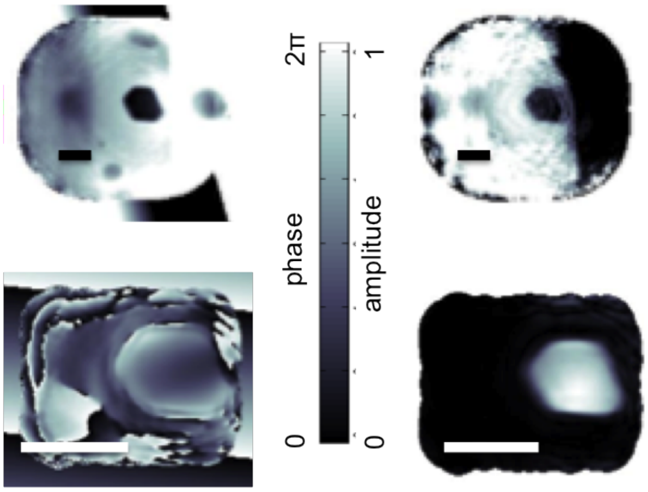

Figure 5.8: Top: Reconstructed phase (l) and amplitude (r) of a gold nanocrystal in the transmission geometry. Bottom: Reconstructed phase (l) and amplitude (r) of a gold nanocrystal in the reflection geometry. Work done in collaboration with Maria Civita [45]. Scale bars, 250nm.

for each measurement collected. Setting the slits opening $30_h \times 60_v \mu$m, produced a KB focused beam of dimensions 900 × 900nm, and a large 88% overlap.

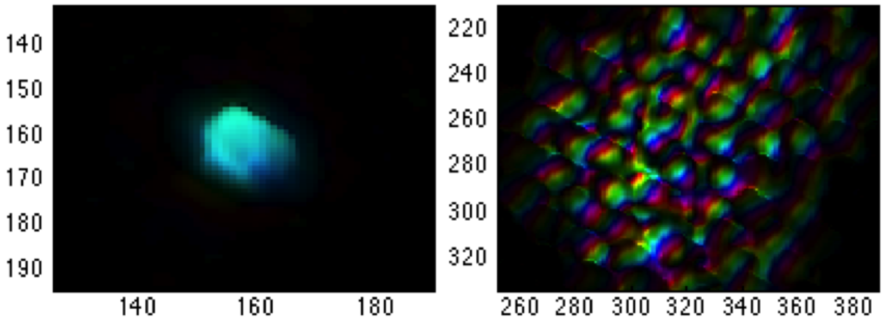

Figure 5.9: Unsuccessful ptychographic reconstruction of a gold nano-crystal.

The reconstruction displayed in Fig.5.9 possibly shows a crystal (in the probe window), while the object presents a collection of small crystals not overlapping. This is explained by the fact the crystal is of comparable size with the scan steps (the crystal size was calculated from the extent of reciprocal fringes, using $\lambda z/N_f \Delta_p$). While the shape and size of the reconstructed crystal can be trusted, its phase realization can not, considering that is an average from many non connected Fourier inversions.

It was then realised from this experiment, that it was the object that was scanning the extents of the probe $p(\mathbf{r})$, and consequently the overlap calculated based on the object dimensions. Manuel Guizar in his 2010 thesis, through a simple numerical simulation, concluded that the advantages of translation diversity are maintained even when the object is contained within the probe. Surprisingly, his ptychographic reconstruction had translation steps comparable to the extent of the object (deduced from five circles drawn around the small simulated object, representing the five positions of the large pupil illumination used in his simulations). To mitigate the findings, numerical simulations follow.

5.1.4 Simulations: crystal contained within the beam

One of the most important criteria in ptychography is the relative strength of the illumination overlap (in principle > 50 %). It was realised during the last experiment described, that for a small sample contained within the beam, it is the object that scan the extents of the probe $p(\mathbf{r})$, and as consequence the overlap should be calculated based on the object dimensions (see Fig.5.10). The objects chosen for the following numerical experiments are derived from the crystal presented in simulation of section 3.4.2. In fact, three sizes were used here, in order to study the relation object-probe size in ptychographic reconstructions. Varying the crystal dimensions was preferred over those of the illumination (see Fig.5.11).

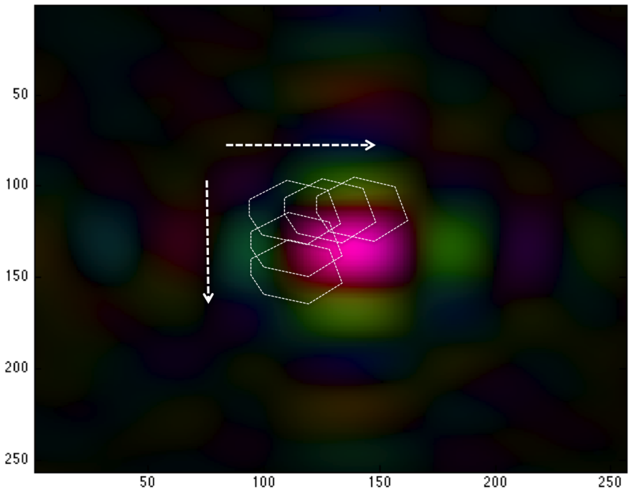

Figure 5.10: Illustration of a crystal scanning the extent of the complex illumination function.

The simulation parameters for the ptychographic simulations (commensurate with the usual experimental conditions at APS), are summarized in the table below.

Properties	Value	unit
Energy	9	KeV
Array size	256	pixels
λ	1.4	A
beam size	$\sim 800(H) \times 800(V)$	nm
detector distance, L	2	m
pixel size	20	μm
pixel resolution	13	nm
scan range	5x5	μm
step size	$150 \mapsto 450$	nm
Number of positions	$440 \mapsto 30$	

The scan range of $5 \times 5\mu$m was chosen so that the crystals would cover the full extent of the illumination pattern but in reality, it should only cover the central spot, where full coherence is guaranteed. The overlap relationship for the three different step sizes used, from both the point of view of the probe and objects are resumed in the table below.

scan steps size	150	250	350	nm
Overlap probe	81	68	56	%
Overlap crystal 400 nm	62	37	12	%
Overlap crystal 600 nm	76	61	46	%
Overlap crystal 900 nm	83	72	61	%

Figures. 5.12 - 5.14 show the reconstructions after 200 iterations of DM. If the model probe is allowed to float from the few first iterations, an exchange between probe and object is observed. As expected, for the smallest crystal, a 50 % overlap from the point of view of the probe gives bad reconstructions as it represents only a 12% crystal overlap. The simulated 600 nm crystal presented superior reconstruction (Fig.5.13) in comparison to the 900 nm one for a same crystal overlap of 61% but which presented a lower probe overlap (Fig.5.14) and indicates that both the crystal and probe overlaps should be kept high. Thus, to meet the requirement for future ptychographical experiments on nano-crystals at beamline 34-ID-C of APS, the KB mirror system should be replaced by a FZP.

5.1.5 Zeolite micro-crystal

Ptychographic measurements were performed on zeolite micro-crystals at beamline 34-ID-C of APS, in the frame of a collaboration with the Group of Professor Kim [163, 166]. Zeolites are a crystalline aluminosilicate minerals nurturing a network of well-defined 0.3-1.5 nm wide pores [163], and which serve as catalysts, sorbents,

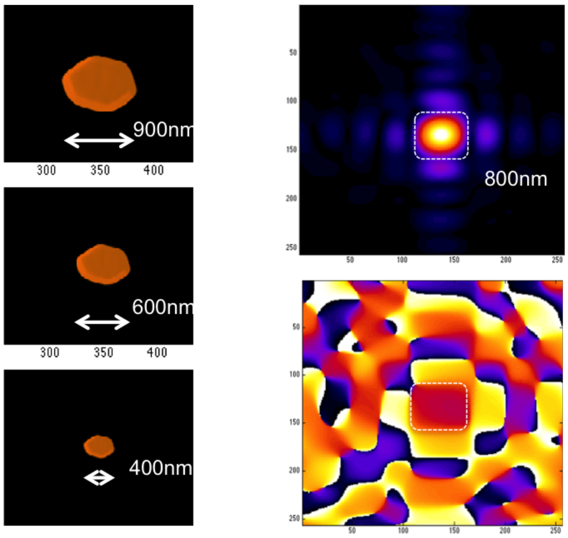

Figure 5.11: Left: Simulated crystals of 900, 600 and 400 nm mean size. Right: Amplitude and phase of a typical KB probe at APS.

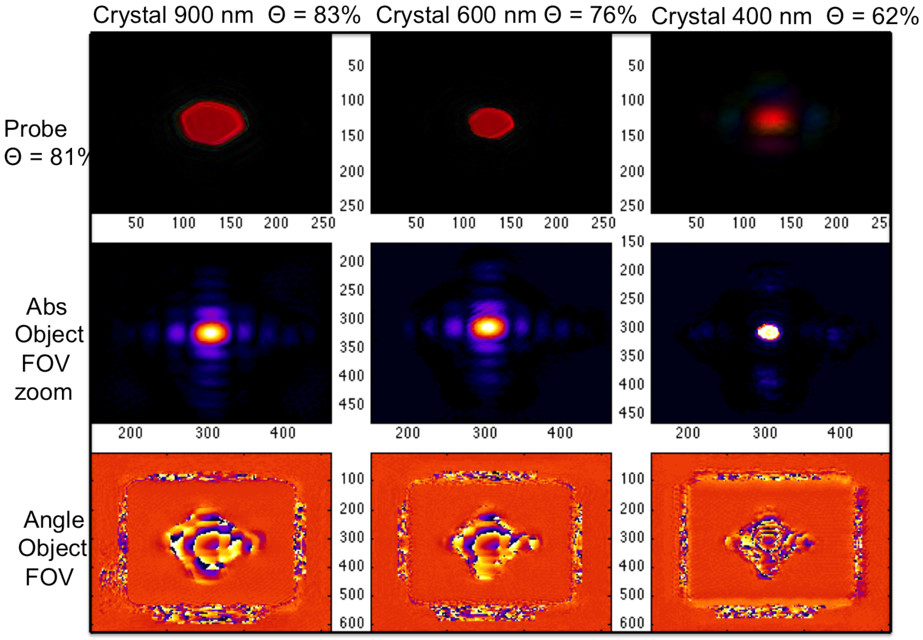

Figure 5.12: Top row: reconstructed crystals for a simulated scan with radial steps of 150 nm found in the probe window. Middle row: reconstructed probes (modulus) for the three different simulated crystals respectively (found in the object part). Lower row: reconstructed probes (phase) for the three different simulated crystals respectively (found in the object part).

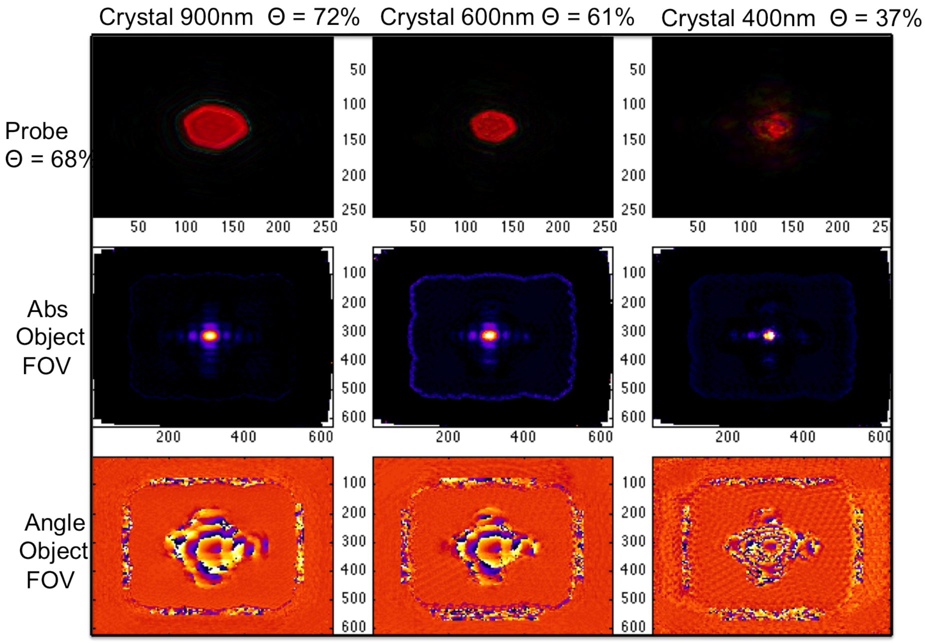

Figure 5.13: Top row: reconstructed crystals for a simulated scan with radial steps of 250 nm found in the probe window. Middle row: reconstructed probes (modulus) for the three different simulated crystals respectively (found in the object part). Lower row: reconstructed probes (phase) for the three different simulated crystals respectively (found in the object part).

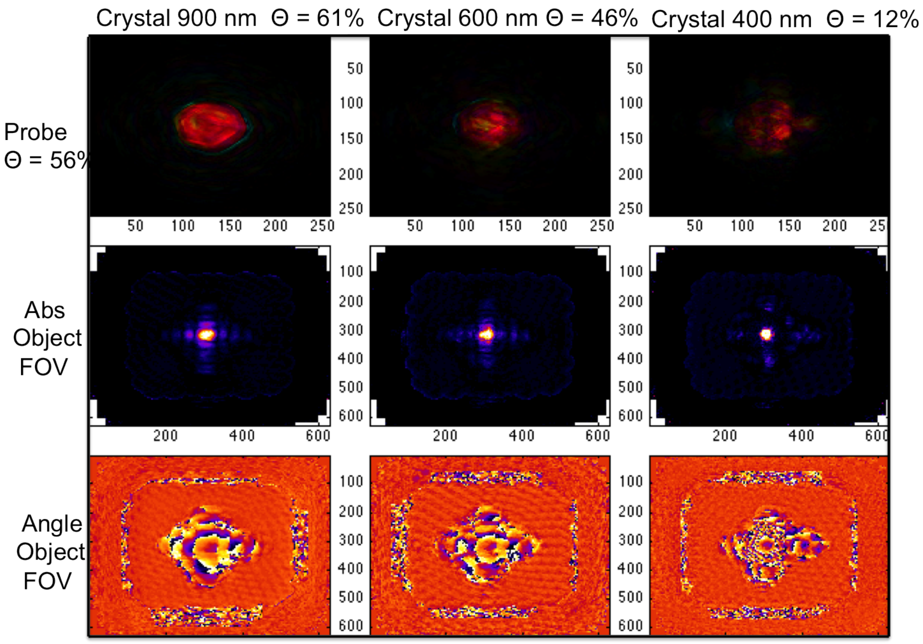

Figure 5.14: Top row: reconstructed crystals for a simulated scan with radial steps of 350 nm found in the probe window. Middle row: reconstructed probes (modulus) for the three different simulated crystals respectively (found in the object part). Lower row: reconstructed probes (phase) for the three different simulated crystals respectively (found in the object part).

and ion exchangers [167]. Their industrial application requires the attachment of the crystals on the substrate followed by a calcination, to finish the synthesis and removal of organic residues. These two operations involve thermal processing during which the crystals undergo a certain degree of distortion, due to complex temperature-dependent anisotropic thermal expansion coefficients [168], and results in the alteration of zeolite efficiencies.

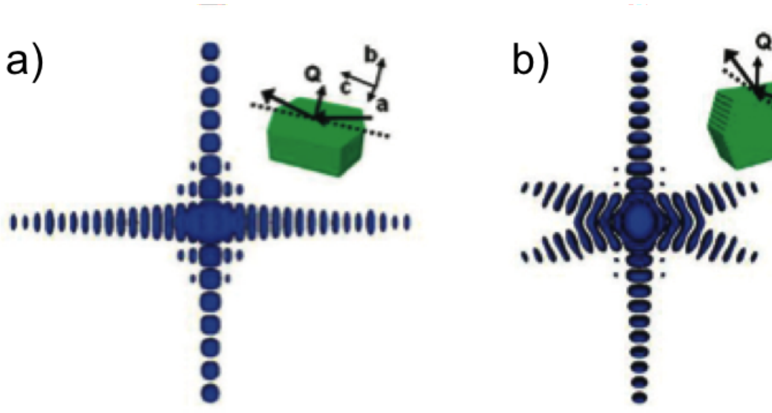

Figure 5.15: Simulated 3D coherent diffraction patterns for an idealised ZSM-5 crystal with wave-vector transfer shown for $Q \parallel b$ (020) and $Q \parallel a$ (200). Figure and caption taken from [163].

The group of Professor Kim [163, 166] explored the characteristic distortion modes that arises from the thermal process using Bragg x-ray CDI, but their main problem was a limitation of the real-space phase to the range $[-\pi/2, \pi/2]$ (which corresponds to a displacement of half the lattice spacing), above which the reconstruction of a crystal is subject to failure. Thereby, a ptychographic test experiment was conducted on one of their synthesized zeolite crystal (ZSM-5), with dimension $1.9 \times 0.8 \times 2.7 \mu m^3$ and lattice constants of 20.02, 19.09 and 13.38 A along the a,b and c axes. The sample was attached on a Si membrane and calcinated at 450 C for 15h. Coherent x-ray photons of 9 keV, and a small angle of four degrees were employed to measure a Bragg peak from the (020) reflection (geometry reported in Fig. 5.15 (b)). To satisfy the ptychographical requirements, a collection of 141 Bragg peaks were collected by mean of a Round-Roi scan of $5 \times 5 \mu$m with radial steps of 0.5μm.

The single projection Bragg ptychographic measurement (no rocking curve) shows successful reconstruction of the phase within the range $[-\pi, \pi]$, Fig.5.16, exceeding by far the limitations of the ER-HIO alternation used in classical CDI. The strain mainly appears at the boundary, a fact explained by a core-shell differential thermal gradient provoked by the organic template leaving fewer residues than the core after the calcination process.

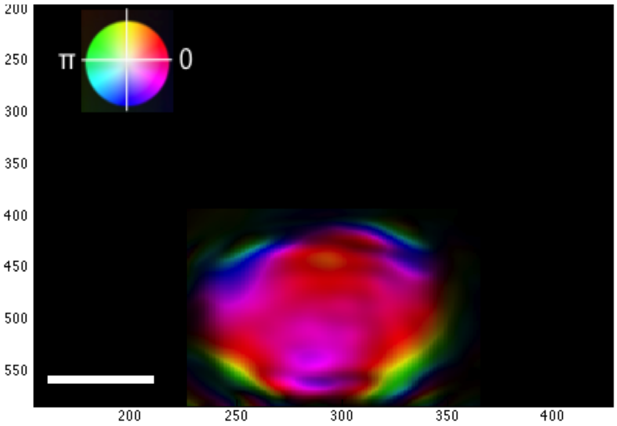

Figure 5.16: Ptychographic reconstruction of zeolite micro-crystal, shown in hue color. Scale bar, 1μm.

As these results gave confidence in the method, similar measurements were performed on metal containing Zeolites Cu-ZSM5. These zeolites have a great potential for the catalysis of many reactions, for example the direct partial oxidation of methane to oxygenates or the conversion of benzene to phenol. As it is known [169], the catalysis takes place inside the zeolite channel and not at the outer surface of the crystal but only a small region of the catalyst particle below the surface is found to be active. This is either because of the limited reactant-gas penetration into the zeolite or the distribution of active copper sites within the crystal. The latter distribution can be mapped by ptychography in small-angle Bragg geometry and potentially lead to improvement of the catalytic efficiency of the Cu-ZSM5 zeolite by identifying the limiting process. Measurements at different times were performed, to ascertain the time dependance of the copper diffusion process. The copper was introduced into the zeolite by ion exchange with a drop of an aqueous copper solutions on the sample. As the diffusion takes place over a 24h time period, the time dependence of the diffusion was mapped by 2h intervals (scan time, 1h). The crystals had a (020) orientation, and thereby 'lying down' on the substrate, presented a similar condition to the one described in section 5.1.3; in which the scanning KB probe was larger than the crystal. Even though the KB focus ($1 \times 1\mu$m) was only slightly larger than the crystal height (0.8μm), this condition prevented successful reconstructions. A fact not well understood at the time of measurements, but highlighted from the simulations of the previous section. It is then advised to use the smaller focus of an FZP for future experiments on nano-crystals at beamline 34 ID-C of APS.

5.2 Bragg projection ptychography of domains in metal thin films

Ptychography for transmission scattering experiments is now well established, however, its realisation in reflection is still under intense development due to complicities of experimental geometries and high quality data that is needed for reconstructions. Bragg ptychography in reflection geometry already been used for imaging of surfaces in thin films, local polarization in ferroelectric thin films [170], lattice distortions and out-of-plane dilatation in semiconductor heterostructures [171], although its implications in nano-structural physics could be far more important. Reflection geometry CDI combined with holography has been recently demonstrated for test samples [172] and will be a complementary method for imaging of surfaces in thin films, buried interfaces in magnetic multilayers, field effect transistors (but does map the strain field, which is the relevant quantity to engineer strain for implementation of new generation semiconductor [173, 149].

3D nanoscale imaging is appealing, but it involves scanning the same area from a number of viewpoints and results in more complex experiments with longer data acquisition times that even with state-of-the-art setups lead to unavoidable positional drifts. The definition of a rotation centre in Bragg experimental setups considered for extended samples can also be problematic [52]. Moreover, the lack of diversity in the direction of the beam propagation brings a supplementary difficulty in providing an appropriate support for the 3D phase-retrieval algorithms [52]. Although, with some *a priori* structural knowledge, recently developed regularization techniques [174] can compensate for the detrimental sparsity of the 3D data set and provide a full 3D quantitative map of strain.

To overcome these problems, we select 'grown-in' thin film samples presenting a 'quasi' three dimensional structure and develop Bragg projection ptychography (BPP) [170] to exploit the use of traditional 2D ptychographic algorithms.

One layer of domains within the information depth means that the three dimensional diffraction volume can be approximated as constant and thus, a single cut through the 3D diffraction volume will result in a valid reconstruction. An alternative selection of cuts through the diffraction volume will result in reconstructions with different projection through the '2D extruded' or columnar structure.

Up to now, the few investigations carried out on the structure of thin films with coherent X-ray diffraction support based methods have failed to be conclusive [175, 52]. On one hand, it could be attributed to the difficulty in providing a complete formulation of a real-space support to domains that naturally extends over the whole crystal surface, and so BPP comes in an obvious solution owing to its ability to disentangle an illumination function (the support) from the extended structural features (the sample). On the other hand it could be attributed to the difficulty in phasing the 'densely' speckled pattern and again, the intimate relation between the diffracting features in the thin film and the observed scattering can be retrieved owing to the redundant approach of ptychography. Bragg diffraction patterns in this experimental geometry encode not only structural information about the shape of the illuminated region on the sample but its lattice perturbations.

Richard bean in his thesis work [52], attempted to reconstruct thin films with Bragg ptychography and did result in produced images of phase structures of an appropriate scale, but the phase and amplitude structure of the reconstructed sample and illumination were inconsistent from run to run. The reported reason for the convergence failures were most likely down to combination of experimental and analytical factors and concluded that despite the apparent robustness of the method, further experiments will require much greater knowledge of the experimental regime, as well as exceptional control and stability. However, his thesis work did indeed pave the way for the set of experiments presented here, and thus constitutes a valuable guide for the further work on improving experimental set-up, scanning method and *a posteriori* refinement methods developed for this thesis.

In the following sections, detailed investigations of a 'grown-in' domain structure in a metal thin film (niobium) prepared by molecular beam epitaxy (MBE) is described. The experiment was completed at APS using the experimental setup described (and 'characterised') in chapter 4 at beamline 34-ID-C.

When phase retrieval is successfully performed, reconstruction of Bragg reflection geometry ptychography should present a real-space phase image of the thin film with nano-scale regions of constant phase corresponding to niobium lattice that have formed a domain structure (to minimize elastic strain). Antiphase type structures are not expected because these nanoscale regions are interrupted by areas where misfit dislocations have caused a shift in the crystal lattice which is not an integral multiple of the Nb lattice spacing.

5.2.1 Introduction to thin films

Thin films grown epitaxially are of importance in many areas of technology and have been developed as a valuable route for the synthesis of elementary building blocks for electronic and nanotechnology [2]. Indeed, these buffer layers or templates of high crystalline quality act as precursor for the growth of other metal thin films and

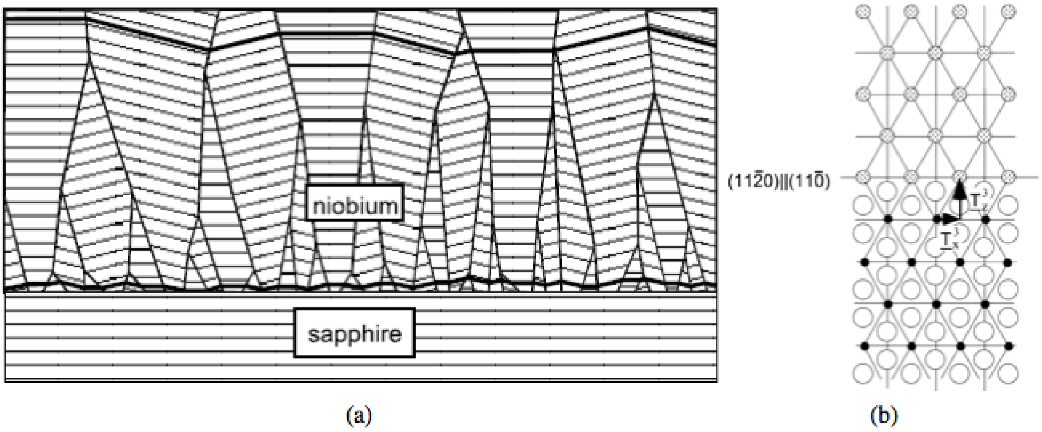

Figure 5.17: Model of the Nb(110) Sapphire(1120) interface

superlattices of rare earth and transition metals. High quality epitaxy is owed to MBE whereas a lower structural quality was obtained by earlier researchers using sputtering.

A classical and important case among these is Nb on sapphire which form films of exquisite crystalline quality. Nb can be epitaxially deposited onto onto a different number of ceramic materials (MgO, GaAs, InAs) but the pair Nb/Sapphire is singled out for its quality, and is consequently the most 'heavily' studied system, with a variety of technique including X-ray diffraction, RHEED and TEM aiming at understanding (and possibly optimising) the defect structure and accompanying strain introduced by lattice mismatch.

But this system also warrants careful and extensive studies because it a useful model system of metal-ceramic interface, commonly seen in engineering applications, where the effect of the microscopic structure of the interface and film on the material properties is important. (Recent research interest has focussed on a superconducting phase found in very thin film Nb on Sapphire films [176].)

The true structure of these systems is broadly complex but common observations show that above the critical thickness for an epitaxial system [177], the unavoidable lattice mismatch between the film and substrate gives rise to elastic strain that is relaxed by misfit dislocations which are observed to form at or near the metal-ceramic interface in the case of Nb-Saphhire [178].

X-ray studies performed in specular reflection have shown rocking curves with a two component lineshape with a broad and sharp features for Niobium thin films up to 500 nm. Wildes [2] gathers and consolidates much of the previous research efforts on this system in his 2001 review, with lengthy discussion about the nature and distribution of misfit dislocations, however its conclusion reports that the nature of these dislocations is somewhat unclear and that no full model for the morphology has been currently found. Only results that are relevant to imaging the mosaicity are restated here.

Domains with lateral broadening and small rotational disorder is a possible model to explain the sharpening of the broad feature in the scattering [2], as seen in Fig.5.17. (The broad component of the scattering would be then explained by the reciprocal of the average domain size). It was therefore considered that a two component profile is characteristic of many epitaxial systems for which there is a lattice mismatch between the film and substrate. This profile is also found on an other quantitative model [177].

Niobium films have been found to be versatile thanks to their ability to grow on sapphire substrates of various surface orientations with an identical three dimensional epitaxial relationship. However, the sapphire substrate surface properties defines the epitaxy of the niobium.

The crystalline structure of niobium is body centred cubic lattice with a lattice parameter of 0.3301 nm, see Fig.5.18. Sapphire is a close match to niobium with a rhombohedral lattice that presents very similar dimensions to Nb b.c.c unit cell of one of the Al sublattices with an angle of $\alpha = 85.7$ and unit cell length $a = 0.350$nm.

The most classic orientation used for the growth of NB on Sapphire (for X-ray studies especially) is Nb(110) on Al_2O_3(1120). A schematic of a proposed interface model for this orientation is shown in Fig. 5.18.

The substrate surface is often stepped due to slight miscut whereby producing steps that facilitate nucleation and layer by layer Frank-van der Merwe type growth of niobium. Flynn propose a step flow model to explain metallic multilayer growth [178]. The step height on one of these viscinal surfaces is incommensurate with spacing of the Nb lattice planes and provides possible nucleation sites for misfit dislocations [177]. Thus, a coherent growth between these dislocations is a possible mechanism to produce domains. As the shift between the domains would exhibit non integer values of the niobium lattice spacing, the difference in scattering from these regions should be revealed from the high phase-contrast mechanism provided by Bragg projection ptychography.

[1]

---

[1] The sample used for experiments presented here is the classic Nb(110) on Al_2O_3(1120) orientation with a thickness of 1000 A . The temperature of the substrate at growth was 900 ° C. The film was grown by K. Ritley in the laboratory of C. P. Flynn at the university of Illinois, Urbana-Champaign.

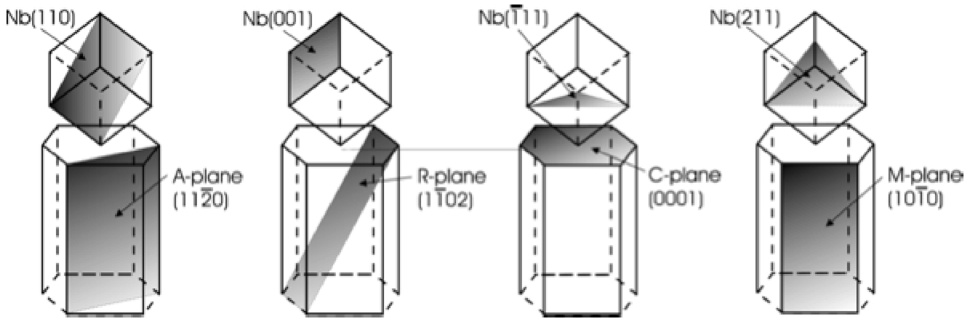

Figure 5.18: Three-dimensional epitaxial relationship between Nb and Al2O3, shown for the different substrate orientations. Figure and caption taken from [2].

5.2.2 Bragg projections

To illustrate the following discussion, a schematic cross section of a focused X-ray beam intersecting at an incident angle corresponding to the Bragg condition of a crystalline thin film is given in Fig. 5.19, together with diffraction vectors corresponding to the specular geometry and idealized k_f projected focused beam.

The general sample projection principle and formalism to describe Bragg diffraction has been established elsewhere [55]. In Bragg diffraction, the far-field 2D coherent diffraction pattern measured at the Bragg condition of a locally illuminated crystal is the Fourier transform of the projection of the crystalline volume along the exit wave vector k_f. Thus, Bragg projection ptychography propose to exploit the 2D Fourier correspondence between Bragg diffraction and the projected thin film illumination function [170]. The most critical operation is then to understand how to enforce the consistency between Bragg diffraction patterns and the projected overlapping sample positions. In previous experiments performed on thin films [52], the ptychographical scans were realised in the plane of the sample surface, and the relationship between the displacements and their resulting projection in the detector plane later adjusted by a set of matrices (Eq.5.9-5.7) during ptychographic reconstructions. In order to remain independant of the Bragg angle and keep symmetric overlap, laboratory frame scans were prefered. In this manner, displacement magnitudes in the reconstruction plane are equivalent to those of the scan, as established by Hruszkewycz in [170]. Thus, in the selected coordinate system of Fig. 5.19, the scan is performed by moving the sample in the xy plane as in transmission (a stationary sample with a moving beam is equivalent). x (out of plane) being common to all projection planes in the specular case, there is hopefully no ambiguity about the displacements or direction of the movements. A movement of the sample along the y direction vector from position a” to b” changes the illumination projection vector into the k_f normal plane by $\overrightarrow{a'b'}$ a mirror reflection about the sample surface; leaving the magnitude unchanged for the ptychographic phasing. However, for more complex Bragg geometries where x and x” do not coincide and the resulting projected beam is dramatically more complex and is not treated here.

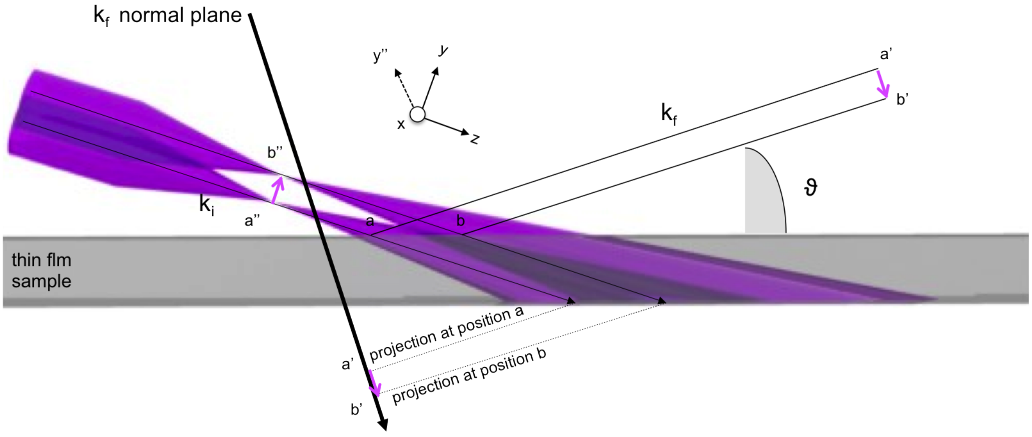

Figure 5.19: Schematic of Bragg projection on a idealised niobium thin film presenting only one layer of structural domain. By performing laboratory scans, the projected overlap after the beam displacement is symmetric and of equal magnitudes within the detector plane ($|a'b'| = -|a''b''|$) for the specular case. Figure and caption derived from [170].

5.2.3 Simulations on domain structure

To help experimental data analyses, simulations are performed on a phase structured domain system with no absorption contrast. The goal is to assess the possibility of convergence of pure phase structure, but also to test parameters for situations which may be encountered in an experiment such as global uncertainty on scan positions and fluctuations in illumination. As the amount of expected phase contrast is not known for the majority of systems, except from those with anti-phase domain like found in the bi-metallic alloy FeAl or Cu_3Au and which is one of the main focuses of Bragg-ptychography; the simulated domain structure is of anti-phase type. However, the key for numerical studies of niobium on sapphire would be a simulated phase structure that mimics the real sample structure used in experiments, i.e., block structure of mosaic domains with different phase shifts relative to each other with added phase ramps due to slightly rotated domains (model in Fig.5.17). The relative phase of each block is determined by its position relative to its neighbours (on some ideal lattice). While the experimentally reconstructed images in Fig.5.38

agree with this model, they are not perfectly unique from run to run and better modelling would help discriminate the relative phase shifts and rotational disorders from remaining global phase ramps and offsets; that were difficult to remove (section.5.2.6). To design a pattern of equally populated region of 0 and π phase (or equivalently $-\pi/2$ and $\pi/2$, the procedure to produce the phase diversity found in section.4.3.1 and illustrated in [52], is recalled. Then, binarization of the smooth array is realised by assigning a value of π to regions higher than $\pi/2$ and 0 to regions presenting lower values. The average size of the phase-only areas is set by the size of the Gaussian kernel used, here 10 pixels. Finally, a complex valued array is produced using the relation $c = \exp(i\phi)$, which leaves a constant amplitude of one everywhere. Parameters used to generate the simulated data are a realistic match to experimental parameters. Specific parameters for the algorithm are included in table. 5.1 and results from simulations are split into parts based on the parameter under investigation.

Properties	Value	unit
Energy	9	KeV
Array size	256	pixels
λ	1.4	Å
beam size	$\sim 1.5(H) \times 1.5(V)$	μm
detector distance, z	1.5	m
detector pixel size	20	μm
pixel resolution	27	nm
scan range	10x10	μm
step size	0.3	μm
Number of positions	300	

Table 5.1: Parameters for the ptychography simulations on a two-phase domains system.

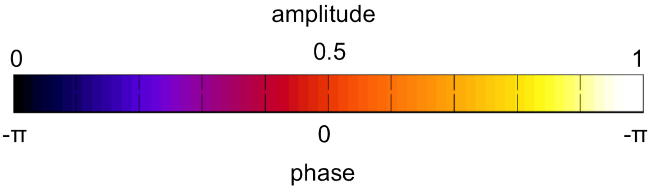

Figure 5.20: The results for this chapter are displayed with a (fire) colour scale. The same black to violet scale is used for the normalised amplitude (from $0 \rightarrow 1$), and for the phase values that range from $(-\pi \rightarrow \pi)$.

To accommodate different ptychographic scan sizes (or fields of view) and also to have the illuminated area defined only by the footprint of the scanning illumination, the phase structure extends up to the edge of the array (see Fig.5.21. The probe used for the simulation is designed based on experimental reconstruction from a pair of KB mirrors at APS.

If the beam were to be nano-sized, calculating the projection of its complex function as a function of incidence angle and thin film thickness for the Bragg condition would be critical. This arises from the fact that the high aspect ratio of the illuminated volume blurs its edges once the local illumination is projected on the k_f vector and changes substantially the illumination function [170]. For a beam approaching micron size and for a thin film thickness $<$ 100 nm, the aspect ratio of the illuminated volume is low and can be ideally approximated as a purely reflecting beam, with no intensity gradients that come to 'spoil' the the outgoing illumination function. Simulating deviations from this idealization by a better beam projection in the plane parallel to the area detector, is only required when the numerical reconstructions aim at perfectly matching those of the experiments. The following simulations, however, aim at reproducing effects from other experimental uncertainties.

The detector pixel pitch size and energy of the X-ray are set to 20 μm and 9 keV respectively. The detector distance is chosen to be 1.5 meters downstream of the sample, which is close to optimum far-field geometry distance for our experiments at APS. Poisson noise was not introduced in the numerical simulations as Signal to Noise Ratio (SNR) does not impose any difficulties for thin film sample experiments because exposure time in real measurements can be substantially increased. The tested overlap is 70% even though larger overlaps may lead to travel faster towards global convergence, the computational time required per area is greater, and not deemed necessary for these simulations.

The series of images in Fig.5.22 show the updating object and illumination function as the algorithm progresses. The starting guess is a simple pupil function of half a micron diameter. Convergence is usually monitored using the difference map error metric in measured data. However for these simulations, a direct visual inspection of reconstructed real-space phases is a better guide and a direction of progress. The domain features already appear after only 30 iterations, converge to an acceptable level after 50 iterations and are completed within 150 iterations (Fig. 5.23).

A parameter of primary importance in Bragg ptychography is the correct projection of the scan position vectors into a plane parallel to the area detector. A scan improperly transformed may severely affect the reconstructions or even produce non unique solutions. To test this hypothesis, a simulation with a fictitious CCD camera set at an angle of 34° (like in Fig. 5.19) and a scan accordingly transformed was

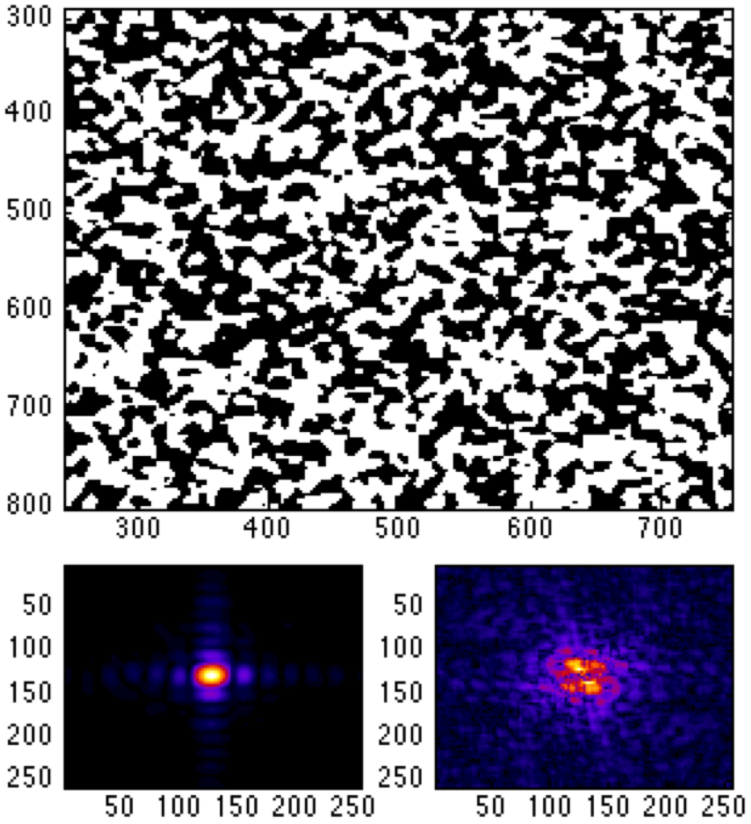

Figure 5.21: The central image represents the simulated object domain sizes of about 10 pixels in average. Black represents a phase value of π, white represents a value of 0. Lower right corner: the probe used for the simulation is designed based on experimental reconstruction at APS from a pair of KB mirrors. Lower right corner: a typical diffraction pattern (256×256 pixels) resulting from the propagated complex exit wave produced at the first scan position

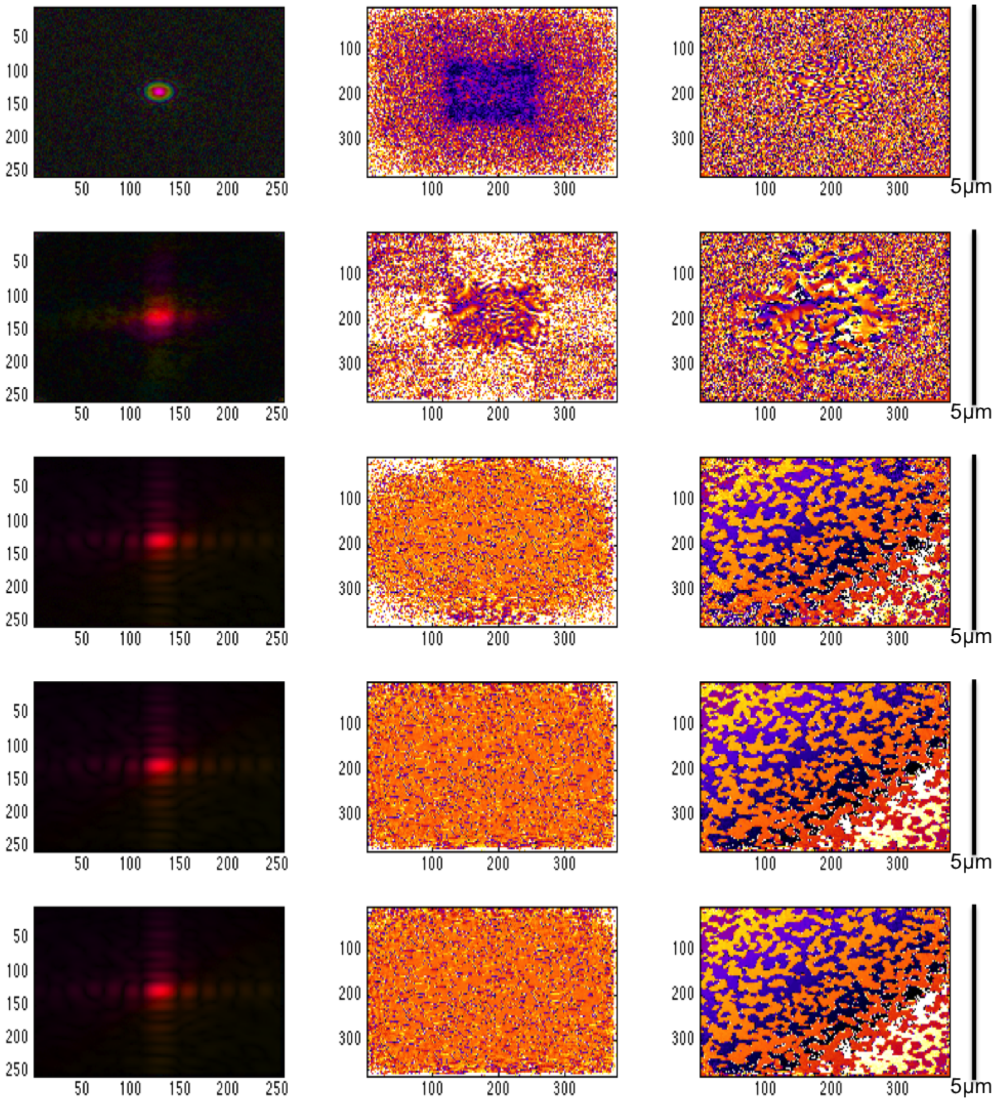

Figure 5.22: Images of the probe (column 1), object amplitude (column 2) and object phase (column 3) respectively from up to down to 10, 30, 50, 80 and 100 iterations of the DM algorithm showing the progress as a function of convergence. The probe update starts after 5 iterations. The object FOV is 300 × 300 pixels or 5 × 5 microns.

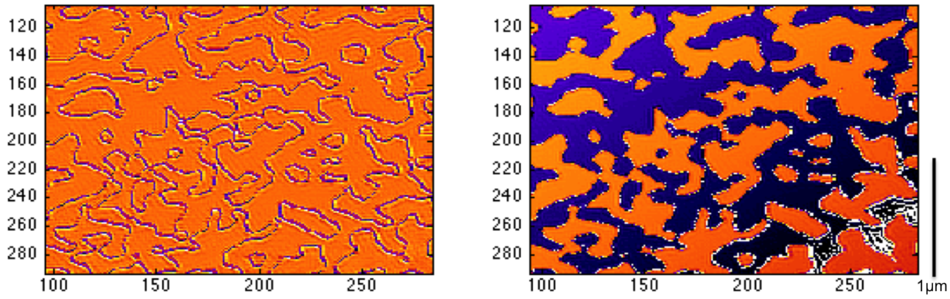

Figure 5.23: Reconstructed amplitude and phase domain for 150 iterations of DM when full convergence is obtained, zoom over the central part of the objects.

performed. This correction was only applied to the simulated data and a ptychographic reconstruction was performed with an uncorrected Round-ROI scan. It can be observed in the reconstruction displayed in Fig. 5.24, that the central part of the object is correctly reproduced whereas the outer part is clearly affected. This is mainly due to the the fact that the difference in vector positions increases as the scan grows in size. By the same token, the conclusion drawn is that central phase domain in which we will be interested in real experiments, is demonstrated to be robust to a global uncertainty in scan positions (global drift). Although, an important loss in illumination fringes was noted.

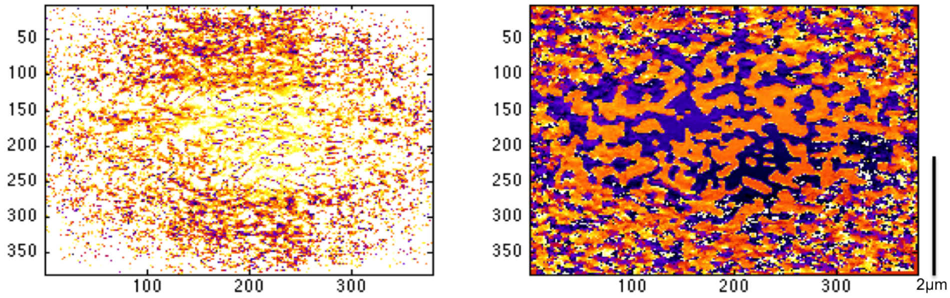

Figure 5.24: Amplitude and phase domain reconstructed from an 'untransformed' scan, zoom over the central part of the objects.

Another uncertainty in the experimental parameters that may produce non-uniqueness is the likely inversion of diffraction patterns caused by the mirror reflection about the thin film sample[2]. To understand the resulting trend in reconstructed domain morphology, diffraction patterns are computed upside-down before feeding into the iterative algorithm. Three different random seeding starts were performed with DM and reported on Fig. 5.25, where it can be observed that domains are quite

---

[2] While it is true that the data inversion cannot be considered a real variable, its effects are nevertheless investigated.

different from what is expected and seem to be non-unique from run to run. One can also observe in the reconstructed images the important loss of recovered fringes of illumination. Most importantly, these simulations shows that the complex contributions of the projected focused beam cannot be correctly separated from those related to the sample, when the experimental parameters are uncertain. It might indicate that the probe fringes should be used as a reconstruction quality (or performance) metric for real experiments performed on thin films.

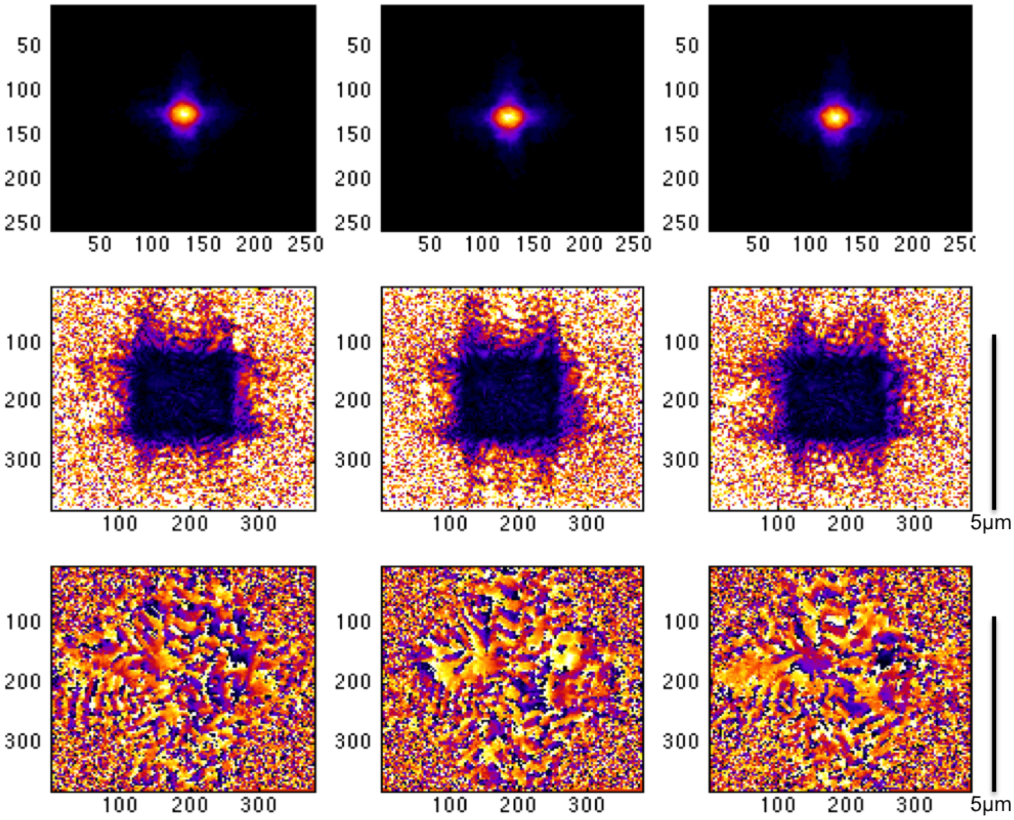

Figure 5.25: Images of the probes (line 1), object amplitude (line 2) and object phase (line 3) respectively from three different random start and 150 iterations of the DM algorithm for reconstructions with diffraction patterns that are computed upside-down (or without taking into account the reflection type of Bragg modes). The probe update starts after 5 iterations.

5.2.4 Experimental parameters

Coherent diffraction patterns from a specular (110) reflection were collected with a focussed 8.9 keV X-rays, a Round-ROI scan, and a CCD detector positioned 2.184 m downstream of the sample. The beam was focussed by a pair of Kirkpatrick-Baez (KB) mirrors to a size of ∼ 900 × 900 nm and made coherent by setting the entrance slits to 30 × 50μm. Rotation matrices were introduced so that an incidence angle of 17 degrees for the sample was correctly accounted for. This way, ptychographic scans are performed in the direction perpendicular to the incident X-ray beam (as in the transmission case), thanks to a 3D piezo stage mounted on the diffractometer goniometer head. Table. 5.2 summarises the experimental parameters used for the ptychographic scans. The Nb specular (110) peak is chosen for ptychographic scan and hence inversion of diffraction patterns. Off-specular peaks can provide information about the depth of the sample but have not been measured. A reciprocal space map of the Nb thin film is shown in Fig.5.26.

Properties	Value	unit
Energy	8.9	KeV
λ	1.4	Å
lattice parameter, a	0.33	Å
θ_{110}	17	°
δ_{110}	34	°
beam size	$\sim 0.9_H \times 0.9_V$	μm
detector distance, z	2.184	m
real-space pixel	15	nm
scan range	2x2	μm
scan step size	150	nm
degree of overlap	$\sim$ 80	%

Table 5.2: Experimental parameters for Ptychography scans on Nb(110) data taken at APS 34 ID-C.

Regions of the film present different crystal characteristics with sub-micron beam length scales, and are thus simultaneously illuminated. The coherent beam-mosaicity interferes when diffracting and modulates the large Nb peak into a densely speckled pattern with mean feature size inversely proportional to the incident beam size. The beam interaction with the crystalline substrate gives rise to bulk Bragg peak (sharpand single peaked) which is of intensity comparable to the central speckles arising from thin film peak. The beam size d could consequently be calculated from the average of minimum to minimum speckle widths s from a series of lineouts through the centre of the Bragg peak, through the relation $d = \lambda z/s$.

A self-consistent ptychographic image is generated from adjacent and well defined scattering regions of a crystal only by inversion of coherent diffraction patterns presenting a high contrast. To keep a constant scattering volume, the method places stringent requirements on beam coherence and instrument vibration during the realisation of a fixed point measurement. Fortunately, the high capabilities of beamline 34-ID-C provided a high and suitable contrast of 80±5%, calculated from the speckle features taken in a line plot at the center of the diffraction pattern (Fig. 5.27). They are oversampled with approximately 8 pixels across each feature.

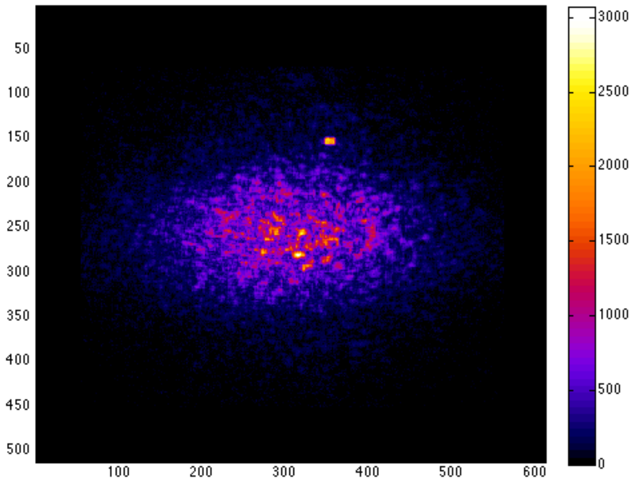

Figure 5.26: Typical coherent diffraction pattern taken at the Nb (110) specular Bragg peak.

5.2.5 Reconstruction attempts

Coherent diffraction data was collected in specular Bragg geometry reflection from Nb(110) crystalline planes. In this geometry, the illumination and the ptychographic scan are kept as simple as possible when projected in the reconstructing plane parallel to the detector area. This plane is also parallel to the plane of the momentum transfer, q, hence sensitivity to the film structure is in the film thickness direction. The detector being set with only one rotation angle (γ) results in a simplification of the scan transformation (y direction only), for the ptychographic reconstructions.

A scan of $2 \times 2\mu m$ with radial steps size of 150 nm distributed 141 scan positions with accumulations of 0.2 sec CCD exposure time taken at each position. Due to the limited memory of the GPU, the data set is reduced to 100 diffraction patterns, corresponding approximately to a scan area cut to $1.5 \times 1.5\mu$m . The diffraction patterns are centered in order to minimize artificial phase gradients. The 512×512 reciprocal-space data were embedded in 1024×1024 pixel array in order to have larger features in the real-space. A single centering adjustment was made based on calculation on the centre of mass of the first diffraction pattern within the 1024×1024 pixel array. In this manner, any shifting of peaks is only due to the change of sample domain profile.

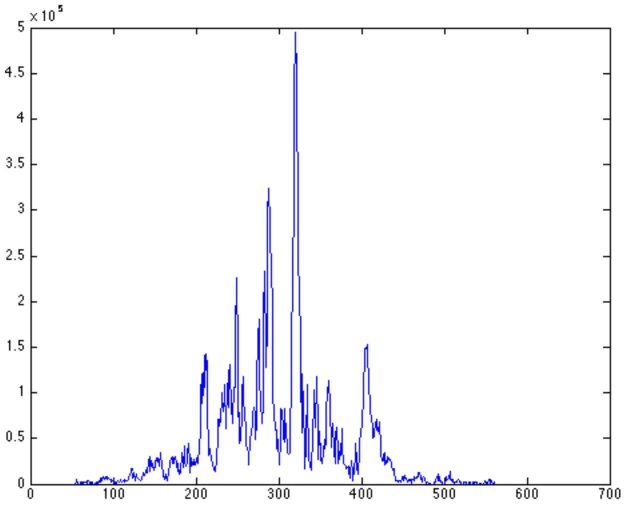

Figure 5.27: Speckle profile taken in the detector x direction at the centre of the Nb(110) specular Bragg peak. Speckle features are high contrast showing a high degree of coherence and are ∼8 pixels per speckle.

To prevent the risk in the algorithm attempting to fit the sapphire peak and hence incorporating artefacts into the object structure, the sapphire bulk diffraction intensity values are set to zero, by an appropriate mask applied to the diffraction patterns. The ptychographic reconstructions are started with a complex illumination reconstructed from test pattern data taken in a transmission geometry (see Fig.) and resampled to match the reflection geometry dimensions. The algorithms start to update the complex illumination function after 60 iterations of DM. A circular support is applied to the CDI window to prevent the algorithm from filling the corners with artefacts of relatively high intensity values. No binning of the data was performed, in order to provide robustness to the algorithm and its correcting schemes.

This first attempt in reconstructing domain structure faced difficulties as previously reported in [175, 52], with real-space images only showing a few promising features, therefore the reconstructions are considered partially successful. The reasons for the failure are investigated in details in this section before the reproducibility of the images is demonstrated. All reconstructed images display object amplitudes across the full array, however for reasons of clarity, only the central region of the object phases is displayed.

The recovered phase structures are split into domains and are one with non-random (Fig. 5.28). They all look very similar but different random seedings give phase results that are not consistent from one run to another. The recovered am-

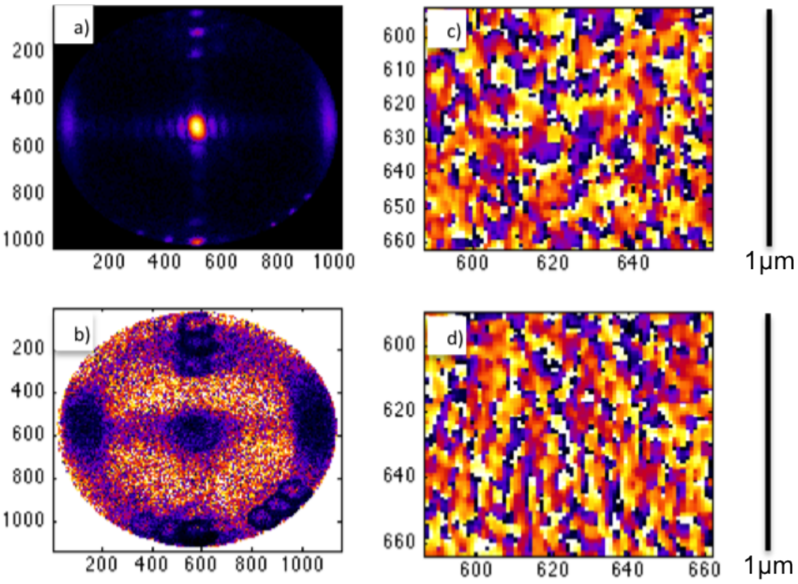

Figure 5.28: Images of first experimental reconstructions of Nb(110) sample. a) illumination amplitude. b) object amplitude c)-d) zoom of phase results for two random start.

plitudes are not located to the areas where the overlapping illumination provides significant intensity. As already encountered with simulations, an illumination function that does not present weak amplitudes well away from the central focus, signals that either the scan transformation is wrong or that the probe is fluctuating over time, or both. An encouraging sign, is that the profile is not corrupted by domains implying that the illumination function can be numerically deconvoluted from such complicated object.

Despite the apparent complexity of the sample under study, the high quality of the coherent diffraction data with the slow modulation of the speckles (from overlap) should enable both the Fourier-space and real-space overlap constraints to produce phase structures uniquely and disentangle a better illumination function. As ways to correct scan point positions and fluctuations in probes have been developed (chapter 3) for the sole purpose of improving sensitive experiments, they will be administered separately in the next subsections and provide a careful analysis of their combined effects. Certainly, it could be argued that probe and scan drift could be dismissed by running reconstructions with fewer scan positions only. Although, reconstructions performed with 20 and 50 positions proved to be difficult with regard to retrieving a probe with sufficient features (only the central portion of the KB could be retrieved as in Fig.5.25). Therefore, it will be seen that exploring multiple probes and position corrections does not amount to giving more degrees of freedom to the reconstruction algorithm but rather provide better constraints. It is also worth reporting that less redundancy presented greater analytical difficulties, and this is why the following section focuses only on the larger overlap data set.

Dynamical scan transformation

As presented in the simulations of section., imaging self-similar small features is feasible. As has been reported [52], the difficulty in imaging domains likely lies in the numerical scan transformation to the Bragg projection geometry. The positional input for computational reconstructions are usually adjusted to the Bragg geometry by rotation matrices (section 5.1.2) but a scan positions correction scheme offers the alternative possibility of iteratively adjusting the scan positions. However, this is only realistic for small scans as the correction for outer vector positions should lie within the range of effectiveness of the employed method [96, 78]. However, once the correct scan transformation is found, the method can be used as a complementary numerical constraint to the matrices.

An effective approach to 'iteratively transform' the scan will be the annealing method, explained in section 3.3, and which is preferred over a cross-correlation based method for this particular case where images fluctuate severely from one iteration to another.

To help us understand 'qualitatively' which correction should be applied to the scan (y direction for now) the annealing method is applied to the set of previously analysed data. The annealing correction is initiated at iteration 200 and sustained for 200 hundred more iterations, and which is clearly enough to 'stabilize' the metric. Annealed positions and corresponding metrics are displayed in Fig. 5.29 for the three different y scan transformations tested: one with a $\cos(34)$ correction, one without correction and the finally one $1/\cos(34)$ correction.

Starting with a $\cos(34).y$ contraction of the scan, it is observed that the outskirt positions are displaced quite far from their original positions towards the outer region of the scan, with a slight asymmetry in the distance travelled.

For a scan with no contraction, which is expected from illustration in Fig. 5.19, we observe that the 'annealed' positions are still trying to go outwards but with an amplitude that is reduced by about half from the previous $(\cos(\theta).y)$ correction.

Finally, by testing a scan expansion,$1/\cos(34).y$, it can be observed that the points are migrating relatively around their original scan points with no global direction. For each of the three scans, the metric stagnates around about 0.4 which represents a respectable improvement of 35%. Retrieving the scan transformation from a correcting scheme seems to be a valid idea since the correction in the x direction is relatively stable, as expected. A proof a non erratic behaviour and reproducibility was brought by running the ptychographic reconstructions several times.

Nevertheless, looking at the resulting probes suggests that finding the right scan transformation and possibly the true scan positions is not sufficient to recover full fringes, as expected from the KB illumination profile. Interestingly, the recovered probes are overall invariant under different scan transformations. Thus, the conclusion to be drawn from these results is that the illumination fluctuates with time and therefore the annealing correction method must be combined with a dynamical probe scheme to a better effect. However, the latter method is first tested apart for a better understanding of its sole capabilities on the ptychographic reconstructions.

Dynamical probe analysis

Artifacts in the retrieved images, may be caused by the phase retrieval algorithms but from changes in the experimental set-up itself, as well. Changes to the shape and intensity of the probe would not be expected from such a ptychography set-up, although it is not surprising to find drifts and damage in the illumination on a time scale approaching an hour [63].

As probe instabilities could be responsible for the poorly formed outer fringes in the reconstructed illumination function, therefore, a dynamical probe method (Eq.3.37) is tested by performing reconstructions with an ever increasing number of illuminations assigned to the scan (up to 16 in steps of 2). The scan being comprised of 100 points, the phase retrieval is fragmented in subset of 50, 25, 12, 10, 8 and 6 scan points respectively. The reconstructions obey the following cycle: for the first 60 iterations, the reconstructions are performed using a pupilar function of 800 nm in diameter (a rough guess to the central KB spot size), then a single probe is updated for 40 iterations before the dynamical probe scheme elucidates for more probes, for a further 300 iterations. A code that optimizes the number of dynamical illuminations over the course of iterations could be envisaged.

Ptychographic reconstructions performed with 2,8 and 14 probes are displayed in Figures.5.30-5.32. A 2 probe scheme already yields noticeable improvement with reconstructed probe fringes extending almost over the entire CDI window, which in the case of complicated samples could be in principle interpreted as an encouraging sign of data convergence. Reconstructions with more illuminations stabilize into the typical shape that one expects to see from the focus of a pair of KB mirrors.

The final error metric values are reported in Fig. 5.33 and expose a net trend: a minima in error metrics when 14 probes are involved in the ptychographic reconstructions. However, for such a number the quality of the illuminations degrades

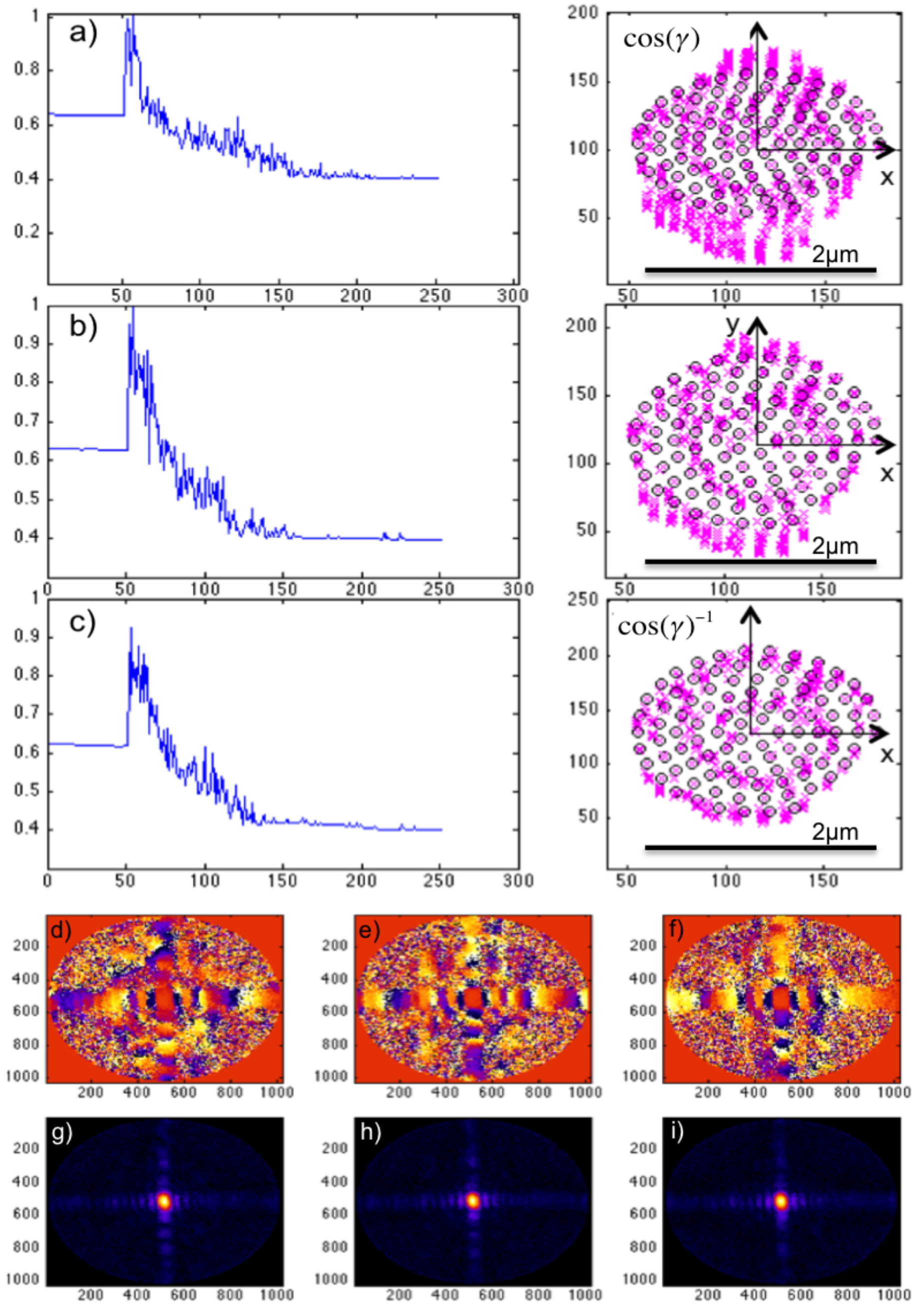

Figure 5.29: a)-c) Difference-map metrics for cos(34), 0, $\cos(34)^{-1}$ scan transformations in y with corresponding positions retrieval. During the annealing process, scan points are plotted in violet each 5 iterations. This means that for each of the 100 scan points there could between 1 to 40 retrieved points plotted. d)- f) Phase of probes corresponding to scans a)-c) respectively. g) - i) Amplitude of probes corresponding to scans a)-c) respectively. The probe are invariant with regard to scan transformation.

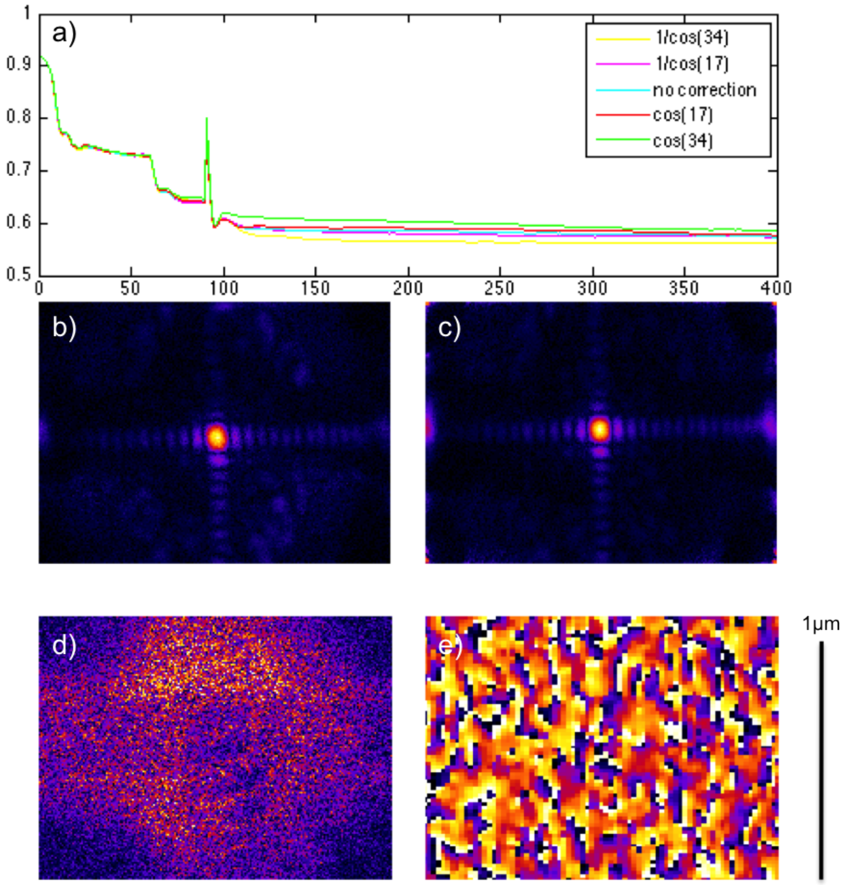

Figure 5.30: Ptychographic reconstruction using 2 dynamical probes. a) Plot of difference map metric. b-c) amplitude for first and second illumination (amplitudes are slightly enhanced). d) Object amplitude. e) Object phase (zoom on central part, $\sim 1 \times 1$ μm).

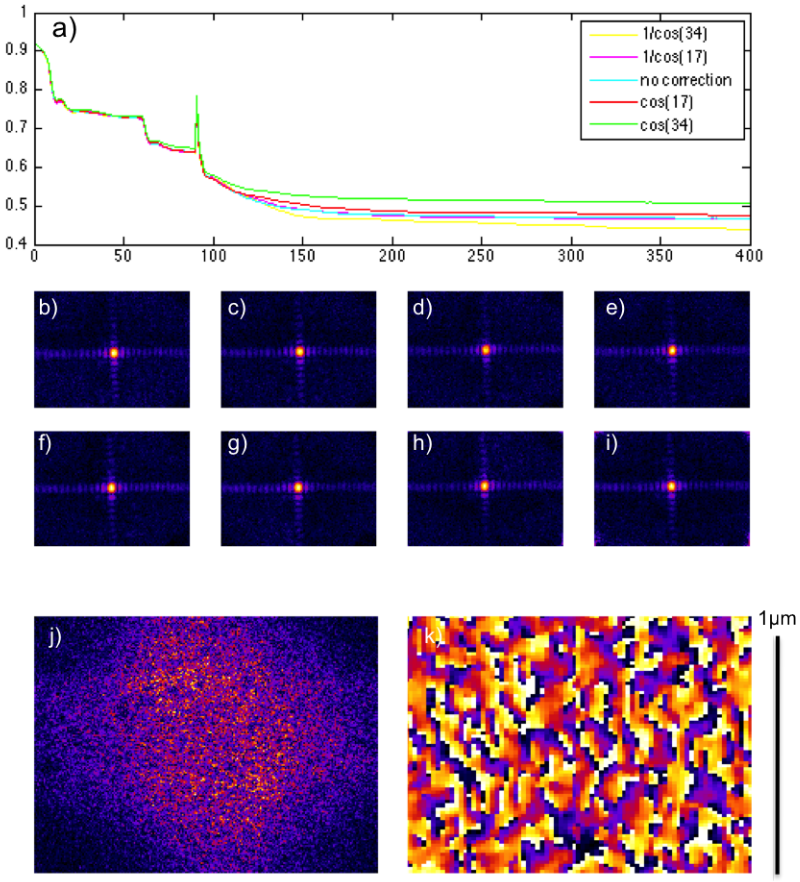

Figure 5.31: Ptychographic reconstruction using 8 dynamical probes. a) Plot of difference map metric. b-f) amplitude for first to fourth illumination (amplitudes are slightly enhanced). g-i) phase for first to fourth illumination j) Object amplitude. k) Object phase (zoom on central part, $\sim 1 \times 1$ μm).

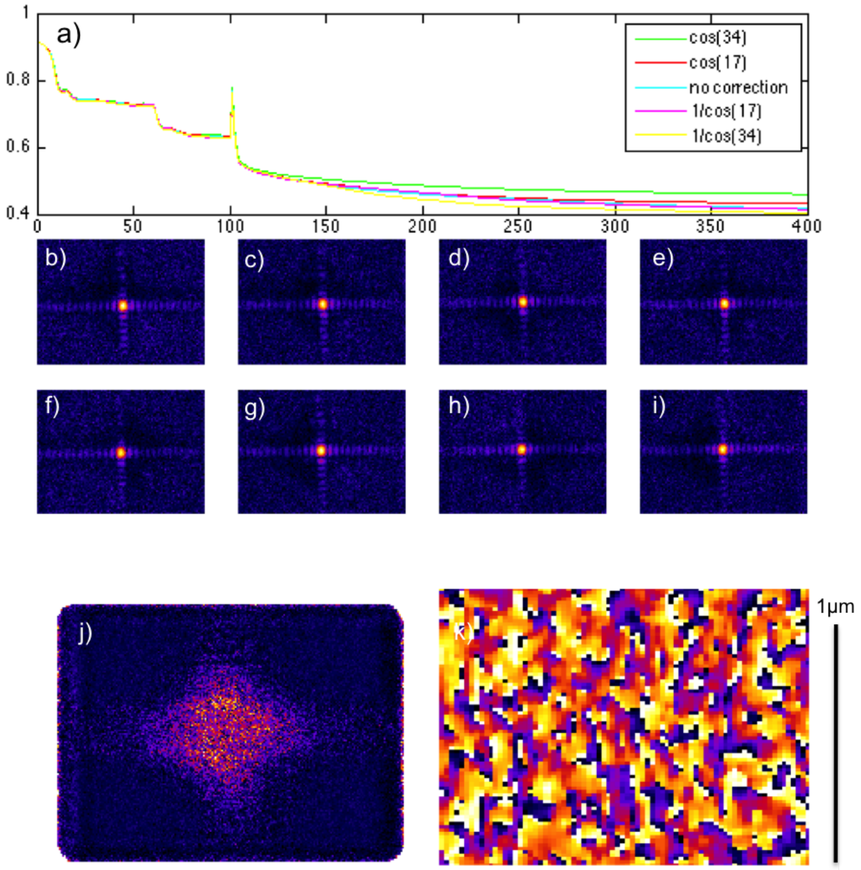

Figure 5.32: Ptychographic reconstruction using 14 dynamical probes. a) Plot of difference map metric. b-f) amplitude for first to fourth illumination (amplitudes are slightly enhanced). g-i) phase for first to fourth illumination j) Object amplitude. k) Object phase (zoom on central part, $\sim 1 \times 1$ μm).

with suppressed fringes and noisy contours (see Fig. 5.32). This is explained by a numerical overlap constraint being weakened by a reduction in closest neighbours, thus the most numerically constrained region of the reconstruction is near the centre of the image. (Hence, a reduced set of metrics does not always mean better quality reconstructions and a compromise has to be found.) As these drifts in illumination could be attributed to instabilities in the source or in the experimental set-up, it is proposed to analyze the latter by introduction of a position correction scheme into the algorithm. Therefore, an examination of the phase structures is not dispensed at this stage. Given the increased complexity in experiment and sample structure, it was thought that a stringent requirement on the *a priori* knowledge of the illumination function would be necessary. It was demonstrated with this method that a rough starting guess is sufficient to recover an illumination that is consistent with the expected KB illumination profile. In conclusion, a realistic guess for the illumination is not needed for this type of study.

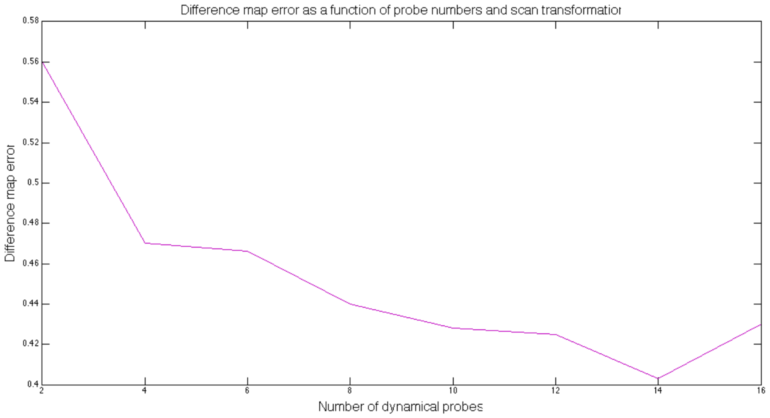

Figure 5.33: Plot of difference map error metric final value as function of illuminations number D in the ptychographic reconstructions .

Combining the refinement schemes

As both the scan points and the illumination inevitably drift during the course of an experiment, a combination of the two previously tested methods should lead to a major improvement of reconstructions at dedicated coherent beamlines. Starting from the 'deduced' $1/\cos(\gamma).y$ scan transformation of the previous section, the performance of reconstructions as a function of the number of 'injected' probes into the 100 adjusted scan positions, are assessed. The three update schemes, to be known the probe, dynamical probe and annealing are not started simultaneously but each begin after exhaustion of their individual capacities. Therefore, 3 plateaus should be observed during the course of the difference map error metric. On Fig. 5.34, it is shown that for an analysis with 8 dynamical probes, the points are on majority stable with no particular trends in direction. This time, a quantitative analysis is given by choosing to calculate mean error for retrieved scan positions in the direction of interest (y) and it is defined as:

$$\Delta r_{avg}^{final} = \frac{\sum_j |r_j^{final} - r_j^{scan}|}{N} = \frac{\sum_j |c_{jj}|}{N}. \tag{5.11}$$

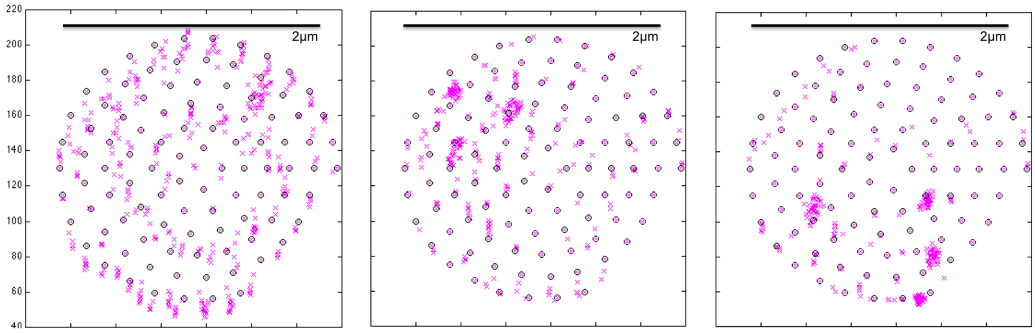

Figure 5.34: Plot of the corrected positional points as a function of illuminations number used in the reconstruction of Nb(110) data. From left to right: 2,4 and 8 probes reconstruction respectively. The points are plotted in violet each 5 iterations during the annealing process. This means that depending on stability, there could between 1 to 40 retrieved points plotted for each of the 100 scan positions.

The reported trend in Fig. 5.35 is clear: the mean error for retrieved scan positions decreases as a function of probe numbers. It reaches the minimum of 2 pixels (30 nm) for 8 and 10 dynamical probes so no further probes are employed. It is then deduced that a better converged probe (or probes) favours a more realistic search in scan positions. In fact, a virtuous cycle is initiated as the favour is returned by the annealing process by helping the illumination to improve in quality.

In Fig.5.36, the reconstruction with a set of 2 probes shows a twofold improvement in metric as expected from a combination of refinement methods that bring net improvements when applied separately. After the 'annealing peak'[3], its metric (yellow plot) initiates a descent that goes well below it starting point. The metrics associated with reconstructions using a superior subset of dynamical probes show a peculiar behaviour. After the 'annealing peak', the metrics oscillate but overall stay at a level higher than their starting point. Hopefully, it will be seen in next

---

[3] The annealing peak is the sudden change in metric due to the introduction of the correcting scheme

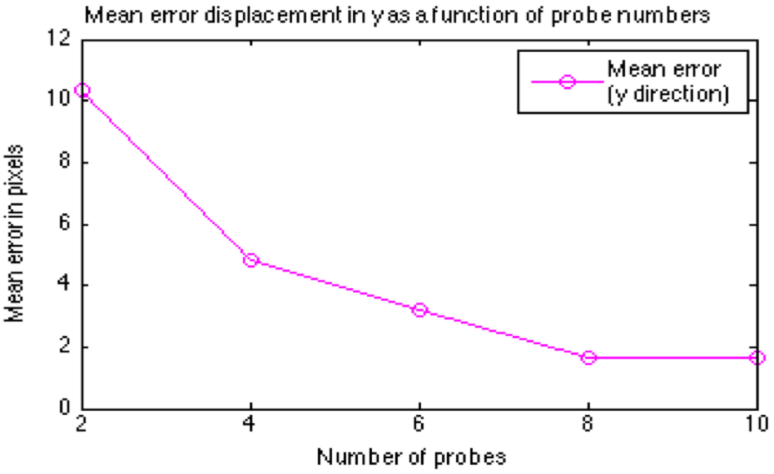

Figure 5.35: Mean error (Δ_{avg}^{final}) as a function of illuminations number (D) used in the ptychographic reconstruction of Nb(110) data. The amplitude of the mean error depends on the ability of the algorithm to retrieve the illumination fluctuations.

section, that the metrics associated with reconstructions of molybdenum data work in a cascade fashion, as predicted.

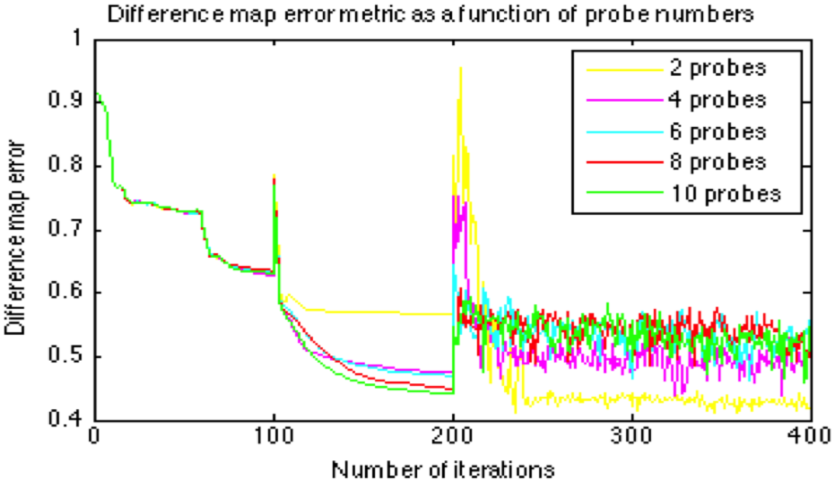

Figure 5.36: Plot of difference map error metrics as a function of illuminations number used in the reconstruction of Nb(110) data. The best error metric (yellow) corresponds to the use of 2 probes.

While the method broadly demonstrates the good stability of the experimental scan, it is difficult to tell whether the positional uncertainties are the true positions. Nevertheless, the positions retrieved with 8 dynamical probes will be kept as a constraint for the following analysis of the images reproducibility.

5.2.6 Analysis of the phase domains

Despite the conundrum in error metrics, the phase structures are analyzed from reconstructions using an 8 dynamical probes reconstruction from two different random seedings respectively, as stability in annealed points was minimal. What can be observed in Fig. 5.38, is that the phase domain patterns are quite unique from one random start to another despite a change in phase ramp and possibly in phase offsets. The phase domains produced by reconstructions involving a different number of illuminations presented a lesser degree of reproducibility. The first ($d = 1$) and last ($d = 8 = D$) of the D retrieved dynamical illuminations are displayed at the bottom of Fig. 5.38 in hue color, and show high quality reconstruction. Apparently, fluctuations between the dynamical illuminations are indeed subtle but still necessary a condition to favour convergence of the domain structure. Different runs leave the illuminations unchanged.

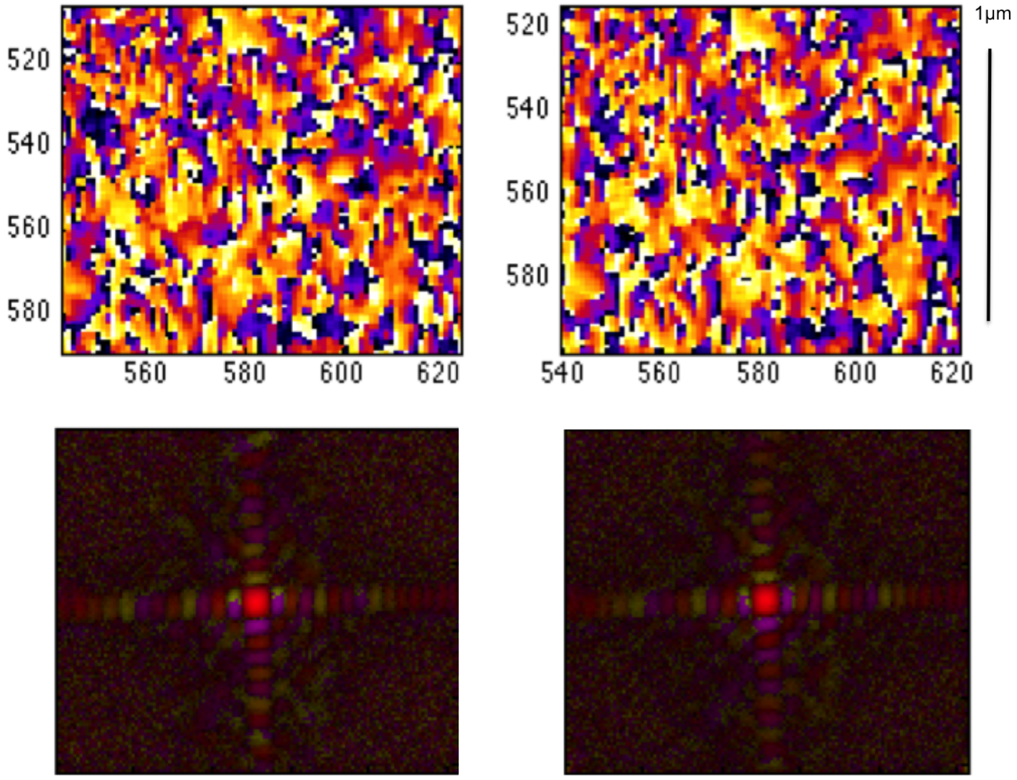

Figure 5.37: First row: central region of phase objects reconstructed with 8 dynamical probes and started from two different random seeds. Second row: first and last illumination (sown in Hue color with amplitudes slightly enhanced). Pixel size, 15 nm.

Linear phase term removal: when preference is given to reconstructing both object and probe, an ambiguity on the linear phase terms arises. Manuel Guizar in

[179] was the first to discuss an alternative solution to a ptychographic image that also satisfies the object domain constraints, by considering:

$$o^{'}(x,y) = o(x,y)\exp\big[i2\pi(bx+cy)\big], \tag{5.12}$$

and

$$p^{'}(x,y) = p(x,y)\exp\big[-i2\pi(bx+cy)\big], \tag{5.13}$$

then:

$$f_n^{'}(x,y) = o^{'}(x-x_n, y-y_n)p^{'}(x,y) = f_n(x,y)\exp\big[-i2\pi(bx_n+cy_n)\big], \tag{5.14}$$

"from this mathematical construction, it is realized that the fields $f_n^{'}(x,y)$ and $f_n(x,y)$ differ by only constant phase terms and consequently still produces the same intensity pattern in the far field, $|F^{'}|^2 = |F|^2$ (and the overlap constraint is satisfied, the functions $o^{'}(x,y)$ and $p^{'}(x,y)$ are solutions for any value of b and c. This is intrinsic and decoupled from reconstruction algorithm when no *a priori* knowledge of the sample or probe is used. It has been then concluded that image quality is not affected by this arbitrary phase ramp as long as the illumination function is reconstructed with a linear phase of equal magnitude but of opposite sign." Linear phase term removal is usually not critical but in this particular case, remaining non-uniqueness in phase domains reconstruction can be attributed to different phase terms that arise from different random seeding. According to the relation in Eq.5.14, the phase ramp found in the complex object can in principle be suppressed by multiplication with the opposite ramp found in the complex illumination function. Therefore , to successfully quantify the ramp in the probe, were studied the several available options which are the mean phase gradient, center of mass, and polynomial fit. A brief overview follows.

Mean gradient: this is a simple method in which the gradient of the phase is computed at each array point, and then the mean of the local gradient phase is calculated from the whole array. The magnitude part of the illumination can also be used as a weight (this method can be found in the package of the SLS code, developed by Pierre Thibault and coworkers [180]).

Center of Mass: the Fourier transform of a translated function introduces a phase tilt across the Fourier domain. In mathematical term it translates into :

$\mathcal{F}f(x+a) = e^{iqa}\mathcal{F}f(x)$. From the same property, a phase ramp across the real-space will result in a shift of the Fourier domain. For example a phase ramp of 2π across the object will result in one pixel shit of the Fourier intensity pattern. Thus, to calculate the phase ramp present in the illumination, we Fourier transform the illumination complex function and calculate the center of mass using the following equation:

$$\Delta a = \frac{\sum(x.|P(x)|^{\alpha})}{\sum(|P(x)|^{\alpha})}. \tag{5.15}$$

As the calculation proceeds on a pixelated array, the precision reached is proportional to the upsampling factor employed,i.e, the array is embedded into a bigger array filled with zeros before performing a FFT. As a GPU is limited in memory the upsampling factor was limited to 30, which allows for a precision in phase of $\frac{\pi}{15}$. After performing an inverse Fourier transform the array is cropped back to its original size.

Polynomial fit: this original way of measuring a phase ramp (first order coefficient) has been privately developed by Fucai Zhang (UCL) and represents an interesting alternative but demands to first unwrap the phase which may result in ambiguities. To avoid noise in the fit, a region of interest is manually selected by the user.

To discriminate between the methods, a reconstructed siemens star presenting a phase ramp was used (besides its spokes the test sample presents a flat phase structure). The center of mass method left a small amount of phase ramp whereas the other failed to remove it or even worsen it. Hence, phase ramps found in each of the D reconstructed illuminations is calculated using the center of mass method. The values are reported in table.5.3 for ptychographic reconstructions using a subset of 2, 4, 6 and 8 dynamical illuminations respectively.

As expected, the phase ramp values change from run to run but surprisingly, also in between each dynamical probes of a same iteration and reconstruction. Despite a smooth change in between neighbouring illumination phase ramps, these latter fluctuations render the phase ramp removal tremendously harder.

Restarting reconstructions with a suppressed phase ramp on each of the D dynamical illuminations retrieved as an input model for the ptychographic reconstructions, and allowing only for the update of the object, comes as an obvious solution. According to Eq.5.14, reconstructions performed in this manner should result in outcoming phase structure presenting no phase ramps and hence structural phase

Phase ramp	P_1	P_2	P_3	P_4	P_5	P_6	P_7	P_8
2 probes	-0.52π	-0.26π	x	x	x	x	x	x
2 probes	-1.86π	-1.46π	x	x	x	x	x	x
4 probes	-0.26π	0.12π	0.4π	0.26π	x	x	x	x
4 probes	0π	0.4π	0.52π	0.52π	x	x	x	x
6 probes	0.4π	0.8π	0.66π	1.06π	1.06π	1.06π	x	x
6 probes	0.26π	0.52π	0.8π	0.88π	0.88π	0.3π	x	x
8 probes	0.2π	0.1π	0.2π	0π	-0.2π	0.3π	-0.3π	-0.1π
8 probes	-0.5π	-0.4π	0.2π	-0.4π	0.2π	0.1π	0.4π	0.1π

Table 5.3: Phase values of ramps found in two random seeding for ptychographic reconstructions using a subset of 2, 4, 6 and 8 dynamical illuminations respectively.

values that are the same from one to another random object starting guess. This method was tested with the $D = 8$ retrieved dynamical probes as input model for the unchanging beams along with addition of the retrieved annealed position. The 8 previously retrieved probes with suppressed phase ramps were stacked in an array (ill_d) and ptychographic reconstructions were performed from two random starts, using the following equation:

$$O_{new}(\mathbf{r}) = \frac{\sum_{d=1}^{D} \sum_{j=(d-1)\frac{N}{D}+1}^{d\frac{N}{D}} ill_d^*(\mathbf{r}+\mathbf{r_j}).\psi_d(\mathbf{r})}{\sum_{d=1}^{D} \sum_{j=(d-1)\frac{N}{D}}^{d\frac{N}{D}+1} |ill_d^*(\mathbf{r}+\mathbf{r_j})|^2}. \tag{5.16}$$

After 400 iterations of DM, the final phase images were rather worsened with a metric that was 10% higher than the respective value reported in Fig. 5.35. The reasons for this are not yet well understood.

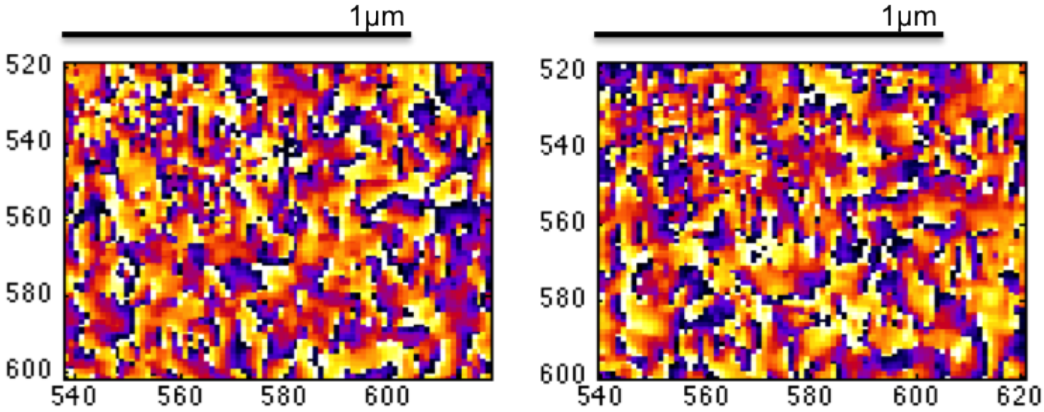

Figure 5.38: Central region of phase objects reconstructed with 8 dynamical probes and started from two different random seeds.

Alternatively, an integral phase ramp cancellation can be performed on each object's subfields by multiplication with the respective conjugate phase ramp found in the dynamical illuminations. In fact, ptychographic Eq.3.37 which updates an object from all the $j = N$ views and D dynamical probes is modified for this purpose:

$$O_{cc} = \frac{\sum_{d=1}^{D}\sum_{j=(d-1)\frac{N}{D}+1}^{d\frac{N}{D}} R_d O(r-r_j)}{\sum_{d=1}^{D}\sum_{j=(d-1)\frac{N}{D}+1}^{d\frac{N}{D}} |R_d O(\mathbf{r}-\mathbf{r_j})|} = \sum_{d=1}^{D}\sum_{j=(d-1)\frac{N}{D}+1}^{d\frac{N}{D}} e^{(\phi_d)}.O(r-(r_j+c_j^{final})), \tag{5.17}$$

where R_d is the ramp array associated with one of the D given dynamical probe. The method was tested for the reconstructions with $D = 8$ dynamical probes (with the ramp values found table. 5.3) and with the previously retrieved positions $(\mathbf{r_j}+\mathbf{c_j})$ overlaid to the object array so that code can correctly suppress the object phase ramps according to area belonging to the respective subset of dynamical probes.

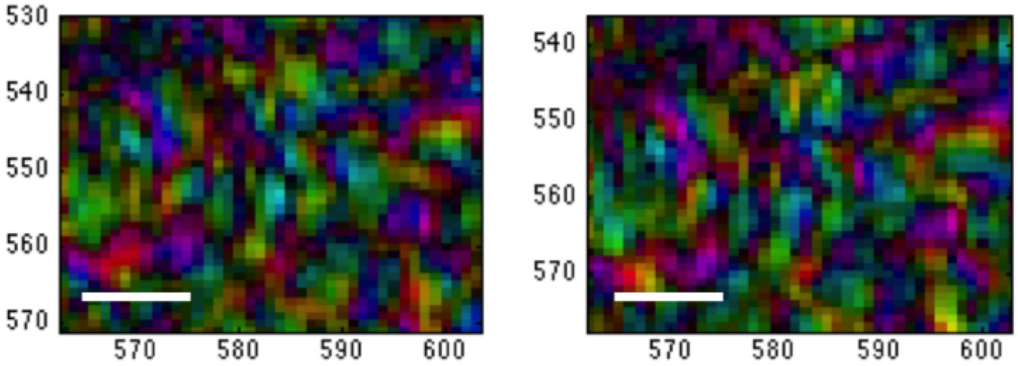

Figure 5.39: Hue rendering of central region of objects with suppressed phase ramp, according to Eq.5.17. Scale bar, 150 nm.

The results from this method are displayed in Fig.5.39, and with hue rendering for a better visibility. The local structures are clearly consistent from run to run, however at this stage a cross-correlation analysis could only be performed on the amplitude part of the arrays, as the phase ramps were not perfectly removed.

5.2.7 Reconstructions of Molybdenum data

Data for a molybdenum thin film were taken with the same conditions and geometry as for the niobium data, with the exception of a slightly increased angle of sample incidence ($\theta = 18$). The data are analyzed with the previous combination of multiprobes and annealing method with the best scan transformation of $1/\cos(\gamma)$.y correction. The algorithm update cycles follows the Niobium data prescription. The experimental parameters are resumed in table.5.4. A reciprocal space map of the molybdenum thin film is shown in Fig.5.40, where it can be seen that a beamstop was used to block the high intensity coming from the Sapphire peak.

Properties	Value	unit
Energy	8.9	KeV
λ	1.4	Å
lattice parameter, a	3.15	Å
θ_{110}	18	°
δ_{110}	36	°
beam size	0.9(H)×0.9 (V)	μm
detector distance, z	2.184	m
real-space pixel	15	nm
scan range	2x2	μm
scan step size	150	nm
degree of overlap	80	%

Table 5.4: Experimental parameters for Ptychography scans on (110) peak of molybdenum at APS 34 ID-C.

The mean errors for the y direction, reported in Fig.5.41, observe (as for niobium data) a decrease in magnitude as a function of probe numbers with a minimum of 2.6 pixels (40 nm) reached with the use of 10 dynamical probe. Although the mean error seem to further improve with more addition of dynamical probes, it is stopped at the number of 10 because it is counterbalanced by the reconstruction metric which increases. The mean error in the x direction decreased slightly from 1 pixel to 0.5 pixel, which is expected, as no transformation is involved in this particular direction.

The metrics seen in Fig. metrixage also behave as expected, with a decrease in metric following each of the refinement cycle (with the 10 probes being an exception to the rule). In this manner, the best 'combination' can be safely extracted (violet metric in Fig. metrixage). Hence, the analysis of the phase uniqueness is based on this set of conditions.

The phase structure in Fig. 5.43 (zoom in hue color) show that reconstructions are seemingly unique. The domains show some slight changes in structure from one run to another and a phase almost constant within boundaries. These encouraging results seem to be have been possible owing to the fine scan step of 150 nm size. The hue color demonstrates in a single image that both the phase and amplitude structure are seemingly unique from run to run.

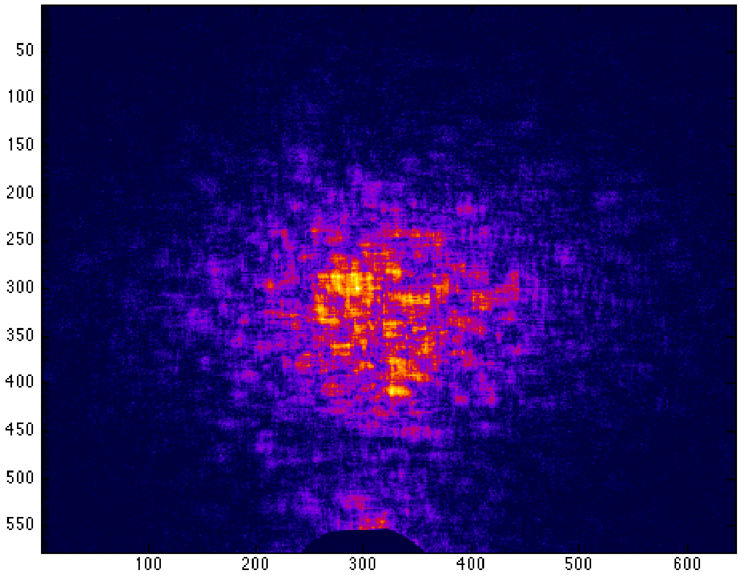

Figure 5.40: Typical coherent diffraction pattern taken at the Mo (110) specular Bragg peak. At the bottom, a beamstop was used to block the high intensity coming from the Saphire peak.

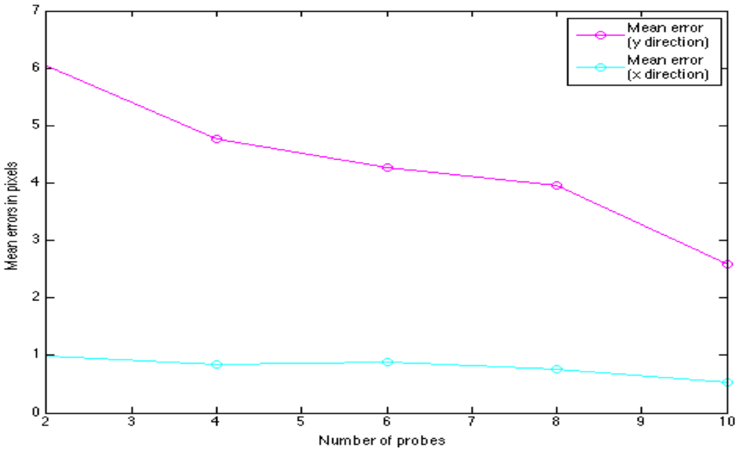

Figure 5.41: Mean error (Δ_{avg}^{final}) as a function of illuminations number used in the reconstruction of data S027. The amplitude of the mean error seems to be depending on the ability of the algorithm to retrieve the illumination fluctuations. Mean error for the x direction is given (cyan plot).

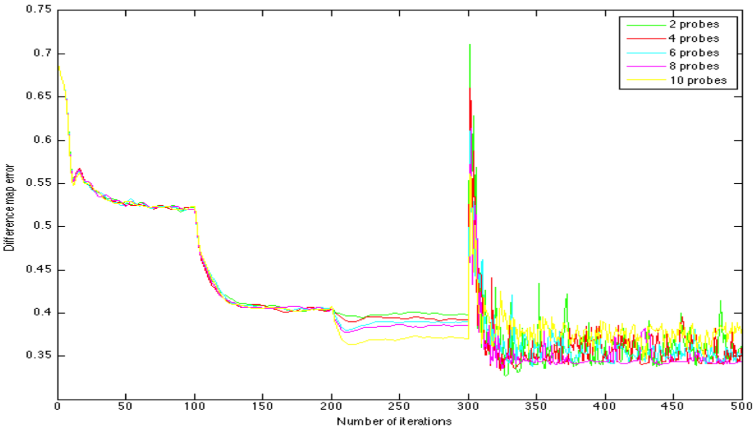

Figure 5.42: Metrics as a function of illuminations number used in the reconstruction of data S036. The best error metric (violet) corresponds to the use of 8 probes.

Discussion

A successful adaptation of ptychography to reflection Bragg geometry of extended thin films was demonstrated, thanks to the general discussions of previous researchers on how the experimental method and analysis factors might be developed to deliver successful reconstructions [52]. Thereby, great care was devoted to demonstrate that neither the self-similarity of the domain structure nor the fact that the samples presented no clear edges to 'guide' the algorithm were the cause of the previous failures. It was also shown that despite the complexity of the investigated samples, no *a priori* knowledge of the illumination profile was required. Ultimately, the correcting mechanisms are also testament to the fact that an exceptional knowledge of the experimental regime, control, stability and single photon detectors are not always necessary. However, the phase ramps present in the phase objects could not be appropriately removed with conventional methods, and thus prevented quantitative analysis of the images reproducibility.

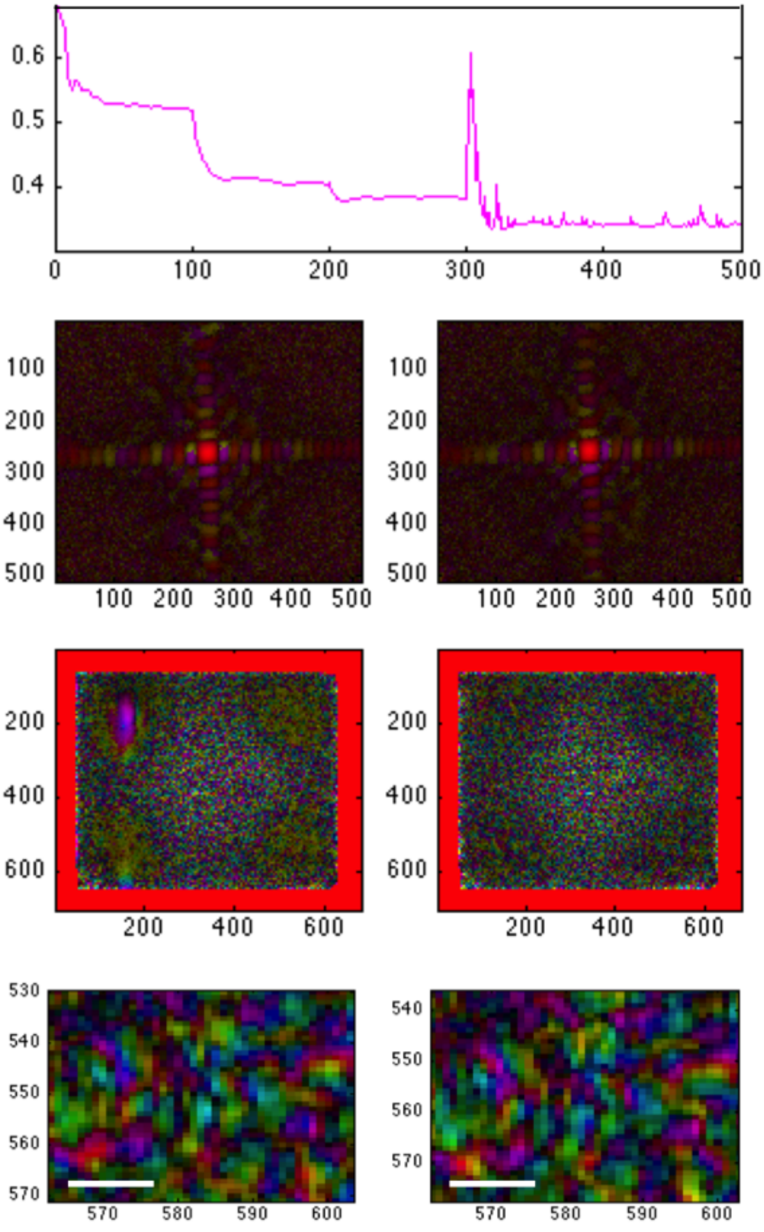

Figure 5.43: Zoom on phase objects reconstructed with 8 dynamical probes. a) Difference map metric. b-b') Probes reconstructed from two random starts (hue color). c-c') Object's amplitude from two different random starts. d-d') Zoom on object's phase from two different random starts. Scale bar, 150 nm.

Chapter 6

Conclusions

In this dissertation, the sphere of applicability of ptychography was extended by adapting its traditional transmission framework to Bragg geometry. Nonetheless, before undertaking the major analytical hurdle of ptychographical diffraction data taken in reflection geometry, the potential of ptychography in the transmission geometry was exploited, with judicious experiments and simulations.

Numerical modelling allowed for special considerations in the formulation of transverse partial coherence correction for ptychography. Systematic analyses were performed, and clearly demonstrated that by incorporation of partial coherence correction in the ptychographic iterative algorithm, reconstructions improve dramatically even with severely degraded coherence. A wide range of degree of coherence parameter (σ/L) values was used, as to formulate the lower cut-off limits to the degree of partial coherence from which below ptychographic reconstructions fail to converge.

Refinement of the complex coherence function during iterative reconstructions, was also investigated with simulation studies. The iterative reconstructions were started with several complex coherence function guesses, to be gradually refined during the reconstruction process. The results evidenced that labourious interferometric measurements of coherence can be avoided at x-ray beamlines. However, the modelling advocates the use of a simple test object to refine the coherence function in real-experiments, similar to the method for extracting a complex probe structure through a well-known test pattern in transmission-geometry.

These results coupled with the experimental findings on probe bandwidth (section.4.2.1 suggest that an appropriate degree of partial coherence of X-rays can be implemented to maximise coherent scattering intensities for sufficient signal-to-noise ratios needed to achieve good quality ptychographic data reconstructions. Furthermore, future studies could extend the two-dimensional Gaussian-Shell model approximation (section.sec:partial) to more complex forms of mutual coherence functions, incorporating multi-modes of X-rays, to explore more intensively the promises of high-resolution diffraction imaging.

Chapter 4 reported the developments of ptychography at beamline 34-ID-C of the Advanced Photon Source along with the performances of experimental measurements using test objects. The remarkable ability of ptychography to characterize complex wavefields was demonstrated by mean of Fresnel propagation and test objects at beamline 34 ID-C, APS. This was a step of vital importance as a good model assists the recovery of highly complex real-objects. The work on the probe characteristics was then extended by investigating the effects of its bandwidth and diversity on the resolution of the reconstructed images. It was then suggested to fabricate a set of irregular test patterns (polycrystalline tungsten) and several random pinhole diffusers, to artificially vary high and low phase-diversity both in the sample and illumination for future studies on improvements of the ptychographical images.

Upon undertaking the work on Bragg-ptychography on thin films, the problems were clear, the reconstructed information on the nanostructural domains were inconsistent from run to run. Thanks to the prescriptions of previous researchers, the experimental and analysis work were taken a step further, to provide a vast improvement in retrieving the mutual arrangement of the domain structure. Except for a new set of piezo-scans to simplify the necessary geometrical transformations for Bragg-ptychography, no extra dedicated instruments were required at the coherent beamline 34 ID-C of APS. Experimental incertitudes such as spatial fluctuations in the x-ray illumination or scan drifts were accounted for computationally. By noting the ability of position correction algorithms to retrieve global tilt through transformation matrices, the correct model for scan transformation in Bragg projection ptychography, was generically deduced for simple geometries. For the case of less symmetric geometries, more complex work steps are likely to be involved. Nevertheless, this work further elevates the experimental procedures for the application of ptychography in Bragg reflection geometry and sets the course for future directions of research, e.g., imaging of orbital ordering domains in strongly correlated electron systems, or spin density waves.

Preliminary studies on crystals demonstrated that Bragg projection ptychography is a superior technique to Bragg CDI with regard to 'high' strain. However the advantage is lost for probes of transversal dimensions larger than those of the specimens, a fact not fully understood at the time of experiments but later deciphered with careful simulations. The successful application of Bragg-ptychography in three-dimensions will still require the solving of experimental stabilities of long-time-scans, even though sophisticated *a posteriori* correcting methods have been made available.

Bibliography

[1] Manuel Guizar-Sicairos, Mirko Holler, Ana Diaz, Joan Vila-Comamala, Oliver Bunk, and Andreas Menzel. Role of the illumination spatial-frequency spectrum for ptychography. *PHYSICAL REVIEW B*, 86(10), SEP 24 2012.

[2] A. R. Wildes, J. Mayer, and K. Theis-Brohl. The growth and structure of epitaxial niobium on sapphire. *Thin Solid Films*, 401(1-2):7–34, 2001.

[3] Thomas Young. *A Course of Lectures on Natural Philosophy and the Mechanical Arts*, volume 1. William Savage, 1807.

[4] J.C Dainty. Laser speckle and related phenomena. *Applied optics*, 23(16):2661–2661, 1984. 0.

[5] W. L. Chao, B. D. Harteneck, J. A. Liddle, E. H. Anderson, and D. T. Attwood. Soft x-ray microscopy at a spatial resolution better than 15nm. *Nature*, 435(7046):1210–1213, 2005.

[6] Weilun Chao, Jihoon Kim, Senajith Rekawa, Peter Fischer, and Erik H. Anderson. Demonstration of 12 nm resolution fresnel zone plate lens based soft x-ray microscopy. *Optics Express*, 17(20):17669–17677, 2009.

[7] D. Sayre. Some implications of a theorem due to shannon. *Acta Crystallographica*, 5(6):843–843, 1952.

[8] nature materials insight. Electron and x-ray microscopy. *nature materials*, 8(4), 2009.

[9] P. E. Batson, N. Dellby, and O. L. Krivanek. Sub-angstrom resolution using aberration corrected electron optics. *Nature*, 418(6898):617–620, 2002.

[10] Joseph W. Goodman. *Introduction to Fourier optics*. Roberts company publishers, 2005.

[11] David G. Voelz. *Computational Fourier Optics: A MATLAB Tutorial.* SPIE Digital Library, 2011.

[12] D. Attwood. *Soft X-Rays and Extreme Ultraviolet Radiation: Principles and Applications.* Cambridge University Press, 2007.

[13] D. Paganin. *Coherent X-Ray Optics.* Oxford University Press, 2006.

[14] Corey Putkunz. *New Methods in Fresnel Coherent Diffractive Imaging.* PhD thesis, La Trobe University, 2011.

[15] Brian Greene. *The Elegant Universe: Superstrings, Hidden Dimensions, and the Quest for the Ultimate Theory.* New York: W.W. Norton., 1999.

[16] Max Born and Emil Wolf. *Principles of Optics.* Cambridge University Press, Cambridge, 1999.

[17] Sandra Stephan. *High-Resolution 3D Ptychography.* PhD thesis, Technishe Universitat Dresden, 2012.

[18] Daniel Parks. *X-ray Scattering Techniques for Coherent Imaging in Reflection Geometry, Measurement of Mutual Intensity, and Symmetry Determination in Disordered Materials.* PhD thesis, University of Oregon, 2013.

[19] E. Hecht. *Optics.* Addison-Wesley Publishing Company, 2 edition, 1987.

[20] V. Kohn, I. Snigireva, and A. Snigirev. Direct measurement of transverse coherence length of hard x rays from interference fringes. *Physical Review Letters*, 85(13):2745–2748, 2000.

[21] Jesse Norman Clark. *Advances in Fresnel Coherent Diffractive Imaging.* PhD thesis, La Trobe University, Australia, 2010.

[22] F. Zernike. The concept of degree of coherence and its application to optical problems. *Physica*, 5:785–795, 1938.

[23] F. R. Elder, A. M. Gurewitsch, R. V. Langmuir, and H. C. Pollock. Radiation from electrons in a synchrotron. *Physical Review*, 71(11):829–830, 1947.

[24] Albert Hofmann. *The Physics of Synchrotron Radiation.* Cambridge University Press, 2004.

[25] T. K. Sham and M. L. Rivers. A brief overview of synchrotron radiation. *Applications of Synchrotron Radiation in Low-Temperature Geochemistry and Environmental Sciences*, 49:117–147, 2002.

[26] Osterhoff. *Wave optical simulations of x-ray nano-focusing optics.* Goettingen series in X-ray Physics, 2012.

[27] P. Kirkpatrick and A. V. Baez. Formation of optical images by x-rays. *Journal of the Optical Society of America*, 38(9):766–774, 1948.

[28] Mike Ross. Kb mirrors harness x-rays science, https://news.slac.stanford.edu/features/k-b-mirrors-harness-x-rays-science.

[29] K. Yamamura, H. Mimura, K. Yamauchi, Y. Sano, A. Saito, T. Kinoshita, K. Endo, Y. Mori, A. Souvorov, M. Yabashi, K. Tamasaku, and D. Ishikawa. Aspheric surface fabrication in nm-level accuracy by numerically controlled plasma chemical vaporization machining (cvm) and elastic emission machining (eem). In *Conference on X-Ray Mirrors, Crystals and Multilayers II*, volume 4782 of *Proceedings of the Society of Photo-Optical Instrumentation Engineers (Spie)*, pages 265–270, 2002.

[30] J. Vila-Comamala, K. Jefimovs, T. Pilvi, M. Ritala, S. S. Sarkar, H. H. Solak, V. A. Guzenko, M. Stampanoni, F. Marone, J. Raabe, G. Tzvetkov, R. H. Fink, D. Grolimund, C. N. Borca, B. Kaulich, and C. David. Advanced x-ray diffractive optics. In *9th International Conference on X-Ray Microscopy*, volume 186 of *Journal of Physics Conference Series*, 2009. Times Cited: 2 Marone, Federica/J-4420-2013; Ritala, Mikko/N-7268-2013; Stampanoni, Marco/J-4099-2013; Jefimovs, Konstantins/K-1268-2014 2.

[31] C. G. Schroer and B. Lengeler. Focusing hard x rays to nanometer dimensions by adiabatically focusing lenses. *Physical Review Letters*, 94(5), 2005.

[32] K. Evans-Lutterodt, A. Stein, J. M. Ablett, N. Bozovic, A. Taylor, and D. M. Tennant. Using compound kinoform hard-x-ray lenses to exceed the critical angle limit. *Physical Review Letters*, 99(13), 2007.

[33] F. Doering, A. L. Robisch, C. Eberl, M. Osterhoff, A. Ruhlandt, T. Liese, F. Schlenkrich, S. Hoffmann, M. Bartels, T. Salditt, and H. U. Krebs. Sub-5 nm hard x-ray point focusing by a combined kirkpatrick-baez mirror and multilayer zone plate. *Optics Express*, 21(16):19311–19323, 2013.

[34] Hidekazu Mimura, Soichiro Handa, Takashi Kimura, Hirokatsu Yumoto, Daisuke Yamakawa, Hikaru Yokoyama, Satoshi Matsuyama, Kouji Inagaki, Kazuya Yamamura, Yasuhisa Sano, Kenji Tamasaku, Yoshinori Nishino, Makina Yabashi, Tetsuya Ishikawa, and Kazuto Yamauchi. Breaking the 10 nm barrier in hard-x-ray focusing. *Nature Physics*, 6(2):122–125, 2010.

[35] Christian G. Schroer. Focusing hard x rays to nanometer dimensions using fresnel zone plates. *Physical Review B*, 74(3), 2006.

[36] X-RAY DATA BOOKLET L.B.N.L. Center for x-ray optics and advanced light source.

[37] *Princeton Instruments CCD Primer.* Princeton Instruments, 2014.

[38] Medipix detectorproject: www.medipix.web.cern.ch/medipix/index.php.

[39] C. Broennimann, E. F. Eikenberry, B. Henrich, R. Horisberger, G. Huelsen, E. Pohl, B. Schmitt, C. Schulze-Briese, M. Suzuki, T. Tomizaki, H. Toyokawa, and A. Wagner. The pilatus 1m detector. *Journal of Synchrotron Radiation*, 13:120–130, 2006. Times Cited: 184 Pohl, Ehmke/I-2408-2012; Schmitt, Bernd/H-9365-2013 Schmitt, Bernd/0000-0002-5778-0680 2 184.

[40] M Howells and al. An assessment of the resolution limitation due to radiation-damage in x-ray diffraction microscopy. *Journal of Electron Spectroscopy and Related Phenomena*, 170(1-3):4–12, 2009.

[41] Albert Rose. The sensitivity performance of the human eye on an absolute scale. *Optics Express*, 38(2):196–208, 1948.

[42] R. H. T. Bates. Fourier phase problems are uniquely solvable in more than one dimension .1. underlying theory. *Optik*, 61(3):247–262, 1982.

[43] Pierre Thibault. *ALGORITHMIC METHODS IN DIFFRACTION MICROSCOPY.* PhD thesis, Cornell University, 2007.

[44] J. W. Miao, P. Charalambous, J. Kirz, and D. Sayre. Extending the methodology of x-ray crystallography to allow imaging of micrometre-sized non-crystalline specimens. *Nature*, 400(6742):342–344, 1999.

[45] Maria Civita. X-ray imaging methods: theory and applications. Master's thesis, University College of London, Condensed Matter and Materials Physics, 2013.

[46] J. R. Fienup. Phase retrieval algorithms - a comparison. *Applied Optics*, 21(15):2758–2769, 1982.

[47] V. Elser. Phase retrieval by iterated projections. *Journal of the Optical Society of America a-Optics Image Science and Vision*, 20(1):40–55, 2003. Times Cited: 243 247.

[48] GARTH JONATHAN WILLIAMS. *MICROSCOPY OF GOLD MICROCRYSTALS BY COHERENT X-RAY DIFFRACTIVE IMAGING*. PhD thesis, University of Illinois at Urbana-Champaign, 2005.

[49] S. Marchesini, H. He, H. N. Chapman, S. P. Hau-Riege, A. Noy, M. R. Howells, U. Weierstall, and J. C. H. Spence. X-ray image reconstruction from a diffraction pattern alone. *Physical Review B*, 68(14), 2003.

[50] R. Harder, M. Liang, Y. Sun, Y. Xia, and I. K. Robinson. Imaging of complex density in silver nanocubes by coherent x-ray diffraction. *New Journal of Physics*, 12, 2010.

[51] Xiaojing Huang, Ross Harder, Gang Xiong, Xiaowen Shi, and Ian Robinson. Propagation uniqueness in three-dimensional coherent diffractive imaging. *Physical Review B*, 83(22):224109, 2011.

[52] Richard Bean. *Domain Structure Imaging with Bragg Geometry X-ray Ptychography*. PhD thesis, University College of London, 2012.

[53] S. Marchesini. A unified evaluation of iterative projection algorithms for phase retrieval. *Review of Scientific Instruments*, 78(1), 2007.

[54] Brian Abbey. From grain boundaries to single defects: A review of coherent methods for materials imaging in the x-ray sciences. *Jom*, 65(9):1183–1201, 2013.

[55] I. K. Robinson, I. A. Vartanyants, G. J. Williams, M. A. Pfeifer, and J. A. Pitney. Reconstruction of the shapes of gold nanocrystals using coherent x-ray diffraction. *Physical Review Letters*, 87(19), 2001.

[56] J. W. Miao, T. Ishikawa, B. Johnson, E. H. Anderson, B. Lai, and K. O. Hodgson. High resolution 3d x-ray diffraction microscopy. *Physical Review Letters*, 89(8), 2002.

[57] H. N. Chapman, A. Barty, S. Marchesini, A. Noy, S. R. Hau-Riege, C. Cui, M. R. Howells, R. Rosen, H. He, J. C. H. Spence, U. Weierstall, T. Beetz, C. Jacobsen, and D. Shapiro. High-resolution ab initio three-dimensional x-ray diffraction microscopy. *Journal of the Optical Society of America a-Optics Image Science and Vision*, 23(5):1179–1200, 2006.

[58] A. Barty, S. Marchesini, H. N. Chapman, C. Cui, M. R. Howells, D. A. Shapiro, A. M. Minor, J. C. H. Spence, U. Weierstall, J. Ilavsky, A. Noy, S. P. Hau-Riege, A. B. Artyukhin, T. Baumann, T. Willey, J. Stolken, T. van Buuren, and J. H. Kinney. Three-dimensional coherent x-ray diffraction imaging of a ceramic nanofoam: Determination of structural deformation mechanisms. *Physical Review Letters*, 101(5), 2008.

[59] D. Shapiro, P. Thibault, T. Beetz, V. Elser, M. Howells, C. Jacobsen, J. Kirz, E. Lima, H. Miao, A. M. Neiman, and D. Sayre. Biological imaging by soft x-ray diffraction microscopy. *Proceedings of the National Academy of Sciences of the United States of America*, 102(43):15343–15346, 2005.

[60] Yoshinori Nishino, Yukio Takahashi, Naoko Imamoto, Tetsuya Ishikawa, and Kazuhiro Maeshima. Three-dimensional visualization of a human chromosome using coherent x-ray diffraction. *Physical Review Letters*, 102(1), 2009.

[61] Changyong Song, Huaidong Jiang, Adrian Mancuso, Bagrat Amirbekian, Li Peng, Ren Sun, Sanket S. Shah, Z. Hong Zhou, Tetsuya Ishikawa, and Jianwei Miao. Quantitative imaging of single, unstained viruses with coherent x rays. *Physical Review Letters*, 101(15), 2008.

[62] J. W. Miao, K. O. Hodgson, T. Ishikawa, C. A. Larabell, M. A. LeGros, and Y. Nishino. Imaging whole escherichia coli bacteria by using single-particle x-ray diffraction. *Proceedings of the National Academy of Sciences of the United States of America*, 100(1):110–112, 2003.

[63] Laura Shemilt. *Coherent Diffraction Imaging and Ptychography of Human Metaphase Chromosomes*. PhD thesis, University College of London, 2014.

[64] John Miao. Coherent diffraction imaging and its applications in nanoscience and biology.

[65] J. M. Zuo, I. Vartanyants, M. Gao, R. Zhang, and L. A. Nagahara. Atomic resolution imaging of a carbon nanotube from diffraction intensities. *Science*, 300(5624):1419–1421, 2003.

[66] S. Kneip, C. McGuffey, J. L. Martins, S. F. Martins, C. Bellei, V. Chvykov, F. Dollar, R. Fonseca, C. Huntington, G. Kalintchenko, A. Maksimchuk, S. P. D. Mangles, T. Matsuoka, S. R. Nagel, C. A. J. Palmer, J. Schreiber, K. Ta Phuoc, A. G. R. Thomas, V. Yanovsky, L. O. Silva, K. Krushelnick, and Z. Najmudin. Bright spatially coherent synchrotron x-rays from a table-top source. *Nature Physics*, 6(12):980–983, 2010.

[67] Richard L. Sandberg, Changyong Song, Przemyslaw W. Wachulak, Daisy A. Raymondson, Ariel Paul, Bagrat Amirbekian, Edwin Lee, Anne E. Sakdinawat, Chan La-O-Vorakiat, Mario C. Marconi, Carmen S. Menoni, Margaret M. Murnane, Jorge J. Rocca, Henry C. Kapteyn, and Jianwei Miao. High numerical aperture tabletop soft x-ray diffraction microscopy with 70-nm resolution. *Proceedings of the National Academy of Sciences of the United States of America*, 105(1):24–27, 2008.

[68] Ruben A. Dilanian, Bo Chen, Garth J. Williams, Harry M. Quiney, Keith A. Nugent, Sven Teichmann, Peter Hannaford, Lap V. Dao, and Andrew G. Peele. Diffractive imaging using a polychromatic high-harmonic generation soft-x-ray source. *Journal of Applied Physics*, 106(2), 2009.

[69] B. D. Patterson, R. Abela, H. H. Braun, R. Ganter, B. Pedrini, M. Pedrozzi, S. Reiche, and M. van Daalen. Ultrafast phenomena at the nanoscale: Novel science opportunities at the swissfel x-ray laser. In *Conference on Short-Wavelength Imaging and Spectroscopy Sources*, volume 8678 of *Proceedings of SPIE*, 2012.

[70] K. J. Gaffney and H. N. Chapman. Imaging atomic structure and dynamics with ultrafast x-ray scattering. *Science*, 316(5830):1444–1448, 2007.

[71] R. Neutze, R. Wouts, D. van der Spoel, E. Weckert, and J. Hajdu. Potential for biomolecular imaging with femtosecond x-ray pulses. *Nature*, 406(6797):752–757, 2000.

[72] John P. Overington, Bissan Al-Lazikani, and Andrew L. Hopkins. Opinion - how many drug targets are there? *Nature Reviews Drug Discovery*, 5(12):993–996, 2006.

[73] P. Godard, M. Allain, and V. Chamard. Imaging of highly inhomogeneous strain field in nanocrystals using x-ray bragg ptychography: A numerical study. *PHYSICAL REVIEW B*, 84(14), OCT 11 2011.

[74] Michael W. M. Jones, Kirstin Elgass, Mark D. Junker, Mac B. Luu, Michael T. Ryan, Andrew G. Peele, and Grant A. van Riessen. Mapping biological composition through quantitative phase and absorption x-ray ptychography. *Scientific Reports*, 4, 2014.

[75] M Dierolf and al. Ptychographic coherent diffractive imaging of weakly scattering specimens. *New journal of physics*, 12(035017), 2010.

[76] Jesse N. Clark, Corey T. Putkunz, Evan K. Curwood, David J. Vine, Robert Scholten, Ian McNulty, Keith A. Nugent, and Andrew G. Peele. Dynamic sample imaging in coherent diffractive imaging. *Optics Letters*, 36(11):1954–1956, 2011.

[77] L. W. Whitehead, G. J. Williams, H. M. Quiney, D. J. Vine, R. A. Dilanian, S. Flewett, K. A. Nugent, A. G. Peele, E. Balaur, and I. McNulty. Diffractive imaging using partially coherent x rays. *PHYSICAL REVIEW LETTERS*, 103(24), DEC 11 2009.

[78] Fucai Zhang, Isaac Peterson, Joan Vila-Comamala, Ana Diaz Felisa Berenguer, Richard Bean, Bo Chen, Andreas Menzel, Ian K. Robinson, and John M. Rodenburg. Translation position determination in ptychographic coherent diffraction imaging. *Optics Express*, 21(11):13592–13606, 2013.

[79] J. M. Rodenburg and H. M. L. Faulkner. A phase retrieval algorithm for shifting illumination. *Applied Physics Letters*, 85(20):4795–4797, 2004.

[80] P. D. Nellist, B. C. McCallum, and J. M. Rodenburg. Resolution beyond the information limit in transmission electron-microscopy. *Nature*, 374(6523):630–632, 1995.

[81] Manuel Guizar-Sicairos and James R. Fienup. Phase retrieval with transverse translation diversity: a nonlinear optimization approach. *Optics Express*, 16(10):7264–7278, 2008.

[82] Manuel Guizar-Sicairos. *Methods for Coherent Lensless Imaging and X-Ray Wavefront Measurement.* PhD thesis, University of Rochester Rochester, New York, 2010.

[83] Pierre Thibault, Martin Dierolf, Oliver Bunk, Andreas Menzel, and Franz Pfeiffer. Probe retrieval in ptychographic coherent diffractive imaging. *Ultramicroscopy*, 109(4):338–343, 2009.

[84] Pierre Thibault, Martin Dierolf, Oliver Bunk, Andreas Menzel, and Franz Pfeiffer. Probe retrieval in ptychographic coherent diffractive imaging. *Ultramicroscopy*, 109(4):338–343, 2009.

[85] Max Hantke. Structure study on giant viruses with x-ray lasers. Master's thesis, University of Goettingen, 2013.

[86] B. C. McCallum and J. M. Rodenburg. 2-dimensional demonstration of wigner phase-retrieval microscopy in the stem configuration. *Ultramicroscopy*, 45(3-4):371–380, 1992.

[87] Fucai Zhang and J. M. Rodenburg. Phase retrieval based on wave-front relay and modulation. *Physical Review B*, 82(12), 2010. Times Cited: 11 11.

[88] S. Marchesini. Iterative algorithms for ptychographic phase retrieval. In archive of Cornell University, 2011.

[89] R. M. Goldstein, H. A. Zebker, and C. L. Werner. Satellite radar interferometry - two-dimensional phase unwrapping. *Radio Science*, 23(4):713–720, 1988.

[90] J. R. Fienup. Invariant error metrics for image reconstruction. *Applied Optics*, 36(32):8352–8357, 1997.

[91] Xiaojing Huang, Hanfei Yan, Ross Harder, Yeukuang Hwu, Ian K. Robinson, and Yong S. Chu. Optimization of overlap uniformness for ptychography. *Optics Express*, 22(10):12634–12644, 2014.

[92] H. Vogel. Better way to construct the sunflower head. *Mathematical Biosciences*, 44(3-4):179–182, 1979.

[93] Andrew M. Maiden and John M. Rodenburg. An improved ptychographical phase retrieval algorithm for diffractive imaging. *Ultramicroscopy*, 109(10):1256–1262, 2009.

[94] P. Thibault and M. Guizar-Sicairos. Maximum-likelihood refinement for coherent diffractive imaging. *New Journal of Physics*, 14, 2012.

[95] Pierre Godard, Marc Allain, Virginie Chamard, and John Rodenburg. Noise models for low counting rate coherent diffraction imaging. *Optics Express*, 20(23):25914–25934, 2012.

[96] A. M. Maiden, M. J. Humphry, M. C. Sarahan, B. Kraus, and J. M. Rodenburg. An annealing algorithm to correct positioning errors in ptychography. *Ultramicroscopy*, 120:64–72, 2012.

[97] Yukio Takahashi, Akihiro Suzuki, Nobuyuki Zettsu, Yoshiki Kohmura, Yasunori Senba, Haruhiko Ohashi, Kazuto Yamauchi, and Tetsuya Ishikawa. Towards high-resolution ptychographic x-ray diffraction microscopy. *Physical Review B*, 83(21), 2011.

[98] Ashish Tripathi, Ian McNulty, and Oleg G. Shpyrko. Ptychographic overlap constraint errors and the limits of their numerical recovery using conjugate gradient descent methods. *Optics Express*, 22(2):1452–1466, 2014.

[99] Alex Shenfield and John M. Rodenburg. Evolutionary determination of experimental parameters for ptychographical imaging. *Journal of Applied Physics*, 109(12), 2011.

[100] Mike Beckers, Tobias Senkbeil, Thomas Gorniak, Klaus Giewekemeyer, Tim Salditt, and Axel Rosenhahn. Drift correction in ptychographic diffractive imaging. *Ultramicroscopy*, 126:44–47, 2013.

[101] Manuel Guizar-Sicairos, Samuel T. Thurman, and James R. Fienup. Efficient subpixel image registration algorithms. *Optics Letters*, 33(2):156–158, 2008.

[102] Samuel Flewett, Harry M. Quiney, Chanh Q. Tran, and Keith A. Nugent. Extracting coherent modes from partially coherent wavefields. *Optics Letters*, 34(14):2198–2200, 2009.

[103] Garth J. Williams, Harry M. Quiney, Andrew G. Peele, and Keith A. Nugent. Coherent diffractive imaging and partial coherence. *Physical Review B*, 75(10), 2007.

[104] C. Chang, P. Naulleau, and D. Attwood. Analysis of illumination coherence properties in small-source systems such as synchrotrons. *Applied Optics*, 42(14):2506–2512, 2003.

[105] A. Singer, I. A. Vartanyants, M. Kuhlmann, S. Duesterer, R. Treusch, and J. Feldhaus. Transverse-coherence properties of the free-electron-laser flash at desy. *Physical Review Letters*, 101(25), 2008.

[106] F. Pfeiffer, O. Bunk, C. Schulze-Briese, A. Diaz, T. Weitkamp, C. David, J. F. van der Veen, I. Vartanyants, and I. K. Robinson. Shearing interferometer

for quantifying the coherence of hard x-ray beams. *Physical Review Letters*, 94(16), 2005.

[107] J. N. Clark, X. Huang, R. Harder, and I. K. Robinson. High-resolution three-dimensional partially coherent diffraction imaging. *NATURE COMMUNICATIONS*, 3, AUG 2012.

[108] Pierre Thibault and Andreas Menzel. Reconstructing state mixtures from diffraction measurements. *Nature*, 494(7435):68–71, 2013.

[109] D. H. Parks, X. Shi, and S. D. Kevan. Partially coherent x-ray diffractive imaging of complex objects. *Physical Review A*, 89(6), 2014.

[110] Nicolas Burdet, Xiaowen Shi, Daniel Parks, Jesse N. Clark, Xiaojing Huang, Stephen D. Kevan, and Ian K. Robinson. Evaluation of partial coherence correction in x-ray ptychography. *Optics Express*, 23(5):5452–5467, 2015.

[111] Keith A. Nugent. Coherent methods in the x-ray sciences. *Advances in Physics*, 59(1):1–99, 2010.

[112] Jesse N. Clark, Xiaojing Huang, Ross J. Harder, and Ian K. Robinson. Dynamic imaging using ptychography. *Physical Review Letters*, 112(11), 2014.

[113] F. Maia. Optimization and parallelization of ptychography reconstruction code. unpublished work, 2013.

[114] Matlab. Matlab parallel computing toolbox, http://uk.mathworks.com/products/parallel-computing/.

[115] Matlab. Using parfor loops getting up and running, http://blogs.mathworks.com/loren/2009/10/02/using-parfor-loops-getting-up-and-running/.

[116] Parellel computing with Matlab on Amazon Elastic Compute cloud.

[117] R. Cerniak. *X-Ray Computed Tomography in Biomedical Engineering.* Springer, 2011.

[118] Nitin P. Ghonge. Computed tomography in the 21st century: Current status future prospects, 2013.

[119] Jan Moritz Feldkamp. *Scanning Small-Angle X-Ray Scanning Small-Angle X-Ray Scattering Tomography.* PhD thesis, Technische Universitat Dresden, 2009.

[120] Martin Dierolf, Andreas Menzel, Pierre Thibault, Philipp Schneider, Cameron M. Kewish, Roger Wepf, Oliver Bunk, and Franz Pfeiffer. Ptychographic x-ray computed tomography at the nanoscale. *NATURE*, 467(7314):436–U82, SEP 23 2010.

[121] W. Denk and H. Horstmann. Serial block-face scanning electron microscopy to reconstruct three-dimensional tissue nanostructure. *Plos Biology*, 2(11):1900–1909, 2004.

[122] Huaidong Jiang, Changyong Song, Chien-Chun Chen, Rui Xu, Kevin S. Raines, Benjamin P. Fahimian, Chien-Hung Lu, Ting-Kuo Lee, Akio Nakashima, Jun Urano, Tetsuya Ishikawa, Fuyuhiko Tamanoi, and Jianwei Miao. Quantitative 3d imaging of whole, unstained cells by using x-ray diffraction microscopy. *Proceedings of the National Academy of Sciences of the United States of America*, 107(25):11234–11239, 2010.

[123] Paul A. Midgley and Rafal E. Dunin-Borkowski. Electron tomography and holography in materials science. *Nature Materials*, 8(4):271–280, 2009.

[124] Ana Diaz, Pavel Trtik, Manuel Guizar-Sicairos, Andreas Menzel, Pierre Thibault, and Oliver Bunk. Quantitative x-ray phase nanotomography. *Physical Review B*, 85(2), 2012.

[125] A. Diaz, M. Guizar-Sicairos, A. Poeppel, A. Menzel, and O. Bunk. Characterization of carbon fibers using x-ray phase nanotomography. *Carbon*, 67:98–103, 2014.

[126] M. Holler, J. Raabe, A. Diaz, M. Guizar-Sicairos, C. Quitmann, A. Menzel, and O. Bunk. An instrument for 3d x-ray nano-imaging. *Review of Scientific Instruments*, 83(7), 2012.

[127] M. Holler, A. Diaz, M. Guizar-Sicairos, P. Karvinen, Elina Farm, Emma Harkonen, Mikko Ritala, A. Menzel, J. Raabe, and O. Bunk. X-ray ptychographic computed tomography at 16 nm isotropic 3d resolution. *Scientific Reports*, 4, 2014.

[128] London Centre for Nanotechnology. Understanding anti corrosion paint, http://www.london-nano.com/research-and-facilities/highlight/understanding-anti-corrosion-paint.

[129] Bo Chen, Manuel Guizar-Sicairos, Gang Xiong, Laura Shemilt, Ana Diaz, John Nutter, Nicolas Burdet, Suguo Huo, Joel Mancuso, Alexander Monteith, Frank Vergeer, Andrew Burgess, and Ian Robinson. Three-dimensional structure analysis and percolation properties of a barrier marine coating. *SCIENTIFIC REPORTS*, 3, JAN 31 2013.

[130] Bo Chen. *X-ray Imaging of Three-dimensional Spatial Structure of Coatings*. PhD thesis, University College of London, 2012.

[131] Elaine Chiu, Fasseli Coulibaly, and Peter Metcalf. Insect virus polyhedra, infectious protein crystals that contain virus particles. *Current Opinion in Structural Biology*, 22(2):234–240, 2012.

[132] Xiaoyun Ji, Geoff Sutton, Gwyndaf Evans, Danny Axford, Robin Owen, and David I. Stuart. How baculovirus polyhedra fit square pegs into round holes to robustly package viruses. *Embo Journal*, 29(2):505–514, 2010.

[133] Mark Pfeiffer. *STRUCTURAL STUDIES OF LEAD NANOCRYSTALS USING COHERENT X-RAY DIFFRACTION*. PhD thesis, University of Illinois at Urbana-Champaign, 2005.

[134] John Allen Pitney. *Coherent X-ray diffraction*. PhD thesis, University of Illinois at Urbana-Champaign, 2000.

[135] Sebastien Boutet. *Coherent X-ray diffractive imaging and nucleation of protein crystals*. PhD thesis, University of Illinois at Urbana-Champaign, 2005.

[136] Johannes Gulden. *Nano Structured Materials Studied by Coherent X-ray Diffraction*. PhD thesis, University of Hamburg, 2013.

[137] APS SCIENCE 2011. *Argonne National Laboratory*, 2012.

[138] Xiaojing Huang, Michael Wojcik, Nicolas Burdet, Isaac Peterson, Graeme R. Morrison, David J. Vine, Daniel Legnini, Ross Harder, Yong S. Chu, and Ian K. Robinson. Quantitative x-ray wavefront measurements of fresnel zone plate and k-b mirrors using phase retrieval. *Optics Express*, 20(21):24038–24048, 2012.

[139] I. K. Robinson, F. Pfeiffer, I. A. Vartanyants, Y. G. Sun, and Y. N. Xia. Enhancement of coherent x-ray diffraction from nanocrystals by introduction of x-ray optics. *Optics Express*, 11(19):2329–2334, 2003.

[140] Miguel A. G. Aranda, Felisa Berenguer, Richard J. Bean, Xiaowen Shi, Gang Xiong, Stephen P. Collins, Colin Nave, and Ian K. Robinson. Coherent x-ray diffraction investigation of twinned microcrystals. *Journal of Synchrotron Radiation*, 17:751–760, 2010.

[141] P. J. Eng, M. Newville, M. L. Rivers, and S. R. Sutton. Dynamically figured kirkpatrick baez x-ray micro-focusing optics. In *Conference on X-Ray Microfocusing - Applications and Techniques*, volume 3449 of *Proceedings of the Society of Photo-Optical Instrumentation Engineers (Spie)*, pages 145–156, 1998.

[142] Graeme Morrison. Technical report: Tungsten test patterns from zoneplates ltd. Technical report, University College of London, 2013.

[143] Nicolas Burdet, Graeme R. Morrison, Xiaojing Huang, Xiaowen Shi, Jesse N. Clark, Fucai Zhang, Maria Civita, Ross Harder, and Ian K. Robinson. Observations of artefacts in the x-ray ptychography method. *Optics Express*, 22(9):10294–10303, 2014.

[144] Cameron M. Kewish, Manuel Guizar-Sicairos, Chian Liu, Jun Qian, Bing Shi, Christa Benson, Ali M. Khounsary, Joan Vila-Comamala, Oliver Bunk, James R. Fienup, Albert T. Macrander, and Lahsen Assoufid. Reconstruction of an astigmatic hard x-ray beam and alignment of k-b mirrors from ptychographic coherent diffraction data. *Optics Express*, 18(22):23420–23427, 2010.

[145] Hidekazu Mimura, Hirokatsu Yumoto, Satoshi Matsuyama, Soichiro Handa, Takashi Kimura, Yasuhisa Sano, Makina Yabashi, Yoshinori Nishino, Kenji Tamasaku, Tetsuya Ishikawa, and Kazuto Yamauchi. Direct determination of the wave field of an x-ray nanobeam. *Physical Review A*, 77(1), 2008.

[146] A. J. Morgan, A. V. Martin, A. J. D'Alfonso, C. T. Putkunz, and L. J. Allen. Direct exit-wave reconstruction from a single defocused image. *Ultramicroscopy*, 111(9-10):1455–1460, 2011.

[147] H. Yumoto, H. Mimura, S. Matsuyama, S. Handa, Y. Sano, M. Yabashi, Y. Nishino, K. Tamasaku, T. Ishikawa, and K. Yamauchi. At-wavelength figure metrology of hard x-ray focusing mirrors. *Review of Scientific Instruments*, 77(6), 2006.

[148] H. M. Quiney, A. G. Peele, Z. Cai, D. Paterson, and K. A. Nugent. Diffractive imaging of highly focused x-ray fields. *Nature Physics*, 2(2):101–104, 2006.

[149] Xiowen Shi. *Coherent X-ray diffraction imaging and ptychography on silicon-on- insulator nanostructures.* PhD thesis, University College of London, 2012.

[150] F. Mastropietro, D. Carbone, A. Diaz, J. Eymery, A. Sentenac, T. H. Metzger, V. Chamard, and V. Favre-Nicolin. Coherent x-ray wavefront reconstruction of a partially illuminated fresnel zone plate. *Optics Express*, 19(20):19223–19232, 2011.

[151] Michael J. Wojcik, Vishwanath Joshi, Anirudha V. Sumant, Ralu Divan, Leonidas E. Ocola, Ming Lu, and Derrick C. Mancini. Nanofabrication of x-ray zone plates using ultrananocrystalline diamond molds and electroforming. *Journal of Vacuum Science Technology B*, 28(6):C6P30–C6P35, 2010.

[152] James E. Butler and Anirudha V. Sumant. The cvd of nanodiamond materials. *Chemical Vapor Deposition*, 14(7-8):145–160, 2008.

[153] Albert Fannjiang and Wenjing Liao. Phase retrieval with random phase illumination. *Journal of the Optical Society of America a-Optics Image Science and Vision*, 29(9):1847–1859, 2012.

[154] Oliver Bunk, Martin Dierolf, Soren Kynde, Ian Johnson, Othmar Marti, and Franz Pfeiffer. Influence of the overlap parameter on the convergence of the ptychographical iterative engine. *Ultramicroscopy*, 108(5):481–487, 2008.

[155] Andrew M. Maiden, Martin J. Humphry, Fucai Zhang, and John M. Rodenburg. Superresolution imaging via ptychography. *Journal of the Optical Society of America a-Optics Image Science and Vision*, 28(4):604–612, 2011.

[156] Zoneplates ltd, 8 south way, claverings industrial estate, london n9 oab, uk, url http://www.zoneplates.com.

[157] Ian Robinson and Ross Harder. Coherent x-ray diffraction imaging of strain at the nanoscale. *Nature Materials*, 8(4):291–298, 2009.

[158] A. A. Minkevich, E. Fohtung, T. Slobodskyy, M. Riotte, D. Grigoriev, T. Metzger, A. C. Irvine, V. Novak, V. Holy, and T. Baumbach. Strain field in (ga,mn)as/gaas periodic wires revealed by coherent x-ray diffraction. *Epl*, 94(6), 2011.

[159] J. N. Clark, L. Beitra, G. Xiong, A. Higginbotham, D. M. Fritz, H. T. Lemke, D. Zhu, M. Chollet, G. J. Williams, M. Messerschmidt, B. Abbey, R. J. Harder, A. M. Korsunsky, J. S. Wark, and I. K. Robinson. Ultrafast

three-dimensional imaging of lattice dynamics in individual gold nanocrystals. *Science*, 341(6141):56–59, 2013.

[160] Neil W. Ashcroft and N. David Mermin. *Solid State Physics*. Harcourt Brace, college, 1976.

[161] Marcus C. Newton, Steven J. Leake, Ross Harder, and Ian K. Robinson. Three-dimensional imaging of strain in a single zno nanorod. *Nature Materials*, 9(2):120–124, 2010.

[162] J. C. H. Spence, U. Weierstall, and M. Howells. Coherence and sampling requirements for diffractive imaging. *Ultramicroscopy*, 101(2-4):149–152, 2004.

[163] Wonsuk Cha, Sanghoon Song, Nak Cheon Jeong, Ross Harder, Kyung Byung Yoon, Ian K. Robinson, and Hyunjung Kim. Exploration of crystal strains using coherent x-ray diffraction. *New Journal of Physics*, 12, 2010.

[164] M. Lohmeier and E. Vlieg. Angle calculations for a 6-circle surface x-ray diffractometer. *Journal of Applied Crystallography*, 26:706–716, 1993.

[165] B. W. Batterman and H. Cole. Dynamical diffraction of x rays by perfect crystals. *Reviews of Modern Physics*, 36(3):681–, 1964. Times Cited: 1062 1064.

[166] Wonsuk Cha, Nak Cheon Jeong, Sanghoon Song, Hyun-jun Park, Pham Tung Cao Thanh, Ross Harder, Bobae Lim, Gang Xiong, Docheon Ahn, Ian McNulty, Jungho Kim, Kyung Byung Yoon, Ian K. Robinson, and Hyunjung Kim. Core-shell strain structure of zeolite microcrystals. *Nature Materials*, 12(8):729–734, 2013.

[167] M. E. Davis. Ordered porous materials for emerging applications. *Nature*, 417(6891):813–821, 2002.

[168] S. H. Park, R. W. G. Kunstleve, H. Graetsch, and H. Gies. The thermal expansion of the zeolites mfi, afi, doh, ddr, and mtn in their calcined and as synthesized forms, 1997 1997.

[169] R. Vonballmoos and W. M. Meier. Zoned aluminum distribution in synthetic zeolite zsm-5. *Nature*, 289(5800):782–783, 1981.

[170] S. O. Hruszkewycz, M. V. Holt, C. E. Murray, J. Bruley, J. Holt, A. Tripathi, O. G. Shpyrko, I. McNulty, M. J. Highland, and P. H. Fuoss. Quantitative

nanoscale imaging of lattice distortions in epitaxial semiconductor heterostructures using nanofocused x-ray bragg projection ptychography. *Nano Letters*, 12(10):5148–5154, 2012.

[171] Martin V. Holt, Stephan O. Hruszkewycz, Conal E. Murray, Judson R. Holt, Deborah M. Paskiewicz, and Paul H. Fuoss. Strain imaging of nanoscale semiconductor heterostructures with x-ray bragg projection ptychography. *Physical review letters*, 112(16):165502–165502, 2014. 0.

[172] S. Roy, D. Parks, K. A. Seu, R. Su, J. J. Turner, W. Chao, E. H. Anderson, S. Cabrini, and S. D. Kevan. Lensless x-ray imaging in reflection geometry. *Nature Photonics*, 5(4):243–245, 2011.

[173] Ross Harder and Ian K. Robinson. Coherent x-ray diffraction imaging of morphology and strain in nanomaterials. *Jom*, 65(9):1202–1207, 2013.

[174] F. Berenguer, P. Godard, M. Allain, J. M. Belloir, A. Talneau, S. Ravy, and V. Chamard. X-ray lensless microscopy from undersampled diffraction intensities. *Physical Review B*, 88(14), 2013.

[175] Lorenz-M. Stadler, Ross Harder, Ian K. Robinson, Christian Rentenberger, H. Peter Karnthaler, Bogdan Sepiol, and Gero Vogl. Coherent x-ray diffraction imaging of grown-in antiphase boundaries in fe(65)al(35). *Physical Review B*, 76(1), 2007.

[176] C. Peroz and C. Villard. Flux flow properties of niobium thin films in clean and dirty superconducting limits. *Physical Review B*, 72(1), 2005.

[177] R. I. Barabash, W. Donner, and H. Dosch. X-ray scattering from misfit dislocations in heteroepitaxial films: The case of nb(110) on al2o3. *Applied Physics Letters*, 78(4):443–445, 2001.

[178] C. P. Flynn. Constraints on the growth of metallic superlattices. *Journal of Physics F-Metal Physics*, 18(9):L195–L200, 1988.

[179] Manuel Guizar-Sicairos, Ana Diaz, Andreas Menzel, and Oliver Bunk. X-ray phase nanotomography through ptychographic coherent lensless imaging. *22nd Congress of the International Commission for Optics: Light for the Development of the World*, 8011, 2011.

[180] csaxs, coherent x-ray scattering group at sls, http://www.psi.ch/coherent-x-ray-scattering/coherent-x-ray-scattering-group.